Fundamental physics with supermassive black holes binaries from the detection of gravitational waves with LISA

Chantal Pitte

To cite this version:

Chantal Pitte. Fundamental physics with supermassive black holes binaries from the detection of gravitational waves with LISA. General Relativity and Quantum Cosmology [gr-qc]. Université Paris-Saclay, 2024. English. NNT : 2024UPASP086 . tel-04957385

HAL Id: tel-04957385
https://theses.hal.science/tel-04957385v1

Submitted on 19 Feb 2025

Fundamental physics with supermassive black hole binaries from the detection of gravitational waves with LISA

Physique fondamentale avec des binaires de trous noirs supermassifs à partir de la détection d'ondes gravitationnelles avec LISA

Thèse de doctorat de l'université Paris-Saclay

École doctorale n° 576, Particules, hadrons, énergie et noyau: instrumentation, image, cosmos et simulation, PHENIICS
Spécialité de doctorat: Physique des particules
Graduate School : Physique. Référent : Faculté des sciences d'Orsay

Thèse préparée dans la unité de recherche **Département de Physique des Particules (Université Paris-Saclay, CEA)**, sous la direction de **Marc BESANÇON**, Directeur de recherche, CEA Université Paris-Saclay (CEA/IRFU/DPhP)

Thèse soutenue à Paris-Saclay, le 23 Septembre 2024, par

Chantal Pitte

THESE DE DOCTORAT

NNT : 2024UPASP086

Composition du jury

Membres du jury avec voix délibérative

Karim NOUI Professeur, Université Paris-Saclay, Laboratoire de Physique des 2 Infinis, Irène Joliot-Curie (IJCLab)	Président
Danièle STEER Professeur, Laboratoire de Physique de l'Ecole Normale Supérieure (LPENS)	Rapporteuse & Examinatrice
Jonathan GAIR Directeur de recherche, Max Planck Institute for gravitational physics, Albert Einstein Institute (AEI)	Rapporteur & Examinateur
Edwige TOURNEFIER Directrice de recherche CNRS, Laboratoire d'Annecy de Physique de Particules (LAPP)	Examinatrice
Yves LEMIERE Maitre de conférence, Normandie Université (UNICAEN), Laboratoire de Physique Corpusculaire (LPCCaen)	Examinateur

université
PARIS-SACLAY

ÉCOLE DOCTORALE
Particules, hadrons, énergie et noyau : instrumentation, imagerie, cosmos et simulation (PHENIICS)

Titre: Physique fondamentale avec des binaires de trous noirs supermassifs à partir de la detection d'ondes gravitationnelles avec LISA

Mots clés: ondes gravitationnelles, binaires de trous noirs, tests de la relativité générale

Résumé: Suite à la publication sur la relativité générale (RG) par Einstein en 1915, la communauté scientifique a exploré ses limites. La découverte des trous noirs (TN) comme solutions aux équations d'Einstein a révélé des potentiels échecs de la RG, indiquant la nécessité d'un cadre plus large. En particulier, les singularités au centre des TN, avec masse et densité d'énergie infinies, perturbent l'espace-temps, tandis que les TN astrophysiques ont masse et énergie finies. Les singularités suggèrent que la RG doit être améliorée ou remplacée par une théorie plus fondamentale, possiblement quantique. Coupler la RG à la théorie quantique des champs montrent des déviations, et l'évaporation des TN par radiation de Hawking introduit le paradoxe de la perte d'information, soulignant le besoin d'une théorie alternative. Ce manuscrit quantifie la sensibilité de l'antenne spatiale interféromètre laser (LISA) à observer des déviations de la RG via le théorème du no-hair, stipulant qu'un TN astrophysique, principalement un TN de Kerr, est caractérisé par sa masse et son spin. Après la collision de deux TN, le TN résiduel se stabilise par radiation d'ondes gravitationnelles dans une phase appelée ringdown, où la forme d'onde est décomposée en ondes amorties caractérisées par des modes quasi-normaux (QNM). En connaissant les QNM d'un TN, on peut déterminer ses paramètres intrinsèques. Dans la RG, la masse et le spin dérivés de chaque QNM doivent être cohérents. Dans certaines théories alternatives, cette cohérence n'est plus valide. La relation entre masse et spin dans les déviations de la RG pour différents QNM est unique à la théorie alternative, souvent nécessitant des paramètres supplémentaires. Évaluer les déviations de la RG est mieux fait en adoptant une approche agnostique au modèle, supposant la RG avec petites déviations. Cette étude suit cette approche en permettant des déviations fractionnelles dans les QNM décrivant le ringdown. J'étudie l'interaction des harmoniques supérieures dans la description complète de l'inspiral-fusion-ringdown observée par le détecteur. La gamme de fréquences des ondes gravitationnelles dépend de la masse des sources. La réponse et la sensibilité de LISA variant avec la fréquence, en consequence le poids relatif des harmoniques supérieures varie selon les sources. Les sources "légères", autour de $10^5 M_\odot$, se trouvent à la limite de la sensibilité haute fréquence de LISA, empêchant l'observation du ringdown. Les sources "lourdes", autour de $10^8 M_\odot$, se trouvent dans la bande de basses fréquences, adoucir l'inspiral avec les phases de fusion et ringdown contribuant principalement à la détectabilité. D'ailleurs, la réponse de LISA dépendante de la fréquence, peut rendre les modes supérieurs $(3,3)$ ou $(4,4)$ plus dominant dans le rapport signal/bruit que l'harmonique principal $(2,2)$. Inclure les harmoniques supérieures et des caractéristiques comme l'excentricité ou la précession est nécessaire pour estimer avec précision les paramètres de la source, essentiels pour les tests de la RG. Comprendre la réponse de LISA selon différents paramètres de la source, combiné à la connaissance des perturbations des TN, fournit une base pour développer des tests de la RG dans la phase de ringdown. J'ai développé un code, Lisaring, intégrant ces concepts et incluant la réponse de LISA pour diverses descriptions de ringdown. Des outils d'analyse des données temporelles dans un cadre bayésien sont également inclus. J'ai évalué la sensibilité de LISA à détecter des déviations de la RG dans la phase de ringdown d'une source. Différentes hypothèses sur le prior de paramètres peut impacter les résultats finaux. Dans des conditions spécifiques, la précision d'estimation des QNM et des déviations fractionnelles peut être calculée pour différentes sources. Notamment, LISA pourrait tester la RG avec une incertitude de $5 \times 10^{-3}\%$ dans le mode $(3,3,0)$, quantifiant ainsi la sensibilité de LISA aux déviations de la RG.

université
PARIS-SACLAY

ÉCOLE DOCTORALE
Particules, hadrons, énergie et noyau :
instrumentation, imagerie, cosmos
et simulation (PHENIICS)

Title: Fundamental physics with supermassive black hole binaries from the detection of gravitational waves with LISA

Keywords: Gravitational Waves, Black Hole Binaries, tests of General Relativity

Abstract: Following the publication of Einstein's General Relativity (GR) in 1915, scientists began exploring its boundaries. The discovery of black holes (BHs) as solutions to Einstein's equations highlighted potential breakdowns of GR, indicating a need for a broader framework. Physical singularities, like those at BH centers with infinite mass and energy density, disrupt spacetime, while astrophysical BHs have finite mass and energy. Singularities suggest GR needs improvement or replacement by a more fundamental theory, possibly a quantum theory of gravity. However, any attempt to couple GR with quantum field theory reveals deviations. This manuscript quantifies Laser Interferometer Space Antenna (LISA) sensitivity to observe deviations from GR in the strong field regime via the no-hair theorem, which states any astrophysical BH, believed to be a Kerr BH, is characterized solely by its mass and spin. After two BHs collide, the remnant BH settles through gravitational wave radiation in a phase called ringdown, during which the gravitational waveform decomposes into damping waves characterized by quasi-normal modes (QNMs). Given the BH's mass and spin, one can compute all possible QNMs. Conversely, knowing a BH's QNMs allows the determination of its intrinsic parameters. Within GR, the mass and spin derived from each QNM should be consistent. In some alternative theories, this consistency does not hold. The relationship between mass and spin deviations from GR for different QNMs is unique to the considered alternative theory, often requiring additional parameters. BH spectra have been computed for static or slowly rotating BHs in some alternative theories using perturbation theory. However, beyond-relativity numerical waveforms are lacking due to complex dynamics. Assessing deviations from GR is best done using a model-agnostic approach, assuming GR while allowing small deviations. This study adopts this approach, permitting fractional deviations from GR in QNMs. Firstly, I study the interplay of higher harmonics in the inspiral-merger-ringdown description observed by the detector. The mass of the sources shifts the gravitational wave emission frequency range. Since LISA's response and sensitivity vary with frequency, the mass affects the relative weight of higher harmonics for different sources. 'Light' sources around $10^5 M_\odot$ fall at LISA's high-frequency sensitivity edge, preventing observation of the ringdown phase. Conversely, 'heavy' sources around $10^8 M_\odot$ fall in LISA's low-frequency band, meaning the inspiral phase is barely observed, with the merger and ringdown phases primarily contributing to detectability. This effect, along with LISA's frequency-dependent response, may make higher modes like $(3,3)$ or $(4,4)$ predominant in the signal-to-noise ratio over the dominant harmonic $(2,2)$. Including higher harmonics and features like eccentricity or precession is necessary to accurately estimate source parameters for GR tests. Understanding LISA's response to different source parameters, combined with theoretical knowledge of BH perturbation, provides a foundation for developing GR tests in the ringdown phase. I developed a code, Lisaring, integrating these concepts and including LISA's response to various ringdown descriptions. Bayesian framework time domain data analysis tools are also included. After verifying its functionality, I assessed LISA's sensitivity to detect deviations from GR in a source's ringdown phase. Considering different hypotheses on the prior parameters knowledge can significantly impact results. Under specific assumptions, the precision in estimating QNMs, and thus possible fractional deviations, can be computed for different sources. Specifically, for a given set of extrinsic parameters, LISA could probe GR to an uncertainty of $5 \times 10^{-3}\%$ in the $(3,3,0)$ mode, achieving the objective of quantifying LISA's sensitivity to GR deviations.

Résumé:

La première détection des ondes gravitationnelles en 2015 a ouvert la voie à des tests de la relativité générale (RG). La coalescence de trous noirs offre un environnement idéal pour tester la RG dans le régime des champs gravitationnels forts. L'observatoire spatial Laser Interferometer Space Antenna (LISA) pourra détecter ces évènements avec un rapport signal-sur-bruit (SNR) élevé, permettant d'obtenir des détails extrêmement précis sur ces phénomènes. Une binaire de trous noirs évolue en trois phases distinctes : une phase spiralante *Inspiral*, suivi de la phase de coalescence *Merger*, pour finir en un trou noir unique qui se relaxe vers son état fondamental durant la phase de *Ringdown.* Cette séquence complète est désignée sous le nom d'IMR (inspiral-merger-ringdown). Cette thèse porte sur l'étude de l'IMR dans son ensemble ainsi que sur l'analyse spécifique du ringdown. La forme d'onde de l'IMR peut être décomposée en harmoniques sphériques décrites par les nombres angulaires polaire et azimutal (l,m). Dans le régime du ringdown, les ondes gravitationnelles émises peuvent être décrites comme une superposition d'ondes qui s'atténuent avec le temps. Chaque onde est caractérisée par une fréquence complexe appelée mode quasi-normal (QNM), indexée par les nombres angulaires polaire, azimutal et d'overtone (l,m,n). La partie réelle de la fréquence correspond a la fréquence d'oscillation, tandis que la partie imaginaire represent l'inverse du temps d'atténuation. En relativité générale, les valeurs des QNM dépendent uniquement de la masse et du spin du trou noir final, en accord avec le théorème du *no-hair*, qui stipule qu'un trou noir est entièrement décrit par ces deux paramètres. Cependant, dans certaines théories alternatives à la RG, la métrique est modifiée, entraînant une dépendance différente des QNM vis-à-vis de la masse et du spin, ainsi que l'apparition de nouveaux paramètres supplémentaires – appelés "cheveux" (hairs) du trou noir – qui signaleraient une déviation par rapport à la RG. La relation entre masse et spin et les déviations de la RG pour différents QNM est unique à la théorie sous-jacente. Par consequence, en analysant le spectre du trou noir, il est possible de tester la RG en comparant les valeurs de masse et de spin obtenues à partir de différents QNM.

Détectabilité des harmoniques supérieures avec LISA: La première question que nous avons étudiée concerne la capacité de LISA à identifier la présence de modes ou harmoniques supérieures dans la forme d'onde complète des binaires de trous noirs. Actuellement, les évènements détectés par Ligo-Virgo-Kagra présentent une faible indication des modes supérieurs dans l'IMR. Toutefois, l'empreinte d'un QNM supérieur a été faiblement identifiée pour le mode (2,2,1) lors du premier évènement GW150914. Dans le but d'explorer la détectabilité des modes supérieurs avec LISA, j'ai effectué une analyse bayésienne en comparant différents modèles. J'ai généré une forme d'onde incluant six harmoniques supérieures : (2,2), (3,3), (4,4), (2,1), (3,2), (4,3). Puis, j'ai construit plusieurs modèles en variant le nombre de modes pris en compte, et j'ai estimé les paramètres sur le même jeu de données avec ces différents modèles. En faisant la comparaison des modèles avec le rapport de leur evidences, j'ai pu quantifier la preference des donnés pour chaque modèle et ainsi détecter la présence des harmoniques supérieures. Notamment, la détectabilité des modes supérieurs dependent fortement du SNR. Même si la contribution

d'un mode est faible en termes de SNR, son absence dans la description de la forme d'onde, peut induire des biais dans l'estimation des paramètres. Néanmoins, la valeur de ces biais dépend du SNR total, car l'incertitude sur l'estimation est également liée au SNR. De plus, j'ai démontré que le nombre de modes utilisés jusqu'à présent est insuffisant pour décrire correctement les binaires attendues avec LISA, surtout si l'on souhaite tester la RG à travers le théorème du *no-hair*.

Cette analyse a été réalisée avec `Lisabeta`, un programme incluant la réponse de LISA aux formes d'ondes phénoménologiques dans le domaine fréquentiel, ce qui est optimal pour calculer la vraisemblance des signaux de trous noirs supermassifs. Afin, d'accélérer ces calculs j'ai utilisé une méthode appelé *heterodyning*, qui exploite la décomposition de la forme d'onde en une partie lentement variable et une partie rapidement variable avec la fréquence. Comme la phase variant lentement peut être définie sur une grille parcimonieuse, cette méthode permet de réduire significativement le temps de convergence.

Analyse du ringdown et test du théorème du no-hair: Dans la deuxième partie de la these, l'analyse se concentre sur le ringdown, dans le but de tester le théorème du no-hair. Pour cela, le signal doit être analysé à partir du début du ringdown, qui correspond à des fréquences différentes selon les modes. Le domaine fréquentiel ne convient donc plus, car chaque mode a une relation temps-fréquence distincte. J'ai donc développé un code `Lisaring` permettant de générer le ringdown avec la réponse de LISA dans le domaine temporel. Ce code permet également d'estimer les paramètres du système dans différents scénarios. Le calcul de la vraisemblance dans le domaine temporel nécessite l'utilisation de la matrice de covariance, ce qui implique une gestion rigoureuse de la stabilité numérique et du temps de calcul. J'ai exploré plusieurs méthodes pour garantir des calculs fiables et rapides, sans introduire de dégénérescences dans les distributions de probabilités, telle qu'un plateau de vraisemblance.

Grace à ce code, j'ai pu étudier la détectabilité des déviations par rapport à la RG en utilisant un modèle simplifié avec trois modes: (2,2,0), (3,3,0), (4,4,0), en tenant en compte des déviations et en ajoutant du bruit dans mes simulations selon deux approches différentes.

1. Première approche : Comparer la masse et le spin obtenus pour chaque fréquence complexe estimée. Une divergence entre ces estimations pourrait indiquer une déviation par rapport à la RG.
2. Deuxième approach: Estimer la masse et le spin du trou noir final à partir de l'IMR et vérifier si les fréquences des QNM respectent les prédictions de la RG. Une déviation non nulle signale alors une violation potentielle du théorème du no-hair.

J'ai testé deux modèles pour évaluer leur performance dans la détection de telles déviations :

- Un modèle agnostique, où seul le nombre de QNM est supposé connu, mais où les écarts entre les masses et spins dérivés permettent de détecter une éventuelle deviation de la RG.

- Un modèle contraint, où les QNM étudiés sont spécifiés à l'avance, ce qui permet une estimation plus précise des déviations potentielles.

Avec les SNR élevés attendus pour LISA, j'ai démontré qu'il sera possible de détecter des déviations par rapport à la relativité générale. À défaut d'en observer, il sera néanmoins possible d'imposer des contraintes sur des théories alternatives à la RG.

Dans ce manuscrit, je fais un rappel des équations régissant les QNM. Je introduis la réponse de LISA dans les domaines temporel et fréquentiel et je présent les méthodes d'analyse ainsi que leurs résultats. Le principal apport de cette recherche est le développement d'un programme dédié à l'étude des déviations par rapport à la RG dans le ringdown, offrant ainsi un outil crucial pour les futurs tests de la relativité générale avec LISA.

To my brother, Facundo

Acknowledgments

As I reach the conclusion of my Ph.D. thesis, I would like to take a moment to express my heartfelt gratitude to the many people who have supported me over the past three years.

First and foremost, I wish to thank my supervisor, Marc Besançon, for giving me the opportunity to explore such an exciting and evolving topic. His guidance allowed me to pursue various directions, broadening my knowledge through the application of diverse methods and techniques. This work would not have been possible without the invaluable assistance of Quentin Baghi, who guided me through LISA data analysis and has consistently been my go-to expert on statistical and data analysis aspects. I am also deeply grateful to Antoine Petiteau for sharing his vast knowledge of the LISA mission and for the philosophical discussions we shared, which greatly enriched my understanding and perspective.

My sincere thanks go as well to Sylvain Marsat, whose insightful discussions have been instrumental in my learning, and to Jean-Baptiste Bayle, who provided essential support by answering my questions and assisting me with coding challenges. I would also like to extend my thanks to the team at the DPhP in CEA for warmly welcoming me, and to CNES, especially Martin Boutelier, head of the Fundamental Physics Group, for their support.

In addition to my professional network, I am thankful for the friendships I formed during my time at CEA. These friends made the daily routine more enjoyable, filling my days with laughter and camaraderie. I am also grateful to my VA friends, who were always there for me whenever I needed a break from my studies, despite our frequent QA sessions on black holes and the mysteries of the Universe.

Finally, I am immensely grateful to my family for their constant emotional support, as well as to my friends from back home, whose encouragement has meant the world to me. Above all, I am profoundly thankful to Sebastian for his unwavering support; none of this would have been possible without you.

Thank you all for being part of this journey.

Contents

Chapter 1

Introduction

I start this manuscript with an introduction to Gravitational Waves (GWs). I briefly describe the framework of General Theory of Relativity (GR) in which gravitational waves arise naturally from perturbations of the spacetime manifold (Sec. 1.2). I revisit their generation, their effect on matter, and their detection. In Sec. 1.3 I present the Michelson interferometer as the optimal instrument to detect GWs, and I finish with an introduction of the different observatories and their characteristics in Sec. 1.4. This chapter is based on [1–3] and I refer the reader to those references for further details. Most of the figures have been produced by me with `pages` unless otherwise specified in the caption.

1.1 General relativity

One can not discuss Gravitational Waves (GWs) without presenting Einstein's General Theory of Relativity (GR) which is built upon two pillars: the equivalence principle and the covariance principle. The equivalence principle states that all bodies in a gravitational field follow the same trajectories and therefore they can not be locally canceled by non-inertial reference systems. To be locally canceled, the referential system should have the same structure as the gravitational field, meaning that gravitational and inertial forces are similar in nature and therefore indistinguishable. The covariance principle tells us that all physical laws should remain invariant under a reference frame transformation. Both statements give rise to the strong equivalence principle, which suggests that gravity is geometrical in nature. Consequently, the transformation between reference systems should be compatible with the gravitational field itself. Therefore, the transformation can only be performed with the Levi-Civita connection ∇, such that the covariant derivative of the metric g remains invariant, i.e. $\nabla g = 0$. The theory of General Relativity published by Albert Einstein in 1915 [4], satisfying the strong equivalence principle as well as the special theory of relativity [5], successfully describes the gravitational field and its interaction with matter.

Following the convention $\eta_{\mu\nu}$ = diag(-1, +1, +1, +1), the line element takes the form,

$$ds^2 = \eta_{\mu\nu} dx^\mu dx^\nu. \tag{1.1.1}$$

In this context, let me introduce the Riemann tensor describing the behavior of the spacetime as

$$R^\mu{}_{\nu\rho\sigma} = \frac{\partial \Gamma^\mu_{\nu\sigma}}{\partial x^\rho} - \frac{\partial \Gamma^\mu_{\nu\rho}}{\partial x^\sigma} + \Gamma^\mu_{\rho\lambda}\Gamma^\lambda_{\nu\sigma} - \Gamma^\mu_{\sigma\lambda}\Gamma^\lambda_{\nu\rho}. \tag{1.1.2}$$

Note that I use the standard notation, using Latin indices $(i, j, k, \cdots)$ to denote space coordinates and Greek indices to denote spacetime coordinates $(\mu, \nu, \cdots)$. The Christoffel symbols read

$$\Gamma^\mu_{\rho\sigma} = \frac{1}{2} g^{\mu\lambda}(\partial_\rho g_{\sigma\lambda} + \partial_\sigma g_{\rho\lambda} - \partial_\lambda g_{\rho\sigma}). \tag{1.1.3}$$

Then, the Einstein's field equation is

$$R_{\mu\nu} - \frac{1}{2} g_{\mu\nu} R + \Lambda g_{\mu\nu} = \frac{8\pi G}{c^4} T_{\mu\nu}, \tag{1.1.4}$$

where $g_{\mu\nu}$ is the metric, c the speed of light, G Newton's constant of gravity and Λ the cosmological constant set to zero in the following since its low value ($\Lambda \simeq 10^{-52}$ m^{-2} [6]), is only relevant for large scales. The Ricci scalars and the Ricci tensors are defined in terms of Riemann's geometry as

$$R = g^{\mu\nu} R_{\mu\nu}, \qquad R_{\rho\sigma} = R^\mu{}_{\rho\mu\sigma}. \tag{1.1.5}$$

The field equation in Eq.(1.1.4) is the culmination of Einstein's work, as it completely describes the interaction between matter and spacetime. To complete Einstein's framework, let me also introduce the geodesic equation,

$$\dot{x}^\nu \nabla_\nu \dot{x}^\mu = 0 \rightarrow \ddot{x}^\mu + \Gamma^\mu_{\nu\rho} \dot{x}^\nu \dot{x}^\rho = 0, \tag{1.1.6}$$

defining the existence of a curve upon which parallel transportation is guaranteed. These geodesics are the previously mentioned trajectories. The dot $(\cdot)$ denotes the derivative of the coordinate x with respect to the *affine parameter* s [1] ($\dot{x} = dx/ds$). Gravitational waves can be easily derived from Einstein's field equations as the result of perturbations in the spacetime manifold.

1.2 Gravitational waves

Finding solutions to Einstein's equations can be very difficult due to their non-linearity, but one can obtain the linearized equations by working in the weak field where the observer is far away from the source. Gravitational waves appear as ripples in the

---

[1] An affine parameter is defined such that its tangent vector $v(s) = \partial_s$ can be parallel transported along itself: $\nabla_v v = 0$

spacetime as a consequence of accelerating massive objects in the weak field. The perturbed metric can be written as a small perturbation $h_{\mu\nu}$ around the flat Minkowski metric of spacetime $\eta_{\mu\nu}$ such that

$$g_{\mu\nu} = \eta_{\mu\nu} + h_{\mu\nu} \qquad |h_{\mu\nu}| \ll 1, \tag{1.2.1}$$

where higher orders of $h_{\mu\nu}$ can be neglected. Now, when introducing this condition to Einstein's filed equations, while adopting the Lorenz gauge defined as

$$\partial_\mu \bar{h}_{\mu\nu} = 0, \tag{1.2.2}$$

where

$$\bar{h}_{\mu\nu} = h_{\mu\nu} - \frac{1}{2}\eta_{\mu\nu} h, \qquad h = \eta_{\mu\nu} h^{\mu\nu}, \tag{1.2.3}$$

one ends up with the linearized equation which, after some work that can be followed in Sec. A.1, reads

$$\Box \bar{h}_{\mu\nu} = -\frac{16\pi G}{c^4} T_{\mu\nu}. \tag{1.2.4}$$

In the case of vacuum $T_{\mu\nu} = 0$, one consequently gets

$$\Box \bar{h}_{\mu\nu} = \Big(-\frac{1}{c^2}\partial t^2 + \nabla^2 \Big) \bar{h}_{\mu\nu} = 0. \tag{1.2.5}$$

The solution to this D'Alembertian equation is a wave propagating at the speed of light. Without digging into the creation of the perturbation, the resulting wave would still exist far away from the source, where it propagates with a plane front. Moreover, every wave solution can be written as the sum of plane waves of the form

$$\bar{h}_{\mu\nu}(x,t) = A_{\mu\nu} e^{i\left(k_\beta \cdot x^\beta\right)}, \tag{1.2.6}$$

with k_β, the wave vector, and $A_{\mu\nu}$ a symmetric tensor carrying the polarization of the wave with six degrees of freedom (d.o.f) in the Lorenz framework. However, the gauge in Eq. (1.2.2) is not completely fixed since every coordinate can be transformed as

$$x^\mu \to x'^\mu = x^\mu + \zeta^\mu. \tag{1.2.7}$$

Therefore, it is also important to fix ζ_μ, with $\Box \zeta^\mu = 0$, to obey the Lorenz gauge. Because in general relativity $\bar{h}_{\mu\nu}$ transforms as

$$\bar{h}_{\mu\nu} \to \bar{h}'_{\mu\nu} = \bar{h}_{\mu\nu} + (\partial_\mu \zeta_\nu + \partial_\nu \zeta_\mu + \eta_{\mu\nu} \partial_\rho \zeta^\rho), \tag{1.2.8}$$

when one fixes ζ_μ, one also fixes $\bar{h}_{\mu\nu}$, constraining four of the six d.o.f in $A_{\mu\nu}$.

Then, one can impose the condition of $\zeta^0 = 0$, which automatically fixes the values of ζ^i due to Lorenz gauge, obtaining

$$h^{0\mu} = 0, \qquad h^i_i = 0, \qquad \partial^i h_{ij} = 0. \tag{1.2.9}$$

This imposition is called the transverse-traceless (TT) gauge and gives rise to two polarizations known as plus and cross $(+, \times)$. Alternative gravity theories could also have scalar or vector polarizations, however not considered here.

Assuming a propagation in the z-axis, i.e. $k_\beta = (0, 0, 0, z/c)$, Eq. (1.2.6) becomes

$$h^{TT}_{\mu\nu} = \begin{pmatrix} 0 & 0 & 0 & 0 \\ 0 & h_+ & h_\times & 0 \\ 0 & h_\times & -h_+ & 0 \\ 0 & 0 & 0 & 0 \end{pmatrix} \sin\left(w(t - z/c)\right). \tag{1.2.10}$$

The spatial representation of the effect of those polarizations acting on the position of test particles in the x and y-axis are shown in Fig. 1.1.

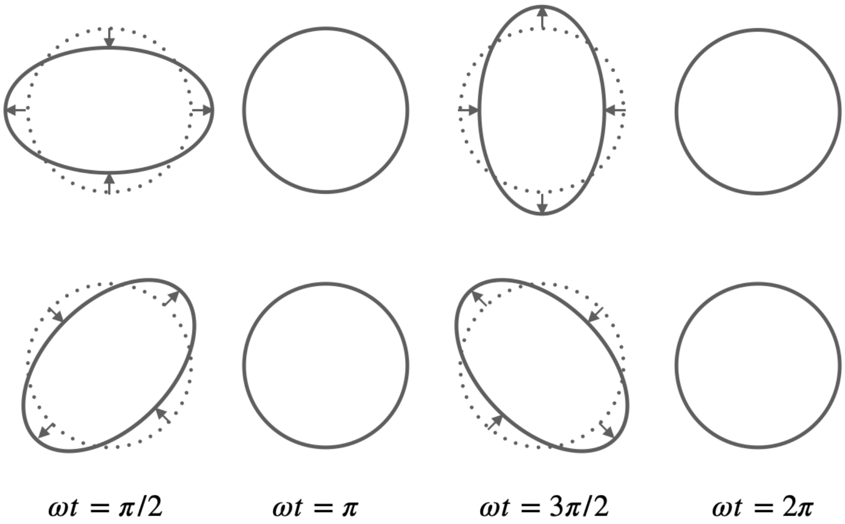

Figure 1.1: Deformation of the spacetime in the x and y-axis by plus polarization (top), and cross polarization (bottom).

1.2.1 Generation

In the following, I review how gravitational waves can emerge from Einstein equations as derived in [1; 2]. In the context of linearized theory, we have to assume very separate sources to satisfy the weak gravitational field.

Keeping in mind that the Lorenz gauge satisfies

$$\partial^\mu \bar{h}_{\mu\nu} = 0 \xrightarrow{then} \partial^\mu T_{\mu\nu} = 0, \tag{1.2.11}$$

is also fulfilled. Then, one can solve Eq. (1.2.4) via Green's function method

$$\bar{h}_{\mu\nu}(\vec{x}) = \frac{4G}{c^4} \int d^3\vec{x}' \frac{1}{|\vec{x} - \vec{x}'|} T_{\mu\nu}(t_{ret}, \vec{x}'), \tag{1.2.12}$$

where $\vec{x}$ is the position where it is measured, while $\vec{x}'$ is the position of the source of emission, and $t_{ret} = t - |\vec{x} - \vec{x}'|/c + \vec{x}' \cdot \hat{n}/c$, is the retarded time given by the measured time minus the time it took for the information to travel from $\vec{x}'$ to $\vec{x}$, along the propagation vector $\hat{n}$. For a TT gauge, one can write

$$\bar{h}_{ij}^{TT}(\vec{x}) = \frac{4G}{r\,c^4}\Lambda_{ij,kl}(\hat{n}) \int d^3\vec{x}'\, T^{kl}(t_{ret}, \vec{x}'), \tag{1.2.13}$$

where I used that at very large distances $|\vec{x} - \vec{x}'| = r$, and where $\Lambda_{ij,kl}(\hat{n})$ is a projector defined on the propagation vector $\hat{n}$ as

$$\Lambda_{ij,kl}(\hat{n}) = P_{ik}(\hat{n})P_{jl}(\hat{n}) - \frac{1}{2}P_{ij}(\hat{n})P_{kl}(\hat{n}) \quad \text{and} \;\; P_{ij}(\hat{n}) = \delta_{ij} - n_i n_j. \tag{1.2.14}$$

With a Fourier transformation, one can perform a multipole expansion of the momentum tensor

$$T^{kl}\Big(t - \frac{r}{c} + \frac{\vec{x}'\hat{n}}{c}, \vec{x}'\Big) \simeq \Big[T^{kl} + \frac{x'^i\, n_i}{c}\partial_0 T^{kl} + \frac{x'^i x'^j\, n_i n_j}{2c^2}\partial_0^2 T^{kl} + ...\Big]\Big(t - \frac{r}{c}, \vec{x}'\Big). \tag{1.2.15}$$

Then, Eq. (1.2.13) becomes

$$\bar{h}_{ij}^{TT}(\vec{x}) = \frac{4G}{r\,c^4}\Lambda_{ij,kl}(\hat{n})\Big[S^{kl} + \frac{n_m}{c}\dot{S}^{kl,m} + \frac{n_m n_p}{2c^2}\ddot{S}^{kl,mp} + ...\Big]\Big(t - \frac{r}{c}\Big), \tag{1.2.16}$$

where I used the definition of the momenta of the stress tensor

$$S^{ij}(t) = \int d^3x\, T^{ij}(t, \vec{x}), \tag{1.2.17a}$$

$$S^{ij,m}(t) = \int d^3x\, T^{ij}(t, \vec{x})x^m, \tag{1.2.17b}$$

$$S^{ij,mp}(t) = \int d^3x\, T^{ij}(t, \vec{x})x^m x^p. \tag{1.2.17c}$$

and the time derivatives

$$\dot{S}^{ij}(t) = \int d^3x\, \dot{T}^{ij}(t, \vec{x}) \tag{1.2.17d}$$

$$\ddot{S}^{ij,m}(t) = \int d^3x\, \ddot{T}^{ij}(t, \vec{x})x^m, \tag{1.2.17e}$$

$$\dddot{S}^{ij,mp}(t) = \int d^3x\, \dddot{T}^{ij}(t, \vec{x})x^m x^p. \tag{1.2.17f}$$

As shown below, the first line, Eq.(1.2.17a), is the conserved mass-energy, the second line is the center of mass, which is also conserved, and the third row is the moment of inertia, which is not conserved. To arrive at these statements is convenient to write those equations in terms of the energy and momentum density, such that

$$M^{i} = \frac{1}{c^2}\int d^3x\, T^{00} x^{i}, \quad P^{j} = \frac{1}{c}\int d^3x\, T^{0j} \tag{1.2.18a}$$

$$M^{ij} = \frac{1}{c^2}\int d^3x\, T^{00} x^{i} x^{j}, \quad P^{j,i} = \frac{1}{c}\int d^3x\, T^{0j} x^{i}. \tag{1.2.18b}$$

From Eq. (1.2.11) and given the conservation of the Momentum/Energy tensor, it is easy to notice that

$$\partial_\mu T^{\mu 0} = 0 \rightarrow \partial_0 T^{00} = -\partial_i T^{i0}, \tag{1.2.19}$$

that leads to

$$\int_V d^3x\, \partial_0 T^{00} = -\int_V d^3x\, \partial_i T^{0i} = -\int_{\partial V} dS^i T^{0i} = 0 \rightarrow c\dot{M} = 0, \tag{1.2.20}$$

resulting in the conservation of Eq. (1.2.17a). After some work, one can write the momentum in terms of the mass, such that

$$\dot{M}^{i} = P^{i} \quad \text{and} \quad \dot{M}^{ij} = P^{i,j} + P^{j,i}\ {}^{2}. \tag{1.2.21}$$

Due to the symmetry of the tensor S^{ij}, the right-hand side results in the conservation of the mass dipole, hence the center of mass written in Eq. (1.2.17b). The mass quadrupole, in Eq. (1.2.17c) is not conserved and thus becomes the leading order of the gravitational radiation,

$$\ddot{M}^{ij} = \dot{P}^{i,j} + \dot{P}^{j,i} = 2S^{ij}. \tag{1.2.22}$$

Finally, the amplitude strain produced on the spacetime by a gravitational wave at first order is related to the mass quadrupole radiation through

$$\left[h^{TT}_{ij}(t,\vec{x})\right]_{quad} = \frac{2G}{r\, c^4}\Lambda_{ij,kl}(\hat{n})\ddot{M}^{kl}\left(t - \frac{r}{c}\right). \tag{1.2.23}$$

In other words, the acceleration of masses is the leading process that can generate GWs. At higher orders, changes in the angular momentum would also contribute to the generation of GWs. However, it is easy to see that a rotating perfect sphere would not create GWs due to energy conservation. I refer the reader to [2] for a detailed description of this topic.

The tensor M^{kl}, being a symmetric tensor, can be decomposed into an irreducible representation of the rotation group as

$$M^{kl} = Q^{kl} + \frac{1}{3}\delta^{kl} M_{ii}, \tag{1.2.24}$$

where M_{ii} is the trace of the tensor M_{ij}. In this representation, the term

$$Q^{kl} \equiv M^{kl} - \frac{1}{3}\delta^{kl} M_{ii} \tag{1.2.25}$$

---

[2] This is because $\int_V d^3x\, \partial_0 T^{00} x^i x^j = -\int_V d^3x\, \partial_i T^{0i} x^i x^j = \int_V d^3x\, T^{0i} \partial_i (x^i x^j)$

is traceless by construction, which is what we need to express the mass density in the TT gauge in terms of a spin-2 operator. Furthermore, the contraction of δ_{kl} with the projector $\Lambda_{ij,kl}$ returns a zero value. So, without loss of generality, one can work with the irreducible representation of the quadrupolar moment Q^{kl} instead of M^{kl}.

Using Green's function, one can take advantage of the spherical symmetry and decompose it in terms of spherical harmonics. To that end, one should start with the Poisson equation

$$\nabla^2 \phi = -4\pi\rho, \tag{1.2.26}$$

which has the solution

$$\phi(x) = \int d^3x' \frac{1}{|x - x'|} \rho(x'). \tag{1.2.27}$$

The density is localized in the center of the spherical coordinates with a radius d, then $\rho = 0$ if $r > d$. Hence, one can write the external potential in the following form

$$\phi(x) = 4\pi \sum_{l=0}^{\infty} \sum_{m=-l}^{l} \frac{Q_{lm}}{2l+1} \frac{Y_{lm}(\theta, \phi)}{r^{l+1}}, \tag{1.2.28}$$

where

$$Q_{lm} = \int d^3 Y^*_{lm}(\theta', \phi') r'^l \rho(x'). \tag{1.2.29}$$

I used that $|x| = r$ and $|x'| = r'$. The asterisk $(^*)$ denotes the complex conjugate and the spherical harmonics are defined as

$$Y_{lm}(\theta, \phi) = \sqrt{\frac{2l+1}{4\pi} \frac{(l-m)!}{(l+m)!}} (-1)^m e^{im\phi} P_{lm}(\cos\theta), \tag{1.2.30}$$

with l the angular polar number, m the azimuthal angular number, and $P_{lm}(\cos\theta)$ the associated Legendre polynomials of degree l and order m,

$$P_{lm}(x) = \frac{(-1)^m}{2^l l!} \left(1 - x^2\right)^{m/2} \frac{\mathrm{d}^{l+m} \left(x^2 - 1\right)^l}{\mathrm{d}x^{l+m}}. \tag{1.2.31}$$

In this context, the Taylor expansion of Eq. (1.2.15) as $r \to \infty$ can be written in terms of spherical harmonics since

$$\frac{1}{|x - x'|} = 4\pi \sum_{l=0}^{\infty} \sum_{m=-l}^{l} \frac{1}{2l+1} \frac{r'^l}{r^{l+1}} Y^*_{lm}(\theta', \phi') Y_{lm}(\theta, \phi). \tag{1.2.32}$$

Nevertheless, keep in mind that in GR, the field ϕ is not a scalar but a tensor field with a solution in the shape of $Q^{\mu\nu}_{lm}$. Then, the decomposition will occur under the spin-weighted spherical harmonics ${}_sY_{lm}$, where the spin takes the value $s = -2$ for gravitational fields. I will refer in the future to modes or harmonics to orders of this multipole expansion based on spin-weighted spherical harmonics. The vector and tensor spherical harmonics are also introduced in Sec. 3.2.1.

1.2.2 Interaction with matter

In the absence of non-gravitational forces, a test mass in a metric with a proper time τ will follow a geodesic defined by

$$\frac{\mathrm{d}^2x^\mu}{\mathrm{d}\tau^2} + \Gamma^\mu_{\nu\rho}(x)\frac{\mathrm{d}x^\nu}{\mathrm{d}\tau}\frac{\mathrm{d}x^\rho}{\mathrm{d}\tau} = 0. \tag{1.2.33}$$

Therefore, a local frame in which the Christoffel symbol vanishes can always be selected, letting that mass fall freely in that particular frame and time. The selection of a gauge fixes the reference frame, so it is important to understand the observable physics related to that frame.

In the case of a flat manifold without any mass distribution, two parallel geodesics would remain parallel forever. But, in the presence of matter or a perturbation, those lines will tend to deviate from the straight path. Therefore, when comparing the geodesics of two neighboring particles, separated by ζ^μ one can relate their difference to the perturbation of a passing GW. That is

$$\frac{\mathrm{d}^2(x^\mu+\zeta^\mu)}{\mathrm{d}\tau^2} + \Gamma^\mu_{\nu\rho}(x+\zeta)\frac{\mathrm{d}(x^\nu+\zeta^\nu)}{\mathrm{d}\tau}\frac{\mathrm{d}(x^\rho+\zeta^\rho)}{\mathrm{d}\tau} = 0, \tag{1.2.34}$$

then, expanding to leading order and subtracting Eq. (1.2.33), one obtains the geodesic deviation

$$\frac{\mathrm{d}^2\zeta^\mu}{\mathrm{d}\tau^2} + 2\Gamma^\mu_{\nu\rho}(x)\frac{\mathrm{d}x^\nu}{\mathrm{d}\tau}\frac{\mathrm{d}\zeta^\rho}{\mathrm{d}\tau} + \zeta^\sigma\partial_\sigma\Gamma^\mu_{\nu\rho}(x)\frac{\mathrm{d}x^\nu}{\mathrm{d}\tau}\frac{\mathrm{d}x^\rho}{\mathrm{d}\tau} = 0. \tag{1.2.35}$$

Moreover, the geodesic deviation can be written in terms of the Riemann tensor. To do so, the introduction of the covariant derivative is necessary

$$\frac{D\zeta^\mu}{D\tau} = \frac{\mathrm{d}\zeta^\mu}{\mathrm{d}\tau} + \Gamma^\mu_{\nu\rho}(x)\zeta^\nu\frac{\mathrm{d}x^\rho}{\mathrm{d}\tau}. \tag{1.2.36}$$

Then

$$\begin{aligned}\frac{D^2\zeta^\mu}{D\tau^2} = {} & \frac{\mathrm{d}^2\zeta^\mu}{\mathrm{d}\tau^2} + \partial_\sigma\Gamma^\mu_{\nu\rho}(x)\zeta^\nu\frac{\mathrm{d}x^\rho}{\mathrm{d}\tau}\frac{\mathrm{d}x^\sigma}{\mathrm{d}\tau} + \Gamma^\mu_{\nu\rho}(x)\frac{\mathrm{d}\zeta^\nu}{\mathrm{d}\tau}\frac{\mathrm{d}x^\rho}{\mathrm{d}\tau} \\ & + \Gamma^\mu_{\nu\rho}(x)\zeta^\nu\Big[-\Gamma^\rho_{\alpha\beta}(x)\frac{\mathrm{d}x^\alpha}{\mathrm{d}\tau}\frac{\mathrm{d}x^\beta}{\mathrm{d}\tau}\Big] + \Gamma^\mu_{\delta\gamma}(x)\frac{\mathrm{d}\zeta^\delta}{\mathrm{d}\tau}\frac{\mathrm{d}x^\gamma}{\mathrm{d}\tau} + \Gamma^\mu_{\delta\gamma}(x)\Gamma^\delta_{\nu\rho}(x)\zeta^\nu\frac{\mathrm{d}x^\rho}{\mathrm{d}\tau}\frac{\mathrm{d}x^\gamma}{\mathrm{d}\tau}.\end{aligned} \tag{1.2.37}$$

When plugging Eq. (1.2.35) into Eq. (1.2.37), some terms will cancel out leading to the wanted relation

$$\frac{D^2\zeta^\mu}{D\tau^2} = -R^\mu{}_{\nu\rho\sigma}\zeta^\rho\frac{\mathrm{d}x^\nu}{\mathrm{d}\tau}\frac{\mathrm{d}x^\sigma}{\mathrm{d}\tau}. \tag{1.2.38}$$

In conclusion, two nearby particles in the presence of mass/energy distribution, will experience a tidal gravitational force determined by the Riemann tensor. Consequently, if no mass distribution is present, the tensor is zero and hence, the geodesic deviation is null.

For the case of the TT frame, most of the components $h^{\mu\nu}$ vanish, except for $\mu, \rho = i, j$. Then, the only component of the Riemann tensor that survives is

$$R^i{}_{0j0} = R_{i0j0} = -\frac{1}{2c^2}\partial_0^2 h_{ij}^{TT}, \tag{1.2.39}$$

thus, the differential geodesic reads

$$\partial_0^2 \zeta^i = \frac{1}{2}\zeta^j \partial_0^2 h_{ij}^{TT}. \tag{1.2.40}$$

The path of a gravitational wave will stretch and compress the spacetime manifold according to its polarization via h_{ij}^{TT} [3].

1.2.3 Detection

If one considers the test mass reference frame, the Christoffel symbol in Eq. (1.2.33) will vanish, leaving the test mass undisturbed by the path of a gravitational wave. This doesn't mean it had no physical effect, rather, the effect was unobservable in that specific reference frame. Taking this consideration and the analysis of the previous subsection into account, it is more convenient to perform a different approach in which one evaluates the proper distance of two bodies where the tidal effect is visible. This section is based on [2; 7]. Thus, I refer the reader to those references for further information.

The line element in a Minkowski metric affected by a GW takes the form

$$ds^2 = (\eta_{\mu\nu} + h_{\mu\nu})\, dx^\mu dx^\nu, \tag{1.2.41}$$

where the gravitational strain propagating in the z-axis is

$$h_{\mu\nu} = \begin{pmatrix} 0 & 0 & 0 & 0 \\ 0 & h_+ & h_\times & 0 \\ 0 & h_\times & -h_+ & 0 \\ 0 & 0 & 0 & 0 \end{pmatrix} \sin\omega(t - z/c). \tag{1.2.42}$$

Knowing that the element line for photons is $ds^2 = 0 \rightarrow dt^2 = g_{ij}dx^i dx^j$, then, for a wave propagating at the speed of light, the proper distance of two test particles at $\vec{x}_1$ and $\vec{x}_2$ is given by

$$\int_0^t c\, dt' \sqrt{g_{tt}} = \int_{\vec{x}_1}^{\vec{x}_2} dx^i dx^j g_{ij}. \tag{1.2.43}$$

Assuming that the coordinate position of the test particles depends only on x, i.e $y = 0$, we can write

---

[3] Note that an observer in the TT frame will not be able to observe the variation, as he will also suffer the same perturbation as the test masses.

$$ct = \int^{L} dx\sqrt{g_{xx}} = \int^{L} dx\sqrt{(1 + h_{+}^{TT}\sin\omega(t - z/c))} \simeq L\Big(1 + \frac{1}{2}h_{+}^{TT}\sin\omega t\Big|_{z=0}\Big), \quad (1.2.44)$$

where $L = |x_1 - x_2|$. Hence, assuming that the distance between the test masses is much larger than the wavelength at which the gravitational field changes, that is $L \ll \lambda_{GW}$, one can define the differential length δL between those two particles, as a consequence of a crossing gravitational strain, as

$$\frac{\delta L}{L} \simeq \frac{1}{2}h_{+}^{TT}. \quad (1.2.45)$$

In the TT frame, one can express the tidal effect on matter of each polarization in the perpendicular coordinates of the propagation of the GW to the initial positions (x_0, y_0):

h_{+} polarization

$$\delta x(t) = \frac{h_{+}}{2}x_0 \sin wt$$

$$\delta y(t) = -\frac{h_{+}}{2}y_0 \sin wt$$

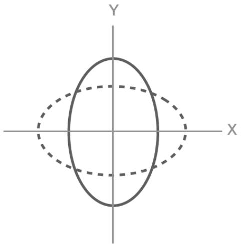

$h_{\times}$ polarization

$$\delta x(t) = \frac{h_{\times}}{2}y_0 \sin wt$$

$$\delta y(t) = \frac{h_{\times}}{2}x_0 \sin wt$$

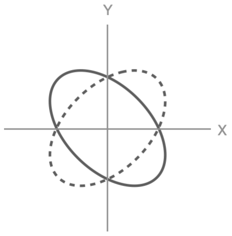

Given the effect that GWs have on the matter, stretching in one direction and simultaneously compressing in a perpendicular one, the best way to measure the amplitude strain (h_A, with $A = +, \times$) is through the measurement of variations of those coordinates.

1.2.4 Sources

In Sec. 1.2.1, I mentioned that GWs are generated by accelerating massive objects or a variation in their angular momentum. In the Universe, several objects can produce GWs, such as coalescing binary systems, continuous waves, unmodeled bursts, and stochastic events. I proceed to describe them in the following. This section is based mostly on [3; 8–11].

Coalescing binary systems

Binaries systems are composed of two compact objects interacting through the gravitational field. When one compact object experiences the gravitational pull of the other, it can be captured within its gravitational potential, leading to inspiral orbits as it gradually falls inward. The energy loss in the orbit's decay is transformed into radiation in the form of GWs. As the bodies draw closer, the velocity generated by gravitational potential increases until they eventually merge into a single object. Depending on the final mass, this merged object will most likely be a final Black Hole (BH). The waveform produced by this kind of event is the direct result of the energy lost by the system, thus each stage of the waveform can be related to each stage of the interaction. The first stage of the dynamics describing the slow approach of the bodies is called the *inspiral* part and is characterized by the progressive increase of the orbital frequency ν. Once the bodies are relatively close to merging, the stage is known as the *merger*. This phase is characterized by the end of the chirp-like signature, which means that the amplitude of the wave has reached its maximum value, the same as the orbital frequency. After the merger is concluded, one final compact object remains in a very perturbed state that will relax to its fundamental state in a stage called the *ringdown*. This last stage is characterized by a damping amplitude. In general, one can refer to the IMR waveform as the complete waveform considering the inspiral, the merger, and the ringdown.

It is worth mentioning that, by compact objects, I refer to White Dwarfs (WDs), Neutron Stars (NSs), or BHs. In a binary system, the gravitational potential from the companion could produce gravitational tides onto the compact object. If instead of compact objects, one considers active stars, when the bodies approach, and the tides become stronger than the gravitational force bounding the star itself, the star could be torn apart, preventing any merger event. However, the torn material could eventually plunge into the compact object as accreted matter, generating a different kind of GW [3]. Nevertheless, in the early inspiral stage of the interaction, active stars can be considered as companions to compact objects to generate GWs.

To quantify the expected strain amplitude for binary compact object mergers, we can approximate Eq. (1.2.23) to

$$h \sim \frac{2G}{R\,c^4} M v^2. \tag{1.2.46}$$

As an example, for an extragalactic binary of 10^6 $\mathrm{M}_\odot$, such as the result of two galaxies somewhat similar to the Milky Way merging, at a distance $R = 26$ Gpc which corresponds to a redshift 3, and a relativistic velocity $v \simeq 0.3$ c; the amplitude of the strain is $h \sim 10^{-16}$. If we take into account Eq. (1.2.45), in order to observe such small variations we will need very long rulers (L) and the ability to observe very small displacements of the order of

$\delta L \sim 10^{-15}$ m. This kind of precision is achieved with interferometry, as I explain later in Sec. 1.3.

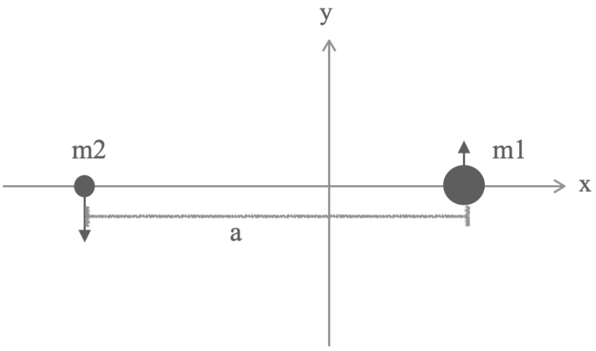

Figure 1.4: Sketch of a binary system of two point masses in an orbit around a center of mass at $(0, 0)$.

More accurately, if one assumes a circular orbit for two bodies with mass m_1 and m_2, total mass M and separation a, the angular orbital frequency according to Kepler's law is $\nu = \sqrt{M/a^3}$, assuming geometric units (G=c=1). If at the time $t = 0$, the bodies are in the x-axis, as shown in Fig. 1.4, then the trajectories of both objects can be written as

$$x_1 = \frac{m_2}{M} a \cos \nu t, \qquad y_1 = \frac{m_2}{M} a \sin \nu t, \tag{1.2.47}$$

$$x_2 = \frac{m_1}{M} a \cos \nu t, \qquad y_2 = \frac{m_1}{M} a \sin \nu t, \tag{1.2.48}$$

then, we can compute the quadrupolar moment M^{ij} from Eq. (1.2.17c):

$$\begin{aligned} S_{00,ij} = \int T^{00} x_i x_j d^3x &= \int \left[\delta(\vec{x} - \vec{x}_1) m_1 + \delta(\vec{x} - \vec{x}_2) m_2\right] x_i x_j d^3x \\ &= m_1 x_1^i x_1^j + m_2 x_2^i x_2^j. \end{aligned} \tag{1.2.49}$$

It is easy to see, for example, that

$$M_{xx} = m_1 \left(\frac{m_2}{M} a \cos \nu t\right)^2 + m_2 \left(\frac{m_1}{M} a \cos \nu t\right)^2 = \frac{m_1 m_2}{M} a^2 \cos^2 \nu t. \tag{1.2.50}$$

Hence, by computing the other quadrupolar terms, the quadrupolar radiation take the form

$$\ddot{M}_{xx} = -\ddot{M}_{yy} = -2\mu a^2 \nu^2 \cos 2\nu t = -2\mu (M\nu)^{2/3} \cos 2\nu t, \tag{1.2.51}$$

$$\ddot{M}_{xy} = \ddot{M}_{yx} = -2\mu a^2\nu^2 \sin 2\nu t = -2\mu(M\nu)^{2/3} \sin 2\nu t, \tag{1.2.52}$$

where μ is the reduced mass ratio $\mu = m_1 m_2/M$.

To obtain the strain of the gravitational radiation, one can assume an observer at a distance R in the x-z plane, which using spherical coordinates $\vec{n} = (\sin\theta\cos\phi, \sin\theta\sin\phi, \cos\theta)$ with $\phi = 0$, it is $\vec{n} = (\sin\theta, 0, \cos\theta)$, see Fig. 1.5 for a visual representation. Knowing that the polarized strain propagated in the z-axis is defined as Eq. (1.2.42) and using the propagator projectors defined in Eq. (1.2.14), we obtain the corresponding expressions for the strain polarizations

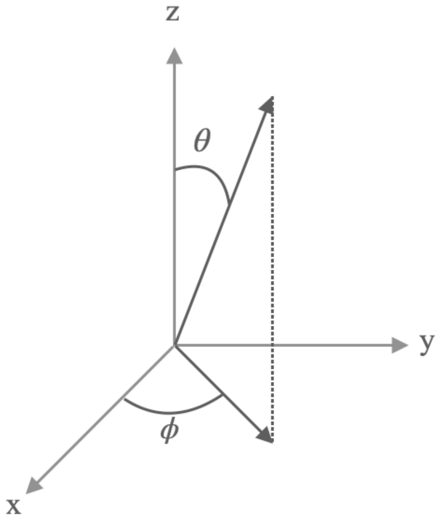

Figure 1.5: Spherical coordinates

$$\begin{aligned} h_+ &= (\Lambda_{xx} - \Lambda_{yy})_{ij}\, \ddot{M}^{ij} = \cos^2\theta \ddot{M}^{xx} - \ddot{M}^{yy} && (1.2.53)\\ h_\times &= 2\Lambda_{xy,ij}\ddot{M}^{ij} = 2\cos\theta\ddot{M}^{xy}. && (1.2.54) \end{aligned}$$

Hence, one can write the inspiral gravitational wave as

$$\begin{aligned} h_+ &= -\,2\left(1+\cos^2\theta\right)\frac{\mu}{R}(M\nu)^{2/3}\cos\left[2\nu(t-R)-\phi_0\right], && (1.2.55)\\ h_\times &= -\,4\cos\theta\frac{\mu}{R}(M\nu)^{2/3}\sin\left[2\nu(t-R)-\phi_0\right], && (1.2.56) \end{aligned}$$

where one computes the waveform for the retarded time $t_{ret} = t - R$, instead of t, then R is the distance to the observer, θ is the angle between the orbital momentum of the binary and the observer, and the initial phase ϕ_0 is considered to be the phase at $t = 0$. Note that the frequency of the GW corresponds to twice the orbital frequency ($\omega = 2\nu$).

Gravitational waves carry energy and angular momentum dissipated by the system expressed as [11]

$$\text{Lum} = -\frac{\mathrm{d}E^{GW}}{\mathrm{d}t} = \frac{1}{5}\langle \dddot{M}_{ij}\dddot{M}_{ij}\rangle = \frac{32}{5}\eta^2\left(M\nu\right)^{10/3}, \tag{1.2.57}$$

where η is the symmetric mass ratio $\eta = (m_1 m_2)/M^2$, and the triangular parenthesis denotes the average on several gravitational wavelengths. At the same time, the energy of the system in a given orbit is

$$E_{orb} = -\frac{m_1 m_2}{2a}. \tag{1.2.58}$$

Assuming the energy loss by the system is completely transformed into gravitational radiation, then

$$\dot{E} = -\frac{32}{5}\eta^2\left(M\nu\right)^{10/3} = \frac{m_1 m_2}{2a^2}\dot{a}. \tag{1.2.59}$$

With this relation, we can integrate over $\dot{a}$ to obtain the variation of the orbital separation, which results in

$$a = \left[\frac{256}{5}\eta M^3(t_c - t)\right]^{1/4}, \tag{1.2.60}$$

where t_c is the time of coalescence defined as the time in which a tends to the zero value ($a \to 0$). One can instead, compute the orbital frequency,

$$\nu = \left[\frac{256}{5}\eta M^{5/3}(t_c - t)\right]^{-3/8}. \tag{1.2.61}$$

Therefore, the time it takes a binary to merge, keeping in mind that the frequency of the GW is twice the orbital frequency ($\omega = 2\nu$) and ($\omega = f_{GW}2\pi$), reads

$$\Delta t = \frac{5}{256\eta M^{5/3}}(\pi f_{GW})^{-8/3}. \tag{1.2.62}$$

Furthermore, in terms of the GW frequency, which I write in the following as f (without the GW index), both polarizations can be written as

$$\tilde{h}_+(f) = \sqrt{\frac{5}{6}}\frac{1}{4\pi^{2/3}}\frac{M_c^{5/6}G}{r\,c^4}f^{-7/6}\left(1+\cos^2\theta\right)e^{i\tilde{\Phi}(f)}, \tag{1.2.63}$$

$$\tilde{h}_\times(f) = \sqrt{\frac{5}{6}}\frac{1}{4\pi^{2/3}}\frac{M_c^{5/6}G}{r\,c^4}f^{-7/6}2\cos\theta e^{i\tilde{\Phi}(f)}, \tag{1.2.64}$$

where M_c is the chirp mass given by $M_c = \eta^{3/5}M$ and the wave phase Φ is given by the evolution of the orbital frequency

$$\Phi_{orb} = \int 2\pi f_{orb}(t)dt.$$

Using the definition of Eq. (1.2.59) and the fact that from Kepler law, $\dot{a}/a = -2/3\,\dot{\nu}/\nu$, the phase at first order is

$$\tilde{\Phi}(f) = 2\pi f t_c + \phi_0 - \frac{\pi}{4} + \frac{3}{4}\left(8\pi M_c f\right)^{-5/3}. \tag{1.2.65}$$

Then, the total strain reads

$$\tilde{h}(f) = \tilde{h}_+(f) - i\tilde{h}_\times(f). \tag{1.2.66}$$

Once the two bodies are very close and the velocity becomes relativistic, this description is no longer valid, and one has to solve Einstein's equations in the strong field by accounting for higher-order expansions. This can be achieved numerically with computers. Nowadays, there is a whole field dedicated to the numerical evolution of the dynamics in the strong field regime, called Numerical Relativity (NR).

Continuous waves

This kind of wave can be generated by asymmetric rapid rotating NSs [12]. Such asymmetry can be the result of a toroidal magnetic field or a protuberance in the surface caused by a crack in the crust through thermal effects. The produced GW would have a periodicity twice its rotation frequency. In addition, each NS has an equation of state that could excite oscillation modes, such as the known r-mode [13]. These oscillations could break the spherical symmetry, giving rise to GWs. Another cause would be the non-isotropic continuous accretion of material. The spin rate of NS remains quasi-constant for long periods, producing continuous GWs with a monochromatic frequency.

Unmodeled bursts

These are short-duration events, usually from a sudden expulsion of excess energy in a system [12]. Even though few sources can generate this type of GW, the most well-known are the Supernova (SN). There are two principal issues with this type of event. Firstly, SN are rarely observed, one per century in the Milky Way is expected, which prevents the determination of the characteristic waveform of its dynamics. Hence, their signatures are unknown. Secondly, the undefined waveform of SN can be easily mistaken for artifact noises such as glitches.

Stochastic background

A Stochastic Gravitational-Wave Background (SGWB) is any random gravitational wave signal produced by a large number of weak, independent, and unresolved sources [8–10]. It can have an astrophysical or a cosmological origin. In the first group, the stochastic background can be composed of an incoherent sum of individual signals over the Universe's lifetime, such as the ones described above, but too faint or too far to be individually distinguishable. The second case with cosmological origin, can also be composed of a large number of unresolved sources but encompass processes in the early Universe unreachable by other techniques. Currently, our most detailed view of the first epoch of the Universe comes from the last photon scattering, which decoupled from matter about 380.000 years after the Big Bang. By studying the Cosmic Microwave Background (CMB), one can portray an accurate picture of the Universe at early times, but the only way of crossing the electromagnetic wall from the last scattering and 'look' at earlier times is through the gravitational field. Indeed, GWs can give us (extra) information about inflation, cosmic strings, and phase transition at primordial times.

The magnitude of the SGWB is usually described by the dimensionless density parameter Ω_{GW}, in terms of the energy density per unit logarithmic frequency over the critical energy density as [8]

$$\Omega_{GW}(f) = \frac{f}{\rho_c}\frac{\mathrm{d}\rho_{GW}}{\mathrm{d}f}, \tag{1.2.67}$$

where $d\rho_{GW}$ is the energy density of GWs in the interval $[f, f+df]$ and $\rho_c = 3H_0^2/8\pi G$ is the critical energy density for a flat Universe. The Hubble parameter is defined as $H_0 = 100\,h_{100}$ km/s/Mpc, where $h_{100} = H_0/100$ is the reduced Hubble constant [4]. The GW density parameter can also be written in terms of the energy density spectrum $S_h(f)$,

$$\Omega_{GW} = \frac{4\pi^2}{3H_0^2} f^3 S_h(f). \tag{1.2.68}$$

The characteristic strain can be expressed in terms of the energy density spectrum as

$$\tilde{h}_c(f) = \sqrt{2fS_h(f)}. \tag{1.2.69}$$

Several theoretical models of gravitational wave backgrounds predict characteristic strains with a power-law dependence in the following way [10],

$$\tilde{h}_c(f) = A_\alpha \Big(\frac{f}{f_{ref}}\Big)^\alpha, \tag{1.2.70}$$

where A_α is the characteristic amplitude associated with the type of source coming from different predictions depending on the theoretical scenario, with a spectral index α that depends on the source, and f_{ref} typically set to 1 year or the most sensitive frequency of the detector [9]. Then, through Eqs. (1.2.68) and (1.2.69), one can write the GW density parameter as

$$\Omega_{GW} = \Omega_\beta \Big(\frac{f}{f_{ref}}\Big)^\beta, \tag{1.2.71}$$

where

$$\Omega_\beta = \frac{4\pi^2}{3H_0^2} f_{ref}^2 A_\alpha^2, \qquad \beta = 2\alpha + 2. \tag{1.2.72}$$

---

[4] Note that $\Omega_{GW}(f)h_{100}^2$ is independent of the Hubble expansion rate, denoting a general description of the GW relative energy density, regardless of the value of H_0 [9].

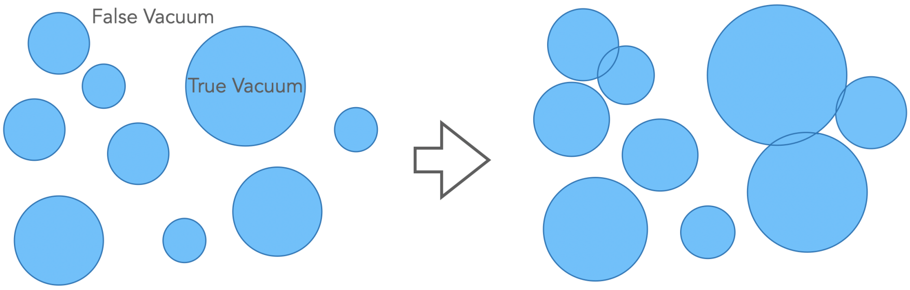

Figure 1.6: Expansion and collision of nucleated bubbles. True vacuum bubbles submerged in false vacuum plasma.

Regarding the spectral index introduced in Eq. (1.2.70), when studying a binary coalescence background, it is necessary to set $\alpha = -2/3$, $\beta = 2/3$, while $\alpha = -1$, $\beta = 0$ for an inflationary background, making the spectrum independent on the frequency, i.e. $\Omega_{GW} = const$. These spectral values can be derived from the power spectral density of the overlap of many source realizations, see e.g. [10].

Phase transitions:

Phase transitions happen daily, for example, the transition of liquid water becoming ice or steam. In those events, a change in the properties of matter occurs, including parameters such as entropy, temperature, and volume. Thus, a transition of phase carries an energy associated with it. Phase transitions are the result of spontaneous symmetry breaking, where a field in an unstable minimum suddenly falls into the stable minima, liberating energy. In a more general context, a system in a metastable minimum or false vacuum undergoes a phase transition through quantum tunneling or thermal fluctuation to reach the true vacuum or the stable minima [14]. In this process, the budget energy is characterized by the order of the extrinsic parameters. It can be classified as First-Order Phase Transition (FOPT), where the thermodynamic quantities are discontinuous, resulting in a jump between the phases, or as second-order phase transition, where the transition parameter is continuous at first order but discontinuous at second-order.

First-order phase transition involves bubble nucleation as a consequence of discontinuities of energy density in the plasma. The true vacuum is contained within the walls of a bubble, immersed in a false vacuum fluid where the symmetry is still conserved, see Fig. 1.6. Once the symmetry is broken, part of the liberated latent heat raises the plasma temperature while the other part is converted into kinetic energy of the bubble's wall and bulk motions of the fluid. Those bubbles can grow, collide, and percolate, generating radiation in the form of gravitational waves [15; 16]. Hence, a signal from the FOPT is expected to contribute to the SGWB. Meanwhile, it is not the case for a second-order transition, where the possible generation of GW has a negligible contribution [16].

To understand the characteristic amplitude of a GW produced by a FOPT, one needs to consider the different contributions to this process. The nucleated bubble expands with constant acceleration, driven by the pressure difference between the low-energy interior and high-energy exterior. However, this action can be counteracted by the friction of the plasma, leading to a constant velocity. In the expansion of the bubbles, the perturbation in the fluid can cause a compression wave surrounding the bubble, giving rise to a sound wave contribution even long after the collision or merger has been completed [17]. Given the spherical symmetry of a bubble, a single bubble produces no gravitational waves. It is only after a collision that the spherical symmetry is broken, and gravitational radiation is emitted. High velocities and large energy densities provide the necessary conditions to produce gravitational radiation [18]. Another contribution associated with the motion of the bubble is the magneto-hydrodynamic turbulence in the surrounding plasma [15]. Finally, one can write the energy density of the gravitational waves produced by a FOPT as the contribution of these three interactions: collision, sound waves, and turbulence.

Considering the early Universe, one can probe the Standard Model (SM) since it is believed that all the forces were once combined in the Grand Unification Theory [19]. As the Universe cooled down, the strong field became distinguishable from the electroweak field, which sometime later also forked into electromagnetic and weak fields by a symmetry breaking. The electroweak phase transition is not an FOPT, but some extensions of the SM could change that statement [20]. Hence, the detection of GWs emitted by these phase transitions would be an unequivocal probe of high-energy physics beyond the SM, inaccessible by other means.

Inflation:

Inflation theory was introduced to solve the flatness problem and the horizon problem [19; 21]. The first one arises from the strange apparent coincidence of the present energy density (that is, radiation, baryonic matter, dark matter, and dark energy) with the critical energy density in the Universe, given by

$$\rho_0 = \frac{3H_0^2}{8\pi G} + \frac{3k}{8\pi G}, \qquad \rho_c = \frac{3H_0^2}{8\pi G}. \tag{1.2.73}$$

This similarity calls for a flat Universe, hence a zero curvature ($k = 0$).

The second issue is visible in the CMB. The frozen picture of the recombination or decoupling time is observed today as a perfect black body emission with a temperature of ~ 2.73 K. Moreover, observations from WMAP [22] and later from Planck [23] found small anisotropies of the order of $\delta T \sim 10^{-5}$K [24]. Those fluctuations are believed to be the seeds of galaxy formation. The real issue is that two points in the sky separated by an angle larger than 1° are supposed to be causally disconnected at the recombination, but instead, they present the same temperature, except for that small fluctuation δT. Then, the question of how can this be possible if they were not causally connected arises.

As previously mentioned, inflation solves both dilemmas. Right after the Big Bang, the Universe underwent an exponential growth of $\sim e^{60}$ [25], possibly as the result of an inflationary scalar field ϕ slowly rolling to a minimum energy state. Once that point was reached, any potential initial curvature was diluted, later, the inflation stopped, and the reheating process began. In that expansion, points that were causally connected were left outside the horizon or frozen out. When those scales re-entered the horizon, they preserved that causal relation observable today in the CMB in the form of similar temperatures, except for the small fluctuations.

If one considers quantum field theory, all fields have quantum fluctuations associated with them. Those variations in the inflationary and gravitation fields give rise to scalar and tensor perturbations, respectively. The scalar fluctuations are established to be the small anisotropies observed in the CMB, while for the gravitational fluctuations, B-modes are expected to be found in the CMB [26]. In the case of SGWB, gravitational waves generated during inflation could be detected at frequencies above 10^{-17} Hz with a spectrum related to the tensor number density n_t [27].

Cosmic Strings:

Cosmic Strings (CS) are hypothetical topological defects that may have formed during a symmetry breaking in the early Universe. In the zero-width approximation, those defects are represented in one dimension, hence strings, whose dynamics are obtained by solving the Nambu-Goto action [28]. The action minimizes the area sheet traced by the string as it travels through spacetime. Consequently, a network of CS grows at the same scale as the expansion of the Universe. This means that CS behaves like radiation in the radiation era and like matter in the matter era.

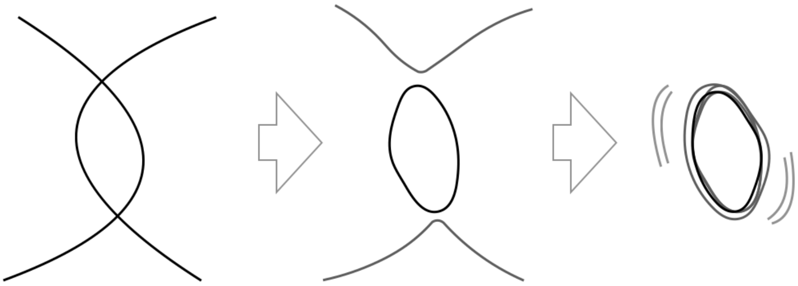

Figure 1.7: Formation of loops. When 2 strings intersect, they exchange partners closing a loop, that will shrink emitting gravitational radiation.

When two points of the same CS or two different strings intersect, there is an exchange of partners, giving rise to loops, a visual aid is shown in Fig. 1.7. This action is known as intercommutation, and the probability of this action taking place is a rapidly decreasing function of time because the string density is falling [29]. Once the loops are created, they oscillate quasi-periodically, losing energy and making the loops shrink while emitting radiation in the form of GWs to finally disappear. Moreover, cusps (points where the string instantaneously reaches the speed of light) and kinks (discontinuities on the tangent vector of a string) propagating on string loops would also generate gravitational bursts. A stochastic background from 10^{-16} to 10^9 Hz could exist, depending on the properties of the loops [30].

Cosmic strings are characterized by the dimensionless tension of the strings, $G\mu \sim (T_c/M_{Pl})^2$ $(c = 1)$, where μ is the mass per unit length, T_c the critical temperature at which the symmetry breaks and M_{Pl} is the Planck mass. In general, a loop of size l

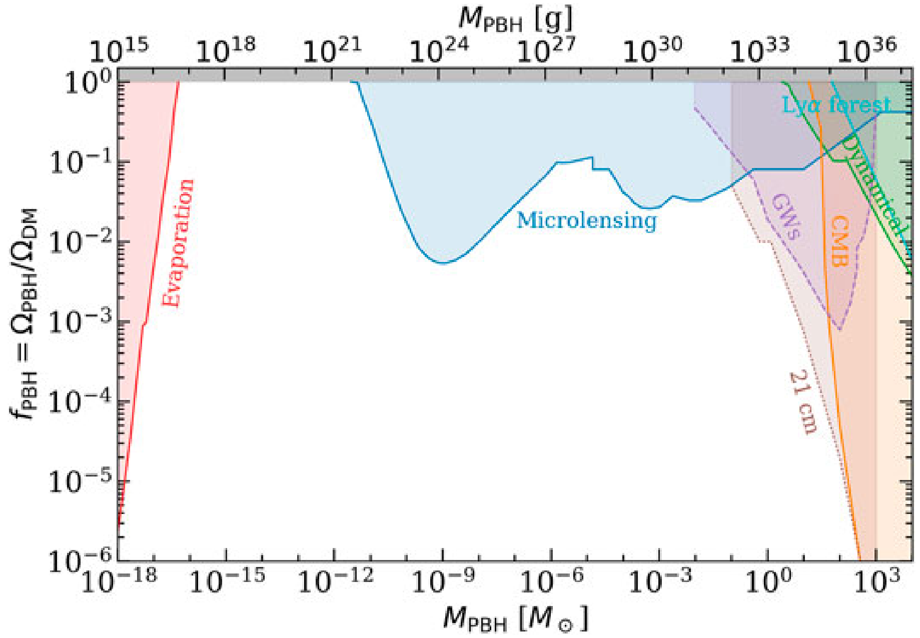

Figure 1.8: Different observational constraints on the PBH fraction for the DM as a function of the PHB mass. *Credits: Villanueva et al.* [31].

emitting gravitational radiation is expected to decay within a time approximated by

$$t = l/(\Gamma G\mu), \tag{1.2.74}$$

where $\Gamma \sim (50 - 100)$ is a coefficient denoting the number of strings in a Hubble volume [29]. The equations involved in the description of the CS are beyond the scope of this manuscript, but in a rough approximation, the produced spectrum can be described as $\Omega_{GW} \propto (G\mu)^2$ [8]. Then, one could relate the observed gravitational radiation with the size of the loops, see Eq.(1.2.74), that would indirectly constrain the lifetime of a loop [8].

Primordial black holes:

Primordial Black Holes (PBH) are small BHs produced in the early Universe, right after the Big Bang. In the inflation epoch, fluctuations in the curvature are believed to occur. As the overdensities re-enter the Hubble radius, they would collapse into PBH. Nevertheless, this is not the only mechanism to produce PBH, as many other possible processes, such as preheating, phase transitions, early matter era, cosmic strings, domain walls, and primordial magnetic fields, among others, were proposed and emerged in the last decade, I refer the reader to [32] for a review on this topic. It is suggested that such PBH could contribute to the undetected Dark Matter (DM) in the Universe or to the seeds for Massive Black Holes (MBHs).

PBH could account for a fraction of the elusive DM. PBH are suspected to be formed before nucleosynthesis since they do not contribute to the baryon abundance, and thus, they can be considered as non-baryonic DM. A fraction of DM is needed to explain the velocity rotation at the arms of spiral galaxies. However, the remaining part could

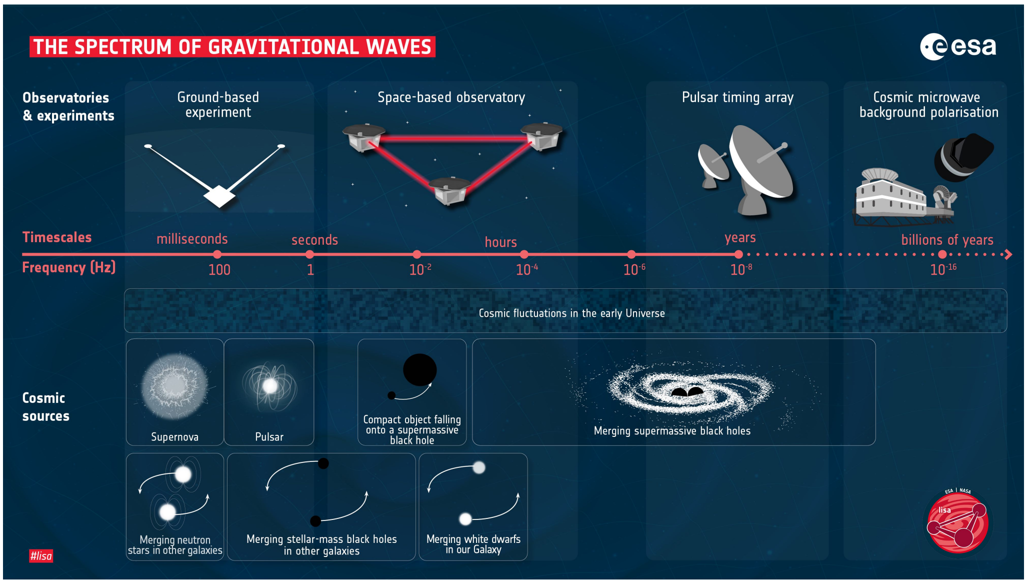

Figure 1.9: Gravitational wave spectrum. *Credits: LISA Red book* [3].

be understood as PBH leading to observable effects, such as microlensing or dynamical effects, see [31] for further information. Based on the same reference, constraints from various observations are imposed on the masses of PBHs and their contribution to the total DM fraction, as illustrated in Fig. 1.8.

After the first detection of GWs due to the coalescence of a Black Hole Binary (BHB), PBH gained credibility [33; 34] as an alternative channel to explain the individual BHs with masses around $\sim 25\ \mathrm{M}_\odot$ as to possible DM in the form of PBH. Additionally, the James Webb Space Telescope (JWST) [35] spotted galaxies at high redshift [36] in an epoch where astrophysical mechanisms fail to explain the existence of MBHs. Therefore, PBH are strong candidates for MBHs in the early Universe, as their masses cannot be achieved through stellar evolution.

In conclusion, PBH are expected to produce an SGWB, either from the merger of PBH with different masses throughout the Universe or from their production at the inflationary stage of the Universe.

Gravitational wave spectrum

To conclude the section on sources, it is essential to identify the frequency at which one expects to observe the mentioned sources. The gravitational wave frequency is twice the orbital frequency of a binary system, so it is straightforward to estimate the detectability band of binary systems depending on their mass and the scale of their orbits. Note that Massive Black Hole Binariess (MBHBs) lie in the low-frequency range of the spectrum, with a downward trend for higher masses. This means that the final phase of the coalescence of galaxies falls between 10^{-3} to 10^{-10} Hz. The SGWB is less evident as it depends on the source producing the stochastic background. In the case of SGWB with cosmological origin, for instance, the electroweak symmetry breaking at $E \sim 160$ GeV, could produce GWs also below the milihertz regime. A sketch of the gravitational-wave spectrum is shown in Fig. 1.9. Note that depending on the frequency scale, different types of observatories are indicated according to their sensitivity, which depends on the size of the arms or rulers, as introduced at the beginning of this section. Keep in mind that a ruler is sensitive to wavelengths larger than its length. In the following, I describe the mechanism that ground-based and space-born detectors use to detect GWs: Interferometry.

1.3 Michelson interferometer

An interferometer works by overlapping two or more light sources to create an interference pattern. The basic configuration of a Michelson interferometer consists of a light source, a beam splitter, a series of mirrors and lenses, and a photodetector that records the interference pattern. Because of their wide application, there exist several sizes and shapes of interferometers, though a simple layout of a basic one is sketched in Fig. 1.10. The light emitted from the source hits the beam-splitter, which due to its disposition at 45°, lets half of the beam pass through in the x-axis while reflecting the other half in a perpendicular beam in the y-axis. Each beam is reflected in a mirror at a distance L, to meet again at the splitter, which redirects both beams to the detector where the interference information is collected.

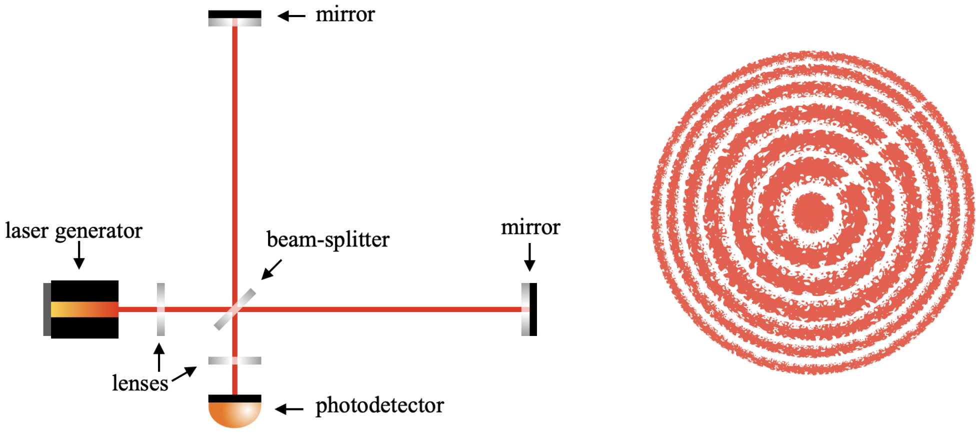

(a) Michelson Interferometer (b) Interferometry fringe pattern

Figure 1.10: Sketch of a Michelson interferometer and the interference pattern alternating from constructive to destructive interference. [5]

Both beams should travel the same distance in a time $\tau = 2L/c$. Then, the resulting interference should be constructive, namely bright interference, since the two waves are in phase. The effect of being completely out of phase would result in destructive interference, while a phase between both stages would create an intermediate interference pattern. By tuning the phases to achieve a destructive interference pattern, a slight displacement would be observable by the change in the pattern from a dark fringe to a bright fringe interference, represented in white and red, respectively, in Fig. 1.10. In the case of a perturbation, such as the one produced by a passing GW, the length of the arms would stretch and compress, producing a difference in the arrival time of the beams. Using Eq. (1.2.44), which accounts for the displacement of the test masses, the difference in the light travel time between the two arms (L) is

$$\delta\tau = \tau_1 - \tau_2 = \frac{2L(1+1/2h_+)}{c} - \frac{2L(1-1/2h_+)}{c} = \frac{2L}{c}h_+. \tag{1.3.1}$$

If one takes into account that a light beam with a frequency ν and amplitude A has an electric field

$$\vec{E} = \vec{A}e^{i2\pi\nu t}, \tag{1.3.2}$$

when both beams recombine in the photodetector, the resulting electromagnetic field is the sum of them: $\vec{E} = \vec{E}_1 + \vec{E}_2$. Therefore, the travel time difference can also be translated into a phase difference $\Delta\phi = 2\pi\nu\Delta\tau$. As the gravitational wave crosses the arms of the interferometer, the interference would vary between destructive and constructive which can be translated as a strain amplitude variation, producing a waveform in time $h(t)$.

1.4 Detectors

The idea of the first gravitational waves detector was developed by Joseph Weber in the 60's [37; 38]. He developed what is now called the Weber antenna, which consists of a solid aluminum cylinder bar of ~ 2 m long by 0.96 m radius, suspended at its center. The method exploits the fact that the energy and momentum carried by a GW would induce the excitation of resonant modes of the object. As the bar rings down the excitation modes, piezoelectric crystals near the center of the bar would translate the vibrations in a voltage difference measuring the strain of the passing GW. Weber claimed several detections over the years with no support from his peers, who attributed the findings to noise [37; 38]. He kept improving the sensitivity of the instrument and claimed the detection of GWs from the supernova SN1987A, although the measurement was never confirmed. The claim was and still is highly questionable since the sensitivity of this mechanism would not have reached the required precision to detect the small displacement due to a GW. Regardless of the validity of his results, his experiment and the enhancements he made to the instrument paved the way for future interferometric detectors.

Nonetheless, it is important to mention that GWs have been detected indirectly in the 80's through observational means. The first indirect observation of GWs was reported in 1989 by Alan Hulse and Joseph Taylor [6] , due to the decreasing orbit of a binary pulsar

---

[6] Their study allowed them to earn the Nobel Prize in 1993.

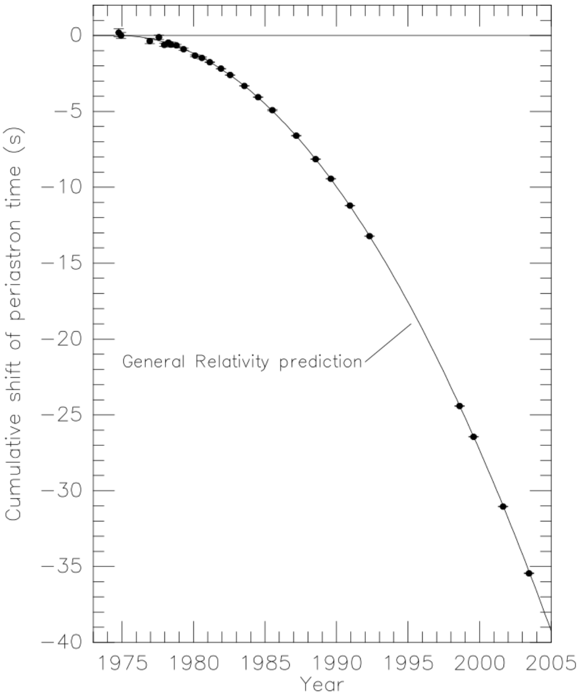

Figure 1.11: Orbital decay of PSR B1913+16. The dots indicate the observed change in the orbital period for a given date while the line illustrates the theoretically expected change for a system emitting gravitational radiation, according to GR. *Credits: Taylor and Weisberg* [39].

named B1913+16. A binary pulsar is composed of two NSs with strong magnetic fields about 10^{8-9} G, rapidly rotating in an axis tilted from the magnetic field dipole, producing a lighthouse effect. Studying the binary, they realized that the period of the orbit had been decreasing over the years, see their results in Fig. 1.11. The energy loss associated with the decreasing period was consistent with GW radiation predicted by GR [39–41], resulting in the first indirect detection of GWs.

1.4.1 Ground-based detectors

The most famous ground-based interferometer is the Laser Interferemeter Gravitational-wave Observatory (LIGO) [42] as it was the first to detect a GW from the coalescence of a BHBs on September 14, 2015 [43]. Nevertheless, there are other detectors such as GEO600 [44], Virgo [45], and Kagra [46]. All these antennas work together in what is called the LIGO-Virgo-KAGRA (LVK) Collaboration to cover the observations over the whole sky. Even though antennas are considered to be all-sky surveys, they have some blind spots. For this reason, the placement of several observatories all over the globe is required to cover all the angles in the sky, which allows us to combine the results and perform a good estimation of the sky localization of the source.

The GEO 600 interferometer is a 600-meter interferometer located near Hanover in Germany. In 2006, GEO600 reached the design sensitivity of $h \sim 3 \times 10^{-22}$ Hz$^{-1/2}$ at about 700 Hz, but up to now no signal has been detected [44]. However, its presence is fundamental, as it was the first antenna to be operational and constitutes the base for second-generation interferometers. It is also frequently used to test technical innovations for next-generation ground-based interferometers.

LIGO consists of three interferometers, H1 with 4 km arms and H2 with 2 km arms located in Hanford, Washington, USA, and L1 also with 4 km arms located in Livingston, Louisiana, USA. They have been operational since 2002, with a current catalog at the end of O4a (first half of the fourth observational run) of about 170 detected sources, where 81 of them are unconfirmed but with significant probability [47]. The current sensitivity allows to detect sources at ∼150 Mpc [47].

The Virgo interferometer located near Pisa, in Cascina, Italy, has 3 km arms and joined the network at the end of the second observation run (O2). Its current sensitivity has been compromised, reaching distances of 40 to 80 Mpc. Nevertheless, with a catalog of many events [45] its participation in the O2 was essential to correctly locate the coalescence of two NSs [48], which enabled the identification of its Electro-Magnetic (EM) counterpart [49], a γ-ray burst observed by Fermi [50]. This event marked the beginning of the multi-messenger astronomy era.

KAGRA is a 3 km arms interferometer placed underground in the Kamioka mine in Japan. Even though the Japan region is known to be seismically active, the underground placement allows to suppress the seismic noise. Contrary to other detectors it operates at cryogenic temperatures with sapphire mirrors to suppress thermal noise. It joined the network at the beginning of 2020, however, it is still tuning its operational mode to achieve the design sensitivity, which at the moment allows it to detect sources at distances no further than 10 Mpc [47].

The LIGO-India will be a 4 km armlength detector and is still in a development stage [51]. It will complete the LVK network.

The construction of third-generation interferometers with higher sensitivity is planned but pending approval. One is Cosmic Explorer, an American project with 40 km arm length [52]. The other is a European collaboration, the Einstein Telescope (ET), that will be placed underground in a European country that has yet to be decided. Instead of two perpendicular arms like previous ground-based detectors, this detector is expected to have three arms forming an equilateral triangle with a 10 km side [53].

Current detectors are in essence Michelson interferometers introduced in Sec. 1.3, nonetheless, they had to evolve to gain sufficient sensitivity to achieve the detectability regime. One property is that ideally the mirrors, also referred to as test masses, should be free-falling. In ground-based laboratories that freedom can be approximated by hanging the masses as pendulums [54]. The test masses are 40 kg cylindrical polish fused silica, with a reflectivity of $\sim 99.99\%$, hanging from a 4th stages pendulum. The first three stages consist of steel wire, while the last stage is made of silica fibers. This layout helps to isolate the mirrors from vibration. This action is complemented by an internal seismic

(a) LIGO in Levingston, USA (b) GEO600 in Hanover, Germany

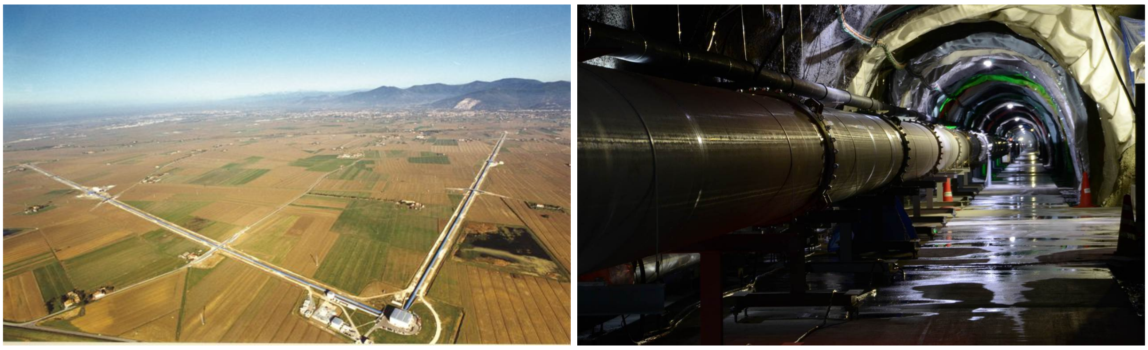

(c) Virgo in Cascina, Italy (d) Kagra in Kamioka, Japan

Figure 1.12: Photos of the LVK Collaboration interferometers. *Credits: LVK Collaboration* [12].

isolation system composed of movement sensors and mechanical devices that counter-act movements generated by environmental vibration, allowing the test masses to be motion-free.

Another important addition consists of another mirror between the splitter and the mirror at the end of each arm [55]. The beam is then reflected several times, about 300, between the test mass in the middle and the one at the end before recombining at the photodetector with the beam from the other arm. This feature increases the effective length of the arms without having to make them explicitly larger. The arm lengths of LIGO are 4 km, but with this adaptation, the effective length becomes 1200 km. For the 3 km arms in Virgo, the effective length is around 850 km. This kind of adaptation is called a Fabry-Pérot resonant cavity [55].

One property of the laser is that the frequency is monochromatic, so it can be set according to the length variation. Increasing the laser power entails an increase in the interferometer's resolving power since it will sharpen the interference fringes. However, too much power, also called shot noise, will inflict too much pressure on the test masses and generate a displacement in the mirrors. So a balance between the shot noise and the pressure radiation has to be set. In the case of LIGO-Virgo, that balance occurs when the laser operates close to 750 kW. Since the input power is about 40 W, power

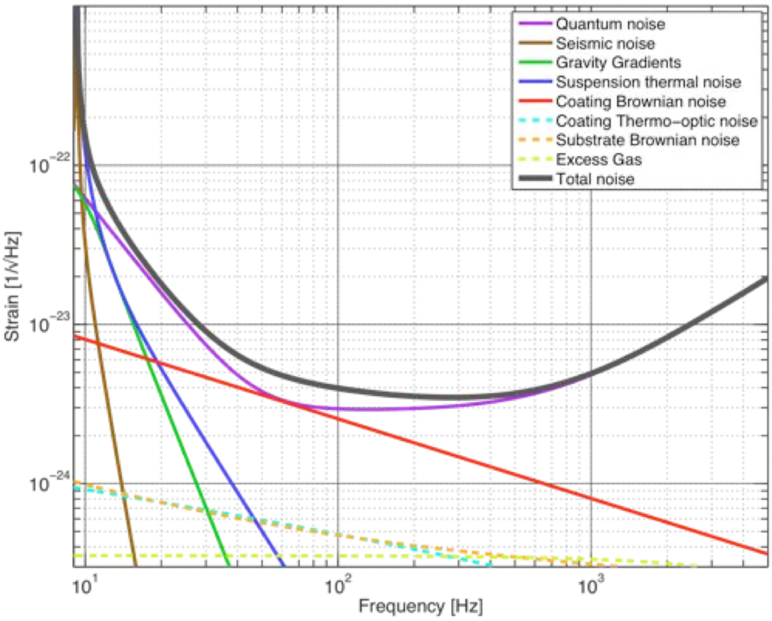

Figure 1.13: Sensitivity curve in advanced Ligo. *Credits: LIGO Collaboration* [55].

recycling mirrors are placed in each arm to increase power. All the light that escapes the Fabry-Perot cavity is constantly reflected into the interferometer by these recycling mirrors, ensuring that nearly all of the laser light entering the arms follows a path back to the reflective side of the power recycling mirror rather than to the photodetector [12]. Signal recycling mirrors are also placed before the photodiode detector to optimize the sensitivity. A given bandwidth selected by the mirror's reflectivity redirects the signal to the interferometer, enhancing its size through resonance.

An ultra-high vacuum is needed to avoid statistical variations in the column density of gas particles in the beam path over the 3 or 4-km tunnel. The noise model is calculated by integrating the molecular velocity distribution. It is also important to prevent the pressure applied by the residual gas components, hydrogen being the most dominant contributor [55].

Sensitivity

The design sensitivity of advanced LIGO is shown in Fig. 1.13. Different noises shape the final sensitivity curve [56]. The most constraining are the quantum noise, the thermal noises, the seismic noise, and gravity gradients.

Quantum noise: This noise includes the effects of statistical fluctuations in shot noise and radiation pressure due to photons' quantum behavior. Shot noise is derived from the Heisenberg principle, which entails an uncertainty in time and energy. This variation can be interpreted as a lag in time or phase, hence mimicking a GW signal. In the high-frequency range, a major contribution from this type is expected, while at low frequencies, the radiation pressure is expected to be the dominant contribution [55]. Of course, the effects of the radiation pressure fluctuations can be reduced by increasing the mass of the mirrors or by decreasing the laser power at the expense of degrading the sensitivity at higher frequencies.

Thermal noise: The operating range of the detector lies between the resonances of the test masses and their pendulum suspensions, and thus the noise in the operating range comes from the tails of these resonant modes [56]. Coating Brownian noise is the dominant of the various test mass thermal noise terms. It arises from mechanical dissipation in the mirror coatings. Mechanical loss in the bulk test masses is responsible for the substrate Brownian noise term. To decrease this kind of noise the test masses should have a shape, whose resonance frequency is not in the operating range.

Suspension thermal noise: It is primarily due to loss in the material of the suspension. Any harmonic oscillator such as a pendulum has an energy described by the pendulum frequency and the material frequency. Then, again a loss factor associated with the resonant frequency is related to the mechanical noise of the material [57]. To lower this noise, fused silica fibers are used in the final stage of the suspension. The four fibers that hold the masses have a circular but variable diameter, being thin in the middle section of the fiber, and about twice as thick near the ends, since this geometry minimizes the thermal noise [55].

Seismic noise and gravity gradients: The ground motion has a severe impact at low frequencies. To minimize this effect it is necessary to isolate the test masses. A combination of passive and active instruments is introduced to make this possible. An inertial free platform balancing over an inverted pendulum composes the active stage, while the passive stage involves the multistage pendulum, which completely attenuates the effect of this noise above 20 Hz.

Indeed, one can observe a cutoff in the lower frequency regime in Fig. 1.13, mainly due to the seismic and thermal suspension noises. Therefore, it is not surprising that having an interferometer in space is considered to overcome these constraints. In space, no thermal suspension affects the free-falling test masses, and no seismic noise is present either. Nevertheless, other noises will gain weight, as I describe in Sec. 2.4. Keep in mind that there is a need to observe the lower frequency band, to open the door to other sources such as MBHBs and Supermassive Black Hole Binarys (SMBHBs). See Fig. 1.9.

1.4.2 Space-born detectors

The idea of space-born interferometers arises naturally as an answer to overcome the seismic noise and the suspension thermal noise when shifting to a lower frequency band.

In this regime, one can find the Laser Interferometer Space Antenna (LISA) that has recently been adopted by the European Space Agency (ESA). The details of the mission are not discussed here, but in Chapter 2, which is completely dedicated to the LISA observatory. However, as a brief description, it is worth mentioning that its objective is to detect GWs in the millihertz band, from 10^{-4} to 0.1 Hz [3]. The constellation consists of three spacecraft in a triangular formation, to produce Michelson interferometers via laser beams exchanged between the three satellites with a 60° angle between arms of 2.5 million km length. The equilateral formation will trail the Earth about 50 million km in the same heliocentric orbit. The mission is expected to be launched at the end of 2035.

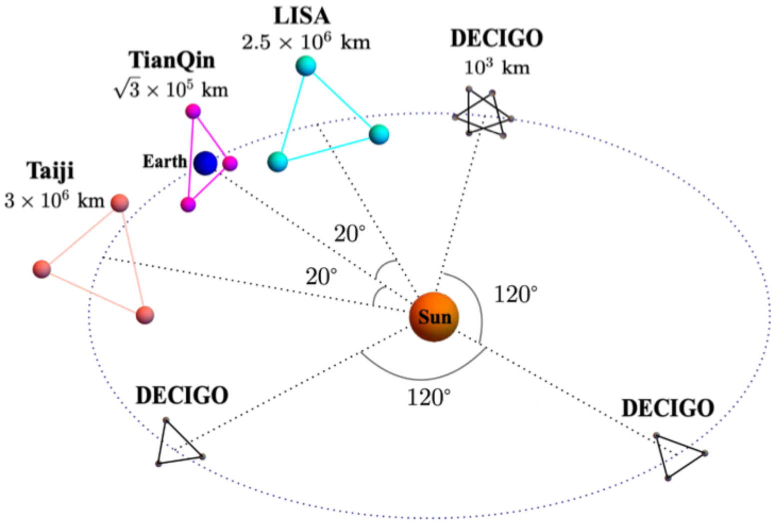

Figure 1.14: Schematic of space-born GW detectors in Earth's orbit. *Credits: Luo et al.* [58]

China has proposed to launch other two space-born telescopes also in the millihertz band, Taiji [59] and TianQin [60]. Both have a similar design concept as LISA but with different arm lengths. In the case of Taiji, the three spacecrafts will precede Earth in its heliocentric orbit. The constellation will have a triangular formation with a length of 3 million km and a possible launch in 2033. TianQin is expected to orbit the Earth in a $\sqrt{3} \times 10^5$ km size triangular setup, which allows reaching slightly higher frequencies, covering part of the frequency gap between LISA and ground-based interferometers.

Other detectors, such as DECihertz Interferometer Gravitational-wave Observatory (DECIGO) and B-DECIGO [61], have been planned to cover frequencies between 0.1 and 10 Hz. The mission is still in the development stage.

A collaboration network between two or more detectors would have great potential to contrast and complement results, which would allow enlarging the science case with GWs in the mHz band and above [58]. See Fig. 1.14 for a sketch of the potential location of the different space-detectors.

1.4.3 Pulsar Timing Array

Pulsar Timing Array (PTA) is a network of many galactic pulsars. A schematic is presented in Fig. 1.15. Pulsars are NS with a strong magnetic field that expels electromagnetic radiation through its poles in the form of jets. If the rotation axis differs from the magnetic axis, the pulsar becomes a beacon with a frequency equal to its rotation.

The rotation or spin of these objects is quite steady being around 10^{-3} to 10 s, with a derivative of the order of $10^{-[12-20]}$ s/s, which makes them very precise clocks.

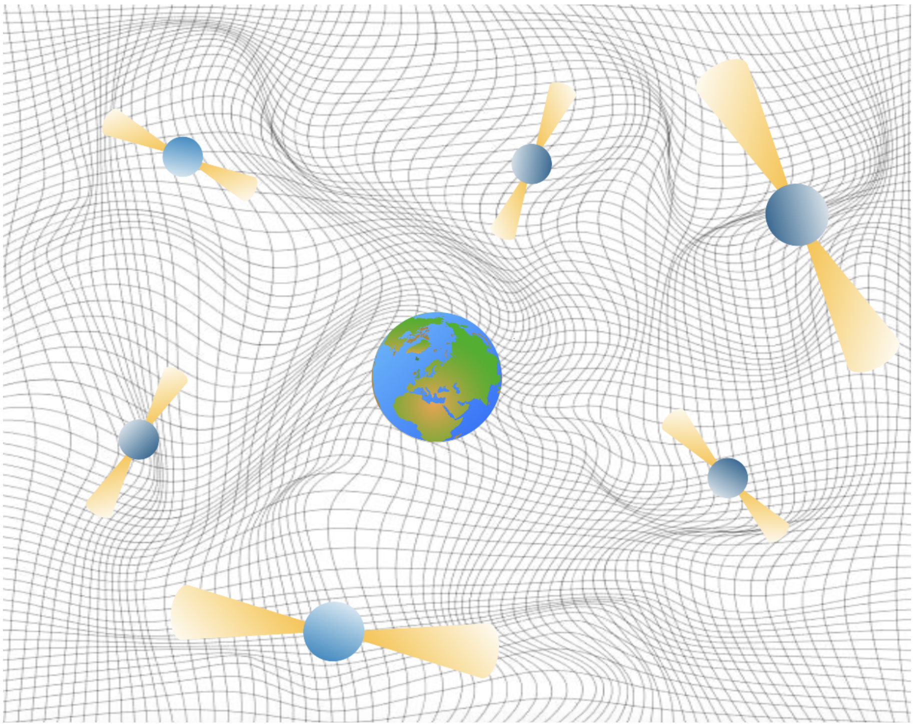

Figure 1.15: Representation of the pulsar timing array in a perturbed spacetime manifold.

To constitute the network of pulsars, only the fastest rotating pulsars with spins of milliseconds are considered. Then, by knowing the precise time of arrival (ToA) one can compute deviations from the expected value. There are several challenging features to take into account when dealing with these astrophysical objects. For instance, the ToA could be perturbed due to a passing cloud of matter in the emission line. Other effects that can impact the ToA are the slowly varying spins that would introduce a residual red noise, or the proper motion of the sources, as well as instrumental noises such as the reference clocks or thermal noise in the telescopes to name but a few. For an isotropic, unpolarized SGWB, the expected correlated response of a pair of pulsars follows the so-called Hellings-Downs curve [62]. Hence, all the measurements of ToA of the pulsars are combined to search for the presence of the Hellings-Down correlation. In an analogy to the interferometer, the distance between the pulsar and the observer is the arm length of the detector. Thanks to these very large rulers, the GW frequency window is from 10^{-9} to 10^{-6} Hz.

Recently studies from three collaborations, the European Pulsar Timing Array (EPTA)[63], the Parkes Pulsar Timing Array (PPTA) [64] and the North American Nanohertz Observatory for Gravitational Waves (NANOGrav) [65], found preliminary evidence of a gravitational wave background [66–74]. Each collaboration collected (and keeps collecting) data for several years with different radiotelescopes and with different arrays of pulsars, so the common signal could not be attributed to instrumental noises. Of course, different analyses were and still are performed to properly identify the common signal. Nevertheless, the most likely candidate is a stochastic background generated by binaries of supermassive black holes.

There are three more collaborations: the Chinese Pulsar Timing Array (CPTA) [75], the MeerKAT Pulsar Timing Array (MPTA) [76], and the Indian Pulsar Timing Array (InPTA) [77] that recently started taking data, but with similar results [78**?**]. The contribution of these collaborations to a single data analysis could shed more light on the nature of the stochastic background. The International Pulsar Timing Array (IPTA), a group including EPTA, PPTA, NANOGrav, and InPTA, plans to perform such analysis [79–81].

Chapter 2

LISA

The Laser Interferometer Space Antenna (LISA) is an European Space Agency (ESA) scientific space mission to detect gravitational waves in the range of millihertz. It consists of three satellites in a triangular formation to produce interferometric measurements. As a GW crosses one arm of the antenna, it will create a deformation of the spacetime changing the relative distance between two test masses in distant spacecrafts. Small distance variations are sensed by interferometry techniques, as I detail in Sec. 1.3.

The constellation will follow Earth at a distance of about 50 million kilometers in the same heliocentric orbit, with an inclination of the constellation plane of 60° to the ecliptic plane, a visual representation is shown in Fig. 2.2. This distance emerges as a compromise between ground communication, and counter-productive gravitational interaction from Earth. The triangular formation is opportune to produce different interferometers with particular combinations of phasemeter measurements. In the following sections, I recall the success of LISA Pathfinder in probing required technologies for LISA in Sec. 2.1. Sec. 2.2 is used to exhibit a general description of the mission. I describe the components of the Spacecraft (S/C) and the interferometry measurements in Sec. 2.3 and the expected associated noises in Sec. 2.4. Afterward, I move to the post-processing description of the interferometric measurements in Sec. 2.5. Once the data time series are produced, the analyses to extract the science take place. In Sec. 2.6 I list the expected observations and the science objectives of LISA in Sec. 2.7. This chapter is based mostly on [3; 82; 83].

2.1 LISA Pathfinder

LISA Pathfinder (LPF) was launched on December 3, 2015, and was in science operation from March 1, 2016 to June 30, 2017. The satellite orbited the L1 point, located some 1.5 million kilometers from Earth in the direction of the Sun. The mission was conceived to test one of the central technologies for LISA. Its objective was to probe the free-fall performance of two test masses, while inside of a spacecraft. A small interferometer with a length of 38 cm was assembled within the spacecraft, with a test mass reflecting the beam at each end of the arm [84]. Each gold-platinum test mass was allowed to free-fall within a vacuum container. The aim was to measure the displacement of the test masses. The displacement yields the geodesic deviation of the test masses due to inertial and EM forces from the container and the spacecraft itself. At low frequency $1 - 30$ mHz the dominant noise was identified as the Brownian motion of the test masses by the residual gas in the container. Above that frequency, the interferometer readout noise was superior to all the other noises.

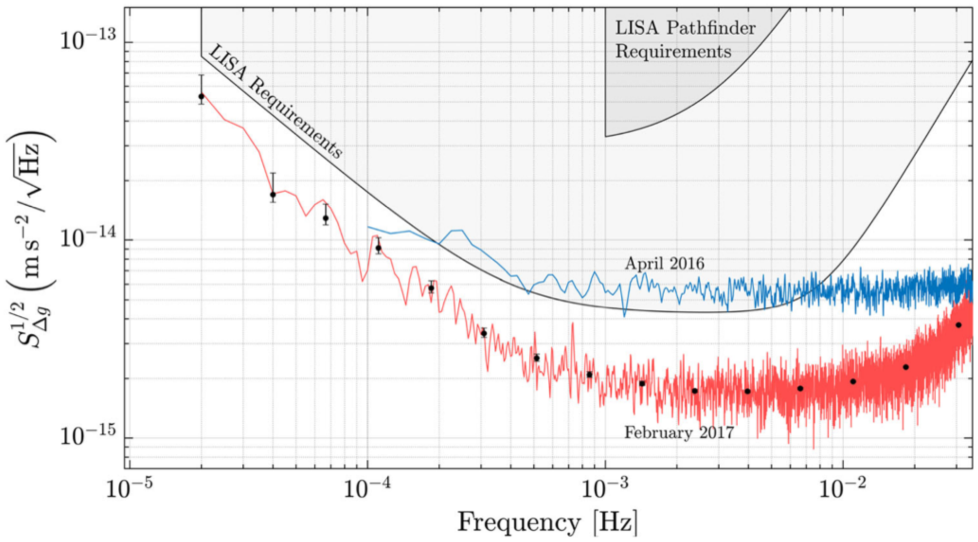

Figure 2.1: Amplitude spectral density of the spurious differential acceleration between the two test masses in LPF. Results from the first publication in blue [84], and the improved results from the second publication in red [85]. Note the required ASD for LISA and LPF mission above the obtained results in grey. *Credits: LPF Collaboration* [85].

Between the first [84] and the second publication [85] of the results, the identification and comprehension of spurious noises, like the pressure of the gas surrounding the test mass, the electrostatic actuation force and the S/C rotation, allowed for an improvement on the measurements. Notably the identification of glitches allowed for a noise reduction. Even though the glitches were not completely understood, their characterization was useful to produce a catalog with a large probability of being seen in LISA and to develop methods to detect them [86]. Consequently, the accuracy of the Amplitude Spectral Density (ASD) of the acceleration deviations exceeded the expectations [85]. The successful results of LPF shown in Fig. 2.1, allow us to demonstrate the feasibility of the drag-free control by the use of inertial sensors, the laser metrology system, and the ultra-precise micro-propulsion system that will be adapted to LISA [87].

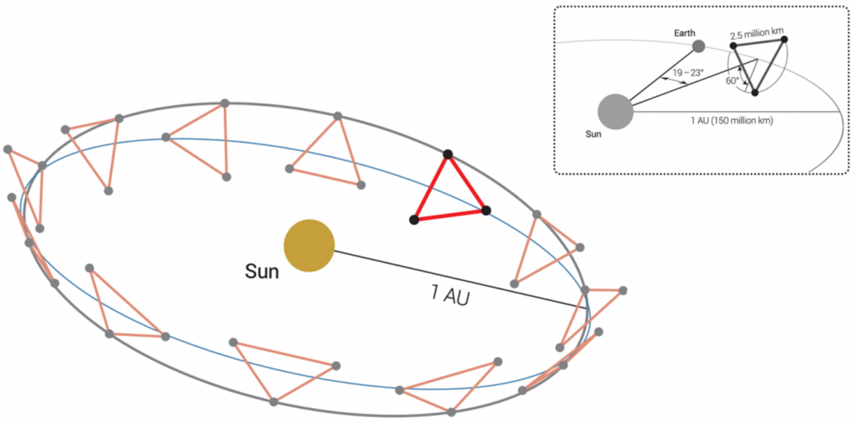

Figure 2.2: Cartwheel motion of the three spacecraft and the constellation orbit position with respect to the Sun and Earth. *Credits: ESA* [87].

2.2 Mission

In 2017 the project became a large mission for ESA. It was selected as an L3 mission in ESA's "Cosmic Vision 2015-2025" with a contribution from the National Aeronautics and Space Administration (NASA) as a junior partner. The milestone of GWs detection in 2015 by LIGO as well as the success of the LPF proof-of-concept, were decisive in tilting the balance positively to its selection. After going through several studies on the science, the technology involved, and the processes to analyze the data, the mission was considered satisfactory for adoption in January 2024. This means that the development will go as planned and in January 2025 the construction of the instrumentation should begin with an estimated launch with Ariane 6.4 at the end of 2035 [87]. Once in space, around 2 years are needed for transfer and commissioning. When each S/C reaches its position in the predefined orbit, the test masses will be set free to follow the geodesics. Each S/C will also follow the free-falling test masses with the help of the Drag-Free Attitude Control System (DFACS). After the deployment and consistency checks are finished, data taking will start for a nominal duration of ~ 4 years.

The first idea of a space interferometer dates from the 70's. The proposed design of the interferometer changed through the years to eventually evolve to the current design of a triangular formation with 2.5 million kilometers of length. Thus, the constellation is composed of three S/C deployed in a quasi-equilateral triangular formation orbiting the Sun at 1 AU (astronomical unit). Each S/C will follow a particular heliocentric orbit generating a motion of the constellation commonly known as a cartwheel, see Fig. 2.2. A direct consequence of the cartwheel motion is that the path length of the arm in one direction will not coincide with the opposite direction, as shown in Fig. 2.3. The constellation as a whole would approximately preserve its formation, but the relative distance between the S/Cs would slowly change through a year's rotation. This movement results

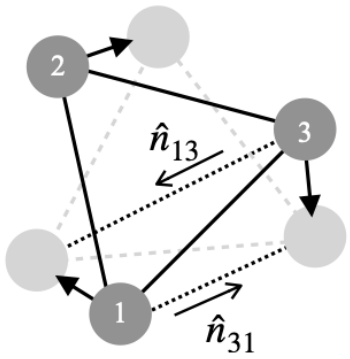

Figure 2.3: Representation of Sagnac effect due to cartwheel motion in LISA. Not to scale.

in a variation of the arm lengths about 50000 km, which represents around 2% of the total distance. Another consequence of moving S/Cs while emitting and receiving signals will imprint a small variation in the response of the instrument to the gravitational wave.

In general, small displacements of the satellites or vibrations of the internal artifacts can mimic the effect of GWs. Therefore the identification and characterization of noise contributions are essential, among which one can consider these two main perturbations, but extended in more detail in Secs. 2.3 and 2.4:

- Displacements of the test mass to the optical bench.
- Acceleration forces acting on the test masses.

The feasibility of LISA measurements relies on the characterization and suppression of the noises via three techniques: *split interferometry*, *time delay interferometry* and *heterodyne interferometry*, that I introduce in the following sections.

2.3 Instrumentation

Laser interferometry allows us to measure small displacements with high precision. However, the constellation will suffer small perturbations, as I previously mentioned. These perturbations can generate a noise that buries the strain of a GW. For that reason their identification is crucial. In this section, I focus on the *split interferometry* and *heterodyne interferometry*, which allow us to measure the test mass to test mass distance [83]. With that goal, I describe now the instruments of the constellation.

In LISA, each S/C carries two Moving Optical Sub-Assembly (MOSA) each composed of an Optical Bench (OB), a laser source, a phasemeter, a telescope, and a Gravitational

Reference Sensor (GRS) where the Test Mass, *often proof mass* (TM) is placed, as shown in Fig. 2.4. I describe each component in the following.

The beam light is generated at the laser source with a wavelength of 1064 nm and a power of 2 W. A small fraction of this beam is redirected within the OB to track the intrinsic motion of the instruments and the rest is sent to the distant S/C. The 30 cm telescope's function is to send and collect the laser beam whose power, after 2.5×10^6 km of traveling, decreases about 10 orders of magnitude, resulting in a received beam of a few hundred picoWatts. This amount is not sufficient to be sent back to the emitted S/C with a simple reflection, therefore a new beam with a locked phase is generated. The locking of the phases is to ensure coherency between the beams. One of the laser beams is chosen to be the master beam, while the others will have a locked phase to the master, with a small frequency shift. The frequency shift, given two beams, serves to obtain a beat note that allows us to perform a heterodyne measurement of the phase difference between those two beams. This technique is called *heterodyne interferometry*. There exist several configurations of phase locking, but one needs to make sure that the frequency difference between two beams lies within the photodetector reading range. For this reason, a so-called frequency plan is developed, see [88] and reference therein for more information on this subject.

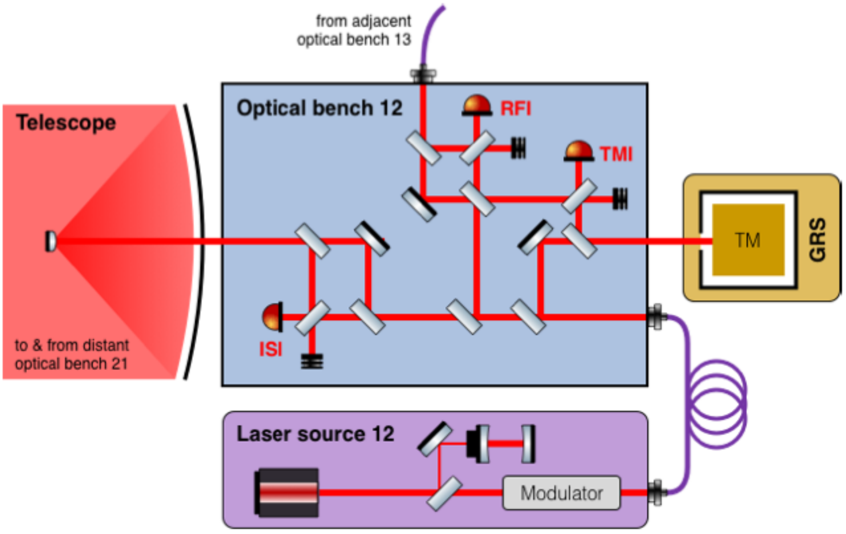

Figure 2.4: Components of the moving optical sub-assembly in spacecraft 1. *Credits: Bayle et al.* [89].

The GRS was designed to contain the test mass and the hardware required to protect and monitor it. The TM is a 46 mm cube made of pure gold-platinum weighing approximately 2 kg. By caging the test mass it remains protected during the launch. Once in flight, it is decaged, positioned, and released in free-fall without any residual inertial forces. The GRS contains sensors to control the transversal displacements of the test mass, and mechanisms to compensate these displacements when required. Such mechanisms consist of actuation forces to counteract rotational or translational accelerations. Moreover, there are diagnostic systems including thermometers, magnetometers, and a radiation monitor to track variations. A UV discharge system surrounding the cube is also in place to neutralize the charge in case of cosmic rays or solar-charged particles. I refer to [3] for further details.

Finally, the OB is where the actual interferometry takes place. The OB consists of a baseplate made of Zerodur to guarantee the stability of the path length in case of temperature variations since the material has a low coefficient of thermal expansion. Several beam splitters, lenses, and mirrors to redirect the beams to different photodiodes complete the bench. The photodiode signals are processed by the phasemeters to extract the phase measurements that translate into displacements. There are three interferometers: the Inter-Satellite Interferometer (ISI), the Test Mass Interferometer (TMI), and the Reference Interferometer (RFI). All three interferometers are combined to compute the test mass to test mass distance that allows us to detect the passing of a GW. The partition of interferometers to asses different displacements or acceleration is known as *split interferometry.* The recombination of the interferometry measurements allows us to perform the GW detection by suppressing the S/C jitter as detailed in Sec. 2.5.2.

The ISI is a long-base interferometer that combines the laser beam generated in the distant S/C with the one generated locally. This measurement carries the imprint of the GWs as well as the information of the laser noise, both S/C jitters and the readout noises. The RFI compares the two adjacent lasers within the same S/C, which allows in particular for the assessment of the backlink noises. The TMI is a local interferometer that follows the same path as the RFI but bounces on the TM before recombination. The phase comparison of these two latter interferometers enables us to measure the displacement of the test mass within the S/C. Note that the laser noise and the readout noise are common to all measurements. See Fig. 2.4 for an elementary sketch.

Three interference measurements are produced per MOSA, resulting in six measurements on board each S/C. The data is then filtered and down-sampled to be digitized to be sent to Earth for post-processing. The rate for sending data to Earth is set to be every 8 hours per day at a frequency of 4 Hz, which would generate glitches or gaps in the measurements due to the antenna pointing. A protected period of up to 14 days is foreseen in case of sources in the proximity of the merger. At that time, no maintenance operations will be allowed to prevent corruption of the data.

2.4 Noises

In this section, I cover the main noises that will appear in the data streams as a consequence of the instruments. Definitions and values are taken from [3; 83; 90]. In the post-processing, several noises can be suppressed leaving a residual noise that will determine the sensitivity of LISA to GWs. The resulting ASD is shown in Fig. 2.5. The dominant noises are taken into account when simulating data and of course in the parameter estimation pipeline.

Regarding the assessment of the noise, I helped in an analysis of the laser injectors' stability in OB prototypes in the ground segment equipment.

2.4.1 Laser noise

The laser implemented in LISA is a standard Nd:YAG laser source with a wavelength of 1064 nm and an optical frequency of 282 THz [3]. The estimated ASD for that laser is of the order of 10^{-13} $\text{Hz}^{-1/2}$, while GWs have amplitudes around 10^{-21}. Then, laser noise is certainly the dominant noise in LISA by several orders of magnitude. It arises from the frequency fluctuation in the laser beam that is transmitted along the whole constellation. In the case of interferometry with coherent light and fixed arms, like ground-based interferometers, the fluctuations cancel out when reaching the photodetector. The complexity added in LISA with continuously varying arm lengths while rotating prevents the suppression with the same techniques. The solution to overcome this issue relies on post-processing called Time Delay Interferometry (TDI) introduced in Sec. 2.5.

2.4.2 Test mass acceleration noise

The Test Mass, *often proof mass* (TM) is supposed to free-fall, but any interacting force would introduce deviations from the geodesic. Displacements from the geodesic mimic the passage of a gravitational wave, therefore shielding the TM from those perturbations is crucial. As I previously described, GRS comprises several instruments to protect, monitor, and act on the TM. All those mechanisms near the test mass will unavoidably introduce inertial forces. Gravitational gradients, particles generating pressure, and EM radiation will all translate into residual noises on the test mass. Nonetheless, the excellent performance of LPF taught us the procedure to achieve the required noise level to observe GWs. The Power Spectral Density (PSD) of the test mass acceleration noise is given by [82]

$$S_{acc}(f) = \left(3 \times 10^{-15}\right)^2 \left[1 + \left(\frac{0.4 \times 10^{-3}\text{Hz}}{f}\right)^2\right] \left[1 + \left(\frac{f}{8 \times 10^{-3}\text{Hz}}\right)^4\right] \text{m}^2\text{s}^{-4}\text{Hz}^{-1}. \tag{2.4.1}$$

As mentioned in Sec. 2.1, the PSD is the result of different effects, such as the Brownian motion, actuation force, stray electrostatic force, magnetic forces, temperature fluctuations, coupling to MOSA and S/C motion and gravitational fluctuation among others [90]. Yet, another noise that deserves to be mentioned is the Tilt-To-Length (TTL) coupling. The TTL is the effect of a small rotation, i.e., a tilt in the TM, which translates into a misalignment between the incident beam and the center of the TM, producing a small pathlength variation. Great efforts to identify and correct it are being developed [91].

2.4.3 Space craft jitter noise

The DFACS is responsible for monitoring the positions of both TMs, enabling the S/C to follow them along their free-fall trajectories. Nevertheless, the S/C should still be able to point the local OB to the OB at the distant S/C and to face the solar panel towards the Sun. In addition, residual forces could produce fluctuations in the free-fall of the S/C. These perturbations can be corrected via the ignition of thrusters. The micro-Newton force achieved by thrusters allows for a precise position and orientation of the S/C. As the S/C corrects its path, the whole assembly suffers perturbations and accelerations that change the relative distance between TM and OB. This agitation noise is mainly a consequence of thruster activity. Therefore, by knowing the TM-S/C coupling as well as the thruster model and DFACS tracking, this noise can be reduced to become negligible in the on-ground data processing [3].

2.4.4 OMS displacement noise

The Optical Metrology System (OMS) displacement noise encloses several artifact noises impacting the effective path of the beams. For reference, this kind of noise was called the readout noise in LPF. Within this noise group, one finds noises related to the laser beam itself and its interaction with the TM or the medium, such as the shot noise, electronic noise, thermoelastic distortion, and photodetectors noise, to name but a few. In the assumption of uncorrelated noises, the estimated PSD results in a quadratic sum of the different noises, with the phase originating in the backlink fibers, the dominant one. The PSD noise then reads

$$S_{oms}(f) = \left(15 \times 10^{-12}\right)^2 \left[1 + \left(\frac{2 \times 10^{-3}\mathrm{Hz}}{f}\right)^4\right] \mathrm{m}^2\mathrm{Hz}^{-1}. \tag{2.4.2}$$

2.4.5 Clock noise

On board each S/C, there is an Ultra-Stable Oscillator (USO) that acts as a very precise clock. Indeed, there are three unconnected clocks in the constellation. Hence, each oscillator could independently drift, yielding a possible maximal shift of around 25 s in a 10-year duration. Another particular effect of the oscillator is the residual timing jitter that can be translated into noise. The clock serves as a reference time for three measurements; then, a residual jitter can affect those three measurements, namely:

- The absolute distance between S/Cs is obtained through a process called ranging. It consists of exchanging pseudo-random codes within the laser beam. The received information is then compared with the local pseudo-random code to estimate the combination of the ranging and the clock drift which could be differentiated later in on-ground data processing.

- The USO triggers the Analog to Digital Converters (ADCs) to digitize the signal of the photodiodes, which is then sent to the phasemeters. In this passage, any time fluctuation will imprint an error in the measured phase.
- Once in the phasemeter, the phase measurements are time-stamped at a sampling rate dependent on the master clock.

Thus, time jitter in the USO would unavoidably introduce fluctuations in the phase measurements as well as erroneous absolute distances from the ranging.

2.4.6 Backlink noise

In the local interferometers, that is in the TMI and the RFI, beams from one MOSA with the adjacent one are combined. Given the arrangement of both MOSAs within the S/C, two approaches to transport the light are possible. The first is with mirrors and lenses to create an optical beam path, and the second is with optical fibers, which is the current baseline. In the beam transfer, the bent cable introduces a phase difference between the path in one direction and the opposite direction. The required ASD for this value is set to be [82]

$$S_\mu(f) = \left(3 \times 10^{-12}\right)^2 \left[1 + \left(\frac{2 \times 10^{-3}\mathrm{Hz}}{f}\right)^4\right] \mathrm{m^2Hz^{-1}}. \tag{2.4.3}$$

Note that this value is below the OMS noise level, which will dominate over this term.

The contribution of all these noises delimits the sensibility of LISA. Of course, several of them can cancel out or strongly be reduced in the on-ground processing. However, many other noises will remain, determining the noise PSD of LISA. Roughly speaking, it has two main contributors: the acceleration noise, which dominates at frequencies below 1 mHz and the OMS displacement, which dominates at higher frequencies. In Fig. 2.5, I show the required ASD from [82] to achieve the science objectives, described in Sec. 2.7. From now on, I will refer to the noise model of Eq. (2.4.1) and Eq. (2.4.2) as to the Science Requirement Document (SciRD) noise, denoted to be the required noise level in [82].

2.5 Data post-processing

In a regular Michelson interferometer, the laser beam is divided in two, forming a 90° angle, albeit other angles are possible. Each beam travels along one arm, reflects off a TM, and returns to the beamsplitter to be recombined in the phasemeter. With measurements of the phase variation, one can infer the crossing of a gravitational wave via length variations suffered by the arms, as explained in Sec. 1.3. However, LISA will have unequal, flexing arms, meaning the triangular formation will neither be equilateral nor stationary, as the arm lengths will vary independently by up to 2%, with velocities not exceeding 12 m/s. Additionally, while the light travels 2.5 million km (about 8.3 seconds) from one S/C to another, the satellites will move, leading to an unequal light travel time

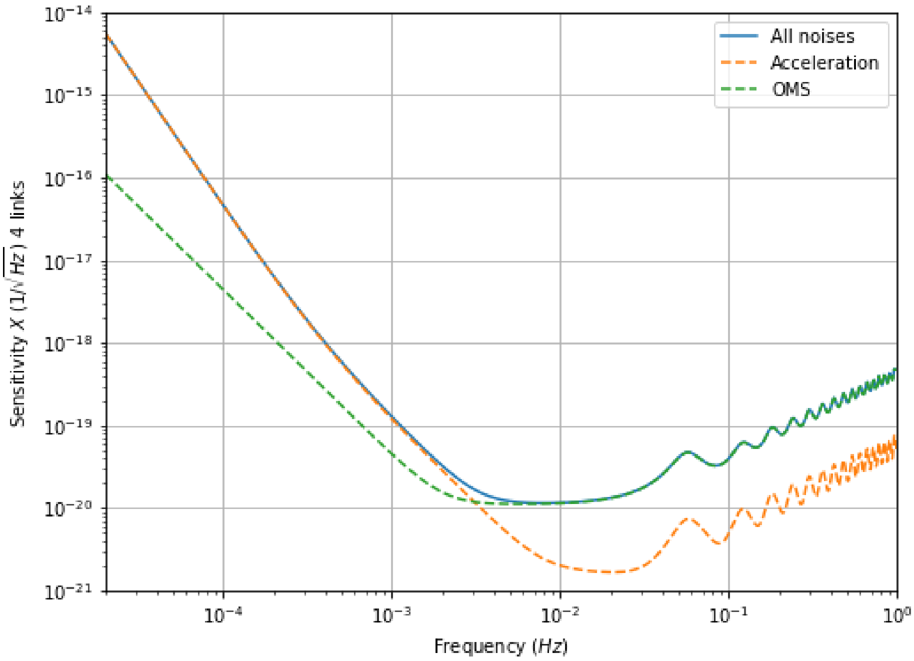

Figure 2.5: Amplitude spectral density required to achieve science objectives in blue. It is dominated by acceleration in orange at low frequencies and OMS displacement at high frequencies in green. The oscillation at high frequencies comes from the arm-length penalty.

(ltt) for the incoming and outgoing beams at a single satellite. This phenomenon, known as the Sagnac effect, will impact phase measurements, causing incomplete cancellation of laser noise during beam recombination. To address this issue, an offline technique called *time delay interferometry* (TDI) has been developed, primarily to reduce laser noise.

2.5.1 Interferometry

To describe the TDI combinations, we need first to understand what is measuring each interferometer. Let's introduce the configuration and indexing convention for the LISA constellation. Fig. 2.6 provides a sketch of the three satellites in their triangular formation, with each S/C labeled 1 through 3. As discussed in Sec.2.3, each satellite comprises two MOSAs along with internal instruments. Both the MOSAs and their internal components are labeled using a two-index system, indicating the receiver and emitter S/C numbers in that specific order, following the convention adopted in [92]. For example, MOSA 23 refers to the MOSA on S/C 2 oriented toward S/C 3. The symbol D denotes the time delay operator, defined later in the description of the TDI channels.

With the proper definitions in place, I will start with the simplest case scenario of

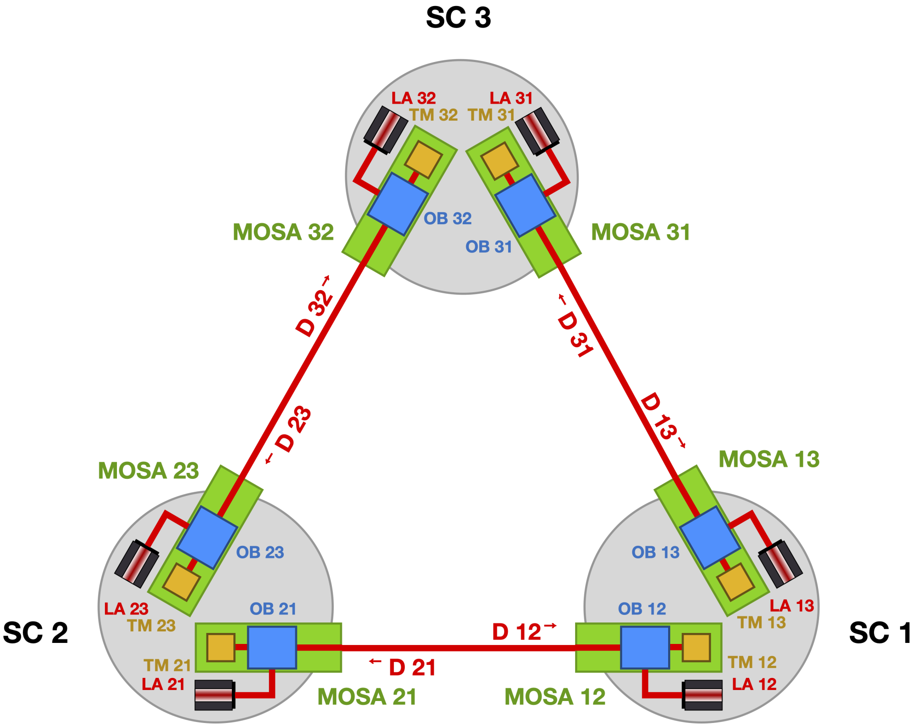

Figure 2.6: Configuration and indices definition of the spacecrafts and its instruments. *Credits: Bayle et al.* [92].

Michelson interferometry and build up from there.

Equal-arm interferometry

The simplest case of Michelson interferometry consists of two equal-length arms, see Fig. 2.7b. In that case, the differential phase measured at the phasemeter is just the difference of the phase at each arm,

$$y(t) = p\left(t - \frac{2L}{c}\right) - p\left(t - \frac{2L}{c}\right) = 0, \tag{2.5.1}$$

where p is the measured phase including all possible laser noises, t the time of measure taking, and L the arm length. Note that the phase variation is the difference in the phase between the time of the data taking and the time of the emission which is twice the arm length over the speed of light. In other words, the measurement corresponds to the evolution of the phase in the ltt through both directions along the arm.

Unequal-arm interferometer

For an unequal-arm-length interferometer, the laser noise will no longer cancel. Moreover, the larger the difference between the arms, the larger the magnitude of the

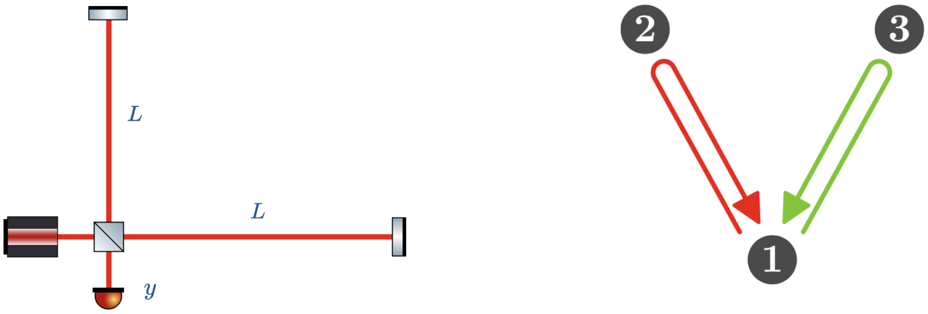

(a) Equal-arm interferometer.

(b) Followed beam path to achieve laser noise suppression for a triangular formation.

Figure 2.7: Equal-arm Michelson interferometer configuration and required path to cancel laser noise. *Credits: Bayle et al.* [83; 89].

laser frequency fluctuations affecting the phase measurements [93]. Consequently one needs to measure the laser phase individually for each arm,

$$y_1(t) = p\left(t - \frac{2L_1}{c}\right) - p(t) + n_1(t), \tag{2.5.2}$$

$$y_2(t) = p\left(t - \frac{2L_2}{c}\right) - p(t) + n_2(t), \tag{2.5.3}$$

where here the n represents other noises entering the phase measurement. Note that each phase measurement has a different phase, *p(t)* for a given time t, and of course, since the traveled path is different, the ltt at each arm would also vary. To obtain the total phase variation one combines both beams in the post-treatment of the measurements,

$$y_1(t) - y_2(t) = p\left(t - \frac{2L_1}{c}\right) - \cancel{p(t)} + n_1(t) - p\left(t - \frac{2L_2}{c}\right) + \cancel{p(t)} - n_2(t). \tag{2.5.4}$$

Even with the assumption of $n_1(t) = n_2(t)$, the previous expression is nonzero, indicating that the interferometric phase is not zero. To achieve the laser cancellation one needs to resend the beam of one arm to the other and vice-versa, see Fig. 2.8 for a visual representation. That is

$$y_1\left(t - \frac{2L_2}{c}\right) = p\left(t - \frac{2L_2}{c} - \frac{2L_1}{c}\right) - p(t - \frac{2L_2}{c}) + n_1(t - \frac{2L_2}{c}), \tag{2.5.5}$$

$$y_2\left(t - \frac{2L_1}{c}\right) = p\left(t - \frac{2L_1}{c} - \frac{2L_2}{c}\right) - p(t - \frac{2L_1}{c}) + n_2(t - \frac{2L_1}{c}). \tag{2.5.6}$$

If we assume to know the noise entering the phase difference $n_1(t)$ and $n_2(t)$ for any t in both arms or if the artifacts share the same perturbations, we can combine previous

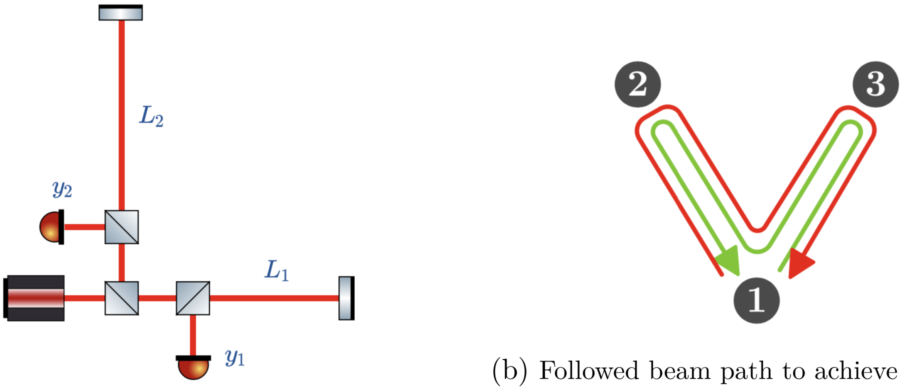

(a) Unequal-arm Michelson interferometer.

(b) Followed beam path to achieve laser noise suppression with TDI 1.5. for a triangular formation.

Figure 2.8: Unequal-arm Michelson interferometer configuration and required path to cancel laser noise with TDI 1.5. The illustration on the right also serves to take into account the Sagnac effect. *Credits: Bayle et al.* [83; 89].

equations to achieve the laser noise suppression,

$$\begin{aligned} y_1\left(t-\frac{2L_2}{c}\right) - y_2\left(t-\frac{2L_1}{c}\right) - (y_1(t) - y_2(t)) = \\ p\left(t-\frac{2L_2}{c}-\frac{2L_1}{c}\right) - p\left(t-\frac{2L_2}{c}\right) - p\left(t-\frac{2L_1}{c}-\frac{2L_2}{c}\right) \\ + p\left(t-\frac{2L_1}{c}\right) - p\left(t-\frac{2L_1}{c}\right) + p\left(t-\frac{2L_2}{c}\right) = 0. \end{aligned} \tag{2.5.7}$$

Flexing-arm interferometer

Now let us imagine that the arm length depends on time, then Eq. (2.5.7) will not be zero. If we use Eqs. (2.5.5) and (2.5.6), with the arm length time dependency, we see that the two terms that no longer cancel are,

$$p\left(t-\frac{2L_2(t)}{c}-\frac{2L_1(t-2L_2/c)}{c}\right) \neq p\left(t-\frac{2L_1(t)}{c}-\frac{2L_2(t-2L_1/c)}{c}\right). \tag{2.5.8}$$

However, this difference can be reduced by repeating another full tour of the photons in the opposite direction, as shown in Fig. 2.9. In the case of a constant velocity of the arms, the suppression of the laser frequency fluctuations is achieved. Naturally, this does not completely reflect the situation for LISA, and some residual laser noise is expected.

2.5.2 Interferometer measurements

In the case of LISA, where the power of the beam is not strong enough to bounce and make the way back to the emitter S/C, one can synthesize a transponder arm off-line,

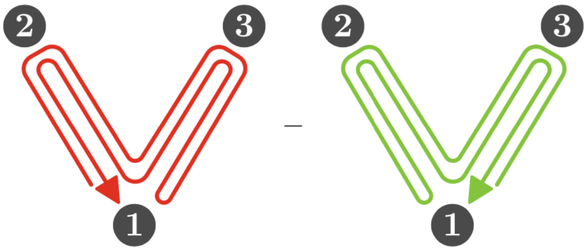

Figure 2.9: Followed beam path to achieve laser noise suppression with TDI 2.0 for a triangular formation. *Credits: Bayle et al.* [83].

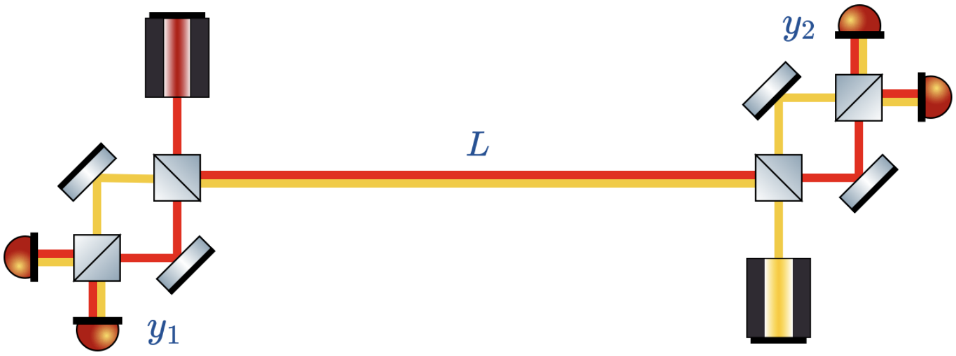

Figure 2.10: LISA equivalent transponder arm. *Credits: Bayle et al.* [89].

by combining the path of a photon in one direction with the reverse path at an arm length travel time before ($\sim t - 8.3$). If we define them as

$$y_1(t) = p_1\left(t - \frac{L}{c}\right) - p_1(t), \tag{2.5.9}$$

$$y_2(t) = p_2\left(t - \frac{L}{c}\right) - p_2(t), \tag{2.5.10}$$

then,

$$y(t) \equiv y_2(t - L) - y_1(t) = p_1(t - 2L/c) - p_1(t), \tag{2.5.11}$$

is the equivalent of a transponder arm. See Fig. 2.10 for a visual representation.

However, since the arm length is not the same for the emitted beam as for the received beam, due to the Sagnac effect [1], one will in general write

$$y_{rs}(t) = p_s\left(t - \frac{L_{rs}}{c}\right) - p_s(t), \tag{2.5.12}$$

---

[1] This notion was introduced in Sec. 2.2, see Fig. 2.3

where the lower indices r, s determine the receiving and sending S/C respectively. Moreover, let's also use the time delay operator D_{rs}, which accounts for the time delay between the emission of a photon in MOSA$_{sr}$ and the reception in the distant MOSA$_{rs}$, see Fig. 2.6. The time delay operator is defined as

$$D_{rs}\, f(t) = f\left(t - \frac{L_{rs}(t)}{c}\right), \tag{2.5.13}$$

where $f(t)$ is any time-dependent function, L_{rs} is the arm length from the sending to the receiving S/C. Its compact form of chained delay operators is

$$D_{i_1 i_2 \cdots i_n} = D_{i_1 i_2} D_{i_2 i_3} \cdots D_{i_{n-1} i_n}. \tag{2.5.14}$$

In the following, I will decompose the intrinsic information collected by the different interferometers within each MOSA. Those measurements allow one to compute the total phase measurement at the end of each arm, known also as the link response.

The ISI corresponds to the resulting phase from the laser combination from the distant OB and the local OB. Hence, one can decompose the signal as the sum of the local laser p_{ij}; the distant laser p_{ji} with the associated time delay D_{ij}; the OMS displacement noises introduced before with the clock noise as N_{ij}^{I} for interferometer I; OB displacements as Δ_{ij}; and a projected gravitational wave crossing the beam H_{ij}. The ISI signal in S/C$_1$ facing S/C$_2$ reads then

$$isi_{12} = \underbrace{H_{12} + D_{12} p_{21} - \left(D_{12} \frac{d\Delta_{21}/dt}{c}\right)}_{\text{distant beam}} - \underbrace{\left(p_{12} + \frac{d\Delta_{12}/dt}{c}\right)}_{\text{local beam}} + \underbrace{N_{12}^{ISI}}_{\text{readout}}. \tag{2.5.15}$$

Note that the interferometer measurements are expressed in dimensionless units. The TMI accounts for the TM displacement within the S/C by comparing the adjacent beam with the local beam. In this path, there is a contribution phase shift from the backlink noise due to the optical fiber connection N_{12}^{bl}, and a contribution from the TM local displacement N_{12}^{δ}. Note that factor 2 indicates twice the displacement since the light bounces in the TM, covering twice that distance. In the MOSA$_{12}$ reads

$$tmi_{12} = \underbrace{p_{13} + \left(\frac{d\Delta_{31}/dt}{c} + N_{12}^{bl}\right)}_{\text{adjacent beam}} - \underbrace{\left(p_{12} + \frac{d\Delta_{12}/dt}{c} + 2N_{12}^{\delta}\right)}_{\text{local beam}} + \underbrace{N_{12}^{TMI}}_{\text{readout}}. \tag{2.5.16}$$

Finally, the RFI measures the acceleration of the S/C and other intrinsic noises

$$rfi_{12} = \underbrace{p_{13} + \left(\frac{d\Delta_{31}/dt}{c} + N_{12}^{bl}\right)}_{\text{adjacent beam}} - \underbrace{\left(p_{12} + \frac{d\Delta_{12}/dt}{c}\right)}_{\text{local beam}} + \underbrace{N_{12}^{RFI}}_{\text{readout}}. \tag{2.5.17}$$

The other five inter-spacecraft interferometers can be obtained with cyclic permutations of the indices. It is important to mention that the Doppler effect due to relative velocities of the S/C, when emitting and receiving photons, is not taken into account in these equations. The reason is that in the codes described in Chapter 4, this effect is not considered either. I refer to [89] if one would like to include it.

To recombine all interferometers to compute the link response, let me introduce the letters ξ and η as combinations of measurements to suppress the S/C jitter and the distant laser noise, respectively:

$$\begin{aligned} \xi_{12} &= isi_{12} + \frac{rfi_{12} - tmi_{12}}{2} + D_{12}\left(\frac{rfi_{21} - tmi_{21}}{2}\right), \\ \eta_{12} &= \xi_{12} + \frac{rfi_{21} - tmi_{23}}{2}. \end{aligned} \tag{2.5.18}$$

Here again, the remaining combinations are obtained by circular permutation of indices.

To cancel the rest of the laser noises one needs to apply *time delay interferometry* described in the next section.

2.5.3 Time delay interferometry

Time Delay Interferometry (TDI) was first proposed by Armstrong, Estabrook, and Tinto [94–97] as a solution to reduce the laser noise due to unequal arm length. Nonetheless, other authors also studied this issue [98; 99]. The method is to apply delays to the phasemeter measurements and combine them linearly to eliminate the laser noise in a set of measurements known as channels X, Y, Z. The technique was later extended to non-stationary satellites [100–102] to account for the flexing of the arms. The first combination is commonly known as TDI 1.0, but if one wants to account for the Sagnac effect, one should use TDI 1.5. The second case for flexing arms is known as TDI 2.0 or second-generation Michelson interferometry.

Continuing with the previous notation one can express the component X for the first-generation TDI as

$$\begin{aligned} X_{1.5} = &\left(1 - D_{121}\right)\left(\eta_{13} + D_{13}\eta_{31}\right) \\ &- \left(1 - D_{131}\right)\left(\eta_{12} + D_{12}\eta_{21}\right), \end{aligned} \tag{2.5.19}$$

and for the second-generation TDI

$$\begin{aligned} X_2 = &\left(1 - D_{121} - D_{12131} + D_{1312121}\right)\left(\eta_{13} + D_{13}\eta_{31}\right) \\ &- \left(1 - D_{131} - D_{13121} + D_{1213131}\right)\left(\eta_{12} + D_{12}\eta_{21}\right). \end{aligned} \tag{2.5.20}$$

The two other components Y, Z can be obtained by cyclic permutations.

Naturally, these channels share instrumental noise, and therefore, they are highly correlated. Over the years, several possible combinations emerged, see [103] for a detailed description. However, there are optimal combinations to obtain quasi-orthogonal channels that allow to minimize the instrumental noise cross-correlation [104]. Named after their inventors, Armstrong, Estabrook, and Tinto, their expressions are the following

$$A_n = \frac{1}{\sqrt{2}}(Z_n - X_n), \quad E_n = \frac{1}{\sqrt{6}}(X_n - 2Y_n + Z_n), \quad T_n = \frac{1}{\sqrt{3}}(X_n + Y_n + Z_n), \qquad (2.5.21)$$

where index n indicates the TDI generation. The channel T has low sensitivity to GWs at low frequency, thus it is a good *null channel* to estimate the noises in the constellation as well as for the search of stochastic backgrounds. However, better performance has been demonstrated with another channel named ξ, see [105].

Nonetheless, there are other techniques to synthesize the passage of a GW in LISA. One approach consists of canceling the laser frequency noise by applying principal component analysis (PCA) to a set of shifted data samples [106]. There also exists another method called TDI∞ [107] that uses a large amount of data and a matrix approach for the delays. However, the most robust approach continues to be the TDI.

2.5.4 End to end pipeline

This section summarizes the transformation of raw data into meaningful information about the Universe. The processing of phase measurements within the S/Cs up to the TDI output channels is termed L0-L1 data, covering Sec.2.5.2 to Sec.2.5.3. Once these raw measurements reach Earth, diagnostics and calibrations are applied, including proper time synchronization between S/Cs, ranging, orbit control, OB motion correction, laser noise reduction via TDI, and clock noise corrections. It is also worth noting that new approaches are being investigated to conduct some onboard processing prior to TDI combination, potentially enhancing LISA's sensitivity [108–110]. The TDI output, or level-1 (L1) data, will then undergo analysis to detect GWs and refine noise levels. At this stage, two main parallel branches emerge: first, a search for GWs based on various source templates, and second, a low-latency pipeline aimed at rapidly detecting MBHB merger events to enable prompt telescope redirection for potential EM counterparts. Later, Parameter Estimation (PE) is performed for all sources, a process known as level-2 (L2) data analysis or the *Global Fit* (GF). Finally, level-3 (L3) data involves the completion of source catalogs, providing the scientific community with comprehensive datasets for further exploration of LISA's discoveries. This process is iterative, with potential feedback loops between L2 and L1 stages. The following section details the steps involved in progressing from L1 to L3. See Fig. 2.11 for an overview.

2.6 Observation

LISA is an all-sky observatory sensitive to all sources simultaneously. Contrary to ground-based interferometers, whose main targets are sources observable for a maximum of a few seconds, LISA-targeted sources remain a long time in the band, which means that several signals will overlap in the data. Given the high complexity, the question of our

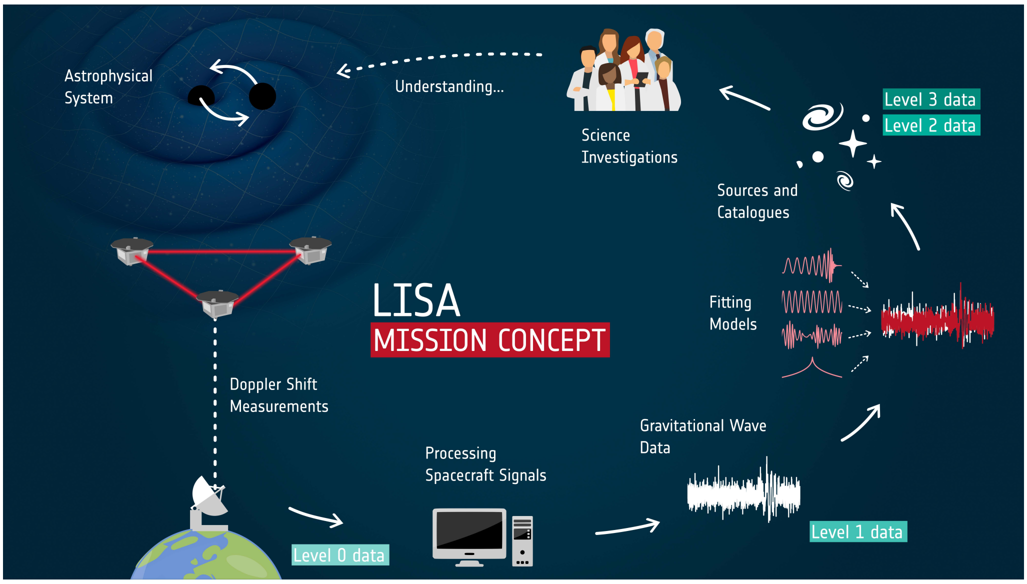

Figure 2.11: Representation of the data levels and the end-to-end pipeline. *Credits: LISA Red book* [3].

ability to disentangle various events is a valid one. In the following section, I outline some expected sources and the data analysis community's efforts toward achieving the *Global Fit*.

In the frequency range of LISA, we expect to observe a lot of different sources, from black hole binaries in many sizes and mass ratios to galactic binaries, up to stochastic backgrounds with astrophysical or cosmological origin. See Fig. 2.12 for possible sources in LISA's frequency band

2.6.1 Sources

The crossing of a GW has a very well-defined signature depending on the source involved, see Fig. 2.13. I will now go through the signatures of the sources that are expected to be detected in the frequency band of LISA.

Massive black hole binary

Massive Black Hole Binaries (MBHB) systems involve two BHs of similar mass, with a mass ratio up to ∼20. One can define the mass ratio as the ratio between the heavier BH over the lighter one, $q = m_1/m_2 \geq 1$. The inverse relation is also accepted. Nevertheless, I will use this convention throughout the manuscript. The mass of the BHs could be of the order of 10^4 up to $\sim 10^8$ $\mathrm{M}_\odot$. The result of two galaxies merging would eventually lead to the coalescence of MBHB of these characteristics. These sources can be observed throughout the Universe, allowing us to study the population of these enormous objects. Some of these events are expected to be very loud, which means that they could have

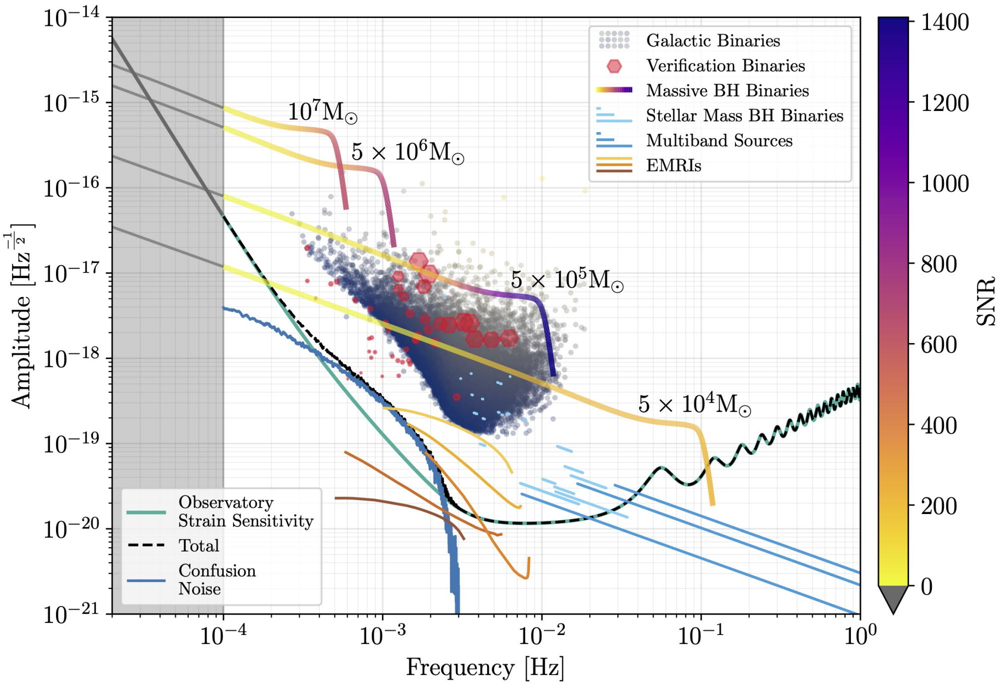

Figure 2.12: Illustration of primary sources expected to be observed by LISA in the Amplitude-frequency plane. Among the sources, we find massive black hole binaries, galactic binaries and their confusion noise, extreme mass ratio inspiral binaries, and solar mass binaries delimited by the sensitivity level of LISA. *Credits: LISA Red book* [3].

an Signal-to-Noise Ratio (SNR) above a few thousand [82]. Indeed, this kind of source would be the loudest one in LISA. Consequently, a precise description of their dynamics is crucial. Systematic errors in the waveform template would unavoidably result in biased parameters. Therefore, a significant effort is being put into the development of accurate waveforms within the dedicated working groups in the LISA Consortium.

There are different methods to describe the dynamics of these sources. The first method is the Post-Newtonian (PN) expansion. As its name states, one works with Einstein's field equations in the weak field and expands them in terms of the velocity, i.e., $v/c \ll 1$. To this day, the expansion is known to be up to 4.5 PN [111], which means that the expansion on v/c is computed until order 9, i.e., $(v/c)^9$. Each PN order informs us on complementary features of the system, such as the spins, spin-orbit coupling, or back reaction, among others. When the velocity approaches the speed of light ($v \sim 0.3c$), this method breaks down. This happens close to the Innermost Stable Circular Orbit (ISCO) [2]. In other words, one can use the PN approach to describe the inspiral of the binary, but not the merger.

The next method is the already mentioned Numerical Relativity (NR). NR is an algorithm that solves numerically Einstein's equations in the strong field. Since the break-

---

[2] This definition is introduced later in Sec. 3.1.

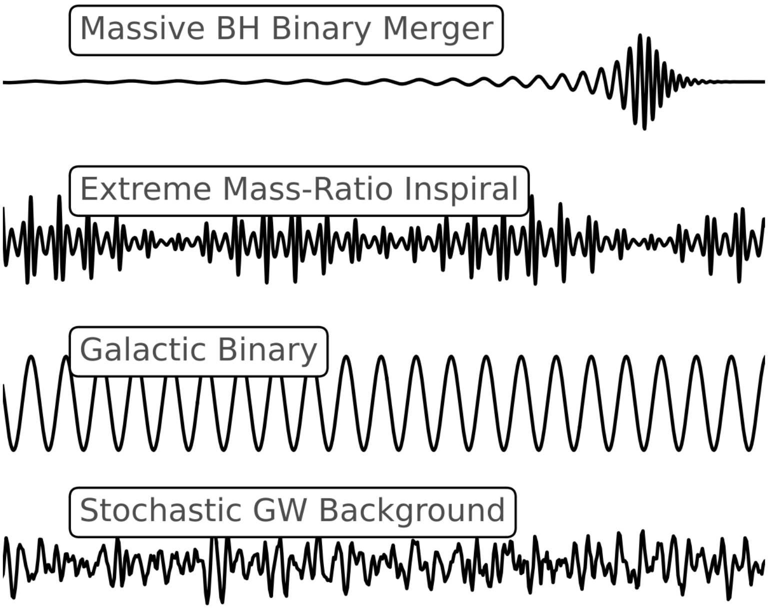

Figure 2.13: Waveforms of gravitational radiation for different sources. *Credits: LISA Red book* [3].

through of Pretorius in 2005 [112] in the convergence of the solutions of the equations, several groups consistently work to generate substantial catalogs of waveforms [113–116] that can cover mass ratios up to ∼18 and different spin configurations, including precession in some cases. Precession arises when the spins of the BHs are not aligned with the normal of the orbital plane. Currently, there are thousands of NR waveforms available. A setback of NR is the amount of time it takes to solve one single system, which can be weeks. If one wants to increase the mass ratio or the number of cycles before the merger, that computational time increases considerably. Therefore, another technique for large mass ratios and a larger number of cycles is in place, the Self-force (SF).

Self-force relies on perturbation theory with expansions of the metric in terms of, by our convention, the inverse of the mass ratio ($\epsilon = m_2/m_1$). It assumes that the massive non-rotating object defines the background metric and the geodesics, while the lighter mass will create a small perturbation of the metric. Given the non-linear nature of GR, the adiabatic term (0PA $\sim \epsilon^{-1}$) involves dissipative effects of the first order self-force (1SF), and the first post-adiabatic term (1PA $\sim \epsilon^{0}$) involves dissipative effects of second order self-force (2SF) along with first-order conservative effects [117; 118]. Recently, there have been improvements accounting for the spin of the secondary object [119; 120], as well as an extension to equal-mass binaries [121; 122]. As its accuracy levels up with other methods, its limitation is yet to be seen. Nevertheless, solutions have been found for Schwarzchild BHs but not for Kerr BHs so far.

The Effective One-Body (EOB) formalism uses the Hamiltonian to describe the system dynamics. It assumes a conservative part of the dynamics (Hamiltonian), which maps the two-body conservative dynamics into a test particle in an effective external metric; a radiation-reaction part that will be the expression for the non-conservative energy *ressumed* from the conservative part; and the radiation of the coalescing system. With these three ingredients, the formalism completely determines the waveform. I refer the reader to [123–127] for more information.

Combining the methods described above, we can produce a waveform of BHBs over a vast parameter space. Nevertheless, to perform PE we need fast waveform generators, which is not the case for all the previous methods. To satisfy this need other methods arose, namely surrogate models which interpolate numerical data sets [128], and phenomenological models such as IMRPhenom [129–131], that generate the waveform as a polynomial expansion of amplitude and phase in terms of the frequency, with coefficients that have been previously calibrated to PN, NR or EOB-NR solutions.

Although there have been new developments in all the approaches, more improvements are needed to achieve unbiased parameter estimation with LISA's sensitivity [132; 133].

Extreme- and intermediate-mass ratio inspiral

Extreme Mass-Ratio Inspirals (EMRIs) and Intermediate Mass-Ratio Inspirals (IMRIs) enclose binary black holes with a large variety of mass ratios from 20-30 up to 10^4. Sources with a mass ratio of $\mathcal{O}(10^8)$ are extremely mass ratio inspirals (XMRI). Moreover, the small object is not required to be a BH, it could be any compact object. This scenario is often encountered in BHs in the center of galaxies with many compact objects orbiting the massive black hole. The orbits from these systems are very dynamic, undergoing three kinds of variations: azimuthal motion, precession of the periapsis, and precession of the orbital plane. Furthermore, given the large mass ratio, higher harmonics will inevitably appear. Remember that higher harmonics are next-to- and higher-next-to-leading order in the decomposition of Einstein's equation in terms of spherical harmonics. Both effects give rise to very complex waveforms staying in the LISA frequency band for long periods. Then, errors in the phase would pile up over the many cycles $\mathcal{O}(10^5)$. For that reason, very accurate waveforms are essential.

A large number of cycles until the plunge is expected, and PN expansion gives the true solution to a given order, but it is not the complete waveform. Other methods, such as SF, are needed. Great efforts to include features of eccentricity, spins of both objects, and inclination are currently ongoing. The augmented analytic kludge (AAK) describes a short segment of the evolution in a fast way. The AAK, see [134] and references therein, uses the quadrupole emission from a Keplerian orbit as the baseline but imposes relativistic effects such as precession and radiation reaction. The obtained parameters are then mapped to match the frequencies of numerical kludge. That is the expressions derived from PN expansions from an exact Kerr geodesic and fit to perturbative calculations from SF waveforms. Nowadays, the most used phenomenological waveform generator is the Fast-EMRI-waveform (FEW) [134–143]. Even though they present good accuracy to truthful waveforms to perform a search, they fail to estimate the parameter of more realistic waveforms, since precession and eccentricity are not yet included.

Galactic binary

GB are systems composed of two compact objects, such as NSs, WDs, BHs, and combinations of them, orbiting around one another. The system of WD-WD slowly loses energy through the emission of GWs with orbital periods of minutes to hours. Thus, they remain in a slowly progressively varying orbit. Consequently, they present a quasi-monochromatic frequency with a frequency derivative of the order of $f/10^3$. They are found mainly in the Galactic plane, although other sky locations are possible. They remain for a long time in the inspiral stage, allowing the waveform to be described as a sinusoidal wave with a slowly time-changing phase Taylor-expanded at 2nd order in frequency [3].

In our Galaxy, there are about 10^7 systems with these characteristics. Only a fraction of them will be observed by LISA [144]. Moreover, some will serve as verification binaries, denoting binaries that we know through EM observations that orbit in the LISA frequency band. However, a large quantity will not be individually resolved, generating a background confusion noise. The amount of detectable binaries and their background is one issue that the Data Analysis (DA) community in LISA is trying to address.

Stellar mass black holes binary

Stellar-Mass Black Hole Binariess (sBHBs) are BHs with masses of the order of the Sun ($M_\odot$), regardless of their origin [3]. Galactic or extra-galactic sBHBs will have even shorter orbital periods than Galactic Binaries (GBs) entering at LISA's high frequency. This will allow us to detect sources in the inspiral stage years before the possible merger in the LVK or ET band, giving birth to GW-multi-band detection [145].

Stochastic background

SGWB are composed of many different sources with low SNR, too low to be individually resolvable. From astrophysical origin, I mentioned already the confusion noise arising from the GBs, but of course, BHB and EMRIs could also produce a stochastic signal, with a typical profile of $\Omega_{GW} \propto f^{2/3}$. Particularly, the GBss follow a characteristic distribution towards the center of the Galaxy. Due to LISA's motion, the galactic confusion noise can be modulated over a year, differentiating it from the rest of the background noise.

Other SGWBs could stem from various phenomena in the early universe, known as sources with cosmological origin. They can come from First-Order Phase Transition (FOPT), which in the frequency band of LISA corresponds to a phase transition at the TeV energy scale [3]. This is the energy scale of the electroweak phase transition, which could probe particle physics beyond the SM. Cosmic Strings (CS) could also probe physics beyond-SM, with a current constrain of $G\mu \sim 10^{-11}$ achieved by PTA at low frequency ($10^{-9} - 10^{-6}$ Hz) and $G\mu < 10^{-14}$ from LVK observations [146]. LISA could extend this boundary up to $G\mu \sim 10^{-17}$ for Nambu-Goto strings [147]. Inflation and PBHs can also contribute to SGWBs. PBHs gained weight to explain DM concentrations. Further details on the nature of cosmological sources were given in Sec. 1.2.4 and references therein.

Most of the SGWB waveforms are determined by one or more frequency-broken power-laws with a characteristic frequency that will mark the peak of the amplitude. The characteristic frequency, as well as the index of the power-law, depend on the assumed model which can be very complex. For example, in the case of the FOPT, the waveform could be described by up to three characteristic frequencies, one per each gravitational wave contribution: collisions $\Omega_{GW}^{(coll)}$, sound waves $\Omega_{GW}^{(sw)}$ or magneto-hydrodynamics $\Omega_{GW}^{(turb)}$, producing a specific waveform for the different contributions. Perhaps the biggest obstacle in terms of DA, besides the expected low SNR, is that these waveforms are hard to differentiate from the instrumental noise. Moreover, the model dependency of the waveforms complicates the search for SGWB. Nevertheless, efforts to generate searches with independent-model waveforms are explored [148; 149].

2.6.2 Global fit

Several of the above-mentioned sources will stay in the LISA frequency band for many days, weeks, months, and even years. This translates into signal-dominated data, where all types of sources would overlap. Thus, a technique to disentangle the different sources is crucial. The fitting is required to account for the overlap of signals, but given the different time scales, the only way to obtain accurate parameters is to perform a PE of all sources all at once. If we estimate source by source and extract it, any biased parameter would damage the possible characterization of another source. To overcome this issue, a methodology called the Global Fit (GF) will be implemented. With this technique, the estimated sources are not subtracted but re-estimated in a sequential iteration with priors from the previous iteration. The procedure is quite complex, although a simple visual representation of the pipeline steps is shown in Fig. 2.14. Note that it is displayed as a wheel to suggest that several iterations are required. After each search, the noise and instrument model is again estimated. This is because the identification of sources and the estimation of parameters will have an impact on the estimation of the noise and the instrument model, and vice-versa.

Probably the most natural way to start is with the MBHBs, as their SNR is large, and their merger is well localized in the time-series data. Once identified, one could carry on with GBss. Note that the SNR of GBss accumulates over time, so they might not be detected at first, but they will become louder as the signal accumulates in time. For this step, one could use techniques like Reverse Jump Monte Carlo Markov Chain (RJMCMC), where extra dimensions in the parameter volume are continuously added or subtracted. With this method, not only the source parameters are estimated, but also the number of sources. Also note that given the frequency dependence of these sources, a frequency domain search is preferred. EMRIs or sBHBs are the next logical sources, and lastly, the SGWB and noise model should be estimated at the same time. The noise model also contains the unresolved GBss, i.e., the time-evolving GBs confusion noise.

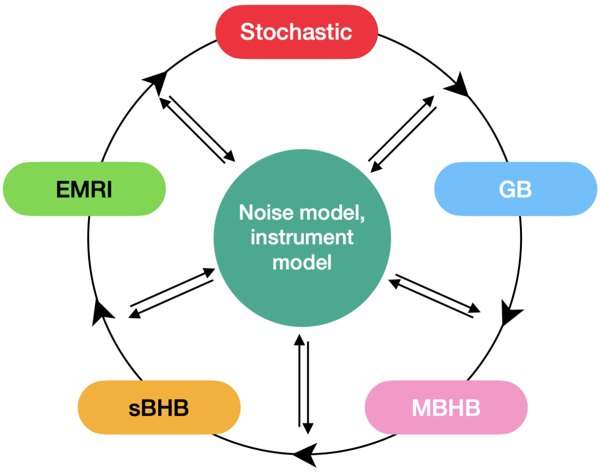

Figure 2.14: Data analysis wheel. It shows the path of the data throughout the pipeline. Note that after the search for a particular source, the noise and the instrument model will be estimated again.

The LISA Data Challenge Working Group (LDCWG) working group, releases every few years, different data analysis challenges for the DA community to solve. Results obtained by several groups [150] on the "Sangria" challenge [151; 152], demonstrated the feasibility of the GF for MBHBs and GBss. A visualization of the Sangria dataset is presented in Fig. 2.15.

The viability of the GF is already proven for those sources in LISA's Red book [3]. The LDCWG is currently working on improving the results and including artifact noises, such as gaps or glitches as well as other sources. Once all the sources are identified and cataloged, the scientific investigation begins.

2.7 Science objectives

The science case of LISA is very broad and rich. The objectives have been describe in a series of "White papers" [147; 153; 154] as well as in the "Red book" [3], exploiting the science one can do with the detection of GWs from a full variety of sources. In the following, I will give a short summary of them, based on [3].

S01: Study the formation and evolution of compact binary stars and the structure of the Universe

By studying GBss as well as BHs, one can infer the population of these sources in the local Universe, so far only known from electromagnetic observations. The parameters

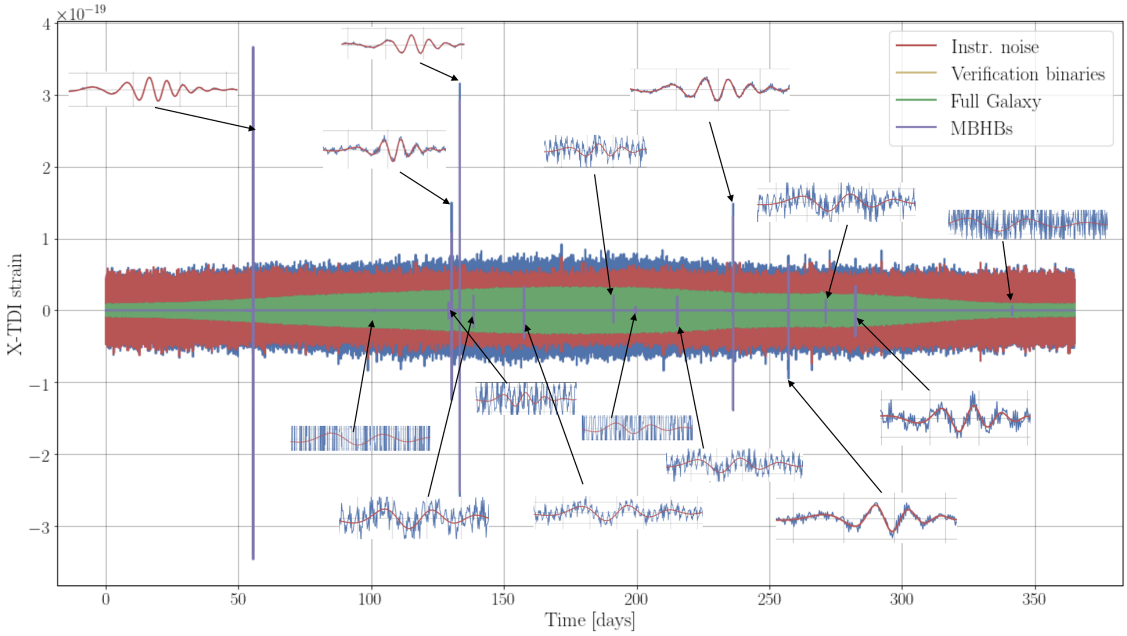

Figure 2.15: Sangria dataset challenge. *Credits: LDC* [151].

inferred from their waveforms could shed light on the evolution of such binaries and the rate of their coalescence, which would also impact explosive events (kilo and supernovae) and heavy material production. As the compact stars become closer, tidal effects would result in mass transfer. Understanding the outcome of this effect could provide valuable insights into the structure and formation history of our Galaxy. The science objectives consist of:

- Formation and evolution pathways of dark compact binary stars in the Milky Way and neighboring galaxies.
- The Milky Way mass distribution.
- The interplay between GWs and tidal dissipation.

S02: Trace the origins, growth, and merger histories of massive black holes

The large SNR from MBHB allows for precise measurements of their masses and spins, sky localization, and distances. All these parameters would help to describe the population of MBHs. With a sensitivity range above z∼10, the history of MBH formation could be unraveled. The science objectives are:

- Discover seed BHs at cosmic ionization.
- Study the growth mechanism and merger history of MBH from the epoch of the earliest quasars.

- Identify the electromagnetic counterparts of MBHB coalescence

S03: Probe the properties and immediate environments of black holes in the local Universe using EMRIs and IMRIs

The phase and amplitude of EMRIs/IMRIs over 10^4 cycles should be known with high accuracy, allowing us to infer the masses, spins, inclination, eccentricity, distance, and sky localization. By studying the relation between spins, inclination, and eccentricity, one could estimate the conditions that made the system evolve to the way it would be detected. Any variation in the phase could indicate the presence of matter surrounding the binary. The science objectives are:

- Study the properties and immediate environment of Milky Way-like MBHs using EMRIs.
- Study intermediate MBH population using IMRIs.

S04: Understand the astrophysics of stellar black holes

Over a hundred sBHBs have been detected in ground-based detectors with high accuracy on their intrinsic parameters. However, given the low inspiral SNR , other parameters such as the eccentricity can not be constrained. Measuring the eccentricity and the inclination of the binary at a lower frequency, as LISA could do years before the merger, would clarify the formation channel of the heaviest sources found by the LVK Collaboration. The science objectives are:

- Study statistical properties of Stellar-Mass Black Holes (sBHs) far from the merger.
- Detecting high mass sBHBs and probing their environment.
- Enabling multiband and multimessenger observations at the time of coalescence.

S05: Explore the fundamental nature of gravity and black holes

Given the large SNR expected for MBHB events and the exact phase knowledge in EMRIs, precise parameters of the systems are estimated. In the presence of new fields the structure of the final BH for the case of mergers or central BH for EMRIs, could display signatures beyond GR. Another type of signature could be extra polarizations of the strain. By studying these sources one could learn about the anatomy of these massive objects in the strong field regime as well as their emission and propagation. The science objectives are:

- Use ringdown characteristics observed in MBHB coalescence to test whether the post-merger objects are the MBHs predicted by GR.
- Use EMRIs to explore the multipolar structure of MBHs and search for the presence of new light fields.

- Test the presence of beyond-GR emission channels.
- Test the propagation properties of GWs.

My thesis focuses on studying the sensitivity of LISA to the first item in this science objective. In the last stage of the event, i.e. the ringdown, the remnant BH will oscillate with a characteristic complex frequency determined only by the mass and the spin. Any deviation of the BH's spectrum could indicate the presence of an alternative theory as we shall see.

S06: Probe the rate of expansion of the Universe with standards sirens

In the case of an MBHB embedded in gas, the material can fall to the BHs during the inspiral and during or after the merger. If so, electromagnetic emission at those moments is expected, transforming them to bright sirens, where the redshift is accurately measured. EMRIs instead, are not expected to have EM counterparts, but their redshift can be obtained through identification with the center of the host galaxy. When combining the bright and dark sirens, one could constrain cosmological parameters such as the Hubble constant H_0, the matter spectral density Ω_M, or the dark energy equation of state parameter w_0. The science objectives are:

- Cosmology from bright sirens: MBHB.
- Cosmology from dark sirens: EMRI.
- Cosmology at all redshifts: combining local and high-redshift LISA standard sirens measurements.

S07: Understand stochastic GW backgrounds and their implications for the early Universe and TeV-scale particle physics

Once all targeted sources are removed from the data, or at least identified, there will remain a stochastic background from astrophysical and cosmological origin. Both types of backgrounds have distinctive signatures that allow for differentiation. The characterization of the parameters within each framework would help to give complementary information on the binaries population and to probe physics beyond the SM respectively. The science objectives are:

- Characterise the astrophysical SGWB.
- Measure, or set upper limits on, the spectral shape of the cosmological SGWB.
- Characterise the large-scale anisotropy of the SGWB.

S08: Search for GW burst and unforeseen sources

Everything that has not been explained, like unforeseen sources or signatures from cosmological features, such as kinks or cusps from cosmic strings. The science objectives are:

- Search for cusps and kinks of cosmic strings.
- Search for unmodelled sources.

Chapter 3

Black hole perturbation

This chapter is dedicated to the description of the reaction of a black hole to perturbations. When a BH is perturbed, resonant modes inside the BH are excited. These modes will later fade away through the emission of gravitational radiation in the form of damped waves. This means that after the perturbation, whatever its origin might be, the BH returns to its fundamental state through the emission of GWs characterized by resonant modes called Quasi-Normal Modes (QNMs). Each QNM is defined by an oscillation frequency and a damping time that only depends on the BH's parameters mass and spin, as we shall see. A deviation from GR in the strong field regime might impact the values of the QNMs that rest on the intrinsic BH's parameters. The main goal of this chapter is to introduce the GR pillars on which the *no-hair* theorem is built. In general, there is an abuse of language when speaking about the *no-hair* theorem since the need for extra parameters to describe the QNMs are not necessarily extra "hairs" in the sense of conserved charges. Throughout this manuscript, I also refer to the *no-hair* theorem as to the absence of parameters beyond the mass and the spin to explain the relaxation of perturbed BHs.

I begin by briefly describing BHs as solutions of Einstein's equations in Sec. 3.1 and with the perturbed Schwarzschild BHs framework in Sec. 3.2. After an introduction to the Newman-Penrose (NP) formalism in Sec. 3.3, I continue with the Kerr BH perturbation in Sec. 3.4. In Sec. 3.5, I indicate the path towards the solution of the QNMs, and I finish with the description of the ringdown as a superposition of QNMs in Sec. 3.6. The following sections are based mostly on the references [155–161], and I refer the reader to those for further details.

3.1 Black holes

Soon after Einstein developed the General Theory of Relativity (GR), he started working on approximate solutions to describe the spacetime surrounding spherical objects such as the Sun or planets. But it was Karl Schwarzschild, a few months after the publication of GR, who discovered an exact solution to the gravity field equation [162].

Under a change of coordinates to work on a spherical basis, the line element of the Minkowski metric can be written as

$$ds^2 = -dt^2 + dr^2 + r^2 \left(d\theta^2 + \sin^2\theta d\phi^2\right), \tag{3.1.1}$$

where constant values of t and r give rise to a sphere in a given volume and a two-sphere in spacetime. Then, the idea of a spherically symmetric spacetime becomes a natural choice for spherical objects.

A spacetime is said to be *stationary* if there exists a timelike Killing [1] vector $\xi^\mu = (\partial/\partial t)^\mu$ in that spacetime. Keep in mind that Latin indices denote space coordinates, while Greek indices denote spacetime coordinates. Then, the group of isometries results in timelike curves. In addition, a spacetime is said to be *static* if there exists a spacelike hyper-surface Σ which is orthogonal to the orbits or curves of the isometry. In other words, spacetime is static, if on top of stationarity, its geometry remains invariant under a time reversal ($t \to -t$), which is a consequence of $\xi_{[\mu}\nabla_\nu \xi_{\rho]}$ [2], where ∇ is the covariant derivative and the squared brackets denote the anti-symmetric component. Hence, a static spherically symmetric spacetime takes the form

$$ds^2 = -f(r)dt^2 + h(r)dr^2 + r^2 \left(d\theta^2 + \sin^2\theta d\phi^2\right), \tag{3.1.2}$$

allowing us to reduce the 10 unknown functions of the spacetime into two, $f(r)$ and $h(r)$.

The exact derivation of the functions $f(r)$ and $h(r)$ are standard and beyond the scope of this chapter, but one can get them by solving Einstein's equations with this metric and imposing $R_{ab} = 0$ for a vacuum spacetime. One can find the full derivation for instance in [156]. Altogether, it gives the expression of the metric found by Schwarzschild in 1916 [162],

$$ds^2 = -\left(1 - \frac{2M}{r}\right) dt^2 + \left(1 - \frac{2M}{r}\right)^{-1} dr^2 + r^2 \left(d\theta^2 + \sin^2\theta d\phi^2\right). \tag{3.1.3}$$

The Schwarzschild solution is the only "spherically symmetric vacuum" solution [3]. Note that one recovers Minkowski space if $M = 0$, and also as $r \to \infty$, which is a property known as *asymptotic flatness* [4]. Here, M is the *Arnowitt-Deser-Misner* (ADM) mass that assumes an asymptotically flat spacetime, which is analog to the Newtonian understanding of the mass.

The Schwarschild metric, which is a BH solution, as we shall see, is not the only solution to Einstein equations since other types of BHs are also solutions. The solution for

---

[1] Killing vectors ξ_ν are those that fulfil the Killing equation $\nabla_\mu \xi_\nu - \nabla_\nu \xi_\mu = 0$. A differential manifold has at most $n(n+1)/2$ Killing vectors with n the dimension. Every Killing vector implies the existence of conserved quantities associated with geodesic motion.

[2] Frobenius theorem guarantees that a vector u is orthogonal to the hyper-surface Σ if and only if this equation is satisfied.

[3] Birkhoff theorem states that any spherically symmetric vacuum solution to Einstein field equations is isometric to Schwarzschild solution.

[4] Asymptotically flat spacetimes represent ideally isolated systems. See, e.g., Ch.11 from [156].

charged BHs was introduced by Reissner and Nordström [163; 164] when considering the Einstein-Maxwell equations. With q being the electric charge of the BH, the line element reads

$$ds^2 = -\left(1 - \frac{2M}{r} + \frac{q^2}{r^2}\right) dt^2 + \left(1 - \frac{2M}{r} + \frac{q^2}{r^2}\right)^{-1} dr^2 + r^2 \left(d\theta^2 + \sin^2\theta d\phi^2\right). \quad (3.1.4)$$

The axially spherically symmetric solution, that is a rotating BH, was discovered by Kerr in 1963 [165]. In the *Boyer-Lindquist* coordinates it reads

$$ds^2 = -\left(1 - \frac{2Mr}{\rho^2}\right) dt^2 - \frac{4Mr}{\rho^2} a \sin^2\theta dt d\phi + \frac{\Sigma}{\rho^2} \sin^2\theta d\phi^2 + \frac{\rho^2}{\Delta} dr^2 + \rho^2 d\theta^2, \quad (3.1.5)$$

where

$$\begin{aligned} a &= J/M, & \rho^2 &= r^2 + a^2\cos^2\theta, \\ \Delta &= r^2 - 2Mr + a^2, & \Sigma &= \left(r^2 + a^2\right)^2 - a^2\Delta\sin^2\theta. \end{aligned} \quad (3.1.6)$$

There also exists the combined solution of a charged and rotating BH, the Kerr-Newman metric [166], that can be written as the Kerr metric but with $\Delta = r^2 - 2Mr + a^2 + q^2$.

For non-rotating BHs, at the Schwarzschild radius $r_{Sch} = 2M$, the escape velocity becomes comparable to the speed of light ($v = c$). Then, it is natural to assume that any particle at this radius will not be able to escape the object. Particles crossing $r_{Sch} = 2M$ are forever trapped inside the sphere. In consequence, the object does not emit nor reflect light and can be considered as a perfect black body. This particularity, plus the singularity at its center discussed in the following subsection, leads these objects to eventually be coined as “black holes”.

One important feature that was discovered by Hawking [167], Carter [168], Israel [169] and Robinson [170] is that there is a “uniqueness” on each solution [5]. In other words, they derived what is known as the *no-hair* theorem, which states that BHs are characterized only by these three [6] conserved parameters : the mass M, the spin a and the charge q. The dependence of the metric on these parameters is further introduced in Sec. 3.4.1, where the direct relation can be observed for instance, in Eq. (3.4.20) in that same section.

3.1.1 Horizons

A remarkable issue of the Schwarzschild solution is that the metric coefficients become singular at $r = 0$ and $r = 2M$. But, because the coefficients $f(r) = h(r)^{-1}$ define the metric, it should be possible to find a new coordinate system in which the coefficients do

---

[5] See also p.292 from Chandrasekhar’s book [171] for a full demonstration.

[6] Three or two or one, depending on the assumed metric.

not generate a singularity. This is true at $r = 2M$, where using, for example, the Regge-Wheeler tortoise coordinate ($r_* = r + 2M \ln\left|\frac{r}{2M} - 1\right|$), one can see that it is a "coordinate singularity". However, it is not possible at $r = 0$, which is a "physical singularity".

Note that for Kerr and Kerr-Newmann solutions, the physical singularity occurs at $\rho = 0 \to r = 0$ and $\theta = \pi/2$, called the ring singularity, and the coordinate singularity occurs at $\Delta = 0 \to r_\pm = M \pm \sqrt{M^2 - a^2 - (q^2)}$, giving rise to two solutions, the inner (r_-) and outer (r_+) solutions. Moreover, these radii are null surfaces ($\xi^\mu \xi_\mu = g_{tt} = 0$) that take the name of *event horizon*. They denote the change in the structure of two casually disconnected regions, the inside timelike ($\xi^\mu \xi_\mu < 0$) region and the outside spacelike ($\xi^\mu \xi_\mu > 0$) region. Once this boundary is crossed in the ingoing direction, nothing can cross again in the outgoing direction, since superluminal (v>c) velocities are required to escape the gravitational potential.

By computing the energy from the static Killing vector ξ^μ and the angular momentum from the rotational Killing $\phi^\mu = (\partial/\partial\phi)^\mu$, one can obtain the gravitational potential of the stationary BH. For a massive particle (with a timelike geodesic $ds^2 = -1$), there are two roots in the gravitational potential depending on the radius, at $r = 6M$ and $r = 3M$. The radius $r = 6M$ is a stable point in the potential, i.e., a minimum value, while $r = 3M$ is an unstable point in the potential, i.e., a maximum value. Thus, the Innermost Stable Circular Orbit (ISCO) is marked at $r = 6M$. Between $3M$ and $6M$, there are no more stable orbits, indicating that nothing can remain in that region for long periods, either they escape, or they fall into the BH. At a radius smaller than $3M$, there are no orbits at all. Hence, depending on the energy of the massive particle in-falling, it can remain in a stable orbit at $r = 6M$ or fall to the singularity with orbital trajectories between $6M$ and $3M$ and plunge directly after that point. If, on the other hand, one considers a photon (with null geodesic $ds^2 = 0$), there is only one unstable root at $3M$, denoting what is known as the *light ring* or *photon sphere*. Photons traveling at a distance of $r = 3M$ with energy lower than the BH's potential at that distance are forever trapped in the photon sphere, while photons traveling at a distance smaller than $3M$ fall directly into the BH. Photons traveling close to the BH, at a distance larger than the light ring, can be deflected. The deflection angle depends on their energy and the mass of the BH, which could result in two outcomes: a small deflection in the trajectory allows the particle to continue its path, while a big deflection in the trajectory results in the particle being trapped by the BH's gravitational potential. The first case gives rise to the known *lensing effect*, that bends the light.

In the case of the Kerr BH, the norm of the timelike Killing field reads

$$\xi^\mu \xi_\mu = g_{tt} = \frac{a^2 \sin^2\theta - \Delta}{\rho^2}, \tag{3.1.7}$$

which becomes positive, thus spacelike, in the region where $r^2 + a^2\cos^2\theta + (q^2) - 2Mr < 0$. The region lying outside the BH is called the *ergosphere*, that is at

$$r_+ < r < M + \sqrt{M^2 - (q^2) - a^2\cos^2\theta}. \tag{3.1.8}$$

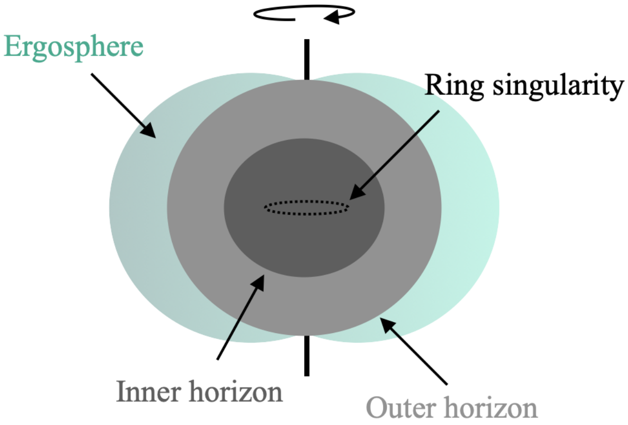

Figure 3.1: Sketch of a rotating black hole with both horizons, the ergosphere region, and the singularity ring at $r = 0$ when $\theta = \pi/2$.

See Fig. 3.1 for a visual representation. This translates into a "drag of the inertial frame" where an observer in this region is forced to rotate in the same direction as the rotation of the BH with an angular velocity equal to

$$\Omega = \frac{\mathrm{d}\phi}{\mathrm{d}t} = -\frac{g_{t\phi}}{g_{\phi\phi}} = \frac{a\left(r^2 + a^2 - \Delta\right)}{\left(r^2 + a^2\right)^2 \Delta a^2 \sin^2\theta}. \tag{3.1.9}$$

Note that in the case of $a \geq M$, that is extremal BHs, Eq. (3.1.8) becomes imaginary, making the horizon disappear. This means that there could be a *naked singularity.* i.e., without a horizon. However, this situation is forbidden by Penrose's *cosmic censorship conjecture* [172], according to which no naked singularities can arise out of non-singular initial conditions in asymptotically flat spacetimes. A consequence of cosmic censorship is that classical BHs do not shrink. The size of a BH is given by the area of the event horizon, which, in analogy to the entropy, can never decrease, giving rise to Hawking's *Area theorem* [173]. However, Hawking showed that BHs can indeed shrink or evaporate through a process called Hawking radiation [174]. In quantum physics, vacuum loops can be generated through the creation and later annihilation of a pair of particles and antiparticles. Hawking radiation is the consequence of such antiparticles entering the BH while particles escape in the opposite direction. As the antiparticles enter the BH, they decrease the energy of the BH and, therefore, the mass.

One of the first questions that arose with this new family of metrics, that is beside the Minkowsky metric, was the stability of the solutions. To probe their stability, small perturbations can be applied. The stability of the Minkowsky metric itself was demonstrated by Christodoulou and Klainerman in 1993 [175]. A thorough analysis of the stability of Schwarzschild and Kerr metrics can be found in [176–178]. I cover the perturbation of the Schwarzschild BH and the Kerr BH in the following sections.

3.2 Perturbation of Schwarzschild BH

The interest in describing the Schwarzschild perturbation is to pave the way for a more complex metric like the Kerr metric. The incorporation of rotation has a large impact not only on the metric but also on the perturbation evolution.

One can consider a massless scalar field ϕ in a curved background such as a Schwarzschild metric, whose evolution is determined by the massless Klein-Gordon equation

$$\Box\phi = (\sqrt{-\mathfrak{g}})^{-1}\partial_\mu\left[(g^{\mu\nu}\sqrt{-\mathfrak{g}})\partial_\nu\right]\phi = 0 \tag{3.2.1}$$

where $\mathfrak{g}$ is the determinant of $g^{\mu\nu}$. Given the spherical symmetry of the background, one can expand $\phi(x)$ in spherical harmonics as

$$\phi(t,r,\theta,\phi) = \frac{1}{r}\sum_{l=0}^{\infty}\sum_{m=-l}^{l} a_{lm}(t,r)Y_{lm}(\theta,\phi), \tag{3.2.2}$$

where $a_{lm}(t,r)$ is the complex amplitude carrying information of the potential and the source, decomposed in spherical harmonics [7].

When introducing Eq. (3.2.2) and the Schwarzschild metric from Eq. (3.1.3) into Eq. (3.2.1), one can see that derivatives of the spherical harmonics arise. To better understand the underlying symmetries of the spherical basis let us introduce the *tetrad formalism*.

The tetrad formalism consists of a four-vector field that generates the hypersurface. In general, it is natural to work on a basis characterized by the symmetry of the studied system or by its conserved charges. This can be achieved through a change of coordinates to a more practical basis. Hence, let me introduce the usual orthonormal basis, which in Cartesian coordinates read

$$e_0 = \frac{\partial}{\partial t}, \qquad e_x = \frac{\partial}{\partial x}, \qquad e_y = \frac{\partial}{\partial y}, \qquad e_z = \frac{\partial}{\partial z}, \tag{3.2.3}$$

and in the spherical basis read

$$e_0 = \frac{\partial}{\partial t}, \qquad e_r = \frac{\partial}{\partial r}, \qquad e_\theta = \frac{1}{r}\frac{\partial}{\partial\theta}, \qquad e_\phi = \frac{1}{r\sin\theta}\frac{\partial}{\partial\phi}. \tag{3.2.4}$$

Since Cartesian coordinates are related to the spherical coordinates through

$$x = r\sin\theta\cos\phi, \qquad y = r\sin\theta\sin\phi, \qquad z = r\cos\theta, \tag{3.2.5}$$

one can always relate both bases through $e^i = \Lambda^i_a e^a$, where i runs over the Cartesian coordinates $(x^1, x^2, x^3 = x, y, z)$ and a [8] runs over the spherical coordinates $(x^1, x^2, x^3 = r, \theta, \phi)$. That is

---

[7] This decomposition, as well as the spherical harmonics, were previously introduced in Sec. 1.2.1.

[8] Note the introduction of Latin indices starting at a for the tetrad basis elements.

$$\begin{pmatrix} e_x \\ e_y \\ e_z \end{pmatrix} = \begin{pmatrix} \sin\theta\cos\phi & \sin\theta\sin\phi & \cos\theta \\ r\cos\theta\cos\phi & r\cos\theta\sin\phi & -r\sin\theta \\ -r\sin\theta\sin\phi & r\sin\theta\cos\phi & 0 \end{pmatrix} \cdot \begin{pmatrix} e_r \\ e_\theta \\ e_\phi \end{pmatrix} \tag{3.2.6}$$

In general, one can write the gradient $\vec{\nabla}$ as

$$\vec{\nabla} = \hat{x}\frac{\partial}{\partial_x} + \hat{y}\frac{\partial}{\partial_y} + \hat{z}\frac{\partial}{\partial_z} = \hat{r}\frac{\partial}{\partial_r} + \hat{\theta}\frac{1}{r}\frac{\partial}{\partial_\theta} + \hat{\phi}\frac{1}{r\sin\theta}\frac{\partial}{\partial_\phi}, \tag{3.2.7}$$

and the Laplacian ∇^2

$$\begin{aligned} \nabla^2 = \vec{\nabla}\cdot\vec{\nabla} &= \left(\hat{r}\frac{\partial}{\partial_r} + \hat{\theta}\frac{1}{r}\frac{\partial}{\partial_\theta} + \hat{\phi}\frac{1}{r\sin\theta}\frac{\partial}{\partial_\phi}\right)\cdot\left(\hat{r}\frac{\partial}{\partial_r} + \hat{\theta}\frac{1}{r}\frac{\partial}{\partial_\theta} + \hat{\phi}\frac{1}{r\sin\theta}\frac{\partial}{\partial_\phi}\right) \\ &= \frac{1}{r^2}\left[\frac{\partial}{\partial_r}\left(r^2\frac{\partial}{\partial_r}\right) + \frac{1}{\sin\theta}\frac{\partial}{\partial_\theta}\left(\sin\theta\frac{\partial}{\partial_\theta}\right) + \frac{1}{\sin^2\theta}\frac{\partial^2}{\partial_\phi^2}\right]. \end{aligned} \tag{3.2.8}$$

The angular momentum in spherical coordinates takes the form

$$\vec{L} = -i\left(\hat{r}\times\nabla\right) = i\left(\hat{\phi}\frac{\partial}{\partial\theta} - \frac{\hat{\theta}}{\sin\theta}\frac{\partial}{\partial\phi}\right) \tag{3.2.9}$$

then, the angular operator is

$$L^2 = -\left(\hat{r}\times\nabla\right)^2 = -r^2\nabla^2 + \frac{\partial}{\partial_r}\left(r^2\frac{\partial}{\partial_r}\right) = -\left[\frac{1}{\sin\theta}\frac{\partial}{\partial_\theta}\left(\sin\theta\frac{\partial}{\partial_\theta}\right) + \frac{1}{\sin^2\theta}\frac{\partial^2}{\partial_\phi^2}\right]. \tag{3.2.10}$$

The spherical harmonic is

$$\begin{aligned} Y_{lm} &= C_{lm}e^{im\phi}P_{lm}(\cos\theta) \\ &= C_{lm}\left(e^{i\phi}\sin\theta\right)^m \sum_{j=0}^{[(l-m)/2]} a_{lmj}(\cos\theta)^{l-m-2j} \end{aligned} \tag{3.2.11}$$

with

$$\begin{aligned} C_{lm} &\equiv (-1)^m\left(\frac{2l+1}{4\pi}\frac{(l-m)!}{(l+m)!}\right)^{1/2}, \\ a_{lmj} &\equiv \frac{(-1)^j}{2^l j!(l-j)!}\frac{(2l-2j)!}{(l-m-2j)!}. \end{aligned} \tag{3.2.12}$$

The angular operator acting on the spherical harmonic Y_{lm} gives

$$L^2Y_{lm} = l(l+1)Y_{lm}. \tag{3.2.13}$$

3.2.1 Spherical harmonics

If one wants to exploit the spherical symmetry, the use of spherical harmonics is very advantageous. In linear theories, the field's multipole components evolve independently of each other. Then, when dealing with scalar fields one can use the *scalar spherical harmonic* decomposition. In the case of vector fields, one must use the *vector spherical harmonics*. Furthermore, for tensor fields where multipole components are coupled together, the use of *tensor spherical harmonics* is required [155]. In the following, I present the construction of the spherical harmonics for the three types of fields and show why they are important in the description of the BH perturbation.

A scalar field can be decomposed in terms of *scalar spherical harmonics* as

$$S(t,r,\theta,\phi) = \sum_{lm} a_{lm}(t,r) Y_{lm}(\theta,\phi). \tag{3.2.14}$$

If instead of a scalar field, one has a vector field, it can be written as

$$V_\mu(t,r,\theta,\phi) = \sum_{\alpha}\sum_{lm} b^\alpha_{lm}(t,r)\left[Y^\alpha_{lm}(\theta,\phi)\right]_\mu , \tag{3.2.15}$$

where the index μ after the brackets denotes the propagation along the coordinate (t,r,θ,ϕ). This is $\left[Y^\alpha_{lm}(\theta,\phi)\right]_\mu = x_\mu Y^\alpha_{lm}(\theta,\phi)$ also written sometimes with a comma for simplicity, as $Y^\alpha_{lm,\mu}(\theta,\phi)$, nonetheless keep in mind that the comma here, does not denote a derivative! And where, α denotes the components of the new tetrad basis, as shown below. For completeness, one can write the propagation as

$$\begin{aligned} \hat{n} &= (\hat{n}_x,\hat{n}_y,\hat{n}_z) \\ &= (\sin\theta\cos\phi, \sin\theta\sin\phi, \cos\theta), \end{aligned} \tag{3.2.16}$$

then,

$$\begin{gathered} \hat{n}_x + i\hat{n}_y = e^{i\phi}\sin\theta, \\ \hat{n}_z = \cos\theta. \end{gathered} \tag{3.2.17}$$

The *vector spherical harmonics* are constructed via [155]

$$Y^{l'}_{lm}(\theta,\phi) = \sum_{m'=-l'}^{l'}\sum_{m''=-1}^{1} (1\,l'm''m'|lm)\xi^{m''}Y^{l'm'} \tag{3.2.18}$$

where $(l''l'm''m'|lm)$ are the Clebsch-Gordan coefficients and the basis vectors $\xi^{m''}$ are defined as [155]

$$\xi^0 = e_z, \qquad \xi^1 = -\frac{e_x + ie_y}{\sqrt{2}}, \qquad \xi^{-1} = \frac{e_x - ie_y}{\sqrt{2}}. \tag{3.2.19}$$

Note that I define the α in the spherical harmonics in Eq. (3.2.15) as $l' = l \pm 1, 0$ components which are combinations of ξ^m. However, these "pure-orbital harmonics" are not optimal to describe radiation, as they are not purely longitudinal nor purely transverse. Hence, a new basis can be constructed for the vector field to be decomposed as

$$V_\mu(t,r,\theta,\phi) = \sum_{lm} \Big(E_{lm}(t,r) Y^{(E)}_{lm,\mu}(\theta,\phi) + B_{lm}(t,r) Y^{(B)}_{lm,\mu}(\theta,\phi) + R_{lm}(t,r) Y^{(R)}_{lm,\mu}(\theta,\phi) \Big) , \tag{3.2.20}$$

where E and B emerge analogously to the electric E and magnetic B fields that are transversal to the propagation, while R is the radial component, longitudinal to the propagation. These three components denote the three d.o.f of a massive spin-1 particle. This new basis is now optimal for describing a "pure-spin vector harmonic" as

$$\begin{aligned} Y^{(E)}_{lm} &= \frac{1}{\sqrt{2l(l+1)}} r \nabla Y_{lm}, \\ Y^{(B)}_{lm} &= \frac{i}{\sqrt{2l(l+1)}} \vec{L} Y_{lm}, \\ Y^{(R)}_{lm} &= \frac{1}{\sqrt{2}} \vec{n}\, Y_{lm}, \end{aligned} \tag{3.2.21}$$

with ∇ the gradient, $\vec{L}$ the angular momentum and $\vec{n}$ the propagation vector. One can see that describing the vector spherical harmonics on this basis is convenient, as the relation to the scalar spherical harmonics is simple. Another reason for working on this basis, is that the electric component and the radial component transform under an even parity, while the magnetic component transforms under an odd parity, i.e.

$$\begin{aligned} Y^{(R)}_{lm} &\to (-1)^l Y^{(R)}_{lm}, \\ Y^{(E)}_{lm} &\to (-1)^l Y^{(E)}_{lm}, \\ Y^{(B)}_{lm} &\to (-1)^{l+1} Y^{(B)}_{lm}. \end{aligned} \tag{3.2.22}$$

If one takes now the case of a tensor field, it could [9] be written as

$$T_{\mu\nu}(t,r,\theta,\phi) = \sum_{\alpha\beta} \sum_{lm} c^{\alpha\beta}_{lm}(t,r) \left[Y^{\alpha\beta}_{lm}(\theta,\phi) \right]_{\mu\nu} \tag{3.2.23}$$

where α and β run over the ten different components from the chosen basis.

The *tensor spherical harmonics* can be generated from a combination of the vector basis, such that [155]

$$t^m = \sum_{m'=-l'}^{1} \sum_{m''=-1}^{1} (1\,1\,m'' m' | 2\,m) \xi^{m'} \otimes \xi^{m''}, \tag{3.2.24}$$

---

[9] As long as the radial part can be separated from the angular part.

and a single basis tensor

$$3^{-1/2}\delta = -\sum_{m'=-l'}^{1}\sum_{m''=-1}^{1}(1\,1\,m''m'|0\,0)\xi^{m'}\otimes\xi^{m''}. \tag{3.2.25}$$

They give rise to six representations of the basis, which in terms of Cartesian coordinates read

$$\begin{aligned} t^{\pm 2} &= \frac{1}{2}\left(e_x\otimes e_x - e_y\otimes e_y\right) \pm \frac{1}{2}i\left(e_x\otimes e_y + e_y\otimes e_x\right), \\ t^{\pm 1} &= \mp\frac{1}{2}\left(e_x\otimes e_z + e_z\otimes e_x\right) - \frac{1}{2}i\left(e_y\otimes e_z + e_z\otimes e_y\right), \\ t^{0} &= \frac{1}{\sqrt{6}}\left(-e_x\otimes e_x - e_y\otimes e_y + 2e_z\otimes e_z\right), \\ \delta &= \left(e_x\otimes e_x + e_y\otimes e_y + e_z\otimes e_z\right). \end{aligned} \tag{3.2.26}$$

By coupling these basis tensors to the spherical harmonics, one obtains the tensor spherical harmonic basis

$$\begin{aligned} Y^{2l',lm}(\theta,\phi) &= \sum_{m'=-l'}^{l'}\sum_{m''=-2}^{2}(l'\,2\,m'm''|lm)Y^{l'm'}(\theta,\phi)\,t^{m''}, \\ Y^{0l,lm}(\theta,\phi) &= -Y^{lm}(\theta,\phi)3^{-1/2}\delta \end{aligned} \tag{3.2.27}$$

with $l' = l\pm 0,1,2$. For fixed l,m,θ,ϕ, the pure-spin tensor spherical harmonics with the proper basis transformation from Eq. (3.2.6), reads

$$\begin{aligned} Y^{L0,lm} &= \vec{n}\otimes\vec{n}\,Y^{lm}, \\ Y^{T0,lm} &= \frac{1}{\sqrt{2}}\left(\delta - \vec{n}\otimes\vec{n}\right)Y^{lm}, \\ Y^{E1,lm} &= \left(\frac{2}{l(l+1)}\right)^{1/2}\left[\vec{n}\otimes r\nabla Y^{lm}\right]^{s}, \\ Y^{B1,lm} &= \left(\frac{2}{l(l+1)}\right)^{1/2}\left[\vec{n}\otimes i\vec{L}Y^{lm}\right]^{s}, \\ Y^{E2,lm} &= \left(2\frac{(l-2)!}{(l+2)!}\right)^{1/2}\left[\vec{L}\vec{L}Y^{lm}\right]^{sTT}, \\ Y^{B2,lm} &= \left(2\frac{(l-2)!}{(l+2)!}\right)^{1/2}\left[ir\nabla\vec{L}Y^{lm}\right]^{sTT}, \end{aligned} \tag{3.2.28}$$

where indices L, T, E, and B represent the longitudinal, transversal, electric-type, and magnetic-type harmonic components with an even parity for the first three and odd parity for the latter component. The index s denotes the symmetric part of the tensor, sTT denotes the symmetric part of the transverse-traceless tensor and the index $l' = 0,1,2$ (second upper-index) denotes the spin of the field.

Combining previous results, one can write a tensor in terms of tensor spherical harmonics as

$$T_{\mu\nu}(t,r,\theta,\phi) = \sum_{lm} \left(A_{lm}(t,r) Y^{(axial)}_{lm,\mu\nu}(\theta,\phi) + B_{lm}(t,r) Y^{(polar)}_{lm,\mu\nu}(\theta,\phi) \right), \tag{3.2.29}$$

where I implicitly make the distinction between the odd parity (axial) and even parity (polar) components. Tensors with this kind of decomposition, are solutions to the Laplace equation $\nabla^2 \Psi = 0$ [155].

Hence, a perturbation on the metric can also be decomposed as

$$h_{\mu\nu}(t,r,\theta,\phi) = \sum_{lm} \left(h^{(axial)}_{lm}(t,r) Y^{(axial)}_{lm,\mu\nu}(\theta,\phi) + h^{(polar)}_{lm}(t,r) Y^{(polar)}_{lm,\mu\nu}(\theta,\phi) \right). \tag{3.2.30}$$

It is important to understand that not all ten components of the metric transform in the same way under a rotation of a two-sphere [10]. Schwarzschild BHs are stationary, which means that the time component t is decoupled from the radial component r and the angular components θ, ϕ. At the same time, due to the spherical symmetry, the radial component r is decoupled from the angular components θ, ϕ. Altogether, this means that one can simplify their transformation by writing

$$\begin{aligned} \left[Y^{tt}_{lm} \right]_{ij} &= \delta^0_i \delta^0_j Y_{lm}, \\ \left[Y^{t\alpha}_{lm} \right]_{ij} &= \delta^0_i Y^{\alpha}_{lm,j}\,, \end{aligned} \tag{3.2.31}$$

where i, j run over the angular coordinates (θ, ϕ). The same is applied to the radial coordinate by changing $t \to r$. Then, the components of the metric perturbation transform as follows

$$h_{\mu\nu} = \begin{pmatrix} \boxed{\text{S}} & \boxed{\text{S}} & \boxed{\quad\text{V}\quad} \\ \boxed{\text{S}} & \boxed{\text{S}} & \boxed{\quad\text{V}\quad} \\ \boxed{\begin{matrix} \\ \text{V} \\ \\ \end{matrix}} & \boxed{\begin{matrix} \\ \text{V} \\ \\ \end{matrix}} & \boxed{\begin{matrix} \\ \quad\text{T}\quad \\ \\ \end{matrix}} \end{pmatrix}. \tag{3.2.32}$$

This means that h_{00}, h_{01} and h_{11} transform as scalars, while (h_{02}, h_{03}) and (h_{12}, h_{13}) transform as vectors and (h_{22}, h_{33}, h_{23}) transform as a tensor. Note that I ignored the symmetric components. This representation gives rise to:

---

[10] I introduced the two-sphere concept when deriving the BH metric in Sec. 3.1 for t and r constant.

$$\begin{aligned} \text{three single scalar components } & S^{1,2,3} = \left[Y^{tt}\right]_{00}, \left[Y^{L0}\right]_{11}, \left[Y^{Rt}\right]_{01}, \\ \text{two vector components } & V^{1,2} = \left[Y^{E1}\right]_{1j}, \left[Y^{B1}\right]_{1j}, \\ \text{and three tensor components } & T^{1,2,3} = \left[Y^{T0}\right]_{ij}, \left[Y^{E2}\right]_{ij}, \left[Y^{B2}\right]_{ij}, \end{aligned} \tag{3.2.33}$$

where here i, j run over the components 2 and 3, i.e. the angular components (θ, ϕ).

To better define the decomposition of the perturbation, let us redo the computation of Eq. (3.2.1) for a scalar field decomposed as Eq. (3.2.2) in the Schwarzschild metric defined in Eq. (3.1.3). If the perturbation produced on the metric can be decomposed as in Eq. (3.2.30) and re-defining $\left[Y^{\alpha\beta}_{lm}\right]_{\mu\nu} \to \left[T^{\alpha\beta}_{lm}\right]_{\mu\nu}$ one can write the ten tensors, known as the Zerilli tensors $\left[T^{\alpha\beta}_{lm}\right]_{\mu\nu}$, with Eqs. (3.2.21) and (3.2.28), such that

$$h_{\mu\nu}(t, r, \theta, \phi) = \sum_{\alpha\beta} \sum_{lm} h^{\alpha\beta}_{lm}(t, r) \left[T^{\alpha\beta}_{lm}\right]_{\mu\nu}, \tag{3.2.34}$$

where

$$T^{tt}_{lm} = \begin{pmatrix} 1 & 0 & 0 & 0 \\ 0 & 0 & 0 & 0 \\ 0 & 0 & 0 & 0 \\ 0 & 0 & 0 & 0 \end{pmatrix} Y_{lm}, \qquad T^{L0}_{lm} = \begin{pmatrix} 0 & 0 & 0 & 0 \\ 0 & 1 & 0 & 0 \\ 0 & 0 & 0 & 0 \\ 0 & 0 & 0 & 0 \end{pmatrix} Y_{lm},$$

$$T^{Rt}_{lm} = \frac{i}{\sqrt{2}} \begin{pmatrix} 0 & 1 & 0 & 0 \\ 1 & 0 & 0 & 0 \\ 0 & 0 & 0 & 0 \\ 0 & 0 & 0 & 0 \end{pmatrix} Y_{lm}, \qquad T^{T0}_{lm} = \frac{r^2}{\sqrt{2}} \begin{pmatrix} 0 & 0 & 0 & 0 \\ 0 & 0 & 0 & 0 \\ 0 & 0 & 1 & 0 \\ 0 & 0 & 0 & \sin^2\theta \end{pmatrix} Y_{lm},$$

$$T^{Et}_{lm} = \frac{ir}{(2l(l+1))^{1/2}} \begin{pmatrix} 0 & 0 & \partial_\theta & \partial_\phi \\ 0 & 0 & 0 & 0 \\ \partial_\theta & 0 & 0 & 0 \\ \partial_\phi & 0 & 0 & 0 \end{pmatrix} Y_{lm}, \quad T^{E1}_{lm} = \frac{r}{(2l(l+1))^{1/2}} \begin{pmatrix} 0 & 0 & 0 & 0 \\ 0 & 0 & \partial_\theta & \partial_\phi \\ 0 & \partial_\theta & 0 & 0 \\ 0 & \partial_\phi & 0 & 0 \end{pmatrix} Y_{lm},$$

$$\begin{aligned}
T^{Bt}_{lm} =& \frac{r}{(2l(l+1))^{1/2}} \begin{pmatrix} 0 & 0 & -(1/\sin\theta)\partial_\phi & \sin\theta\partial_\theta \\ 0 & 0 & 0 & 0 \\ -(1/\sin\theta)\partial_\phi & 0 & 0 & 0 \\ \sin\theta\partial_\theta & 0 & 0 & 0 \end{pmatrix} Y_{lm}, \\
T^{B1}_{lm} =& \frac{ir}{(2l(l+1))^{1/2}} \begin{pmatrix} 0 & 0 & 0 & 0 \\ 0 & 0 & -(1/\sin\theta)\partial_\phi & \sin\theta\partial_\theta \\ 0 & -(1/\sin\theta)\partial_\phi & 0 & 0 \\ 0 & \sin\theta\partial_\theta & 0 & 0 \end{pmatrix} Y_{lm}, \\
T^{E2}_{lm} =& r^2 \left(\frac{(l-2)!}{2(l+2)!}\right)^{1/2} \begin{pmatrix} 0 & 0 & 0 & 0 \\ 0 & 0 & 0 & 0 \\ 0 & 0 & W & X \\ 0 & 0 & X & -\sin^2\theta W \end{pmatrix} Y_{lm}, \\
T^{B2}_{lm} =& -ir^2 \left(\frac{(l-2)!}{2(l+2)!}\right)^{1/2} \begin{pmatrix} 0 & 0 & 0 & 0 \\ 0 & 0 & 0 & 0 \\ 0 & 0 & -(1/\sin\theta)X & \sin\theta W \\ 0 & 0 & \sin\theta W & \sin\theta X \end{pmatrix} Y_{lm},
\end{aligned} \tag{3.2.35}$$

with the operators X, W defined as

$$\begin{aligned}
X &= 2\partial_\theta\partial_\phi - 2\cot\theta\partial\phi, \\
W &= \partial^2_\theta - \cot\theta\partial_\theta - \frac{1}{\sin^2\theta}\partial^2_\phi.
\end{aligned} \tag{3.2.36}$$

Note that the Zerilli tensors can be separated in an angular and a radial part as

$$\left[T^{\alpha\beta}_{lm}\right]_{\mu\nu} = c^{\alpha\beta}(r)\left[t^{\alpha\beta}_{lm}(\theta,\phi)\right]_{\mu\nu}. \tag{3.2.37}$$

This means that the radial coefficients $c^{\alpha\beta}(r)$ can be absorbed in $h^{\alpha\beta}_{lm}(t,r)$, leading to

$$h_{\mu\nu}(t,r,\theta,\phi) = \sum_{\alpha\beta}\sum_{lm} h^{\alpha\beta}_{lm}(t,r)\left[t^{\alpha\beta}_{lm}(\theta,\phi)\right]_{\mu\nu}. \tag{3.2.38}$$

Keep in mind that, from Eq. (3.2.29), the perturbation can be separated into an axial polarization and a polar polarization. Thus, the perturbation consists of three components with axial polarization (Bt, B1, B2) and seven components with polar polarization (tt, L0, Rt, T0, Et, E1, E2).

3.2.2 Regge-Wheeler gauge

In 1957, Tulio Regge and John A. Wheeler [158] found a framework to work with BH perturbations for the axial polarization by choosing a gauge. So, the first thing one should do is to find the gauge that allows one to work with the axial polarization.

The transformation of a vector, presented already in Chapter 1, takes the form

$$x^\mu \to x'^\mu = x^\mu + \zeta^\mu, \tag{3.2.39}$$

then, a metric perturbation transforms as

$$h_{\mu\nu} \to h'_{\mu\nu} = h_{\mu\nu} + D_\mu \zeta_\nu + D_\nu \zeta_\mu, \tag{3.2.40}$$

where D_μ is the covariant derivative associated with the metric via the Christoffel symbols in the following way

$$D_\mu \zeta_\nu = \partial_\mu \zeta_\nu - \Gamma^\rho_{\nu\mu} \zeta_\rho. \tag{3.2.41}$$

From Eqs. (3.2.20) and (3.2.21) is straightforward to see that a four-vector field ζ_μ can be decomposed into vector spherical harmonics with an axial and a polar polarization, such that

$$\begin{aligned} \zeta_0 =& \sum_{l=0}^{\infty} \sum_{m=-l}^{l} \zeta^{(t)}_{lm} Y_{lm}, \\ \zeta_i =& \sum_{l=0}^{\infty} \sum_{m=-l}^{l} \zeta^{(R)}_{lm} n_i \, Y_{lm} \\ &+ \sum_{l=1}^{\infty} \sum_{m=-l}^{l} \left[\zeta^{(E)}_{lm} \partial_i \, Y_{lm} + \zeta^{(B)}_{lm} \frac{i}{r} L_i Y_{lm} \right]. \end{aligned} \tag{3.2.42}$$

With this decomposition, one could fix an axial gauge, such that $\zeta^{(t)}_{lm} = \zeta^{(R)}_{lm} = \zeta^{(E)}_{lm} = 0$. In that case, the notation of the gauge takes the form

$$\zeta^{ax}_0(\vec{x}) = 0, \qquad\qquad \zeta^{ax}_i(\vec{x}) = \sum_{l=1}^{\infty} \sum_{m=-l}^{l} \Lambda_{lm}(t,r) \frac{i}{r} L_i \, Y_{lm}, \tag{3.2.43}$$

where $\zeta^{(B)}_{lm}$ is redefined as $\Lambda_{lm}(t,r)$. Keeping in mind that i runs over the spherical space components and μ over the spherical spacetime components, we can re-write

$$\zeta^{ax}_\mu(\vec{x}) = \sum_{l=1}^{\infty} \sum_{m=-l}^{l} \Lambda_{lm}(t,r) \left(0, 0, -\frac{1}{\sin\theta} \partial_\phi Y_{lm}, \sin\theta \partial_\theta Y_{lm} \right). \tag{3.2.44}$$

In order to apply the transformation to the axial vectors ζ^{ax}_α, let us first write the components of the axial perturbation $h^{(axial)}_{\mu\nu}$ directly from Eqs. (3.2.35)

$$h^{(axial)}_{\mu\nu} = \begin{pmatrix} 0 & 0 & h^{Bt} \frac{1}{\sin\theta} \partial_\phi & -h^{Bt} \sin\theta \partial_\theta \\ 0 & 0 & h^{B1} \frac{1}{\sin\theta} \partial_\phi & -h^{B1} \sin\theta \partial_\theta \\ * & * & 2h^{B2} \left(\frac{1}{\sin\theta} \partial_\theta \partial_\phi - \frac{\cos\theta}{\sin^2\theta} \partial\phi \right) & h^{B2} \left(\cos\theta \partial_\theta + \frac{1}{\sin\theta} \partial^2_\phi - \sin\theta \partial^2_\theta \right) \\ * & * & * & -2h^{B2} \left(\sin\theta \partial_\theta \partial_\phi - \cos\theta \partial\phi \right) \end{pmatrix} Y_{lm}, \tag{3.2.45}$$

where the asterisk $(^*)$ is the symmetric element of the matrix and where h^{Bj} are functions depending on the time and on the radial component $h^{Bj}(t,r)$, that need to be defined with Einstein's equations.

Then, using Eq. (3.2.40) with Eqs. (3.2.41) and (3.2.45) ones sees that the transformation for the axial perturbation is

$$h^{Bt}_{lm} \to h^{Bt}_{lm} + \partial_0 \Lambda_{lm} \qquad (l \geq 1), \tag{3.2.46a}$$

$$h^{B1}_{lm} \to h^{B1}_{lm} + \left(\partial_r - \frac{2}{r}\right)\Lambda_{lm} \qquad (l \geq 1), \tag{3.2.46b}$$

$$h^{B2}_{lm} \to h^{B2}_{lm} - \Lambda_{lm} \qquad (l \geq 2). \tag{3.2.46c}$$

If one chooses $\Lambda_{lm} = h^{B2}_{lm}$ then, when transforming the last axial component (B2), it will vanish. Note that h^{B2}_{lm} is defined for $l \leq 2$ then, l=1 can be chosen to cancel the h^{Bt}_{1m} transformation. Hence, the perturbation in this Regge-Wheeler (RW) gauge takes the form

$$h^{RW}_{\alpha\beta} = \sum_{l=2}^{\infty}\sum_{m=-l}^{l} h^{Bt}_{lm}\left[t^{Bt}_{lm}\right]_{\alpha\beta} + \sum_{l=1}^{\infty}\sum_{m=-l}^{l} h^{B1}_{lm}\left[t^{B1}_{lm}\right]_{\alpha\beta}. \tag{3.2.47}$$

or in another more common representation where $h^0_{lm} = h^{Bt}_{lm}$ and $h^1_{lm} = h^{B1}_{lm}$,

$$h^{RW}_{\alpha\beta} = \begin{pmatrix} 0 & 0 & h^0_{lm}\frac{1}{\sin\theta}\partial_\phi & -h^0_{lm}\sin\theta\partial_\theta \\ 0 & 0 & h^1_{lm}\frac{1}{\sin\theta}\partial_\phi & -h^1_{lm}\sin\theta\partial_\theta \\ * & * & 0 & 0 \\ * & * & 0 & 0 \end{pmatrix} Y_{lm}. \tag{3.2.48}$$

With this metric, one can now compute Einstein's equations keeping in mind that the metric transformation will affect the Ricci tensor such that

$$\begin{aligned} R'_{\mu\nu} &\to R_{\mu\nu} + \delta R_{\mu\nu}, \\ \delta R_{\mu\nu} &= \delta\Gamma^\rho_{\mu\rho,\nu} - \delta\Gamma^\rho_{\mu\nu,\rho}, \\ \delta\Gamma^\rho_{\mu\rho} &= \frac{1}{2}g^{\mu\lambda}(\partial_\rho h_{\sigma\lambda} + \partial_\sigma h_{\rho\lambda} - \partial_\lambda h_{\rho\sigma}). \end{aligned} \tag{3.2.49}$$

Thus, by computing the Christoffel symbols for the perturbation one can see that only three Ricci components are non-trivially satisfied ($\delta R_{\mu\nu} = 0$),

$$\delta R_{t\phi} : A(r)\left(\partial_r^2 h^0 - \partial_t\partial_r h^1 - \frac{2}{r}\partial_t h^1\right) + \frac{1}{r^2}\left[\frac{4M}{r} - l(l+1)\right]h^0 = 0, \tag{3.2.50a}$$

$$\delta R_{r\phi} : \frac{1}{A(r)}\left(\partial_t^2 h^1 - \partial_t\partial_r h^0 + \frac{2}{r}\partial_t h^0\right) + \frac{1}{r^2}\left[l(l+1) - 2\right]h^1 = 0, \tag{3.2.50b}$$

$$\delta R_{\theta\phi} : \frac{1}{A(r)}\partial_t h^0 - \partial_r\left(A(r)h^1\right) = 0, \tag{3.2.50c}$$

with $A(r) = \left(1 - \frac{2M}{r}\right)$ and where I suppressed the lm dependency for clarity. Note that Eq. (3.2.50a) is automatically satisfied if the other two are satisfied [11]. Then, one can define a new function

$$Q_{lm}(t,r) = \frac{1}{r} A(r) h^1_{lm}(t,r), \tag{3.2.51}$$

such that Eq. (3.2.50c) becomes

$$\partial_t h^0_{lm} = A(r)\partial_r (rQ_{lm}). \tag{3.2.52}$$

Then, Eq. (3.2.50b) is

$$\partial_t^2 \left(\frac{rQ_{lm}}{A(r)}\right) - \partial_r \left(A(r)\partial_r rQ_{lm}\right) + \frac{2}{r} A(r)\partial_r rQ_{lm} + \frac{1}{r^2}\left[l(l+1) - 2\right] rQ_{lm} = 0. \tag{3.2.53}$$

If one considers the tortoise coordinate $r_* = r + 2M \ln \left|\frac{r}{2M} - 1\right|$ instead of the radial coordinate, one could easily find that

$$\partial_{r_*} = \left(1 - \frac{2M}{r}\right)\partial_r, \tag{3.2.54}$$

then, introducing the change in Eq. (3.2.53), one could, after some work, re-write the equation as

$$\left(\partial_t^2 - \partial_{r_*}^2\right) Q_{lm} + V_l^{RW}(r) Q_{lm} = 0, \tag{3.2.55}$$

with the RW potential as

$$V_l^{RW}(r) = \left(1 - \frac{2M}{r}\right)\left[\frac{l(l+1)}{r^2} - \frac{6M}{r^3}\right]. \tag{3.2.56}$$

Now, if one performs a Fourier transform to the function Q_{lm}

$$Q_{lm}(t,r) = \int_{-\infty}^{\infty} \frac{d\omega}{2\pi} \tilde{Q}_{lm}(\omega, r) e^{-i\omega t}, \tag{3.2.57}$$

then, one could find the one-dimensional Schrödinger-type wave equation

$$\frac{\mathrm{d}^2}{\mathrm{d}r_*^2}\tilde{Q}_{lm} + \left[\frac{\omega^2}{c^2} - V_l^{RW}\right]\tilde{Q}_{lm} = \tilde{S}^{ax}_{lm}, \tag{3.2.58}$$

where $\tilde{S}^{ax}_{lm}$ is the source term decomposed also in terms of axial tensor spherical harmonics, taken to be zero in the development of the equations as we are far away from the source. Nevertheless, one should consider their contribution to the wave equation and impose boundary conditions tending to zero as the observer distances from the source.

---

[11] One has to take the derivative of Eq. (3.2.50a) and change the $\delta_t h^0_{lm}$ and $\delta_t^2 h^1_{lm}$ with their definition from Eqs. (3.2.50c) and (3.2.50b).

3.2.3 Zerilli gauge

The framework to obtain the polar solution to a perturbed BH was developed by Frank Zerilli in 1970 [159]. In contra-position to the three components for the axial polarization, the polar polarization has seven components, as we saw. Following the same steps as for the RW gauge, first, we have to choose the polar gauge. The four-vector field takes the form

$$\begin{aligned}\zeta^{pol}_{\alpha}(x) =& \sum_{l=0}^{\infty}\sum_{m=-l}^{l}\left(\zeta^{(t)}_{lm}(t,r)Y_{lm}, \zeta^{(R)}_{lm}(t,r)Y_{lm}, 0, 0\right) \\ &+ \sum_{l=1}^{\infty}\sum_{m=-l}^{l}\zeta^{(E)}_{lm}(t,r)\left(0,0,\partial_\theta Y_{lm}, \partial_\phi Y_{lm}\right).\end{aligned} \tag{3.2.59}$$

Then, the polar perturbation $h^{(polar)}_{\mu\nu}$ is

$$h^{(polar)}_{\mu\nu} = \begin{pmatrix} A(r)H_0 & H_1 & h_0\partial_\theta & h_0\partial_\phi \\ * & \frac{H_2}{A(r)} & h_1\partial_\theta & h_1\partial_\phi \\ * & * & r^2\left[K + G\partial_\theta\partial_\theta\right] & G\left(\partial_\theta\partial_\phi - \cot\theta\partial_\phi\right) \\ * & * & * & r^2\left[K\sin^2\theta + G\left(\partial_\phi\partial_\phi - \sin\theta\cos\theta\partial_\phi\right)\right] \end{pmatrix} Y_{lm}, \tag{3.2.60}$$

where $H_0, H_1, H_2, h_0, h_1, K, G$ are functions of the time and the radial coordinate. They depend on the angular numbers (l, m) and are connected to the seven components $tt, Rt, L0, Et, E1, T0, E2$ respectively. One can obtain the transformation using Eqs. (3.2.40) and (3.2.41), which results in

$$h^{tt}_{lm} \to h^{tt}_{lm} - \left[2\partial_0\zeta^{(t)}_{lm} - \frac{A(r)2M}{r^2}\zeta^{(R)}_{lm}\right], \tag{3.2.61a}$$

$$h^{Rt}_{lm} \to h^{Rt}_{lm} - \left[\partial_0\zeta^{(R)}_{lm} + \partial_r\zeta^{(t)}_{lm} - \frac{2M}{A(r)r^2}\zeta^{(t)}_{lm}\right], \tag{3.2.61b}$$

$$h^{L0}_{lm} \to h^{L0}_{lm} - \left[2\partial_0\zeta^{(R)}_{lm} + \frac{2M}{A(r)r^2}\zeta^{(R)}_{lm}\right], \tag{3.2.61c}$$

$$h^{T0}_{lm} \to h^{T0}_{lm} - \left[2rA(r)\zeta^{(R)}_{lm} - l(l+1)\zeta^{(E)}_{lm}\right], \tag{3.2.61d}$$

$$h^{Et}_{lm} \to h^{Et}_{lm} - \left[\zeta^{(t)}_{lm} + \partial_0\zeta^{(E)}_{lm}\right], \tag{3.2.61e}$$

$$h^{E1}_{lm} \to h^{E1}_{lm} - \left[\left(\partial_r - \frac{2}{\partial_2}\right)\zeta^{(E)}_{lm} + \zeta^{(R)}_{lm}\right], \tag{3.2.61f}$$

$$h^{E2}_{lm} \to h^{E2}_{lm} - \zeta^{(E)}_{lm}. \tag{3.2.61g}$$

In this case, when fixing $\zeta^{(E)}_{lm}$ to h^{E2}_{lm}, the transformation will become zero for $l \geq 2$. In h^{E1}_{lm}, one can also choose $\zeta^{(R)}_{lm}$ to cancel the transformation for $l \geq 1$ and then also

$\zeta^{(t)}_{lm}$ for $l \geq 1$ to cancel h^{Et}_{lm}. When fixing these components, the remaining parts of the equations can no longer be constrained, as there are only three d.o.f. Hence, the four remaining components that construct the polar perturbations or Zerilli (Z) gauge read

$$\begin{aligned} h^{Z}_{\alpha\beta} = &\sum_{l=0}^{\infty}\sum_{m=-l}^{l}\left[h^{tt}_{lm}\left[t^{tt}_{lm}\right]_{\alpha\beta} + h^{L0}_{lm}\left(t^{L0}_{lm}\right)_{\alpha\beta}\right] \\ &+ \sum_{l=1}^{\infty}\sum_{m=-l}^{l} h^{Rt}_{lm}\left[t^{Rt}_{lm}\right]_{\alpha\beta} + \sum_{l=2}^{\infty}\sum_{m=-l}^{l} h^{T0}_{lm}\left[t^{T0}_{lm}\right]_{\alpha\beta}. \end{aligned} \tag{3.2.62}$$

In the matrix representation, the decomposition takes the form

$$h^{Z}_{\alpha\beta} = \begin{pmatrix} h^{tt}_{lm} & h^{Rt}_{lm} & 0 & 0 \\ * & h^{L0}_{lm} & 0 & 0 \\ 0 & 0 & h^{T0}_{lm} & 0 \\ 0 & 0 & 0 & h^{T0}_{lm}\sin^2\theta \end{pmatrix} Y_{lm}, \tag{3.2.63}$$

where I used

$$\begin{aligned} h^{tt}_{lm}(t,r) &= A(r)H_0, \\ h^{L0}_{lm}(t,r) &= A^{-1}(r)H_2, \\ h^{T0}_{lm}(t,r) &= r^2 K, \\ h^{Rt}_{lm}(t,r) &= H_1. \end{aligned} \tag{3.2.64}$$

For this metric, seven Ricci components survive, namely

$$\begin{aligned} A(r)\Big(A(r)\partial_r\partial_r K + \left(3 - \frac{5M}{r}\right)\frac{1}{r}\partial_r K - \frac{A(r)}{r}\partial_r H_2 \\ - \frac{1}{r^2}\left[(H_2 - K) + \frac{l(l+1)}{2}(H_2 + K)\right]\Big) = 0, \end{aligned} \tag{3.2.65a}$$

$$\partial_t\left(\partial_r K + \frac{1}{r}(K - H_2) - \frac{M}{r(r-2M)}K\right) - \frac{l(l+1)}{2r^2}H_1 = 0, \tag{3.2.65b}$$

$$\begin{aligned} \frac{1}{A(r)}\Big(\frac{1}{A(r}\partial_t\partial_t K - \frac{1 - M/r}{r}\partial_r K - \frac{2}{r}\partial_t H_1 + A(r)\partial_r H_0 \\ + \frac{1}{r^2}(H_2 - K) + \frac{l(l+1)}{2r^2}(K - H_0)\Big) = 0, \end{aligned} \tag{3.2.65c}$$

$$\partial_r\left(A(r)H_1\right) - \partial_t(H_2 + K) = 0; \tag{3.2.65d}$$

$$-\partial_t H_1 + A(r)\partial_r(H_0 - K) + \frac{2M}{r^2}H_0 + \frac{1-M/r}{r}(H_2 - H_0) = 0, \tag{3.2.65e}$$

$$\begin{gathered}-\frac{1}{A(r)}\partial_t\partial_t K + A(r)\partial_r\partial_r K + A(r)\frac{2}{r}\partial_r K - \frac{1}{A(r)}\partial_t\partial_t H_2 \\ +2\partial_r\partial_t H_1 - A(r)\partial_r\partial_r H_0 + \left(1 - \frac{M}{r}\right)\left[\frac{2}{r-2M}\partial_t H_1 - \frac{1}{r}\partial_r H_2\right] \\ -\frac{1}{r}\left(1+\frac{M}{r}\right)\partial H_0 - \frac{1}{2r^2}l(l+1)(H_2 - H_0) = 0,\end{gathered} \tag{3.2.65f}$$

$$\frac{1}{2}(H_0 - H_2) = 0. \tag{3.2.65g}$$

Following the same steps as before changing the radial coordinate to the tortoise coordinate, and implementing a Fourier transform one can find after some work, a single wave equation known as the Zerilli equation,

$$\frac{\mathrm{d}^2}{\mathrm{d}r_*^2}\tilde{Z}_{lm} + \left[\frac{\omega^2}{c^2} - V_l^Z\right]\tilde{Z}_{lm} = \tilde{S}^{pol}_{lm}, \tag{3.2.66}$$

where $\tilde{S}^{pol}_{lm}$ is the source term decomposed also in terms of polar tensor spherical harmonics, and with the Zerilli potential defined as

$$V_l^Z(r) = \left(1 - \frac{2M}{r}\right)\frac{2\lambda^2(\lambda+1)r^3 + 6\lambda^2 M r^2 + 18\lambda M^2 r + 18M^3}{r^3(\lambda r + 3M)^2}, \tag{3.2.67}$$

$$\lambda = \frac{(l-1)(l+2)}{2}. \tag{3.2.68}$$

The Zerilli function, independently of the chosen gauge [12], is defined as [179]

$$Z(t,r) \equiv \frac{4re^{4v}k_2 + l(l+1)rk_1}{l(l+1) - 2 + 6M/r} \tag{3.2.69}$$

where $e^v = 1 - 2M/r$ and that is connected to the components through

$$\begin{aligned} G &= k_3, \\ h_1 &= k_4, \\ K &= k_1 - \frac{e^{2v}}{r}\left[r^2\partial_r k_3 - 2k_4\right], \\ H_2 &= 2e^{2v}k_2 + r\partial_r k_1 + (1 + r\partial_r v)\,k_1 - e^v\partial_r\left[r^2 e^v\partial_r k_3 - 2e^v k_4\right]. \end{aligned} \tag{3.2.70}$$

---

[12] Indeed, the chosen gauge was the one in which $G = h_0 = h_1 = 0$, when fixing $h^{Et}_{lm}, h^{E1}_{lm}, h^{E2}_{lm}$ transformations.

For completeness, it is worth mentioning that Chandrasekhar [157] showed that the Regge-Wheeler and the Zerilli potentials are equivalent since both potentials can be written as

$$V^{RW,Z} = 6M\partial_{r_*} f + (6M)^2 f^2 + \kappa f, \tag{3.2.71}$$

where

$$\kappa = \lambda(\lambda + 2), \qquad f = \frac{A(r)}{r(\lambda r + 6M)}. \tag{3.2.72}$$

This feature is known as iso-spectrality and means that the solutions to a wave equation with a RW potential will also be solutions to a wave equation with a Zerilli potential.

3.3 Newman-Penrose formalism

This section introduces the Newman-Penrose (NP) [13] formalism, which is crucial for the description of the Kerr BH perturbation. In the previous section, we saw that, for a Schwarzschild BH, the stationarity and the spherical symmetry of the metric, enabled the decoupling of the metric perturbation into a radial part and an angular part described by spherical harmonics. In the case of a rotating BH, which tends to an oblate shape, the spherical symmetry is broken. That means that the previous decomposition is no longer possible and other approaches are needed. In 1973 Teukolsky [160] found a way to separate the perturbation wave equation into a radial and an angular part by implementing the NP formalism to describe Kerr's metric. Hence, the need for this section where I introduce the framework that Teukolsky used. For this section, I use the references [157; 160; 161; 180].

As I previously mentioned, the tetrad formalism serves to change to another basis system, where symmetries of the object or structure in question can be exploited. Moreover, the tetrad does not need to be a coordinate basis such as the Cartesian or the spherical coordinates, they can be a non-coordinate basis. To understand the notation for the tetrad formalism let us first review some properties. A tetrad field is denoted by

$$e^{\alpha}_{(a)}, \quad \text{for} \quad a = 1, 2, 3, 4, \tag{3.3.1}$$

where (a) labels denote the tetrad component and α the tensor coordinate component. Note that the notation with the parenthesis is to highlight the non-coordinate basis. Each tetrad vector field allows us to change from the coordinate basis to the non-coordinate or tetrad basis via

$$e_{(a)} = e^{\alpha}_{(a)} e_{\alpha}, \quad e^{(a)} = (e^{-1})^{(a)}_{\alpha} e^{\alpha}, \quad \text{where} \quad e_{\alpha} = \frac{\partial}{\partial x^{\alpha}}. \tag{3.3.2}$$

Then, if one applies a change of basis onto a tensor, it transforms as

---

[13] Not to be confused with Post-Newtonian (PN) expansion.

$$T^{(a)(b)}_{(c)} = (e^{-1})^{(a)}_{\alpha}(e^{-1})^{(b)}_{\beta} e^{\gamma}_{(c)} T^{\alpha\beta}_{\gamma}. \tag{3.3.3}$$

Analogous to the Christoffel symbols in a coordinate basis, the *Ricci rotation coefficients* inform us on the differentiation of the metric in different directions in a non-coordinate basis. They are defined as [14]

$$\gamma^{(a)}_{(b)(c)} = e^{(a)}\nabla_{(b)}e_{(c)}. \tag{3.3.4}$$

Where ∇ is the *affine connection*, which acts as [15]

$$\begin{aligned}
\nabla_{(b)}e_{(c)} =& \nabla_{e_b}\left(e^{\gamma}_{(c)}e_{\gamma}\right) = e^{\beta}_{(b)}\nabla_{\beta}\left(e^{\gamma}_{(c)}e_{\gamma}\right) = e^{\beta}_{(b)}\partial_{\beta}e^{\gamma}_{(c)}e_{\gamma} + e^{\gamma}_{(c)}e^{\beta}_{(b)}\nabla_{\beta}\left(e_{\gamma}\right)\\
&= e^{\beta}_{(b)}\partial_{\beta}e^{\gamma}_{(c)}e_{\gamma} + e^{\gamma}_{(c)}e^{\beta}_{(b)}\Gamma^{\alpha}_{\beta\gamma}e_{\alpha} = e^{\beta}_{(b)}\left(\partial_{\beta}e^{\gamma}_{(c)} + e^{\alpha}_{(c)}\Gamma^{\gamma}_{\beta\alpha}\right)e_{\gamma}\\
&= e^{\beta}_{(b)}\left(\partial_{\gamma}e^{\alpha}_{(c)} + e^{\alpha}_{(c)}\Gamma^{\gamma}_{\beta\alpha}\right)(e^{-1})^{(a)}_{\gamma}e_{(a)} \equiv \gamma^{(a)}_{(b)(c)}e_{(a)}.
\end{aligned} \tag{3.3.5}$$

A consequence of this transformation is that, given two tetrad vectors on a non-coordinate basis they no longer commute and tensors representing the structure emerge. Correspondingly, these tensors are called the *structure constants* and they can be written in terms of the *Lie brackets* as

$$\left[e_{(a)}, e_{(b)}\right] = \left(\gamma^{(c)}_{(b)(a)} - \gamma^{(c)}_{(a)(b)}\right)e_{(c)} = C^{(c)}_{(a)(b)}e_{(c)}. \tag{3.3.6}$$

Continuing with the metric description in the tetrad basis, the Riemann tensors take the form [16]

$$\begin{aligned}
R_{(a)(b)(c)(d)} =& \partial_{(c)}\gamma_{(a)(b)(d)} - \partial_{(d)}\gamma_{(a)(b)(c)} + \gamma_{(b)(a)(f)}\left[\gamma^{(f)}_{(c)(d)} - \gamma^{(f)}_{(d)(c)}\right]\\
&+ \gamma_{(f)(a)(c)}\gamma^{(f)}_{(b)(d)} - \gamma_{(f)(a)(d)}\gamma^{(f)}_{(b)(c)}.
\end{aligned} \tag{3.3.7}$$

And finally the Bianchi identity $\nabla_{[\sigma}R_{\gamma\delta]\alpha\beta} = 0$ [17] can be expressed as

$$\begin{aligned}
\nabla_{[(f)}R_{(c)(d)](a)(b)} = \frac{1}{6}\sum_{(c)(d)(f)} & \partial_{(f)}R_{(a)(b)(c)(d)} - \left[\gamma^{(m)}_{(a)(f)}R_{(m)(b)(c)(d)} + \gamma^{(m)}_{(b)(f)}R_{(a)(m)(c)(d)}\right.\\
&\left.+\gamma^{(m)}_{(c)(f)}R_{(a)(b)(m)(d)} + \gamma^{(m)}_{(d)(f)}R_{(a)(b)(c)(m)}\right].
\end{aligned} \tag{3.3.8}$$

---

[14] Keep in mind that the Christoffel symbols are defined as $\Gamma^{\alpha}_{\beta\gamma} = e^{\alpha}\nabla_{\beta}e_{\gamma}$.

[15] I use here the above Christoffel's equation and that $\nabla_{\beta}e^{\gamma}_{(c)} = \partial_{\beta}e^{\gamma}_{(c)}$.

[16] Note that it differs from Eq. (1.1.2) since in non-coordinate basis the second term does not cancel, $\gamma^{(f)}_{(c)(d)} \neq \gamma^{(f)}_{(d)(c)}$, while in a coordinate basis, they cancel since the Christoffel symbols are symmetric $\Gamma^{\alpha}_{\beta\gamma} = \Gamma^{\alpha}_{\gamma\beta}$.

[17] Keep in mind that the squared brackets denote the anti-symmetric component of the tensor.

The Newman-Penrose formalism is based on a special choice of basis vectors, the *null tetrads*. This means that it is constructed upon a series of null vectors, see Fig. 3.2 for a visual representation in the Cartesian basis. For a Riemann metric, the components of the Weyl tensor, introduced later in Eq. (3.3.16), are projected along these null vectors. Consequently, this formalism allows us to consider perturbations on the curvature of the metric, instead of perturbations on the BH. The four vectors defined by Ezra Newman and Roger Penrose [180] are

$$z^{\mu}_{(a)} = (l^{\mu}, n^{\mu}, m^{\mu}, \bar{m}^{\mu})\,. \tag{3.3.9}$$

The vectors l^{μ} and n^{μ} are real, while m^{μ} is complex and $\bar{m}^{\mu}$ is its complex conjugate. These vectors are chosen to satisfy

$$\begin{aligned} g_{\mu\nu}l^{\mu}l^{\nu} = g_{\mu\nu}n^{\mu}n^{\nu} = g_{\mu\nu}m^{\mu}m^{\nu} = g_{\mu\nu}\bar{m}^{\mu}\bar{m}^{\nu} = 0, \\ g_{\mu\nu}l^{\mu}m^{\nu} = g_{\mu\nu}l^{\mu}\bar{m}^{\nu} = g_{\mu\nu}n^{\mu}m^{\nu} = g_{\mu\nu}n^{\mu}\bar{m}^{\nu} = 0, \\ g_{\mu\nu}l^{\mu}n^{\nu} = -1, \qquad\qquad g_{\mu\nu}m^{\mu}\bar{m}^{\nu} = 1. \end{aligned} \tag{3.3.10}$$

Then, the metric takes the form

$$g_{\mu\nu} = g^{\mu\nu} = \begin{pmatrix} 0 & -1 & 0 & 0 \\ -1 & 0 & 0 & 0 \\ 0 & 0 & 0 & 1 \\ 0 & 0 & 1 & 0 \end{pmatrix}. \tag{3.3.11}$$

Therefore, it can be written as

$$g^{\mu\nu} = -l^{\mu}n^{\nu} - n^{\mu}l^{\nu} + m^{\mu}\bar{m}^{\nu} + \bar{m}^{\mu}m^{\nu}. \tag{3.3.12}$$

A Minkowsky metric in Cartesian coordinates can be defined in terms of these null tetrads as

$$\begin{aligned} l^{\mu} &= \frac{1}{\sqrt{2}}(1,0,0,1), & m^{\mu} &= \frac{1}{\sqrt{2}}(0,1,i,0), \\ n^{\mu} &= \frac{1}{\sqrt{2}}(1,0,0,-1), & \bar{m}^{\mu} &= \frac{1}{\sqrt{2}}(0,1,-i,0). \end{aligned} \tag{3.3.13}$$

The covariant derivative operators also have different symbols, represented by

$$\nabla_{(a)} = (l^{\mu}\nabla_{\mu}, n^{\mu}\nabla_{\mu}, m^{\mu}\nabla_{\mu}, \bar{m}^{\mu}\nabla_{\mu}) \equiv \left(D, \mathit{\Delta}, \delta, \bar{\delta}\right) \tag{3.3.14}$$

And the Ricci rotation coefficients γ_{abc} called now *spin coefficients*, are designated by Greek letters [18] in the following way

---

[18] Note that there is a (-) sign with respect to NP's paper [180], because of the their chosen metric signature convention (+,-,-,-).

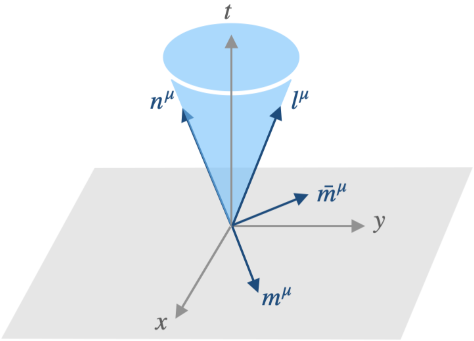

Figure 3.2: Representation of the Newman-Penrose null tetrad in Cartesian coordinates.

$$
\begin{aligned}
\kappa &\equiv -\gamma_{131} = -(\nabla_\nu l_\mu) l^\mu m^\nu, & \varrho &\equiv -\gamma_{134} = -(\nabla_\nu l_\mu) m^\mu \bar{m}^\nu, \\
\sigma &\equiv -\gamma_{133} = -(\nabla_\nu l_\mu) m^\mu m^\nu, & \tau &\equiv -\gamma_{132} = -(\nabla_\nu l_\mu) m^\mu n^\nu, \\
\lambda &\equiv \gamma_{244} = (\nabla_\nu n_\mu) \bar{m}^\mu \bar{m}^\nu, & \mu &\equiv \gamma_{243} = (\nabla_\nu n_\mu) \bar{m}^\mu m^\nu, \\
\nu &\equiv \gamma_{242} = (\nabla_\nu n_\mu) \bar{m}^\mu n^\nu, & \pi &\equiv \gamma_{241} = (\nabla_\nu n_\mu) \bar{m}^\mu l^\nu, \\
\epsilon &\equiv -\frac{1}{2}\left[\gamma_{121} - \gamma_{341}\right] = -\frac{1}{2}\left[(\nabla_\nu l_\mu) n^\mu l^\nu - (\nabla_\nu m_\mu) \bar{m}^\mu l^\nu\right], \\
\gamma &\equiv -\frac{1}{2}\left[\gamma_{122} - \gamma_{342}\right] = -\frac{1}{2}\left[(\nabla_\nu l_\mu) n^\mu n^\nu - (\nabla_\nu m_\mu) \bar{m}^\mu n^\nu\right], \\
\alpha &\equiv -\frac{1}{2}\left[\gamma_{124} - \gamma_{344}\right] = -\frac{1}{2}\left[(\nabla_\nu l_\mu) n^\mu \bar{m}^\nu - (\nabla_\nu m_\mu) \bar{m}^\mu \bar{m}^\nu\right], \\
\beta &\equiv -\frac{1}{2}\left[\gamma_{123} - \gamma_{343}\right] = -\frac{1}{2}\left[(\nabla_\nu l_\mu) n^\mu m^\nu - (\nabla_\nu m_\mu) \bar{m}^\mu m^\nu\right].
\end{aligned}
\tag{3.3.15}
$$

Note that for clarity, I suppress the parenthesis () notation indicating the tetrad basis, and will remain suppressed in the following.

3.3.1 Representation of the Weyl, the Ricci, and the Riemann tensors

In a hypersurface, the Weyl tensor $C_{\mu\nu\rho\sigma}$ is defined as

$$
\begin{aligned}
C_{\mu\nu\rho\sigma} = R_{\mu\nu\rho\sigma} - \frac{1}{2}\left(g_{\mu\rho}R_{\nu\sigma} - g_{\mu\sigma}R_{\nu\rho} - g_{\nu\rho}R_{\mu\sigma} - g_{\nu\sigma}R_{\mu\rho}\right) \\
+\frac{1}{6}R\left(g_{\mu\rho}g_{\nu\sigma} - g_{\mu\sigma}g_{\nu\rho}\right).
\end{aligned}
\tag{3.3.16}
$$

The Weyl tensors carry only the trace-free part of the Riemann tensors, due to the the contraction of any pair of indices being zero $C^\mu{}_{\nu\mu\rho} = 0$. Moreover, they have the same symmetric and antisymmetric properties as the Riemann tensor,

$$C_{\mu\nu\rho\sigma} = C_{\rho\sigma\mu\nu} = -C_{\nu\mu\rho\sigma}. \tag{3.3.17}$$

Furthermore, Weyl tensors have the property of being invariant under conformal transformations [19], and thus, they determine the causal structure of the manifold.

Knowing that the Riemann tensors are related to those of Weyl and Ricci via Eq. (3.3.16), one can obtain

$$\begin{aligned}
R_{1313} &= C_{1313}, \qquad R_{1234} = C_{1234}, \qquad R_{2323} = C_{2323},\\
R_{1212} &= C_{1212} + R_{12} - \frac{1}{6}R, \qquad R_{1314} = \frac{1}{2}R_{11},\\
R_{1324} &= C_{1324} + \frac{1}{12}R, \qquad R_{2324} = \frac{1}{2}R_{22},\\
R_{3434} &= C_{3434} - R_{34} - \frac{1}{6}R, \qquad R_{3132} = -\frac{1}{2}R_{33},\\
R_{1213} &= C_{1213} + \frac{1}{2}R_{13}, \qquad R_{1334} = C_{1334} + \frac{1}{2}R_{13},\\
R_{1223} &= C_{1223} - \frac{1}{2}R_{23}, \qquad R_{2334} = C_{2334} + \frac{1}{2}R_{23},
\end{aligned} \tag{3.3.18}$$

and the additional complex-conjugate relations via the exchange of indices 3 and 4.

In the NP formalism, one can compute the Weyl tensors via Eq. (3.3.16) using the NP metric from Eq. (3.3.11). Nevertheless, it is easy to see from Eqs. (3.3.18) that only ten of the Weyl tensors are independent. They are represented by five complex scalars known as the *Weyl scalars* in the following way

$$\begin{aligned}
\Psi_0 &\equiv C_{1313} = C_{\mu\nu\rho\sigma} l^\mu m^\nu l^\rho m^\sigma,\\
\Psi_1 &\equiv C_{1213} = C_{\mu\nu\rho\sigma} l^\mu n^\nu l^\rho m^\sigma,\\
\Psi_2 &\equiv C_{1342} = C_{\mu\nu\rho\sigma} l^\mu m^\nu \bar{m}^\rho n^\sigma,\\
\Psi_3 &\equiv C_{1242} = C_{\mu\nu\rho\sigma} l^\mu n^\nu \bar{m}^\rho n^\sigma,\\
\Psi_4 &\equiv C_{2424} = C_{\mu\nu\rho\sigma} n^\mu \bar{m}^\nu n^\rho \bar{m}^\sigma.
\end{aligned} \tag{3.3.19}$$

The remaining five tensors can be derived via a linear combination of tensors $Q_{\mu\nu\rho\sigma} z^\mu_{(a)} z^\nu_{(b)} z^\rho_{(c)} z^\sigma_{(d)}$, that will survive or vanish under contractions of the vectors $z^\mu_{(a)}$. The vectors here, are NP vectors (e.g. l^μ), and the coefficients $Q_{\mu\nu\rho\sigma}$ represent the Weyl tensors [20]. Finally, one can write

$$\begin{aligned}
C_{1334} &= -\Psi_1, \qquad C_{1212} = C_{3434} = \left(\Psi_2 + \Psi_2^*\right),\\
C_{2443} &= -\Psi_3, \qquad C_{1234} = -\left(\Psi_2 - \Psi_2^*\right).
\end{aligned} \tag{3.3.20}$$

An interesting property on the Weyl scalars is that [180]:

---

[19] A conformal transformation has the form $g_{\mu\nu}(x) \rightarrow g'_{\mu\nu}(x) = e^{2\phi(x)} g_{\mu\nu}(x)$, with $\phi(x)$ an arbitrary function.

[20] See Chandrasekhar's book [157], Eqs. (295-299) for a detailed computation.

- Ψ_0 is the ingoing transversal gravitational radiation and asymptotically behaves as $\Psi_0 \sim 1/r^5$
- Ψ_1 is the ingoing longitudinal gravitational radiation and asymptotically behaves as $\Psi_1 \sim 1/r^4$
- Ψ_2 is the Coulomb term, representing the monopole of the source and asymptotically behaves as $\Psi_2 \sim 1/r^3$
- Ψ_3 is the outgoing longitudinal gravitational radiation and asymptotically behaves as $\Psi_3 \sim 1/r^2$
- Ψ_4 is the outgoing transversal gravitational radiation and asymptotically behaves as $\Psi_4 \sim 1/r$

The ten components of the Ricci tensor are defined in terms of seven scalars known as the *Ricci scalars*. Four of them are real $(\Phi_{00}, \Phi_{11}, \Phi_{22}, \Lambda)$, and three of them are complex $(\Phi_{01}, \Phi_{02}, \Phi_{12})$ with their respectively complex conjugate $(\Phi_{10}, \Phi_{20}, \Phi_{21})$,

$$\begin{aligned}
\Phi_{00} &\equiv \frac{1}{2}R_{11} = \frac{1}{2}R_{\mu\nu}l^\mu l^\nu, & \Phi_{11} &\equiv \frac{1}{4}(R_{12}+R_{34}) = \frac{1}{4}R_{\mu\nu}\left(l^\mu n^\nu + m^\mu \bar{m}^\nu\right), \\
\Phi_{22} &\equiv \frac{1}{2}R_{22} = \frac{1}{2}R_{\mu\nu}n^\mu n^\nu, & \Lambda &\equiv \frac{1}{12}(R_{12}-R_{34}) = \frac{1}{12}R_{\mu\nu}\left(l^\mu n^\nu - m^\mu \bar{m}^\nu\right), \\
\Phi_{02} &\equiv \frac{1}{2}R_{33} = \frac{1}{2}R_{\mu\nu}m^\mu m^\nu, & \Phi_{20} &\equiv \frac{1}{2}R_{44} = \frac{1}{2}R_{\mu\nu}\bar{m}^\mu \bar{m}^\nu, \\
\Phi_{01} &\equiv \frac{1}{2}R_{13} = \frac{1}{2}R_{\mu\nu}l^\mu m^\nu, & \Phi_{10} &\equiv \frac{1}{2}R_{14} = \frac{1}{2}R_{\mu\nu}l^\mu \bar{m}^\nu, \\
\Phi_{12} &\equiv \frac{1}{2}R_{23} = \frac{1}{2}R_{\mu\nu}n^\mu m^\nu, & \Phi_{21} &\equiv \frac{1}{2}R_{24} = \frac{1}{2}R_{\mu\nu}n^\mu \bar{m}^\nu.
\end{aligned} \tag{3.3.21}$$

With these expressions, one can find the Bianchi identities. To that end let us first consider the commutation relation given by the Lie brackets in Eq. (3.3.6). Then, by using the definition in Eq. (3.3.14), one can write [21]

$$\begin{aligned}
[e_2, e_1] = [\Delta, D] &= (\gamma_{c12} - \gamma_{c21})\, e^c \\
&= (\gamma_{112} - \gamma_{121})\, e^1 + (\gamma_{212} - \gamma_{221})\, e^2 + (\gamma_{312} - \gamma_{321})\, e^3 + (\gamma_{412} - \gamma_{421})\, e^4 \\
&= \gamma_{121}\Delta - \gamma_{212}D + (\gamma_{312} - \gamma_{321})\, \bar{\delta} + (\gamma_{412} - \gamma_{421})\, \delta.
\end{aligned} \tag{3.3.22}$$

Considering the other commutators and expressing them in terms of Eqs. (3.3.15), one can write them in the following way

$$\Delta D - D\Delta = -\left(\gamma + \bar{\gamma}\right) D - \left(\epsilon + \bar{\epsilon}\right) \Delta + \left(\bar{\tau} + \pi\right) \delta + \left(\tau + \bar{\pi}\right) \bar{\delta}, \tag{3.3.23a}$$

$$\delta D - D\delta = -\left(\bar{\alpha} + \beta - \bar{\pi}\right) D - \kappa\Delta + \left(\bar{\varrho} + \epsilon - \bar{\epsilon}\right) \delta + \sigma\bar{\delta}, \tag{3.3.23b}$$

---

[21] Keep in mind that $e_1 = -e^2 = D, e_2 = -e^1 = \Delta, e_3 = e^4 = \delta, e_4 = e^3 = \bar{\delta}$.

$$\delta\mathit{\Delta} - \mathit{\Delta}\delta = -\left(\tau - \bar{\alpha} - \beta\right)\mathit{\Delta} + \bar{\nu}D - \left(\mu - \gamma + \bar{\gamma}\right)\delta - \bar{\lambda}\bar{\delta}, \tag{3.3.23c}$$

$$\bar{\delta}\delta - \delta\bar{\delta} = -\left(\bar{\mu} - \mu\right)D - \left(\bar{\varrho} - \varrho\right)\mathit{\Delta} - \left(\alpha - \bar{\beta}\right)\delta + \left(\beta - \bar{\alpha}\right)\bar{\delta}. \tag{3.3.23d}$$

If one compares now with Eq. (3.3.6), it is easy to see that the structure constants can be written in terms of the spin coefficients, such that

$$\begin{aligned}
&C^1_{21} = -\left(\gamma + \bar{\gamma}\right), \quad C^1_{31} = \bar{\pi} - \bar{\alpha} - \beta, \quad C^1_{32} = \bar{\nu}, \quad C^1_{43} = \mu - \bar{\mu}\\
&C^2_{21} = -\left(\epsilon + \bar{\epsilon}\right), \quad C^2_{31} = -\kappa, \quad C^2_{32} = \bar{\alpha} + \beta - \tau, \quad C^2_{43} = \varrho - \bar{\varrho}\\
&C^3_{21} = \left(\bar{\tau} + \pi\right), \quad C^3_{31} = \epsilon + \bar{\varrho} - \bar{\epsilon}, \quad C^3_{32} = \gamma - \bar{\gamma} - \mu, \quad C^3_{43} = \bar{\beta} - \alpha,\\
&C^4_{21} = \left(\tau + \bar{\pi}\right), \quad C^4_{31} = \sigma, \quad C^4_{32} = -\bar{\lambda}, \quad C^4_{43} = \bar{\alpha} - \beta.
\end{aligned} \tag{3.3.24}$$

Keeping in mind that the Riemann tensors have the form of Eq. (3.3.7), one can express them in terms of the Weyl scalars, Ricci scalars and the spin coefficients in the following way

$$R_{1313}: \; D\sigma - \delta\kappa = \sigma\left(3\epsilon - \bar{\epsilon} + \varrho + \bar{\varrho}\right) + \kappa\left(\bar{\pi} - \tau - 3\beta - \bar{\alpha}\right) + \Psi_0 \tag{3.3.25a}$$

$$R_{1314}: \; D\varrho - \bar{\delta}\kappa = \left(\varrho^2 + \sigma\bar{\sigma}\right) + \varrho\left(\epsilon + \bar{\epsilon}\right) - \bar{\kappa}\tau - \kappa\left(3\alpha + \bar{\beta} - \pi\right) + \Phi_{00} \tag{3.3.25b}$$

$$R_{1312}: \; D\tau - \mathit{\Delta}\kappa = \varrho\left(\tau + \bar{\pi}\right) + \sigma\left(\bar{\tau} + \pi\right) + \tau\left(\epsilon + \bar{\epsilon}\right) - \kappa\left(3\gamma + \bar{\gamma}\right) + \Psi_1 + \Phi_{00} \tag{3.3.25c}$$

$$\vdots$$

I write here only the first three components as an example, but the expression for all 18 tensors can be found in the Appendix A.2, and the remaining 18 tensors are complex conjugates of those.

If one considers the Bianchi identities defined in Eq. (3.3.8) and the relation of Riemann tensors with Weyl tensors as in Eq. (3.3.18), one can write the identity

$$\begin{aligned}
\nabla_{[4}R_{13]13} &= \nabla_4 R_{1313} + \nabla_1 R_{1334} + \nabla_3 R_{1341} = 0\\
&= \nabla_4 C_{1313} + \nabla_1\left(C_{1313} + \frac{1}{2}R_{12}\right) - \frac{1}{2}\nabla_3 R_{11},
\end{aligned} \tag{3.3.26}$$

where the first term takes the form

$$\begin{aligned}
\nabla_4 C_{1313} &= \partial_4 C_{1313} - g^{pq}\left[\gamma_{p14}C_{q313} + \gamma_{p34}C_{1q13} + \gamma_{p14}C_{13q3} + \gamma_{p34}C_{131q}\right]\\
&= \partial_4 C_{1313} - 2\left(\gamma_{214} + \gamma_{344}\right)C_{1313} + 2\gamma_{314}\left(C_{1213} + C_{4313}\right)\\
&= \bar{\delta}\Psi_0 - 4\alpha\Psi_0 + 4\varrho\Psi_1.
\end{aligned} \tag{3.3.27}$$

The second term is

$$\begin{aligned}
\nabla_1 C_{1334} &= \partial_1 C_{1334} - g^{pq}\left[\gamma_{p11}C_{q334} + \gamma_{p31}C_{1q34} + \gamma_{p11}C_{13q4} + \gamma_{p31}R_{133q}\right]\\
&= \partial_1 C_{1334} - \left[\left(\gamma_{211} + \gamma_{341}\right)C_{1334} + \gamma_{131}\left(C_{1234} - C_{3434}\right)\right.\\
&\quad \left. + \gamma_{231}C_{1314} + \gamma_{141}C_{1332} + \gamma_{131}C_{1324} + \gamma_{241}C_{1331}\right]\\
&= -D\Psi_1 + 2\epsilon\Psi_1 - 3\kappa\Psi_2 + \pi\Psi_0,
\end{aligned} \tag{3.3.28}$$

and the last two Ricci terms are

$$\begin{aligned}\frac{1}{2}\left(\nabla_1 R_{12} - \nabla_3 R_{11}\right) =& D\Phi_{01} - \delta\Phi_{00} - 2\left(\epsilon + \bar{\varrho}\right)\Phi_{01} - 2\sigma\Phi_{10} \\ &+ 2\kappa\Phi_{11} + \bar{\kappa}\Phi_{02} - \left(\bar{\pi} - 2\bar{\alpha} - 2\beta\right)\Phi_{00}.\end{aligned} \tag{3.3.29}$$

All together reads

$$\begin{aligned}\nabla_{[4}R_{13]13} : \left(\bar{\delta} - 4\alpha + \pi\right)\Psi_0 + \left(4\varrho - D + 2\epsilon\right)\Psi_1 - 3\kappa_2^{\Psi} = -2\kappa\Phi_{11} \\ -\bar{\kappa}\Phi_{02} + \left(\bar{\pi} - 2\bar{\alpha} - 2\beta\right)\Phi_{00}.\end{aligned} \tag{3.3.30}$$

Following the same steps one can find the remaining seven Bianchi identities, which can be found in Appendix A.3. However, because we will need it later, I will also write $\nabla_{[2}R_{13]13}$

$$\begin{aligned}\nabla_{[2}R_{13]13} :& \mathit{\Delta}\Psi_0 - \delta\Psi_1 - (4\gamma - \mu)\Psi_0 + 2(2\tau + \beta)\Psi_1 - 3\sigma\Psi_2 = -D\Phi_{20} + \delta\Phi_{01} \\ &+ 2(\bar{\pi} - \beta)\Phi_{01} - 2\kappa\Phi_{12} - \bar{\lambda}\Phi_{00} + 2\sigma\Phi_{11} + (\bar{\varrho} + 2\epsilon - 2\bar{\epsilon})\Phi_{02}.\end{aligned} \tag{3.3.31}$$

Keep in mind that Einstein's field equations are expressed in terms of the Ricci tensors and scalars via,

$$R_{ab} - \frac{1}{2}g_{ab}R = \frac{8\pi G}{c^4}T_{ab} \longrightarrow R_{ab} = \frac{8\pi G}{c^4}\left(T_{ab} - \frac{1}{2}g_{ab}T\right). \tag{3.3.32}$$

Then, in vacuum, the right-hand side of Eqs.(3.3.30) and (3.3.31) will cancel. Nevertheless, in general, one should include them in terms of the energy-momentum components, since

$$R_{ab}z^a z^b = \frac{8\pi G}{c^4}\bar{T}_{ab}z^a z^b, \tag{3.3.33}$$

where $\bar{T}_{ab} = \left(T_{ab} - \frac{1}{2}g_{ab}T\right)$ is the traceless energy-momentum tensor.

3.3.2 Tetrad transformations

To complete the tetrad formalism let me introduce Lorentz transformations to the null tetrad basis vectors, which can be separated into three classes of transformations:

1. Class I: leave the vector **l** unchanged,

2. Class II: leave the vector **n** unchanged,

3. Class III: leave directions **l**, **n** unchanged, but rotate an angle θ in the **m**-**m*** plane.

Thus, each class of transformation can be written as

$$\begin{aligned}
\mathbf{I}: \mathbf{l} \to \mathbf{l},\ \mathbf{m} \to \mathbf{m} + a\mathbf{l},\ \mathbf{m}^* \to \mathbf{m}^* + a^*\mathbf{l},\ \mathbf{n} \to \mathbf{n} + a^*\mathbf{m} + a\mathbf{m}^* + aa^*\mathbf{l}; \qquad (3.3.34)\\
\mathbf{II}: \mathbf{n} \to \mathbf{n},\ \mathbf{m} \to \mathbf{m} + b\mathbf{n},\ \mathbf{m}^* \to \mathbf{m}^* + b^*\mathbf{n},\ \mathbf{l} \to \mathbf{l} + b^*\mathbf{m} + b\mathbf{m}^* + bb^*\mathbf{n}; \qquad (3.3.35)\\
\mathbf{III}: \mathbf{l} \to A^{-1}\mathbf{l},\ \mathbf{n} \to A\mathbf{n},\ \mathbf{m} \to e^{i\theta}\mathbf{m},\ \mathbf{m}^* \to e^{-i\theta}\mathbf{m}^*. \qquad (3.3.36)
\end{aligned}$$

where a and b are complex functions and A and θ are real functions.

For the class I, the corresponding Weyl scalars transform as

$$\begin{aligned}
&\Psi_0 \to \Psi_0,\ \Psi_1 \to \Psi_1 + a^*\Psi_0,\ \Psi_2 \to \Psi_2 + 2a^*\Psi_1 + (a^*)^2\Psi_0,\\
&\Psi_3 \to \Psi_3 + 3a^*\Psi_2 + 3(a^*)^2\Psi_1 + (a^*)^3\Psi_0,\\
&\Psi_4 \to \Psi_4 + 4a^*\Psi_3 + 6(a^*)^2\Psi_2 + 4(a^*)^3\Psi_1 + (a^*)^4\Psi_0.
\end{aligned} \qquad (3.3.37)$$

For the class II, the transformation of the Weyl scalars are

$$\begin{aligned}
&\Psi_4 \to \Psi_4,\ \Psi_3 \to \Psi_3 + b\Psi_4,\ \Psi_2 \to \Psi_2 + 2b\Psi_3 + b^2\Psi_4,\\
&\Psi_1 \to \Psi_1 + 3b\Psi_2 + 3b^2\Psi_3 + b^3\Psi_4,\\
&\Psi_0 \to \Psi_0 + 4b\Psi_1 + 6b^2\Psi_2 + 4b^3\Psi_3 + b^4\Psi_4.
\end{aligned} \qquad (3.3.38)$$

And finally, for the class III transformations, the Weyl scalars take the form

$$\begin{aligned}
&\Psi_0 \to A^{-2}e^{2i\theta}\Psi_0,\ \Psi_1 \to A^{-1}e^{i\theta}\Psi_1,\ \Psi_2 \to \Psi_2,\\
&\Psi_3 \to A^{1}e^{-i\theta}\Psi_3,\ \Psi_4 \to A^{2}e^{-2i\theta}\Psi_4.
\end{aligned} \qquad (3.3.39)$$

Consequently, one can also find the spin coefficients for all classes.

When looking at the above Weyl scalars in Eqs. (3.3.37) to (3.3.39), one notes that depending on the Lorentzian transformation, the scalars undergo a characteristic change. Then, it is possible to choose a frame in which some scalars vanish. This leads to a classification known as the *Petrov classification* and is defined as:

i. Petrov type I : $\Psi_0 = 0$,

ii. Petrov type II : $\Psi_0 = \Psi_1 = 0$,

iii. Petrov type III : $\Psi_0 = \Psi_1 = \Psi_2 = 0$,

iv. Petrov type D : $\Psi_0 = \Psi_1 = \Psi_3 = \Psi_4 = 0$,

v. Petrov type N : $\Psi_0 = \Psi_1 = \Psi_2 = \Psi_3 = 0$,

vi. Petrov type O : $\Psi_0 = \Psi_1 = \Psi_2 = \Psi_3 = \Psi_4 = 0$.

From this classification, the *Goldberg-Sachs theorem* [181] emerged, which states that in vacuum:

1. if the Riemann tensor is of type II and $\Psi_0 = \Psi_1 = 0$, then $\kappa = \sigma = 0$, and conversely if $\kappa = \sigma = 0$ then $\Psi_0 = \Psi_1 = 0$, and hence the tensor is of type II;
2. if the Riemann tensor is of type D and $\Psi_0 = \Psi_1 = \Psi_3 = \Psi_4 = 0$, then $\kappa = \sigma = \nu = \lambda = 0$, and conversely.

In the NP formalism, all the GR black hole solutions are Riemann tensors of type *D*, which allows for a simple description, as we shall see.

3.4 Perturbation of Kerr BH

A Minkowsky metric in the NP formalism takes the form of Eq. (3.3.13), while the Kerr metric in Boyer-Lindquist coordinates can be written as

$$\begin{aligned} l^\mu &= \frac{1}{\Delta}\left(r^2+a^2, \Delta, 0, a\right), \\ n^\mu &= \frac{1}{2\rho^2}\left(r^2+a^2, -\Delta, 0, a\right), \\ m^\mu &= \frac{1}{\sqrt{2}}\frac{1}{r+ia\cos\theta}\left(ia\sin\theta, 0, 1, \frac{i}{\sin\theta}\right), \end{aligned} \tag{3.4.1}$$

where, a, Δ and ρ are defined in Eq. (3.1.6), and $\bar{m}^\mu$ is the complex conjugate of m^μ. This vector field is known as the *Kinnersley tetrad* and completely determines the metric of black holes. The covariant derivatives are

$$\begin{aligned} D &= \frac{1}{\Delta}\left[(r^2+a^2)\partial_t + \Delta\partial_r + a\partial_\phi\right], \\ \Delta &= \frac{1}{2\rho^2}\left[(r^2+a^2)\partial_t - \Delta\partial_r + a\partial_\phi\right], \\ \delta &= \frac{1}{\sqrt{2}}\frac{1}{r+ia\cos\theta}\left[(ia\sin\theta)\partial_t + \partial_\theta + \frac{i}{\sin\theta}\partial_\phi\right]. \end{aligned} \tag{3.4.2}$$

The covariant form of the *Kinnersley tetrad* is

$$\begin{aligned} l_\mu &= \frac{1}{\Delta}\left(-\Delta, r^2+a^2\cos^2\theta, 0, a\Delta\sin^2\theta\right), \\ n_\mu &= \frac{1}{2\rho^2}\left(-\Delta, -r^2-a^2\cos^2\theta, 0, a\Delta\sin^2\theta\right), \\ m_\mu &= \frac{1}{\sqrt{2}}\frac{1}{r+ia\cos\theta}\left(-ia\sin\theta, 0, r^2+a^2\cos^2\theta, i(r^2+a^2)\sin\theta\right). \end{aligned} \tag{3.4.3}$$

The non-vanishing spin coefficients for this null tetrad depending on the γ-symbols are given by

$$\begin{aligned}
\gamma_{122} &= \frac{1}{(r^2+a^2\cos^2\theta)^2}\left[(r-M)(r^2+a^2\cos^2\theta)-r\Delta\right], & \gamma_{134} &= \frac{2ia\cos\theta}{r^2+a^2\cos^2\theta},\\
\gamma_{132} &= -\sqrt{2}\frac{ia\sin\theta}{(r^2+a^2\cos^2\theta)(r+ia\cos\theta)}, & \gamma_{324} &= \frac{ia\Delta\cos\theta}{(r^2+a^2\cos^2\theta)^2},\\
\gamma_{213} &= \sqrt{2}\frac{a^2\sin\theta\cos\theta}{(r^2+a^2\cos^2\theta)(r+ia\cos\theta)}, & \gamma_{334} &= -\frac{(ia+r\cos\theta)}{\sqrt{2}(r+ia\cos\theta)^2\sin\theta},\\
\gamma_{243} &= \frac{\Delta}{2(r^2+a^2\cos^2\theta)(r+ia\cos\theta)}, & \gamma_{341} &= \frac{1}{r+ia\cos\theta},
\end{aligned} \tag{3.4.4}$$

and thus,

$$\begin{aligned}
&\kappa=\sigma=\lambda=\nu=\epsilon=0, && \pi=-\frac{ia\sin\theta}{\sqrt{2}(r-ia\cos\theta)^2},\\
&\varrho=\frac{1}{r-ia\cos\theta}, && \tau=\frac{ia\sin\theta}{\sqrt{2}(r^2+a^2\cos^2\theta)},\\
&\beta=\frac{\cot\theta}{2\sqrt{2}(r+ia\cos\theta)}, && \mu=-\frac{\Delta}{2(r^2+a^2\cos^2\theta)^2(r-ia\cos\theta)},\\
&\alpha=\bar{\beta}-\pi, && \gamma=-\mu+\frac{r-M}{2(r^2+a^2\cos^2\theta)}.
\end{aligned} \tag{3.4.5}$$

Because of the previously mentioned Goldberg-Sachs theorem, the fact that κ, σ, λ and ν vanish, means that Ψ_0, Ψ_1, Ψ_3 and Ψ_4 vanish as well. I will not demonstrate it here [22], but when developing Eq. (3.3.19) using the spin coefficients, it is straightforward to see that the Goldberg-Sachs conditions are satisfied. Moreover, one can also find that

$$\Psi_2 = \frac{M}{(r-ia\cos\theta)^3} = M\varrho^3. \tag{3.4.6}$$

3.4.1 Teukolsky master equation

With all the definitions in place, let us start introducing a perturbation to a Kerr BH in the NP formalism, as implemented in 1973 by Saul Teukolsky [160]. This is done through a decomposition of the tetrads such that

$$\mathbf{l}=\mathbf{l}^A+\mathbf{l}^B, \qquad \mathbf{n}=\mathbf{n}^A+\mathbf{n}^B, \qquad \mathbf{m}=\mathbf{m}^A+\mathbf{m}^B, \tag{3.4.7}$$

where A is the unperturbed metric and B is the perturbation at first order (linear order). In the same way, all the other NP quantities also decompose into a background metric and the perturbed metric

$$\Psi_2=\Psi_2^A+\Psi_2^B, \qquad D=D^A+D^B, \qquad \text{etc.} \tag{3.4.8}$$

---

[22] One can find the derivation in [157], Sec.56

For the case of the Schwarzschild metric, it was shown in the previous section that the wave equation can be decoupled into a radial and an angular part. Since in the NP formalism, the Schwarzschild and the Kerr metric are very similar, then the Kerr wave equation should also allow for a two-functions decoupling [160]. The gravitational quantities of interest are the ingoing and the outgoing radiation Ψ_0, Ψ_4, respectively.

Let us decompose the Bianchi identities defined in Eqs. (3.3.30), (3.3.31) and the Riemann tensor defined in Eq. (3.3.25a) into the background metric A and the perturbation B,

$$\begin{aligned}
\left(\bar{\delta} - 4\alpha + \pi\right)^A \Psi_0^B + (4\varrho - D + 2\epsilon)^A \Psi_1^B - 3\kappa^B \Psi_2^A &= 4\pi \Big[(\delta + \bar{\pi} - 2\bar{\alpha} - 2\beta)^A T_{ll}^B \\
&\quad + (2\bar{\varrho} + 2\epsilon - D)^A T_{lm}^B\Big] \qquad (3.4.9)\\
(\mathit{\Delta} - 4\gamma + \mu)^A \Psi_0^B - (\delta - 4\tau - 2\beta)^A \Psi_1^B - 3\sigma^B \Psi_2^A &= 4\pi \Big[(\delta + 2\bar{\pi} - 2\beta)^A T_{lm}^B \\
&\quad - (D - \bar{\varrho} - 2\epsilon + 2\bar{\epsilon})^A T_{mm}^B\Big] \qquad (3.4.10)\\
(D - 3\epsilon + \bar{\epsilon} - \varrho - \bar{\varrho})^A \sigma^B - (\bar{\pi} - \tau - 3\beta - \bar{\alpha} + \delta)^A \kappa^B - \Psi_0^B &= 0, \qquad (3.4.11)
\end{aligned}$$

where I use that $\kappa^A, \sigma^A, \Psi_0^A, \Psi_1^A$ vanish for a Kerr metric and that the Ricci scalars Φ^A vanish for vacuum, but keeping the source term tensor for the perturbation Φ^B. In the following, I suppress the background metric index A for clarity. As a result of vanishing terms in other Bianchi identities, the background Ψ_2 satisfies

$$D\Psi_2 = 3\varrho\Psi_2, \qquad \delta\Psi_2 = 3\tau\Psi_2. \tag{3.4.12}$$

If these relations are introduced in Eq. (3.4.11), one finds

$$(D - 3\epsilon + \bar{\epsilon} - 4\varrho - \bar{\varrho})^A \Psi_2 \sigma^B - (\delta + \bar{\pi} - 4\tau - 3\beta - \bar{\alpha}) \Psi_2 \kappa^B - \Psi_0^B \Psi_2 = 0. \tag{3.4.13}$$

Now, the key point to derive the Teukolsky master equation is to eliminate Ψ_1 from previous Bianchi identities in Eqs. (3.4.9) and (3.4.10). It can be achieved by using the following commutation

$$\begin{aligned}
&[D - (p+1)\epsilon + q\varrho + \bar{\epsilon} - \bar{\varrho}] (\delta - p\beta + q\tau) \\
&- [\delta - (p+1)\beta + q\tau - \bar{\alpha} + \bar{\pi}] (D - p\epsilon + q\varrho) = 0,
\end{aligned} \tag{3.4.14}$$

with p and q arbitrary constants. This commutation does not affect other relations of the Type D metric [160]. The following step is to multiply $(D - 3\epsilon - 4\varrho + \bar{\epsilon} - \bar{\varrho})$ to Eq. (3.4.10) and $(\delta - 4\tau - 3\beta - \bar{\alpha} + \bar{\pi})$ to Eq. (3.4.9), and subtract them.

$$\begin{aligned}
&\left(\bar{\delta} - 4\alpha + \pi\right)(\delta - 4\tau - 3\beta - \bar{\alpha} + \bar{\pi})\,\Psi_0^B - 3\,(\delta - 4\tau - 3\beta - \bar{\alpha} + \bar{\pi})\,\kappa^B\Psi_2 \\
&\qquad - (D - 2\epsilon - 4\varrho)\,(\delta - 4\tau - 3\beta - \bar{\alpha} + \bar{\pi})\,\Psi_1^B = \mathbf{T}_1
\end{aligned}$$

$$-$$

$$\begin{aligned}
&(\Delta - 4\gamma + \mu)\,(D - 3\epsilon - 4\varrho + \bar{\epsilon} - \bar{\varrho})\,\Psi_0^B - (D - 3\epsilon - 4\varrho + \bar{\epsilon} - \bar{\varrho})\,3\sigma^B\Psi_2 \\
&\qquad -(\delta - 4\tau - 2\beta)\,(D - 3\epsilon - 4\varrho + \bar{\epsilon} - \bar{\varrho})\,\Psi_1^B = \mathbf{T}_2
\end{aligned}$$

$$\begin{aligned}
&\left(\bar{\delta} - 4\alpha + \pi\right)(\delta - 4\tau - 3\beta - \bar{\alpha} + \bar{\pi})\,\Psi_0^B - (\Delta - 4\gamma + \mu)\,(D - 3\epsilon - 4\varrho + \bar{\epsilon} - \bar{\varrho})\,\Psi_0^B \\
&\qquad +3\,(D - 3\epsilon - 4\varrho + \bar{\epsilon} - \bar{\varrho})\,\sigma^B\Psi_2 - 3\,(\delta - 4\tau - 3\beta - \bar{\alpha} + \bar{\pi})\,\kappa^B\Psi_2 = \mathbf{T}_1 - \mathbf{T}_2,
\end{aligned} \tag{3.4.15}$$

where $\mathbf{T}_i$ is just a constant representing the right-hand side of Eqs. (3.4.9) and (3.4.10), which depend on the source tensors (or Ricci tensors). Indeed, the Ψ_1 component vanishes via the commutation relation from Eq. (3.4.14) when $p = 2$ and $q = -4$. Furthermore, the residuals depend on Ψ_2,and are solutions of Eq. (3.4.13), thus, they can be replaced by $\Psi_0\Psi_2$, leading to

$$\begin{aligned}
&\Big[\left(\bar{\delta} - 4\alpha + \pi\right)\,(\delta - 4\tau - 3\beta - \bar{\alpha} + \bar{\pi}) \\
&\qquad - (\Delta - 4\gamma + \mu)\,(D - 3\epsilon - 4\varrho + \bar{\epsilon} - \bar{\varrho}) + 3\Psi_2\Big]\,\Psi_0^B = 4\pi\mathbf{T}_0,
\end{aligned} \tag{3.4.16}$$

where

$$\begin{aligned}
\mathbf{T}_0 = {}&(\delta + \bar{\pi} - 2\bar{\alpha} - 2\beta)\,T_{ll}^B - (\delta - 4\tau - 3\beta - \bar{\alpha} + \bar{\pi})\,(2\bar{\varrho} + 2\epsilon - D)\,T_{lm}^B \\
&+ (D - \bar{\varrho} - 2\epsilon + 2\bar{\epsilon})\,T_{mm}^B - (D - 3\epsilon - 4\varrho + \bar{\epsilon} - \bar{\varrho})\,(\delta + 2\bar{\pi} - 2\beta)\,T_{lm}^B.
\end{aligned} \tag{3.4.17}$$

This set of equations is the decoupled equation for Ψ_0. Note that the derivatives of $\mathbf{l}$ and $\mathbf{n}$ (i.e. D, Δ) acting on Ψ_0, do not mix with the derivatives of $\mathbf{m}$ and $\mathbf{m}^*$ (i.e. $\delta, \bar{\delta}$), enabling the decoupling. Moreover, given that the choice of $\mathbf{l}$ and $\mathbf{n}$ are invariant in the NP formalism, it is possible to obtain the decoupled equation for the outgoing radiation Ψ_4 by exchanging $\mathbf{l} \leftrightarrow \mathbf{n}$ and $\mathbf{m} \leftrightarrow \mathbf{m}^*$. Hence,

$$\begin{aligned}
&\Big[(\delta - \tau + 4\beta)\left(\bar{\delta} - \bar{\tau} + \bar{\beta} + 3\alpha + 4\pi\right) \\
&\qquad - (D + 4\epsilon - \varrho)\,(\Delta - 3\gamma - 4\mu + \bar{\gamma} - \bar{\mu}) + 3\Psi_2\Big]\,\Psi_4^B = 4\pi\mathbf{T}_4,
\end{aligned} \tag{3.4.18}$$

with

$$\begin{aligned}
\mathbf{T}_4 = {}&\left(\bar{\delta} - \bar{\tau} + 2\alpha + 2\bar{\beta}\right)T_{nn}^B - \left(\bar{\delta} + 4\pi + 3\alpha - \bar{\tau} + \bar{\beta}\right)(\Delta + 2\bar{\mu} + 2\gamma)\,T_{nm^*}^B \\
&+ (\Delta + \bar{\mu} + 2\gamma - 2\bar{\gamma})\,T_{m^*m^*}^B - (\Delta + 3\gamma + 4\mu - \bar{\gamma} + \bar{\mu})\,(\delta - 2\bar{\tau} + 2\alpha)\,T_{nm^*}^B.
\end{aligned} \tag{3.4.19}$$

Consequently, the Teukolsky master equation takes the form

$$\begin{aligned}\left[\frac{(r^2+a^2)^2}{\Delta}-a^2\sin^2\theta\right]\frac{\partial\Psi^2}{\partial_t^2}+\frac{4Mar}{\Delta}\frac{\partial\Psi^2}{\partial_t\partial_\phi}+\left[\frac{a^2}{\Delta}-\frac{1}{\sin^2\theta}\right]\frac{\partial\Psi^2}{\partial_\phi^2}\\ -\Delta^{-s}\frac{\partial}{\partial_r}\left(\Delta^{s+1}\right)\frac{\partial\Psi}{\partial_r}-\frac{1}{\sin\theta}\frac{\partial}{\partial_\theta}\left(\sin\theta\frac{\partial\Psi}{\partial_\theta}\right)-2s\left[\frac{a(r-M)}{\Delta}-\frac{i\cos\theta}{\sin^2\theta}\right]\frac{\partial\Psi}{\partial_\phi}\\ -2s\left[\frac{M(r^2-a^2)}{\Delta}-r-ia\cos\theta\right]\frac{\partial\Psi}{\partial_t}+\left(s^2\cot^2\theta-s\right)\Psi=4\pi\rho\mathbf{T},\end{aligned}\tag{3.4.20}$$

where s is the *spin weight* of the field, $\mathbf{T}$ is the source term associated to the field, and Ψ is the field quantity. For instance, in the case of outgoing gravitational radiation, the values are

$$s=-2,\quad \Psi=\rho^4\Psi_4\quad \text{and}\quad T=2\rho^4\mathbf{T}_4;\tag{3.4.21}$$

and for ingoing gravitational radiation

$$s=2,\quad \Psi=\Psi_0\quad \text{and}\quad T=2\mathbf{T}_0.\tag{3.4.22}$$

For other fields, such as scalar $s=0$, neutrino $s=\pm1/2$, or electromagnetic $s=\pm1$, I refer the reader to Teukolsky's paper [160].

Keeping in mind that the Weyl scalar depends on the Weyl tensor

$$\Psi_4=C_{2424}=C_{\mu\nu\rho\sigma}n^\mu\bar{m}^\nu n^\rho\bar{m}^\sigma,\tag{3.4.23}$$

and that the gravitational radiation depends on the Riemann tensor

$$R_{0\mu0\nu}=-\frac{1}{2}\ddot{h}^{TT}_{\mu\nu},\tag{3.4.24}$$

which, at the same time depends on the Weyl scalar (see Eqs. (3.3.18)), one can relate the Weyl scalar for outgoing radiation with the gravitational radiation strain in the following way,

$$\begin{aligned}\Psi_4&=R_{2424}=R_{0\mu0\nu}n^0\bar{m}^\mu n^0\bar{m}^\nu\\ &=-\frac{1}{4}\ddot{h}^{TT}_{\mu\nu}\bar{m}^\mu\bar{m}^\nu=-\frac{1}{8}\left(\ddot{h}^{TT}_{xx}-\ddot{h}^{TT}_{yy}-2i\ddot{h}^{TT}_{xy}\right)=-\frac{1}{4}\left(\ddot{h}^{TT}_{+}-i\ddot{h}^{TT}_{\times}\right),\end{aligned}\tag{3.4.25}$$

where I use the definition of Eq. (3.3.13).

To conclude the Teukolsky derivation, it is worth mentioning again, that the most important result from Teukolsky's work is that, a Kerr metric written in the NP formalism can be decomposed into its radial and angular components such that

$$\Psi(t,r,\theta,\phi) = e^{-i\omega t} e^{im\phi} R(r) S(\theta), \tag{3.4.26}$$

where $R(r)$ and $S(\theta)$ satisfy

$$\Delta^{-s} \frac{\partial}{\partial_r}\left(\Delta^{s+1}\right)\frac{\partial R}{\partial_r} + \left(\frac{K^2 - 2is(r-M)K}{\Delta} + 4is\omega r - \lambda\right) R = 0, \tag{3.4.27}$$

$$\begin{aligned}&\frac{1}{\sin\theta}\frac{\partial}{\partial_\theta}\left(\sin\theta\frac{\partial S}{\partial_\theta}\right)\\ &\quad+\left(a^2\omega^2\cos^2\theta - \frac{m^2}{\sin^2\theta} - 2a\omega s\cos\theta - \frac{2ms\cos\theta}{\sin^2\theta} - s^2\cot^2\theta + s + \mathcal{A}\right) S = 0,\end{aligned} \tag{3.4.28}$$

where, $K \equiv (r^2+a^2)\omega - am$, $\lambda \equiv \mathcal{A} + a^2\omega^2 - 2am\omega$ and $\mathcal{A}$ is the *separation constant*. For fixed values of $s, m, a\omega$ the eigenvalues are labeled by l. Consequently the eigenfunctions are labelled as $R = {}_sR_{lm}(r, a\omega)$ and $S = {}_sS_{lm}(\theta, a\omega)$, as well as $\mathcal{A} = {}_s\mathcal{A}_{lm}(a\omega)$.

3.4.2 Eigenfunctions

Radial equation

For the radial function, it is useful to make the following transformation

$$\mathcal{R}_{lm} = \Delta^{s/2}(r^2+a^2)^{1/2} R_{lm}, \qquad \frac{\mathrm{d}r_*}{\mathrm{d}r} = \frac{r^2+a^2}{\Delta}, \tag{3.4.29}$$

leading the radial equation to become

$$\partial^2_{r_*}\mathcal{R} + \left[K^2 - \frac{2is(r-M)K + \Delta(4is\omega r - \lambda)}{(r^2+a^2)^2} - G^2 - \partial_{r_*}G\right]\mathcal{R} = 0, \tag{3.4.30}$$

with $G = s(r-M)/(r^2+a^2) + r\Delta/(r^2+a^2)^2$. Then, when $r \to \infty$ ($r_* \to \infty$), it is possible to write the radial equation as

$$\partial^2_{r_*}\mathcal{R} + \left(\omega^2 + 2is\omega/r\right)\mathcal{R} \approx 0, \tag{3.4.31}$$

with asymptotic solutions $\mathcal{R} = r^{\pm s} e^{\mp i\omega r_*}$. The radial function for outgoing gravitational radiation, that is, spin $s = -2$, takes the form

$$\begin{aligned} R &\sim e^{-i\omega r_*}/r \qquad &\textbf{(outgoing waves)},\\ R &\sim r^3 e^{i\omega r_*} \qquad &\textbf{(ingoing waves)}.\end{aligned} \tag{3.4.32}$$

For the event horizon $r \to r_+$ ($r_* \to -\infty$), one can write

$$\partial^2_{r_*}\mathcal{R} + \left[k^2 - \frac{2is(r_+ - M)k}{2Mr_+} - \frac{s^2(r_+ - M)^2}{(2Mr_+)^2}\right]\mathcal{R} \approx 0, \tag{3.4.33}$$

with $k = \omega - ma/2Mr_+$ and where the asymptotic solution for the radial transformation $\mathcal{R} = \Delta^{\pm s/2}e^{\pm ikr_*}$ with spin $s = -2$ takes the form

$$\begin{aligned} &R \sim \Delta^2 e^{-ikr_*} && \textbf{(outgoing waves)},\\ &R \sim e^{ikr_*}, && \textbf{(ingoing waves)}. \end{aligned} \tag{3.4.34}$$

Combining both boundaries, one can write

$$R = \begin{cases} A_{in}e^{ikr_*} + A_{out}\Delta^2 e^{-ikr_*} & (r_* \to -\infty) \\ B_{in}r^3 e^{i\omega r_*} + B_{out}\frac{1}{r}e^{-i\omega r_*} & (r_* \to \infty). \end{cases} \tag{3.4.35}$$

Note that the ingoing or outgoing index depends on the natural description of the wave, not on the physical space of the BH. At the horizon, the outgoing waves refer to waves falling into the black hole. Thus, the boundary conditions are determined by $B_{in}r^3e^{i\omega r_*}$ at infinity ($r_* \to \infty$); and $A_{out}\Delta^2e^{-ikr_*}$ at the horizon ($r_* \to -\infty$). These two conditions will bind the system.

Angular equation

The angular equation can be written as an eigenvalue equation involving two operators, such that

$$(\mathfrak{h}_0 + \mathfrak{h}_1)\, S = -ES, \tag{3.4.36}$$

where

$$\begin{aligned} \mathfrak{h}_0 &= \frac{1}{\sin\theta}\partial_\theta\left(\frac{1}{\sin\theta}\partial_\theta\right) - \left(\frac{m^2 + s^2 + 2ms\cos\theta}{\sin^2\theta}\right), \\ \mathfrak{h}_1 &= a^2\omega^2\cos^2\theta - 2a\omega s\cos\theta. \end{aligned} \tag{3.4.37}$$

Note that the first operator depends on θ, m and s while the second operator depends on θ, a and ω. Therefore, one can in general write the part of the equation that does not depend on the rotation ($a\omega = 0$) in the following way

$$\mathfrak{h}_0 S = -ES, \tag{3.4.38}$$

that has known solutions, such that

$$\begin{aligned} S(\theta,\phi) =& {}_sY_{lm}(\theta,\phi), \qquad l = |s|, |s|+1, \dots, \\ E =& l(l+1) \qquad -l \leq m \leq l. \end{aligned} \tag{3.4.39}$$

The functions ${}_sY_{lm}(\theta,\phi)$ are a complete set of functions called *spin-weighted spherical harmonics*, and are defined as

$$\begin{aligned} {}_sY_{lm}(\theta,\phi) &= \sqrt{\frac{2l+1}{4\pi}}\, d^l_{m,s}(\theta) e^{im\phi} \\ d^l_{m,s} &= \sum_{k=k_1}^{k=k_2} \frac{(-1)^k}{k!} \frac{\sqrt{(l+m)!(l-m)!(l-s)!(l+s)!}}{(k-m-s)!(l+m-k)!(l-k+s)!} \cos\left(\frac{\theta}{2}\right)^{2l+m-2k+s} \sin\left(\frac{\theta}{2}\right)^{2k-m-s} \end{aligned} \tag{3.4.40}$$

with $k_1 = \max(0, m+s)$ and $k_2 = \min(l+m, l+s)$. The tensor spherical decomposition introduced in Sec. 3.2.1 can also be written in terms of these spin-weighted spherical harmonics when using the NP formalism, see for instance [155].

The addition of the operator $\mathfrak{h}_1$ can be understood as a perturbation in the form of a rotation, changing the spherical solution ($a\omega = 0$) to the spheroidal solution ($a\omega \neq 0$). Hence, in the perturbation approximation, the eigenvalue problem becomes

$$\begin{aligned} {}_sE_{lm}(a\omega) =& l(l+1) - \langle slm|\mathfrak{h}_1|slm\rangle + \dots, \\ {}_sS_{lm}(\theta,\phi,a\omega) =& {}_sY_{lm}(\theta,\phi) + \sum_{l'\neq l} \frac{\langle sl'm|\mathfrak{h}_1|slm\rangle}{l(l+1) - l'(l'+1)} {}_sY_{l'm}(\theta,\phi) + \dots, \end{aligned} \tag{3.4.41}$$

where

$$\langle sl'm|\mathfrak{h}_1|slm\rangle = \int d\Omega\, {}_sY_{l'm}(\theta,\phi)\, \mathfrak{h}_1\, {}_sY_{lm}(\theta,\phi). \tag{3.4.42}$$

For this operator, one could use the formulation [161]:

$$\begin{aligned} \langle sl'm|\cos^2\theta|slm\rangle =& \frac{1}{3}\delta_{ll'} + \frac{2}{3}\left(\frac{2l+1}{2l'+1}\right)^{1/2} \langle l2m0|l'm\rangle \langle l2-s0|l'-s\rangle , \\ \langle sl'm|\cos\theta|slm\rangle =& \left(\frac{2l+1}{2l'+1}\right)^{1/2} \langle l1m0|l'm\rangle \langle l1-s0|l'-s\rangle , \end{aligned} \tag{3.4.43}$$

where $\langle l_1 l_2 m_1 m_2 | LM\rangle$ are the Clebsh-Gordan coefficients. Thus, the eigenvalue for spin $s \neq 0$, can be written as

$$ {}_sE_{lm}(a\omega) = l(l+1) - 2a\omega \frac{s^2 m}{l(l+1)} + \mathcal{O}\left[(a\omega)^2\right] \qquad (s \neq 0). \tag{3.4.44}$$

For simplicity, the eigenfunctions can be written in the spherical harmonic representation, as

$$ {}_sS_{lm}(\theta,\phi,a\omega) = \sum_{l'} {}_sC_{mll'}(a\omega)\, {}_sY_{l'm}(\theta,\phi), \tag{3.4.45}$$

where ${}_sC_{mll'}$ are known as the *mode-mixing* coefficients.

To conclude, because the operator $\mathfrak{h}_1$, defined in Eq. (3.4.37), depends on the angle via a *cosine*, the following symmetries apply

$$\begin{aligned} {}_{-s}S_{lm}(\theta,\phi,a\omega) &= {}_sS_{lm}(\pi-\theta,\phi,a\omega), \quad & {}_{-s}E_{lm}(a\omega) &= {}_sE_{lm}(a\omega), \\ {}_sS_{lm}(\theta,\phi,-a\omega) &= {}_sS_{l-m}(\pi-\theta,\phi,a\omega) \quad & {}_sE_{lm}(-a\omega) &= {}_sE_{l-m}(a\omega). \end{aligned} \tag{3.4.46}$$

3.5 Solution to the perturbation

The next step would be to obtain and understand the solutions of this Sturm-Liouville problem. I will not cover the numerical methods to solve the problem, since one can see for example [182; 183], for complete reviews. One approach is an eigenvalue problem which can be solved using Leaver's continued fraction method [184] or the spectral eigenvalue approach [185]. Many other methods have been studied over the years, however, these two approaches are the most used nowadays given their convergence. To understand the problem we are facing, let me describe the method of Green's functions since it is the simplest way to appreciate its physical meaning. This section is based on [13; 186–188].

3.5.1 Green's function

The wave equation has boundary conditions given by the radial equation at the horizon and at spatial infinity. A technique that allows the inclusion of these boundary conditions as initial data is the *Laplace transform*, which similarly to Fourier transform, converts a real variable t in the time domain, to a variable s in the frequency domain, although the s variable in this case, is complex. The Laplace transform for a solution to the wave equation in the time domain, such as in Eqs. (3.4.30) and (3.4.36), is

$$\hat{\Phi}(s,x) = \int_0^\infty e^{-st}\Phi(t,x)dt, \tag{3.5.1}$$

for Re(s)> 0. Then, the transform $\hat{\Phi}(s,x)$ satisfies the differential equation

$$\hat{\Phi}''(s,x) + \left(-s^2 - V(x)\right)\hat{\Phi}(s,x) = \mathcal{I}(s,x), \tag{3.5.2}$$

where the source term $\mathcal{I}(s,x)$ is determined by the initial data

$$\mathcal{I}(s,x) = -s\,\Phi\big|_{t=0} - \left.\frac{\partial \Phi}{\partial t}\right|_{t=0}. \tag{3.5.3}$$

Conversely, given a solution of Eq. (3.5.2), the time-dependent perturbation can be obtained via

$$\Phi(t,x) = \frac{1}{2\pi i}\int_{\varepsilon - i\infty}^{\varepsilon + i\infty} e^{st}\hat{\Phi}(s,x)ds, \tag{3.5.4}$$

where $\varepsilon > 0$ is an infinitesimal quantity in the real plane, chosen to cover all singularities in the complex s-plane.

One should first find the homogeneous solution of the differential equation

$$\hat{\Phi}''(s,x) + \left(-s^2 - V(x)\right)\hat{\Phi}(s,x) = 0. \tag{3.5.5}$$

Given a Green function $\hat{G}(s,x,x')$, that satisfies

$$\left[\partial_x^2 - s^2 - V(x)\right]\hat{G}(s,x,x') = \delta(x - x'), \tag{3.5.6}$$

the corresponding inhomogeneous solution is given by

$$\hat{\Phi}(s,x) = \int_{-\infty}^{\infty}\hat{G}(s,x,x')\mathcal{I}(s,x')dx'. \tag{3.5.7}$$

The Green function is constructed as

$$\hat{G}(s,x,x') = \frac{1}{W(s)}\left[\theta(x-x')\hat{\Phi}_-(s,x')\hat{\Phi}_+(s,x) + \theta(x'-x)\hat{\Phi}_-(s,x)\hat{\Phi}_+(s,x')\right], \tag{3.5.8}$$

where $\hat{\Phi}_-(s,x)$ and $\hat{\Phi}_+(s,x)$ are two linearly independent solutions for the homogeneous solution, and $W(s) = \hat{\Phi}_-(s,x)\partial_x\hat{\Phi}_+(s,x) - \hat{\Phi}_+(s,x)\partial_x\hat{\Phi}_-(s,x)$ is the Wronskian of those functions.

Then, $\hat{\Phi}(s,x)$ can be written using Eqs. (3.5.7) and (3.5.8) as

$$\begin{aligned}\hat{\Phi}(s,x) =& \frac{1}{W(s)}\hat{\Phi}_+(s,x)\int_{-\infty}^{x}\hat{\Phi}_-(s,x')\mathcal{I}(s,x')dx' \\ &+ \frac{1}{W(s)}\hat{\Phi}_-(s,x)\int_{x}^{\infty}\hat{\Phi}_+(s,x')\mathcal{I}(s,x')dx'.\end{aligned} \tag{3.5.9}$$

It is useful to close the integral path of Eq. (3.5.4), to evaluate the integral through the residue theorem

$$\oint e^{st}\hat{f}(s,x)ds = 2\pi i \sum_q \mathrm{Res}\left(e^{st}\hat{f}(s,x), s_q\right). \tag{3.5.10}$$

Consequently, the solution will be given by the poles of the function which corresponds to the zeros of the Wronskian. Altogether this reads

$$\begin{aligned}\Phi(t,x) &= \frac{1}{2\pi i}\int_{\varepsilon-i\infty}^{\varepsilon+i\infty} e^{st}\hat{\Phi}(s,x)\int_{-\infty}^{\infty}\hat{G}(s,x,x')\mathcal{I}(s,x')dx'\,ds \\ &= \frac{1}{2\pi i}\oint e^{st}\frac{1}{W(s)}\left[\hat{\Phi}_+(s,x)\int_{-\infty}^{x}\hat{\Phi}_-(s,x')\mathcal{I}(s,x')dx'\right. \\ &\qquad\qquad \left.+\hat{\Phi}_-(s,x)\int_{x}^{\infty}\hat{\Phi}_+(s,x')\mathcal{I}(s,x')dx'\right] ds \\ &= \sum_q e^{s_q t}\mathrm{Res}\left(\frac{1}{W(s)}, s_q\right)\left[\hat{\Phi}_+(s,x)\int_{-\infty}^{x}\hat{\Phi}_-(s,x')\mathcal{I}(s,x')dx'\right. \\ &\qquad\qquad \left.+\hat{\Phi}_-(s,x)\int_{x}^{\infty}\hat{\Phi}_+(s,x')\mathcal{I}(s,x')dx'\right].\end{aligned} \tag{3.5.11}$$

The solution to this equation is a set of discrete complex frequencies $\omega = \omega_R + i\omega_I$, called Quasi-Normal Modes (QNMs), see Fig. 3.3 for a visual representation. They behave like resonant normal modes, but their imaginary part is associated with a damping time, which calls for the prefix quasi. Quasi-normal modes are formally defined by solutions that satisfy purely outgoing boundary conditions [23],

$$\Psi(x)_{x\to-\infty} \to e^{-i\omega x}, \quad \Psi(x)_{x\to+\infty} \to e^{+i\omega x}, \tag{3.5.12}$$

for a time dependence of $e^{-i\omega t}$. Then, quasi-normal frequencies of stable systems must have a negative imaginary part. In other words, if the integral admits solutions whose amplitudes grow in time, that is, if the imaginary part is positive ($\omega_I > 0$), then the BH becomes unstable. As a result, a small perturbation would generate growing waves, absorbing the energy of the BH away. If on the contrary, the imaginary part is negative ($\omega_I < 0$), the BH is stable as it will radiate energy for a small amount of time. Vishveshwara [189] showed that the Sturm-Liouville equation for the Schwarzschild BH, only has a solution of frequencies with a negative imaginary part, which prevents any instability, since the modes exponentially decay with time.

In contra-position, normal modes are solutions of classical oscillating objects, which means that they are resonant modes given by real frequencies ($\omega \in \mathbb{R}$). The dynamics of that object can be described as a sum of stationary waves, where each wave oscillates at a given frequency in time but whose amplitude does not move in space.

---

[23] Note that this notation might look contra-intuitive because of the chosen convention for the time dependence, which is negative.

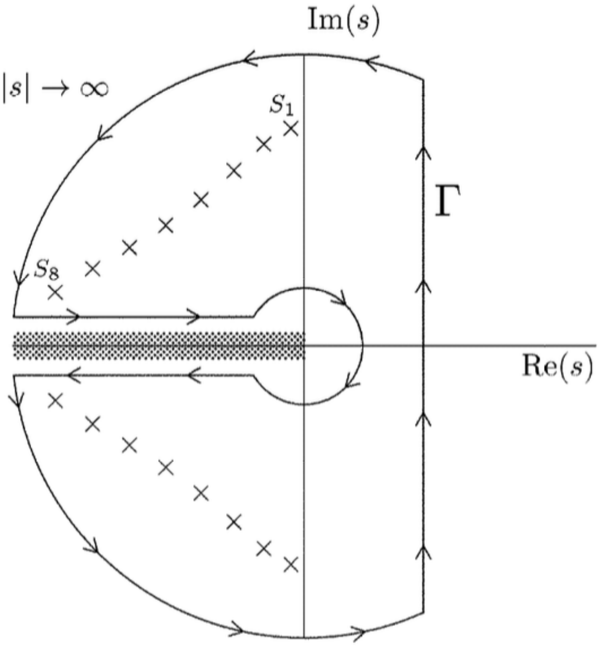

Figure 3.3: Integration path Γ in the complex s-plane for the inverse Laplace transformation, where $S_1, \ldots, S_8$ are the first eight poles of the Green's function. *Credits: Nollert* [186].

3.5.2 Teukolsky solution via Green's function

It is straightforward to identify the functions and variables to write the Teukolsky equation in the Green formalism. However, one needs to consider the boundary conditions for the rotating BH already studied in the asymptotically radial behavior in Sec. 3.4.2. Given the negative time convention, the imaginary part of the complex frequency should be negative in order to obtain stable solutions, consequently, this effect will change the natural interpretation of the wave radiation. Note that it differs from Detweiler's notation [188] where $\omega = -\sigma$ and the time has a positive sign. Imposing the condition that nothing can escape from the singularity towards the horizon ($r_* \to -\infty$) for $R_{r+}(\omega, r_*)$ and that no wave can come from the spatial infinity ($r_* \to \infty$) for $R_\infty(\omega, r_*)$, one can express their asymptotic behaviors as

$$R_{r_+}(\omega, r_*) \simeq \begin{cases} \Delta^2 e^{ikr_*} & (r_* \to -\infty), \\ A_{out}(\omega) r^3 e^{i\omega r_*} + A_{in}(\omega) \frac{1}{r} e^{-i\omega r_*} & (r_* \to \infty), \end{cases} \tag{3.5.13}$$

and

$$R_\infty(\omega, r_*) \simeq \begin{cases} B_{out}(\omega) e^{ikr_*} + B_{in}(\omega) \Delta^2 e^{-ikr_*} & (r_* \to -\infty), \\ r^3 e^{i\omega r_*} & (r_* \to \infty), \end{cases} \tag{3.5.14}$$

where $k = -\omega + ma/2Mr_+$ is updated from the previously definition in Eq. (3.4.35). Then, the Wronskian of these two independent solutions is a function that only depends on ω,

$$\begin{aligned} W(\omega) &= R_{r_+}(\omega, r_*)\partial_{r_*}R_\infty(\omega, r_*) - R_\infty(\omega, r_*)\partial_{r_*}R_{r_+}(\omega, r_*) \\ &= 2i\omega A_{in}(\omega) = 2i\omega B_{out}(\omega). \end{aligned} \tag{3.5.15}$$

For the differential equation

$$\mathcal{R}''_{lm}(\omega, r_*) + \left[\omega^2 - V(r_*)\right]\mathcal{R}_{lm}(\omega, r_*) = \mathcal{I}(\omega, r_*), \tag{3.5.16}$$

the solution in terms of Green's function takes the form

$$\begin{aligned} \mathcal{R}_{lm}(\omega, r_*) &= \int_{-\infty}^{\infty} G(\omega, r_*, r'_*)\mathcal{I}(\omega, r'_*)dr'_* \\ \mathcal{R}_{lm}(\omega, r) &= \frac{R_\infty(\omega, r_*)}{W(\omega)}\int_{r_+}^{r}\frac{r'^2 + a^2}{\Delta(r')}R_{r_+}(\omega, r')\mathcal{I}(\omega, r)dr' \\ &\quad + \frac{R_{r_+}(\omega, r_*)}{W(\omega)}\int_{r}^{\infty}\frac{r'^2 + a^2}{\Delta(r')}R_\infty(\omega, r')\mathcal{I}(\omega, r)dr'. \end{aligned} \tag{3.5.17}$$

Since we are interested in the gravitational radiation at spatial infinity ($r \to \infty$), we can write

$$\begin{aligned} \mathcal{R}_{lm}(\omega, r \to \infty) &= \lim_{r\to\infty}\frac{R_\infty(\omega, r_*)}{W(\omega)}\int_{r_+}^{r}\frac{r'^2 + a^2}{\Delta(r')}R_{r_+}(\omega, r')\mathcal{I}(\omega, r)dr' \\ &= \frac{r^3 e^{i\omega r_*}}{2i\omega A_{in}}\int_{r_+}^{r}\frac{r'^2 + a^2}{\Delta(r')}R_{r_+}(\omega, r')\mathcal{I}(\omega, r)dr' \\ &= r^3 e^{i\omega r_*}Z^{out}_{lm}, \end{aligned} \tag{3.5.18}$$

where Z^{out}_{lm} is the function that carries all the information of the boundaries A_{in} and on the source terms $\mathcal{I}$.

Finally, the gravitational radiation can be expressed as

$$\begin{aligned} \Psi(t, r \to \infty, \theta, \phi) &= \sum_{l=0}^{\infty}\sum_{m=-l}^{l} e^{-i\omega t}e^{im\phi}R_{lm}(\omega, r)S_{lm}(\omega, \theta) \\ &= \frac{r^3\left(1 - 2M/r\right)}{2\pi}\sum_{l=0}^{\infty}\sum_{m=-l}^{l} e^{im\phi}\int_{\infty-i\varepsilon}^{\infty+i\varepsilon} e^{-i\omega(t-r_*)}Z^{out}_{lm}(\omega, r)S_{lm}(\omega, \theta)d\omega, \end{aligned} \tag{3.5.19}$$

where I used the definition of Eq. (3.4.29). The last step is to close the contour path of the integration to obtain the remaining solutions. Its derivation is beyond the scope of this chapter. Nevertheless, it is important to mention that when closing the contour path, a power-law tail appears as a consequence of the branch cut. In general, its contribution to gravitational radiation is small and negligible for QNMs detection. I present in Fig. A.1 in Appendix A.4 a visual representation of the tail with its explanation. Its introduction here would require detailed information given in the next sections.

3.6 Ringdown waveform

This final section is intended to translate all the previous information into the description of the ringdown, the last stage of the BHB coalescence. Once the two BHs have merged into a final one, it will be an excited state. As it relaxes, it will emit GWs described by BH perturbation theory.

The function that solves the wave equation with the boundary conditions can be decomposed into a radial part $R_{lm}(r,\omega)$ and an angular part $S_{lm}(\theta,\omega)$, such that

$$\Psi(t,r,\theta,\phi) = \frac{1}{2\pi}\int \sum_{l=0}^{\infty}\sum_{m=-l}^{l} e^{-i\omega t} e^{im\phi} R_{lm}(r,\omega) S_{lm}(\theta,\omega) d\omega. \tag{3.6.1}$$

The radial and angular eigenfunctions depend on the complex frequency and the separation constant for a given pair of (l,m), see Eqs. (3.4.27), in consequence, both (angular and radial equations) need to be solved at the same time. This can be done, for instance, with Leaver's fractional method [184] or via the spectral approach [185].

The zeros of the Wronskian and therefore, the Zeros of A_{in}, in the Sturm-Lioville problem for a perturbed BH are known as QNMs as mentioned in Sec. 3.5.1, and represent the characteristic complex frequencies ($\omega = \omega_{Re} + i\omega_{Im}$) of a perturbed BH, also known as BH spectrum. Since A_{in} does not depend on the source terms $\mathcal{I}(\omega,r)$, the values of the QNMs depend only on the metric and thus on the parameters of the BH, regardless of the origin of the perturbation itself. The boundary conditions associated with BHs give rise to complex frequencies with a negative imaginary part ($\omega_{Im} < 0$), which conditions the stability of the BH. This means that BHs are stable under perturbations since they return to their stationary state through the emission of gravitational radiation during a period given by the damping time $\tau = 1/\omega_{Im}$.

Considering the following approximations

$$\Psi_4 = \Psi\rho^{-4} \propto \frac{1}{r}\sum_{lm} e^{-i\omega t} e^{im\phi} A_{lm} S_{lm}(\theta,\omega), \tag{3.6.2}$$

$$\Psi_4 \sim \ddot{h} = \ddot{h}_+ - i\ddot{h}_\times \rightarrow h \sim \frac{\Psi_4}{\omega^2}, \tag{3.6.3}$$

one can, without loss of generality, express the gravitational emission of a perturbed BH as

$$h(t,r,\theta,\phi) = \frac{M}{r}\sum_{lmn} A_{lmn}\,{}_2S_{lmn}(\theta,\phi)e^{-i\omega_{lmn}t}. \tag{3.6.4}$$

Here, A_{lmn}, not to be confused with the separation constant $\mathcal{A}_{lm}$, is the amplitude of each QNM absorbing the ω_{lmn}^{-2} factor from Eq. (3.6.3). I include the index n for the overtones since the solution for a given pair (l,m) and fixed parameters has n solutions, n poles. Then, the waveform will be a sum of solutions (ω_{lmn}) decomposed in spin-weighted spheroidal harmonics $S_{lmn}(\theta,\phi) = e^{im\phi}S_{lmn}(\theta)$, also labeled by (l,m,n) as polar and azimuthal angular numbers, and overtone respectively. The radial dependency enhances the decomposition in terms of spin-weighted spheroidal harmonics labeled by (l,m,n), which, contrary to spherical harmonics, do not present a complete set and, thus, some solutions can degenerate.

3.6.1 BH spectrum

In order to find the QNMs values, one needs to solve the Sturm-Liouville problem with the boundary conditions at the horizon and spatial infinity. There are several methods to obtain the solutions. One example is to consider a Pöschl-Teller potential [190; 191], which will return an exact analytical solution. However, in general, one needs to call upon approximations or numerical methods to solve the equation. Such is the case of the WKB method, although it presents an issue since it involves a Taylor series expansion where convergence is not guaranteed. Other methods with similar issues are also applicable, see [182] for a summary of different methods. The continued fraction method, or Leaver's method in the BH perturbation context, is one of the few methods along with the spectral eigenvalue approach [185] that shows convergence. The main idea is to consider the angular function satisfying Eq. (3.4.27) which can be expressed as

$${}_sS_{lm} = e^{a\omega u}(1+u)^{k_-}(1-u)^{k_+}\sum_{p=0}^{\infty} a_p(1+u)^p, \tag{3.6.5}$$

where $k_\pm = |m \pm s|/2$ and $u = \cos\theta$. The expansion coefficients a_p are obtained from the three-term recurrence relation

$$\alpha_0 a_1 + \beta_0 a_0 = 0, \qquad \alpha_p a_{p+1} + \beta_p a_p + \gamma_p a_{p-1} = 0, \qquad p = 1,2,\ldots \tag{3.6.6}$$

where

$$\begin{aligned}
\alpha_p =& -2(p+1)(p+2k_-+1),\\
\beta_p =& \, p(p-1) + 2p(k_- + k_+ + 1 - 2a\omega) - \left[a^2\omega^2 + s(s+1) + \mathcal{A}_{lm}\right]\\
&- \left[2a\omega(2k_- + s + 1) - (k_- + k_+)(k_- + k_+ + 1)\right],\\
\gamma_p =& \, 2a\omega(p + k_- + k_+ + s).
\end{aligned} \tag{3.6.7}$$

For a given a, m, ω and s, the separation constant $\mathcal{A}_{lm}$ can be found by the continued fraction equation, resulting from Eqs. (3.6.6), and finding the zeros for increasing p

$$0 = \beta_0 - \frac{\alpha_0 \gamma_1}{\beta_1 - \frac{\alpha_1 \gamma_2}{\beta_2 - \frac{\alpha_2 \gamma_3}{\beta_3 - \dots}}}. \tag{3.6.8}$$

Given the similarity of the radial expression and the boundary conditions, the radial function can be written similarly (see Leaver's paper [184] for its definition). In that case, the complex frequency ω can be found by the continued fraction method, given the values of $a, m, \mathcal{A}_{lm}$ and s. Therefore, both equations are simultaneously solved until convergence. The separation constant tends to $\mathcal{A}_{lm} = l(l+1) - s(s+1)$ as $a \to 0$, then it is natural to start with the Schwarzschild case and slowly compute the solutions for higher angular momentum.

QNM values

Nowadays, the values of the QNMs are known with fairly high precision, as various authors worked on their numerical computation [13; 186; 192]. I base this section on those references. Moreover, E. Berti made publicly available a code to compute them [193], and there also exists a python package called `qnm` [194] that returns the wanted QNM for a given set of (s, l, m, n, a) parameters. Although the latter employs the spectral eigenvalue approach [185] rather than the fractional method.

From now on, I will write the complex frequency or QNMs as

$$\tilde{\omega}_{lmn} = \omega_{lmn} - i/\tau_{lmn}, \tag{3.6.9}$$

to differentiate the real part from the imaginary part of the frequency.

Each QNM solution has a positive and a negative real part ($\pm\omega_{lmn} > 0$), being both solutions to the eigenvalue problem, see Fig. 3.4 for a visual representation. The solutions are often called *ordinary* modes if $\omega_{lmn} > 0$ and *mirror* modes if $\omega_{lmn} < 0$. When the rotation is included ($a \neq 0$), the spectrum splits into the different values of $m = -l, \dots, l$ as shown in Fig. 3.5.

Depending on the sign of the angular number m and the sign of ω_{lmn}, one defines the modes as *prograde* or *retrograde*, depending on the literature (see e.g.[195; 196]). Furthermore, the frequencies with positive m are related to the negative m by the following symmetry

$$-\omega_{lmn} = \omega_{l-mn}, \qquad \tau_{lmn} = \tau_{l-mn}, \qquad \mathcal{A}^*_{lmn} = \mathcal{A}_{l-mn}. \tag{3.6.10}$$

This effect can be seen in Fig. 3.6, where I use the same convention as in [197], calling prograde modes the QNMs with positive frequency values and retrograde modes the ones with negative frequency values.

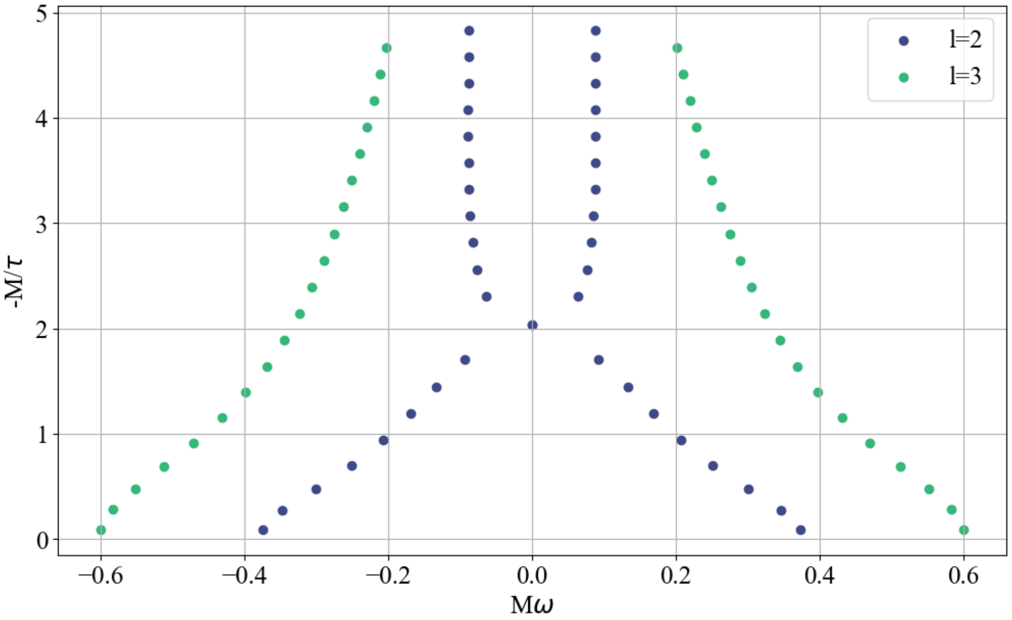

Figure 3.4: Quasi-normal modes spectrum for a Schwarzschild BH (j=0), for $l = 2, 3$ and $n = 0, \dots, 20$ denoting the points from the bottom to the top in that order. Generated with `qnm` [194].

A fitting that relates the QNM values and the BH intrinsic parameters is useful to obtain the inverse relation. That is, given a QNM value, we want to know the BH parameters $(M, j = a/M)$ [24]. This was first studied by Echevarria [198], then by Berti et al. [192] and later improved by London et al. [199]. As an example, I write here the parametrization from [192]:

$$M\omega_{lmn} = f_1 + f_2(1-j)^{f_3}, \tag{3.6.11a}$$

$$\omega_{lmn}\tau_{lmn}/2 = q_1 + q_2(1-j)^{q_3}, \tag{3.6.11b}$$

where f_1, f_2, f_3, q_1, q_2 and q_3 are the fitted coefficients listed in Table 3.1. The complete tables can be found in [192] as Tables (VIII, IX, X). Indeed, this fit allows us to obtain the values of the spin and the mass of the BH for any pair of $(\omega_{lmn}, \tau_{lmn})$.

Overtones and starting time

The initial time of the ringdown is still a topic under discussion, since it is ill-defined, from a physical point of view [200]. Where does the linear perturbation theory become valid in a non-linear theory such as GR? The answer is elusive and perhaps not even well posed. The common practice to understand linear behavior is to fit the superposition

---

[24] There is an abuse of language regarding a_f and j, as sometimes both are used to indicate the adimensional spin $|j| < 1$. Even though $j = a/M$.

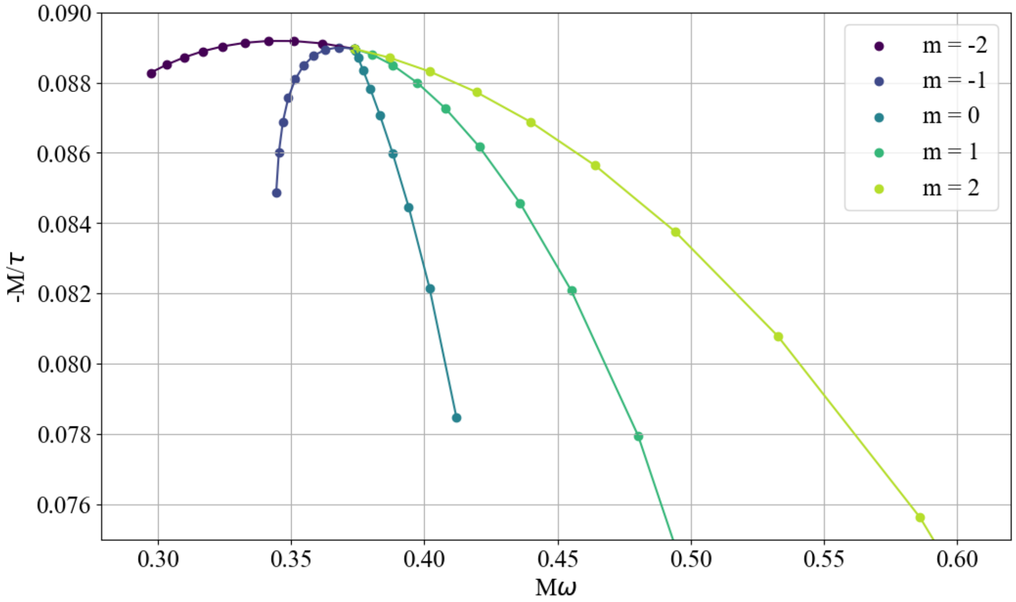

Figure 3.5: Quasi-normal modes spectrum for a Kerr BH with spin $j = [0.0, 0.1, \ldots 0.9]$ for l=2, n=0. Generated with `qnm` [194].

m	n	f_1	f_2	f_3	q_1	q_2	q_3
2	0	1.5251	-1.1568	0.1292	0.7000	1.4187	-0.4990
	1	1.3673	-1.0260	0.1628	0.1000	0.5436	-0.4731
	2	1.3223	- 1.0257	0.1860	-0.1000	0.4206	-0.4256

Table 3.1: Fitting coefficients for the frequencies $\tilde{\omega}_{lmn}$ with $l = 2$. *Credits: Table adapted from Berti et al.* [192].

of waves characterized by the QNM onto highly precise NR waveforms. The hypothesis that the merger occurs at the luminosity peak, that is when Ψ_4 is maximal, marks the beginning of the ringdown [25]. However, due to the presence of non-linear effects, the start of the ringdown should be shifted to a more retarded time. Several analyses showed that the starting time varies for each QNM index since the amplitude of each mode becomes constant at different times [197; 200–203]. The accepted time is considered to be around $10t_M$, where $t_M = t\, c^3/M\, G$ is an adimensional value. Nevertheless, this accepted time is not engraved in stone, and in general, several starting times in the vicinity of the luminosity peak should be investigated. See for example [197; 201; 204–206] for further discussion.

Overtones are ordered according to their damping time. This means that the fundamental overtone ($n = 0$), has the longer damping time and thus, it is the longer-living QNM in the waveform. The closer one moves to the merging time, higher overtones will dominate the waveform. However, analyses over NR waveforms showed that higher over-

---

[25] Even though $t_{peak}(\Psi_4) < t_{peak}(h)$ [200].

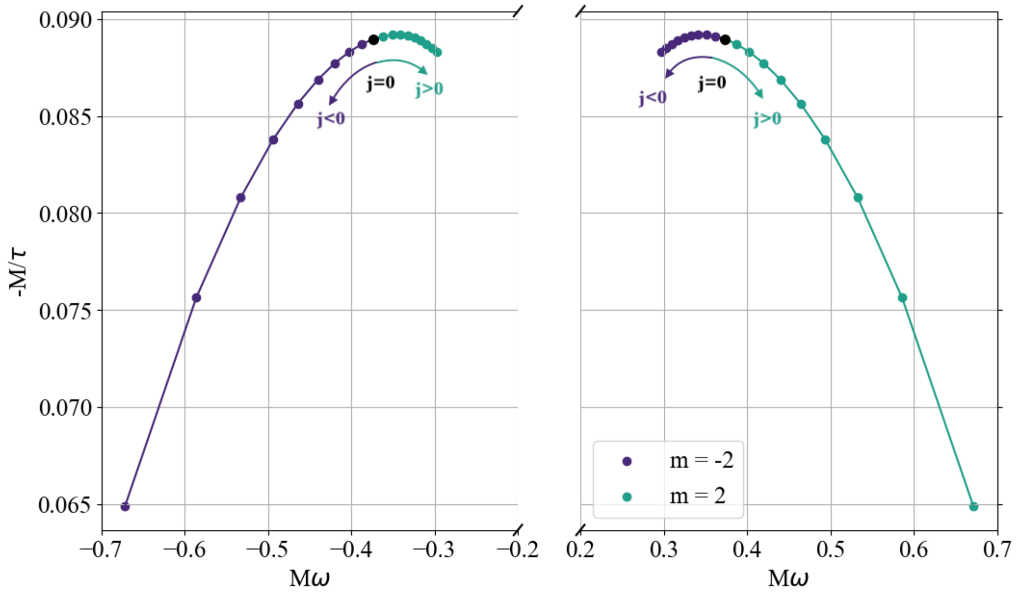

Figure 3.6: Quasi-normal modes spectrum for a Kerr BH with spin $j = [0.0, 0.1, \ldots 0.9]$ for l=2, m=|l|, n=0. The left side corresponds to retrograde modes, while prograde modes are on the right side of the figure. Generated with `qnm` [194].

tones are detectable up to a given point, Baibhav et al. [200] define this limit as $n = 2$, since higher overtones could be fitting features introduced by the non-linear nature of GR. For further discussion on these topics and their connection, I refer the reader to [200–203] for example. Nevertheless, it is worth mentioning that the presence of the first overtone of the dominant QNM, i.e. (2,2,1), has been inferred for the event GW150914 (see the discussion on its detectability [201; 207–211]).

Amplitudes

The amplitude and phase of each QNM, have also been an element of study for some time [197; 204; 212–214]. From Eqs. (3.6.1) and (3.5.19) one can observe that the amplitudes carry information of the source terms and the complex frequency ω_{lmn}. Then, the amplitudes will be given by the initial state of the BH, that is, before the perturbation, which in the case of a merger binary is related to the parameters of the two initial BHs, i.e., the progenitors. This was studied by Kamaretsos et al. [212; 213]. Analyzing NR waveforms, they found a relation between the amplitudes and the symmetric mass ratio for non-spinning BHs. The study was later expanded, among others, by London et al. [204] to include the final spin dependency for rotating BHs, and also by Cheung et al. [197] albeit, with a dependency on the plus and minus adimensional spins,

$$\chi_- = (q\chi_1 - \chi_2)/1 + q, \qquad \chi_+ = (q\chi_1 + \chi_2)/1 + q, \tag{3.6.12}$$

where χ_1, χ_2 are the individual adimensional aligned spin of the progenitors and q the mass ratio. Then, one can write each amplitude and phase as a function of the intrinsic parameters Ξ,

$$\begin{aligned} A_{lmn}(m_1, m_2, \chi_1, \chi_2) &= A_{lmn}(\Xi), \\ \phi_{lmn}(m_1, m_2, \chi_1, \chi_2) &= \phi_{lmn}(\Xi). \end{aligned} \tag{3.6.13}$$

Mode mixing

The mixing of the modes is a feature that arises naturally when expressing the spin-weighted spheroidal harmonics in terms of the spin-weighted spherical harmonics as I previously introduced in Sec. 3.4.2:

$${}_sS_{lm}(\theta, \phi, a\tilde{\omega}) = {}_sY_{lm}(\theta, \phi) + \sum_{l' \neq l} \frac{\langle sl'm|\mathfrak{h}_1|slm\rangle}{l(l+1) - l'(l'+1)} {}_sY_{l'm}(\theta, \phi) + \dots \tag{3.6.14}$$

It can be expressed as

$${}_sS_{lm}(\theta, \phi, a\tilde{\omega}) = \sum_{l'} {}_s\sigma_{l'm'lm}(a\tilde{\omega}) {}_sY_{l'm}(\theta, \phi), \tag{3.6.15}$$

and where ${}_s\sigma_{l'm'lm}$ are the mode-mixing coefficients, previously defined as ${}_2C_{ml'l}$. From now on, I fix the gravitational field spin $s = -2$ and I also include the overtone index, since $\tilde{\omega}_{lmn}$ depends on the overtone n. Various authors [131; 215] computed the values of spherical-spheroidal mixing coefficients, defined as

$${}_{-2}\sigma_{l'm'lmn}(a\tilde{\omega}_{lmn}) = \delta_{m'm} \int_\Omega {}_{-2}Y^*_{l'm'}(\theta) {}_{-2}S_{lmn}(a\tilde{\omega}_{lmn}, \theta) d\Omega, \tag{3.6.16}$$

where I used that $S_{lmn}(\theta, \phi) = e^{im\phi} S_{lmn}(\theta)$ and $Y_{lm}(\theta, \phi) = e^{im\phi} Y_{lm}(\theta)$. Since $\delta_{m'm}$ is the Kronecker delta, one can drop the prime in the first m. Consequently, these coefficients can be found in the literature without the first m at all $\sigma_{l'lmn}$ or even written as $\mu_{ml'ln}$. With this representation, the gravitational strain at the ringdown takes the form

$$h(t, r, \theta, \phi, \Xi) = \frac{M}{r} \sum_{l'} \sum_{lmn} A_{l'mlmn}(\Xi, a\tilde{\omega}_{lmn}) {}_{-2}Y_{l'm}(\theta, \phi) e^{-i\tilde{\omega}_{lmn}(t - t_0)}, \tag{3.6.17}$$

where

$$A_{l'mlmn}(\Xi, a\tilde{\omega}_{lmn}) = A_{lmn}(\Xi) {}_{-2}\sigma_{l'mlmn}(a\tilde{\omega}_{lmn}). \tag{3.6.18}$$

Note that I also include in the equation the starting time t_0, previously discussed.

To complete this subject, QNMs can also be mixed as a result of the reference frame choice or the extraction point in terms of NR computations. This effect was first observed in NR waveforms by B. Kelly and J. Baker. [216] and further analyzed for example in [195; 197].

Non-linearity

In the weak field, the linear approach is allowed as it dominates over the non-linear features. However, in the strong field, the linear approach falls short of describing the gravitational dynamics as non-linear effects become relevant. In the perturbation theory framework, one could try to include second-order effects as done for instance in [217–220]. In that case, second-order QNMs appears in the ringdown under the following condition

$$\omega_{lm}^{(2)} = \omega_{l_1 m_1} + \omega_{l_2 m_2}, \tag{3.6.19}$$

if and only if

$$|l_1 - l_2| < l < l_1 + l_2 \quad \text{and} \quad m = m_1 + m_2 < |l|, \tag{3.6.20}$$

where the upper index (2) denotes the second-order contribution. Furthermore, this feature was observed in NR waveforms first by London et al.[204] when performing QNM analysis in the ringdown regime. In addition, one can also see [196; 221].

3.7 Deviations from GR

In previous sections, I describe the framework of perturbation theory, in which the test of the no-hair theorem enables us to probe GR in the ringdown regime. However, neither the cause of deviations from GR nor their signatures are introduced. This small section, based on [183; 222; 223], introduces the framework for modified gravity.

The theory of general relativity is the accepted standard theory of gravity, as it successfully describes the interplay between matter and spacetime in all scales, except at the quantum level, at the order of Planck's mass [225]. This is, of course, assuming, that the cosmological constant Λ_{CDM} accelerating the cosmic expansion is an external field. Indeed, there are different opinions on the role of a cosmological constant, as it should be included in the metric of GR as well, rather than as an external field. Moreover, to include the high energy regime, there is a great effort in connecting the classical field of gravity with quantum field theory, giving rise to quantum gravity. To cover all scales, there has been the development of a plethora of modified theories of gravity over the years, see Fig. 3.7 for an informative sketch. The list of alternative theories is long, and their description would take me a long time, thus I refer the reader to [154; 222–224] for detailed reviews. Nevertheless, it is important to mention that Lovelock's theorem [226; 227], imposes that GR is the only theory of gravity in four dimensions, that fulfills the local gravitational action which contains only second derivatives in the equations of motion. Then, to construct alternative theories of gravity, one should implement at least one of the following requirements:

- break diffeomorphism invariance (non-minimal coupling);

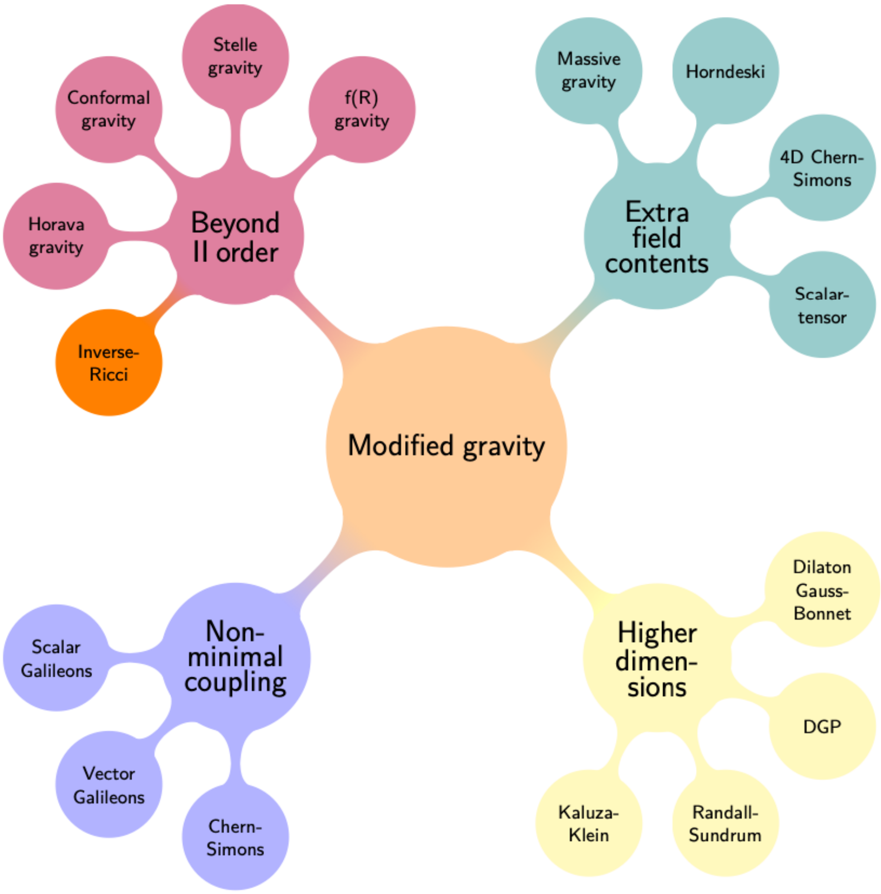

Figure 3.7: A map of various modified gravity models proposed in the literature. *Credits: Shankaranarayanan et al.* [224]

- allow for higher dimensions (than 4-D);
- allow for higher derivatives (beyond 2nd order);
- include more fields than the metric tensor (add extra degrees of freedom).

Regarding the first point, diffeomorphism invariance can be restored via the Stückelberg technique [228], which introduces an extra field called the Stückelberg field [229]. Regarding the second point, only 4 dimensions have been detected and higher dimensional theories have an effective description in 4 dimensions, which is sufficient to describe low-energy phenomena [225]. This leaves us with two more detectable possibilities, the addition of higher derivatives and the addition of fields.

The addition of extra fields, such as scalars, vectors, or tensor fields, leads to an additional dynamical equation for the corresponding field. In this group, one could mention the Brans-Dicke theory [230] or the Horndeski theory [231] to name but a few. In the case of theories with higher-order derivatives, they could also yield more d.o.f as extra propagating modes appear. In general, from a mathematical point of view, these theories can be very complicated to deal with. In this group, the f(R) gravity is probably the most general model [232]. Nevertheless, the detectability of this new d.o.f. need to be suppressed at the Solar System scale, where GR is well tested and no extra d.o.f. has been detected [233]. Therefore, in the case of a modified theory, there are *screening mechanisms* to suppress any modification to GR at that scale, see e.g. [222] for a review on screening mechanisms.

Since a modification to GR, involves either a modification to the background metric, to the dynamics, and/or to the boundary conditions, the spectrum of QNMs is also expected to be modified. In general, these modifications change the QNM values depending on the considered theory. Additionally, keep in mind, that the separation of a metric into a radial and an angular component depends on the symmetries of the problem. This means that the description of a modified theory, in terms of a separable wave equation analogous to the Teukolsky master equation, is not straightforward. Another important feature of alternative theories is that iso-spectrality [26] is rarely fulfilled. Despite these issues, there have been several recent developments in the calculation of non-GR QNMs. For that, on top of the perturbation, an expansion in the spin or the coupling constant is considered. This is the method used primarily for slowly rotating BHs in different alternative theories, e.g. [234–237]. For rapidly rotating BHs in effective field theories with higher derivatives, there is the work from [238; 239], for Einstein-dilaton Gauss-Bonnet gravity (EdGB), see [240; 241]; for dynamical Chern-Simons (dCS), see [242]; and for new numerical software to compute the QNM values in beyond-GR theories, such as Einstein-scalar-Gauss-Bonnet with the spectral method, see [243; 244].

As an example, in the case of higher derivatives in an effective field theory, one can write the action as [238]

$$S_{EFT} = \int \frac{1}{16\pi} d^4x \sqrt{|g|} \left[R + \ell^4 \left(\lambda_{even}\mathcal{R}^3 + \lambda_{odd}\bar{\mathcal{R}}^3\right) + \ell^6 \left(\varepsilon_1 \mathcal{C}^2 + \varepsilon_2 \mathcal{C}\bar{\mathcal{C}} + \varepsilon_3 \bar{\mathcal{C}}^2\right) + \mathcal{O}(\ell^8)\right], \tag{3.7.1}$$

where

$$\mathcal{R}^3 = R_{\mu\nu}{}^{\rho\sigma} R_{\rho\sigma}{}^{\delta\gamma} R_{\delta\gamma}{}^{\mu\nu}, \qquad \bar{\mathcal{R}}^3 = R_{\mu\nu}{}^{\rho\sigma} R_{\rho\sigma}{}^{\delta\gamma} \bar{R}_{\delta\gamma}{}^{\mu\nu} \tag{3.7.2}$$

$$\mathcal{C} = R_{\mu\nu\rho\sigma} R^{\mu\nu\rho\sigma}, \qquad \bar{\mathcal{C}} = R_{\mu\nu\rho\sigma} \bar{R}^{\mu\nu\rho\sigma}, \tag{3.7.3}$$

with $\lambda_{even}, \lambda_{odd}, \varepsilon_1, \varepsilon_2, \varepsilon_3$ coupling constants, ℓ the length scale, and the top bar $(\bar{\ })$ representing the dual space,

$$\bar{R}^{\mu\nu\rho\sigma} = \frac{1}{2}\epsilon^{\mu\nu\alpha\beta} R_{\alpha\beta}{}^{\rho\sigma}. \tag{3.7.4}$$

Then, the potential in the wave equation can be written as the GR black hole's potential plus a perturbation depending on the spin ($V \to V^{RW} + \delta V_s$), which results in a perturbation of the eigenvalues with respect to GR eigenvalues, given by

---

[26] I introduced this concept at the end of Sec. 3.2.3.

$$\omega_{lmn}^{\pm} = \omega^{Kerr} + \frac{\alpha_q}{M}\Delta\omega_{lmn}^{q,\pm}, \tag{3.7.5}$$

where the q index represents the spin expansion order, and where the sign ± is the parity. Note that this specific model depends on the coupling constant α and the mass of the object M, so this kind of theory might be suppressed for supermassive objects. Nevertheless, perturbations in the QNMs are seen across different theories beyond GR where the metric solution is not a Kerr BH and small perturbations in the potential could lead to instabilities [229; 245]. Consequently, in general, one considers a model-independent description of the QNM. This means, that one measures deviations from GR, in the sense of differences between non-GR QNMs and GR QNMs. Retaking the complex frequencies of Eq. (3.6.9), one can write

$$\omega_{lmn}^{\mathrm{non-GR}} = \omega_{lmn}^{\mathrm{GR}}(M_f, a_f) + \Delta\omega_{lmn}, \tag{3.7.6a}$$
$$\tau_{lmn}^{\mathrm{non-GR}} = \tau_{lmn}^{\mathrm{GR}}(M_f, a_f) + \Delta\tau_{lmn}, \tag{3.7.6b}$$

where $\Delta\omega_{lmn}$ and $\Delta\tau_{lmn}$ are the difference of the frequency and damping time in the (l, m, n) mode. However, a more common parametrization is used, that is

$$\omega_{lmn}^{\mathrm{non-GR}} = \omega_{lmn}^{\mathrm{GR}}(M_f, a_f)(1 + \delta\omega_{lmn}), \tag{3.7.7a}$$
$$\tau_{lmn}^{\mathrm{non-GR}} = \tau_{lmn}^{\mathrm{GR}}(M_f, a_f)(1 + \delta\tau_{lmn}), \tag{3.7.7b}$$

where $\delta\omega_{lmn}$ and $\delta\tau_{lmn}$ are the *fractional deviations* of the frequency and damping time in the (l, m, n) mode.

3.8 Short summary

In this chapter, I presented the theoretical framework needed for the development of my work. After the coalescence of two BHs, they merge to produce a final BH. That perturbed BH will settle down through the emission of GWs which can be described as a superposition of oscillating waves characterized by a complex frequency. The values of these frequencies, called QNMs, are solutions to the Teukolsky master equation, thus they depend only on the mass and the spin of Kerr BH. The use of Newman-Penrose tetrad formalism allowed Teukolsky to separate the wave equation into a radial and an angular part, enabling the computation of the spectrum of rotating BHs. The solution for Schwarzschild BHs was previously found by Regge and Wheeler for the axial polarization and by Zerilli for the polar polarization. All these historical developments at a time when GWs were not yet detected, paved the way for tests of GR in the ringdown, which is one of the science objectives of LISA. In the following sections, I describe my work toward that end, based on the description of fractional deviations from GR.

Chapter 4

Methodology

The goal of this thesis is to analyze the possibility of testing the *no-hair* hypothesis with the detection of GWs produced by the coalescence of MBHBs with LISA. Consequently, before being able to say something about the detection and sensitivity of LISA to possible deviations from GR, some previous analysis and consistency checks are in order. I start with an introduction to the general context and state-of-the-art as well as the steps to achieve my goal in Sec. 4.1. I then describe the response of LISA as a transformation applied to the signal in Sec. 4.2. Then, Sec. 4.3 explains the Bayesian framework to analyze the data. The tools to generate an injection as well as the templates are covered in Secs. 4.4 and 4.5, leaving the results for the next chapter. This chapter, along with the subsequent chapters containing the results and conclusions, represent the core of my work and have been, or are in the process of being published [132; 246].

4.1 General context

The first detection of gravitational waves with LIGO [42; 247] produced by the coalescence of a black hole binary GW150914 [43], marked the beginning of the GW astronomy era. At the same time, its detection opened a window to probe physics beyond the standard model and general relativity. Since that first detection, the scientific community has been eager to test GR in the strong field regime [248–251].

Indeed GR can be tested for instance, through the *no-hair* theorem by analyzing the *ringdown* phase. The no-hair theorem, as previously presented, is a prediction of GR, that states that any Kerr BH is characterized by only two parameters: its mass and its spin (M_f, a_f) [167–170; 252]. In the last stage of the coalescence, once formed, the perturbed BH is expected to settle down to a Kerr BH through the emission of GWs. As detailed in the previous section, the radiation of a Kerr BH can be written a superposition of damped sinusoidals [160; 161]. The strain in the plus and cross polarizations reads

$$h_+(t) - ih_\times(t) = \sum_{lmn} h_{lmn}(t)_{-2}S_{lmn}(a_f\tilde{\omega}_{lmn};\theta,\varphi), \tag{4.1.1}$$

where,

$$h_{lmn}(t) = A_{lmn} e^{i(\phi_{lmn} - \tilde{\omega}_{lmn} t)}. \tag{4.1.2}$$

The complex frequencies $\tilde{\omega}_{lmn}$ are the solution of Teukolsky master equation, Eq. (3.4.27), where the real part is the oscillation frequency, while the imaginary part corresponds to the inverse of the damping time

$$\tilde{\omega}_{lmn} = \omega_{lmn} - i/\tau_{lmn}. \tag{4.1.3}$$

The values of the QNMs are characterized by the metric structure and thus for a remnant Kerr BH, they depend only on the mass and spin (M_f, a_f)[168]. In contrast, the amplitude and phase associated with each mode (A_{lmn}, ϕ_{lmn}) correspond to their excitation in the pre-merger, thus depending on the initial BHs parameters [212; 213]. In the presence of an alternative theory to GR, the values of the complex frequency might deviate from those of GR [234; 235; 252]. Thus, one approach to probe the *no-hair* conjecture is with *BH spectroscopy* [198; 253]. Since in GR, the values of the BH spectrum are defined solely by the mass M_f and spin a_f of the final BH, when studying the spectrum of the remnant BH, one can recover those two parameters, for example with Eqs.(3.6.11) relating the mass and spin with the frequency and damping time of each mode. Then, the comparison of pairs of mass and spin obtained from different QNMs should be consistent with each other, while in the presence of an alternative theory, the pairs of values could deviate from each other [192; 212; 214; 253]. Note that more than one QNM is required to perform this analysis. Another method where only one QNM is needed, involves the comparison of estimated parameters in the pre- and post-merger regime. A third method called the "merger-ringdown" test has also been proposed to check for consistency between both regimes [254]. It is based on the relation between the amplitude and phase of the QNMs with the properties of the progenitors.

During the fourth observational run (O4), over a hundred sources have been confidently observed by the LVKCollaboration [47]. Hints of spherical higher harmonics have been found [255] in the full Inspiral-Merger-Ringdown (IMR) waveform for some events. Nevertheless, the signatures of QNMs (analyzing only the ringdown) seem to hide below the noise floor. However, the presence of the first overtone of the dominant QNM, i.e. $(2, 2, 1)$, has possibly been inferred for the first event GW150914 [201; 207] (see the discussion on its detectability [208–211]). As the sensitivity of current and future interferometers increases [53; 82; 247], we expect to be able to detect more QNMs, hopefully already from O4. However, the question of whether a deviation from GR is unmistakably observable remains. Up to the O3 catalog, various analyses were made with results always in accordance with GR [248–251; 256; 257]. A more reliable analysis to confidently discriminate any alternative theory would be to carry out a null hypothesis comparison in a Bayesian analysis. However, this endeavor presents quite a challenge since that means that BH's spectra should be solved for alternative theories. There have been various developments in computing beyond-GR BH's spectra, primarily for static or slowly rotating BHs in different alternative theories, e.g. [234–236; 240], see however [239] for rapidly rotating BHs in effective field theories and references in Sec. 3.7. Given the lack of waveform catalogs including deviations from GR, the best we can do is to allow for deviations from GR in a model-independent way in the injection and search templates.

To the best of my knowledge, when I started this project, nobody had considered the detailed response of LISA in studying QNMs. Therefore, I began with the simplest case, gradually adding more complex features as I progressed. In consequence, the study is divided into two stages. The first stage examines LISA's capability to distinguish and identify different spherical harmonics, referred to as "*Detectability of higher harmonics*". The second stage focuses on identifying deviations from general relativity in the ringdown phase, which I will refer to as "*Detectability of deviations from GR in QNMs.*"

4.1.1 Detectability of higher harmonics

For the *Detectability of higher harmonics*, I use the full IMR waveform and the reason is two-fold. One property of phenomenological waveforms such as IMRPhenom-family [129; 130; 204], besides its rapid generation is that the description of the waveforms is decomposed in terms of spin-weighted spherical harmonics, similar to NR waveforms. Thus, the analysis of harmonics is straightforward. Moreover, phenomenological waveforms, which are parameterized functions dependent on the frequency, can incorporate LISA's response as a transfer function, which also depends on the frequency as we shall see. This approach enables the generation of very fast waveforms for data simulation and inference in the Frequency Domain (FD). Operating in the FD is advantageous because it allows for the diagonalization of the covariance matrix, yielding the Power Spectral Density (PSD).

The frequency-dependent nature of phenomenological waveforms poses a significant challenge for ringdown analysis. Each harmonic exhibits a unique frequency dependence, leading to variations in frequency across harmonics at any given moment. Considering that LISA's response also depends on the frequency, it implies an impossibility to segment the signal precisely at the start of ringdown[1] without contamination because each mode will have a different initial frequency. Using the same frequency grid for all modes will unavoidably introduce pre-ringdown information. Alternatively, one could consider applying a window in the Time Domain (TD) at t_0 for all modes before performing the analysis in the FD. The inconvenience of this method is that any sharp window will introduce leakage in the Fourier transform, and any smooth window will introduce pre-ringdown information. This obstacle can be avoided by conducting the entire analysis in the TD. Nevertheless, this approach has its challenges. Computing each likelihood in the TD adds extra complexity because the covariance matrix can no longer be diagonalized. Additionally, one must consider the increased computational time required for the (inverse) Fourier transform and the high numerical sensitivity of the manipulation of matrices.

Another reason to use the full IMR waveform is that the decomposition is done in

---

[1] The start of the ringdown is ill-defined, but in general, one uses the luminosity peak as a reference point. See Sec. 3.6.1 and references therein.

terms of spherical harmonics. However, during the ringdown phase, the use of spheroidal harmonics inherently leads to mode mixing [2]. Phenomenological waveforms are calibrated to NR waveforms but use the first order approximation for spherical-spheroidal mixing ${}_sS_{lm}(\theta, \phi, a\tilde{\omega}) \simeq {}_sY_{lm}(\theta, \phi)$. Consequently, the ringdown regime of these waveforms is not suited to be described as QNMs solutions with high precision. Due to these constraints, I assess the detectability of higher harmonics through the detection of spherical harmonics in the full IMR waveform, postponing the QNMs analysis for the second stage.

Investigating the role of higher harmonics in MBHB signals is essential because of the high SNR these events will have in LISA. The analysis of such strong signals will be sensitive to many subdominant features in the waveform and, in particular, to higher harmonics beyond the dominant $(2, 2)$ mode. Modes with different m are often considered orthogonal since their phases scale differently with the orbital phase as $m\phi_{\mathrm{orb}}$, leading to destructive interference. In LISA, this is no longer the case for the merger-ringdown phase, where a large SNR is accumulated over only a few wave cycles. Cross-terms of the harmonics yield an SNR contribution in the likelihood, which can also affect the parameter inference. Thus, the absence of higher harmonics in the template will induce biases in the parameter estimation.

The correct estimation of the parameters of the full waveform is crucial, in particular, to test the *no-hair* theorem. In one of the methods introduced in Sec. 4.1 to test GR in the ringdown, the estimated final parameters from the full IMR or pre-merger waveform are compared with those obtained from the ringdown [249]. The difference between these two sets of estimated parameters could be understood as a possible deviation from GR. Therefore, one should know the intrinsic parameters such as the total mass M, the mass ratio q, and the individual spins S_i of the initial BHs with enough accuracy and precision to avoid possible biases. Keep in mind that with the progenitors' parameters, one can compute the values of final mass and spin (M_f, a_f) (see, e.g., [129; 258]), thus allowing one to perform BH spectroscopy. Nonetheless, one should also determine the extrinsic parameters from the IMR or premerger estimation to analyze the ringdown regime.

Before this work, the full LISA response (including high-frequency effects) had not been taken into account to study ringdown signals. In this study, I evaluate our ability to identify and differentiate modes of a plausible source detected by LISA and investigate the possible consequences of ignoring modes. To this end, I make use of the software `lisabeta` [259], which incorporates LISA's response to the source waveform, as described in Sec. 4.2.1. I then explain the study methodology in Sec. 4.4, including the analysis of the contribution of the modes to the total SNR for general cases. Results and discussions are given in the next chapter.

4.1.2 Detectability of GR deviations with QNMs

In this exploratory study, I address the question of the extent to which LISA becomes sensitive to a deviation from GR in the ringdown phase of BHB coalescence. Possible devi-

---

[2] See Sec. 3.6.

ations from GR with LISA sources have been studied in [260] using the pSEOBNRv5HM waveform [257; 261]. In that work, the full IMR has been taken into account to find deviations present only in the ringdown. While using the full IMR is an advantage for low SNR sources it has its downside for high SNR, as systematic errors in the full IMR waveform, derived from the non-inclusion of eccentricity, precession or higher harmonics might bias the estimated parameters of the remnant. In this work, I consider a more flexible prior knowledge of parameters, assuming a raw posterior distribution of the final BH parameters estimated from the IMR as uniform priors for this analysis. Moreover, in [260], the analysis assumes deviations in the spherical harmonics representation, while I perform the study with possible deviations in the QNMs, that is, the spheroidal harmonics representation. I use two approaches to analyze LISA sensitivity to detect deviations from GR, namely an *agnostic* approach and the *deviations* approach, as we shall see in Sec. 4.5. I will also discuss the outcome of different assumptions on the priors.

This study is performed in the time domain. The description of the ringdown as a superposition of waves characterized by the QNMs is well defined in the TD, as well as the starting point of the signal[3]. The inclusion of LISA's response in the TD is also possible, but this approach requires more computational time compared to the FD. Several tools, such as `LISA gwresponse`, `PyTDI` and `LISAinstrument` packages [262–264], are available to simulate noise and data in the TD. However, these tools are computationally expensive, as they were designed for robust data simulation rather than for data analysis. Therefore, the development of a particular code to generate fast ringdown signals, incorporating the response of LISA and a TD data analysis framework is needed.

My contribution to the LISA community includes not only the analyses detailed below but also the development of a code in collaboration with J-B. Bayle and Q. Baghi [265], which will soon be publicly available. This code `Lisaring`, facilitates TD data analysis for MBHB sources. A key advantage of this code is its flexibility, as various theories or tests can easily be included. For instance, I will soon incorporate tools to perform the analysis and parameter estimation of signals with memory effect [266]. The memory effect is the signature of the passage of a GW, where the relative distances of freely falling observers are permanently modified with respect to the original ones. In particular, the displacement or non-linear memory effect is a prediction of GR that could be observable with LISA [267]. The ultimate goal is to develop a GR-test pipeline for MBHBs, that would constitute another piece of the global fit puzzle.

4.2 LISA Response

This section describes the transformation of a signal when it enters the LISA detector, which is crucial to performing reliable data analysis. In the traceless-transverse gauge, the gravitational strain is expressed as [2]

---

[3] Although the physical starting point of the ringdown is not well-defined, the start of a signal at t_0 is.

$$h^{TT} = \mathbf{e}_+ h_+ + \mathbf{e}_\times h_\times, \tag{4.2.1}$$

where functions $\mathbf{e}_{+,\times}$ are the polarization tensors given by

$$\begin{aligned}\mathbf{e}_+ &= \vec{u}\otimes\vec{u} - \vec{v}\otimes\vec{v},\\ \mathbf{e}_\times &= \vec{u}\otimes\vec{v} + \vec{v}\otimes\vec{u}.\end{aligned} \tag{4.2.2}$$

The vectors $\vec{v}$ and $\vec{u}$ together with the propagation vector $\vec{k}$, in spherical coordinates, locate the source in the observational frame,

$$\vec{u} = \{\sin\lambda, -\cos\lambda, 0\}, \tag{4.2.3a}$$
$$\vec{v} = \{-\sin\beta\cos\lambda, -\sin\beta\sin\lambda, \cos\beta\}, \tag{4.2.3b}$$
$$\vec{k} = \{-\cos\beta\cos\lambda, -\cos\beta\sin\lambda, -\sin\beta\}. \tag{4.2.3c}$$

In the Solar System Barycenter (SSB) frame, β, λ is the ecliptic latitude and ecliptic longitude respectively, see Fig. 4.1a for a visual representation.

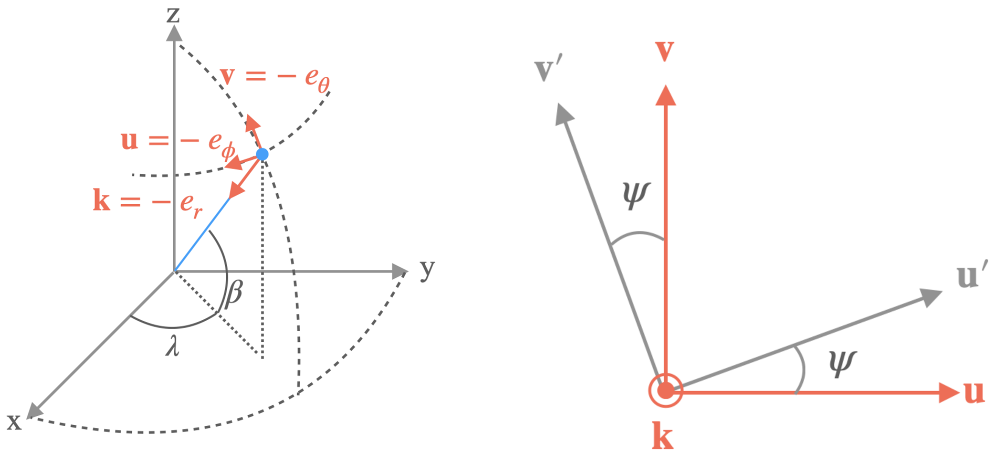

(a) Source location in the SSB frame (b) Polarization angle

Figure 4.1: Geometric representation of the localization of the source in the SSB frame.

There is another degree of freedom characterized by the polarization angle ψ introduced by a rotation along the propagation vector between the source frame and the SSB frame, see Fig. 4.1b for a sketch. In the SSB frame, the transformation of the polarization tensors reads

$$\begin{aligned}\epsilon_+ &= \mathbf{e}_+\cos 2\psi + \mathbf{e}_\times \sin 2\psi,\\ \epsilon_\times &= -\mathbf{e}_+\sin 2\psi + \mathbf{e}_\times\cos 2\psi.\end{aligned} \tag{4.2.4}$$

Combining all the geometric definitions, the source's gravitational strain projected onto the arms of LISA in the direction of the propagation of the laser $\hat{\mathbf{n}}$, reads

$$\begin{aligned} H_{rs}(t) &= \hat{\mathbf{n}}_{rs}(t)\left[\epsilon_+ h_+(t) + \epsilon_\times h_\times(t)\right]\hat{\mathbf{n}}_{rs}(t), \\ &= \left(h_+(t)\cos 2\psi\, - h_\times(t)\sin 2\psi\right)\, \hat{\mathbf{n}}_{rs}(t)\cdot\mathbf{e}_+\cdot\hat{\mathbf{n}}_{rs}(t) \\ &\quad + \left(h_+(t)\sin 2\psi\, + h_\times(t)\cos 2\psi\right)\, \hat{\mathbf{n}}_{rs}(t)\cdot\mathbf{e}_\times\cdot\hat{\mathbf{n}}_{rs}(t), \end{aligned} \tag{4.2.5}$$

where 'r' stands for receiver and 's' stands for sender. That means that those letters take the values 1,2 or 3, according to the three S/Cs. Consequently, the are two measurements per pair of S/Cs, one in each direction, resulting in six combinations [4]. The unit vector $\hat{\mathbf{n}}_{rs}$ is the vector from the emitting to the receiving S/C, thus denoting the laser trajectory, as shown in Fig. 4.2.

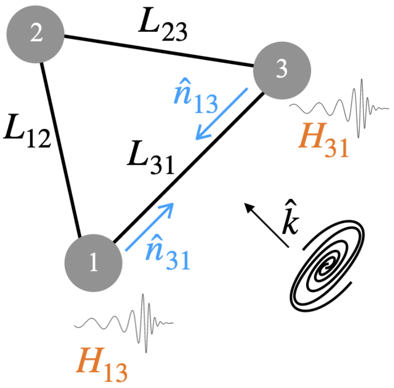

Figure 4.2: Representation of the gravitational strain projected onto the LISA arms depending on the direction of propagation of the lasers.

The output data from a GW signal seen by LISA will be transformed because of the synthetic transponder arm introduced in Secs. 2.5.2 and 2.5.3. To simulate the transfer function applied onto a GW signal, let us study the trajectory of a photon from the laser source generated in S/C$_3$ facing S/C$_1$. In the presence of a perturbation, the line element of a photon can be written as

$$\begin{aligned} ds^2 &= (\eta_{\alpha\beta} + h_{\alpha\beta})dx^\alpha dx^\beta \\ &= -c^2dt^2 + (\delta_{ij} + h_{ij})\, dx^i dx^j. \end{aligned} \tag{4.2.6}$$

Then, the time that the photon takes to travel from one S/C to the other, i.e. the light travel time (ltt), is given by

$$\int dt = \frac{1}{c}\int_{\vec{x}_3}^{\vec{x}_1} \sqrt{\delta_{ij} + h_{ij}dx^i dx^j}. \tag{4.2.7}$$

---

[4] Note the ordering of those indices, which follows the last convention adopted in [92].

Note that instead of the gravitational strain, we want to measure the time-dependent gravitational strain as seen by LISA, then we exchange $h_{ij} \to H_{rs}(t)$, also note that the space interval is just the arm length between the two S/Cs, i.e. L$_{31}$, and that the time is already measured in a unique time reference t, being t_1 the departure time from S/C$_1$ and t_3 the arrival time at S/C$_3$. In the case of a moving constellation, the measured strain H_{ij}, defined in Eq. (4.2.5), will depend on the position of the detector, which varies with time. Consequently, one can write the integration of the the strain depending on the position of measurement $\vec{x}(r')$, as

$$\int_{t_1}^{t_3} dt' \simeq \frac{1}{c} \int_0^{L_{31}} \sqrt{1 + H_{31}(t(r'), \vec{x}(r'))dr'}, \tag{4.2.8}$$

which expanded in a series of Taylor at first order, leading to

$$\int_{t_1}^{t_3} dt' \simeq \frac{1}{c} \int_0^{L_{31}} 1 + \frac{1}{2} H_{31}(t(r'), \vec{x}(r'))dr', \tag{4.2.9}$$

In general, the arm length L$_{31}$ will not remain constant, as both S/Cs slowly move through space, then $L_{31} \to L_{31}(\vec{x}(t))$. However, as an approximation, one can assume that the distance of the S/Cs remains constant by fixing the ltt at ~ 8.3 s, simulating fixed arm length [5]. While this assumption will not have a large impact on the low-frequency response, it will affect high frequencies and thus, its variation must be considered in a "real-like" simulation. Hence, the position of the photon can be approximated to the departure's position from S/C$_1$, plus the distance traveled in the $\hat{n}_{31}$ direction, and analogously for the time, then

$$\vec{x}(r') \simeq \vec{x}_1(t_1) + r' \cdot \hat{\mathbf{n}}_{31}(t_1), \tag{4.2.10}$$

$$t(r') \simeq t_1 + r'/c \tag{4.2.11}$$

Now, if we want to measure the projected strain H_{31} at a given time t', one should consider the time t at which the GW crossed the arm at a given position, plus the time it took a photon in that point, to arrive to the detector, i.e the retarded time. This allows one to write the projected GW on the L_{31} path as

$$H_{31}(\vec{x}(r'), t(r')) \to H_{31}\left(t(r') - \frac{\vec{k} \cdot \vec{x}(r')}{c}\right) \tag{4.2.12}$$

$$= H_{21}\left(t_1 - \frac{\vec{k} \cdot \vec{x}_1(t_1)}{c} + \frac{1 - \vec{k} \cdot \hat{\mathbf{n}}_{31}(t_1)}{c} r'\right), \tag{4.2.13}$$

where $\vec{k}$ is the propagation vector of the GW defined in Eq. (4.2.3). Then, the ltt becomes

$$t_3 \simeq t_1 + \frac{L_{31}}{c} + \frac{1}{2c} \int_0^{L_{31}} H_{31}\left(t_1 - \frac{\vec{k} \cdot \vec{x}_1(t_1)}{c} + \frac{1 - \vec{k} \cdot \hat{\mathbf{n}}_{31}(t_1)}{c} r'\right) dr'. \tag{4.2.14}$$

---

[5] Keep in mind that ~ 8.3 s is the time that a photon takes to travel 2.5×10^6 km.

In Sec. 1.3, I said that since the Michelson interferometer is sensitive to frequencies and phases, then we should try to obtain this equation in terms of the frequency shift, which can be obtained by integrating and computing its derivative with respect to the emitted time t_1, arriving to

$$y_{31}(t_1) \simeq \frac{1}{2\left(1-\vec{k}\cdot\hat{\mathbf{n}}_{31}(t_1)\right)}\left[H_{31}\left(t_1-\frac{\vec{k}\cdot\vec{x}_1(t_1)}{c}\right)-H_{31}\left(t_1-\frac{\vec{k}\cdot\vec{x}_3(t_3)}{c}+\frac{L_{31}}{c}\right)\right] \tag{4.2.15}$$

where $\vec{x}_3(t_3) \simeq \vec{x}_1(t_1)+L_{31}\hat{\mathbf{n}}_{31}(t_1)$ is the receiver position at reception time. Note that the above equation depends on both, the emission and the reception time t_1, t_3, however, it is possible to write it only in terms of the reception time t_3. If one assumes that the S/Cs move slowly enough, such that $\vec{x}_1(t_1) \simeq \vec{x}_1(t_3)$ and thus $\mathbf{n}_{31}(t_1) \simeq \mathbf{n}_{31}(t_3)$, one can write the link response for any pair of receiving, emitting S/Cs indexed by r, s as

$$y_{rs}(t_r) \simeq \frac{1}{2\left(1-\vec{k}\cdot\hat{\mathbf{n}}_{rs}(t_r)\right)}\left[H_{rs}\left(t_r-L_{rs}(t_r)-\vec{k}\cdot\vec{x}_r(t_r)\right)-H_{rs}\left(t_r-\vec{k}\cdot\vec{x}_s(t_r)\right)\right], \tag{4.2.16}$$

where I used $c = 1$. Keep in mind that these links' responses are the inputs to generate the TDI channels X, Y, and Z, introduced in Sec. 2.5.3 as

$$\begin{aligned} X = & \left(1-D_{121}-D_{12131}+D_{1312121}\right)\left(y_{13}+D_{13}y_{31}\right) \\ & -\left(1-D_{131}-D_{13121}+D_{1213131}\right)\left(y_{12}+D_{12}y_{21}\right) \end{aligned} \tag{4.2.17}$$

where D_{ij} is the delay operator and its combined operator reads,

$$D_{rs}\, f(t) = f\left(t-L_{rs}(t)\right), \qquad D_{i_1 i_2 \cdots i_n} = D_{i_1 i_2} D_{i_2 i_3} \cdots D_{i_{n-1} i_n}. \tag{4.2.18}$$

with $f(t)$ any function dependent on t and where the quasi-orthogonal channels are constructed by

$$A = \frac{1}{\sqrt{2}}(Z-X), \tag{4.2.19a}$$

$$E = \frac{1}{\sqrt{6}}(X-2Y+Z), \tag{4.2.19b}$$

$$T = \frac{1}{\sqrt{3}}(X+Y+Z). \tag{4.2.19c}$$

Indeed, the orbital motion of the constellation translates into a time variation in the orientation of the detector relative to the SSB frame. Note that this introduces modulations on the signal observed by LISA, as is noticeable from the explicit time-dependent functions, and the delays in the instrumental response given by Eqs. (4.2.5), (4.2.16) and (4.2.17). In LISA's frequency band, the observation of MBHBs can last from days to weeks, depending on the total mass and frequency evolution. Consequently, their waveforms can strongly be affected by these modulations. In other words, the time delays and the variation of those delays will leave an imprint on the measured signal.

Depending on the signal that one wants to study, it is convenient to work in the time domain or the Fourier domain. Another method called wavelets, considering the time-to-frequency correspondence is also possible, however not used here, see e.g. [268]. While working in the TD, the response of LISA can be included rather in a straightforward way through the previous equations, its inclusion in the FD requires some computation.

4.2.1 Response in Fourier domain

An interesting feature about working in Fourier's domain, besides the uncorrelated noise that can be diagonalized, is that the waveform can be completely characterized for each mode by an amplitude and a phase. In terms of the response of LISA, it was shown e.g. in [269], that the modulations and delays introduced by LISA can be interpreted as a transfer function. I proceed to describe this operation, for which I need to recall the MBHB waveforms. This section is based on [11; 269; 270].

MBHB waveform

The full IMR strain of an MBHB can be decomposed in spin-weighted spherical harmonics, such that

$$\tilde{h}(f) = \sum_{l\geq 2} \sum_{m=-l}^{l} {}_{-2}Y_{lm}(\iota,\varphi)\tilde{h}_{lm}(f), \tag{4.2.20}$$

where ${}_{-2}Y_{lm}$ is the gravitational field spherical harmonics defined in Eq. (3.4.40), the inclination and the initial phase are denoted by (ι,φ), which I drop in the following for clarity. Note that I use the inclination instead of θ to define the angle between the normal of the orbital plane and the line of sight. Consequently, each polarization can be written in terms of the modes as

$$\tilde{h}_+ = \frac{1}{2}\sum_{l,m}\left(Y_{lm}\tilde{h}_{lm} + Y^*_{l-m}\tilde{h}^*_{lm}\right), \tag{4.2.21a}$$

$$\tilde{h}_\times = \frac{1}{2}\sum_{l,m}\left(Y_{lm}\tilde{h}_{lm} - Y^*_{l-m}\tilde{h}^*_{lm}\right). \tag{4.2.21b}$$

The gravitational strain h_{lm} for each mode in the full IMR waveform can be described in terms of an amplitude A_{lm} and a phase Φ_{lm}, both depending on the intrinsic parameters of the source and the frequency, as follows

$$\tilde{h}_{lm}(f,\Xi) = A_{lm}(f,\Xi)\, e^{i\Phi_{lm}(f,\Xi)}. \tag{4.2.22}$$

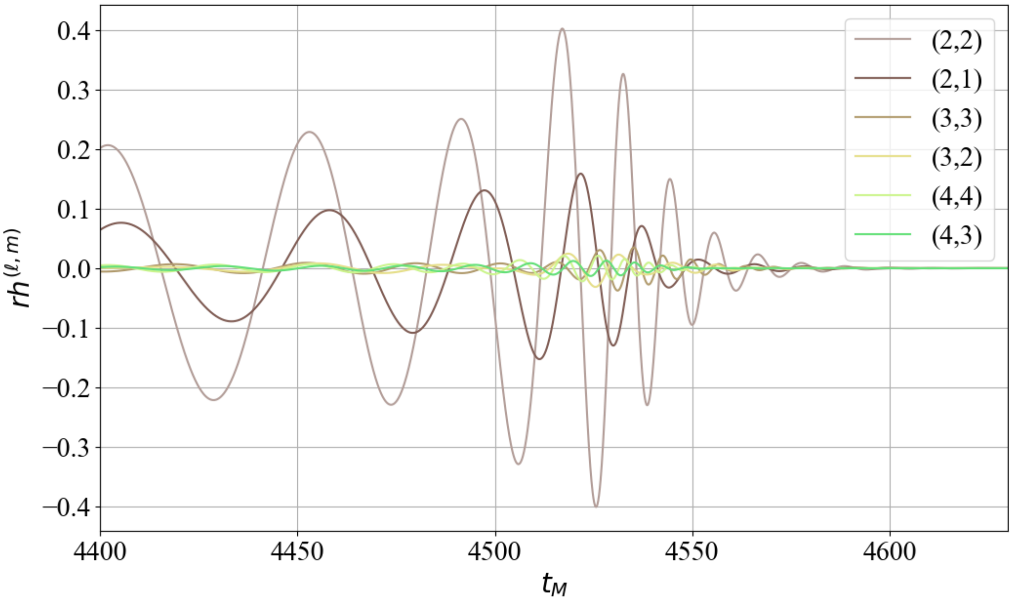

Figure 4.3: Decomposition of the gravitational strain h_{lm} in the time domain, in its spherical components labeled by the angular numbers (l, m) indicated in the legend. *Produced with* `BH toolkit` *package* [271].

In phenomenological waveforms, the amplitude and phase for each mode are expressed as concatenations of three polynomial functions of frequency, corresponding to the inspiral, merger, and ringdown stages. These functions have coefficients calibrated to PN, NR, and/or sEOBNR waveforms. A visual representation in the time domain of an NR waveform decomposed in spherical harmonics is shown in Fig. 4.3.

Non-precessing binary systems have an advantageous symmetry relation between prograde m and retrograde $-m$ modes given by

$$\tilde{h}_{l-m}(f) = (-1)^l \tilde{h}^*_{lm}(-f). \tag{4.2.23}$$

Note that here the definition of prograde and retrograde modes differs from the one used for QNMs in Sec. 3.6. In the case of an isolated BH, there is no orbital angular momentum to refer to, and the direction of the modes depends solely on the direction of its angular momentum J. However, in the case of a binary system, where each BH's spin and the orbital angular momentum can have a different orientation, the orbital referential frame is used to define prograde or retrograde modes, regardless of the total angular momentum. In addition, an approximation often employed in the FD is to consider only positive or negative frequencies, in consequence, we have

$$\tilde{h}_{lm}(f) \simeq 0 \,\text{for}\, m > 0,\ f < 0, \tag{4.2.24a}$$
$$\tilde{h}_{lm}(f) \simeq 0 \,\text{for}\, m < 0,\ f > 0, \tag{4.2.24b}$$

$$\tilde{h}_{l0}(f) \simeq 0. \tag{4.2.24c}$$

This approximation allows us to describe each polarization as

$$\tilde{h}_{+,\times}(f) = \sum_{l} \sum_{m>0} K_{lm}^{+,\times} \tilde{h}_{lm}(f), \tag{4.2.25}$$

where I introduce

$$K_{lm}^{+} = \frac{1}{2} \left({}_{-2}Y_{lm} + (-1)^l {}_{-2}Y_{l-m}^{*} \right), \tag{4.2.26a}$$

$$K_{lm}^{\times} = \frac{i}{2} \left({}_{-2}Y_{lm} - (-1)^l {}_{-2}Y_{l-m}^{*} \right). \tag{4.2.26b}$$

Combining previous equations, one obtains the final expression for the strain observed by LISA in the SSB frame as

$$\tilde{h}^{SSB}(f) = \sum_{l,m} P_{lm} \tilde{h}_{lm}(f), \tag{4.2.27}$$

where

$$\begin{aligned} P_{lm} &= \epsilon_{+} K_{lm}^{+} + \epsilon_{\times} K_{lm}^{\times} \\ &= \frac{1}{2} \left[{}_{-2}Y_{lm} (\mathbf{e}_{+} + i\, \mathbf{e}_{\times}) e^{-2i\psi} + (-1)^l {}_{-2}Y_{l-m}^{*} (\mathbf{e}_{+} - i\, \mathbf{e}_{\times}) e^{2i\psi} \right]. \end{aligned} \tag{4.2.28}$$

Note that P_{lm} depends not only on (l, m) and (ι, φ) due to the spherical harmonics, but also on the parameters defining the reference frame, such as the sky localization (β, λ) and the polarization ψ introduced in Eqs.(4.2.2), (4.2.3) and (4.2.4).

Modulation and time delays in FD

A time modulation $F(t)$ to a time-varying delay $D(t)$ in the strain can be expressed as [269]

$$s(t) = F(t) h_D(t), \quad \text{where } h_D(t) = h(t + D(t)). \tag{4.2.29}$$

With the convention to Fourier transform a function F being

$$\tilde{F}(f) = \int dt\, e^{2i\pi f t} F(t), \tag{4.2.30}$$

a time delay in the frequency domain takes the form

$$h_D(t) = \int df\, e^{-2i\pi f (t + D(t))} \tilde{h}(f). \tag{4.2.31}$$

Now, if one performs a Fourier transformation with the modulation $F(t)$ and the delay $D(t)$, it could be expressed as [269]

$$\begin{aligned}\tilde{s}(f) &= \int dt\, e^{2i\pi f t} F(t) \int df'\, e^{-2i\pi f'(t+D(t))} \tilde{h}(f') \\ &= \int df' \tilde{h}(f-f') \int dt\, e^{2i\pi f t} \underbrace{e^{-2i\pi(f-f')D(t)} F(t)}_{G(f-f',t)} .\end{aligned} \tag{4.2.32}$$

The second term can be related to a frequency-dependent function of time $G(f,t)$ and thus its transformation will be $\tilde{G}(f,f')$. Note that $\tilde{h}(f-f')$ appears because of the delay, which can be Taylor expanded to recover the leading order in time. Then, it is possible to approximately express the response of each link in terms of the spherical harmonics in the frequency domain as

$$\tilde{y}_{rs}(f) = \sum_{lm} \mathcal{T}^{lm}_{rs}(f)\, \tilde{h}_{lm}(f), \tag{4.2.33}$$

where $\mathcal{T}^{lm}_{rs}(f) = G^{lm}_{rs}(f, t^{lm}_f)$ is the kernel carrying information on the modulation and time-delay of the links response. It is defined as [269]

$$\begin{aligned} G^{lm}_{rs}(f,t) =& \frac{i\pi f L_{rs}}{2} \operatorname{sinc}\Big[\pi f L_{rs} \left(1 - \vec{k}\cdot \hat{\mathbf{n}}_{rs}(t)\right)\Big] \times \\ & e^{i\pi f \left(L_{rs} + \vec{k}\cdot[\vec{x}_r(t) + \vec{x}_s(t)]\right)}\, \hat{\mathbf{n}}_{rs}(t)\cdot P_{lm} \cdot \hat{\mathbf{n}}_{rs}(t). \end{aligned} \tag{4.2.34}$$

The way to relate the frequency variation with time is through a time-to-frequency correspondence such as in the Stationary Phase Approximation (SPA), see [272; 273] for more information. This approximation works only for the slowly increasing phase, namely the inspiral-merger part, however, it is possible to extend it to the merger-ringdown when defined as [269; 270]

$$t^{lm}_f \equiv -\frac{1}{2\pi}\frac{d\Phi^{lm}}{df}. \tag{4.2.35}$$

To simplify the transfer function in the frequency domain, some assumptions can be made:

- the arm length is the same in both directions since the motion of the beam relative to the S/C is not taken into account, i.e. $L_{12} = L_{21}$;
- the constellation forms an equilateral triangle, then the arms will remain equal and constant, i.e. $L_{12} = L_{23} = L_{31} = L$.

Using these assumptions and after factoring out several terms, one can write the response in terms of channels A, E, T as

$$\tilde{A} = \frac{i\sqrt{2}\sin(2\pi f L)}{e^{-2i\pi f L}} \left[(1+z)(\tilde{y}_{13} + \tilde{y}_{31}) - \tilde{y}_{32} - z\tilde{y}_{23} - \tilde{y}_{12} - z\tilde{y}_{21}\right], \tag{4.2.36a}$$

$$\tilde{E} =\frac{i\sqrt{2}\sin(2\pi fL)}{\sqrt{3}e^{-2i\pi fL}}\left[(1-z)(\tilde{y}_{31}+\tilde{y}_{13})+(2+z)(\tilde{y}_{21}-\tilde{y}_{23})+(1+2z)(\tilde{y}_{12}-\tilde{y}_{32})\right], \tag{4.2.36b}$$

$$\tilde{T} =\frac{4\sin(\pi fL)\sin(2\pi fL)}{\sqrt{3}e^{-3i\pi fL}}\left[\tilde{y}_{12}-\tilde{y}_{21}+\tilde{y}_{23}-\tilde{y}_{32}+\tilde{y}_{31}-\tilde{y}_{13}\right], \tag{4.2.36c}$$

with $z \equiv e^{2i\pi fL}$. Note that, under these assumptions, the response is for a detector with a fixed triangular equilateral setup.

4.3 Bayesian inference

In a Bayesian analysis, the posterior distribution of a set of parameters $\boldsymbol{\theta}$ for a given model M on the observed data d, is expressed as

$$p(\boldsymbol{\theta}|d,M)=\frac{p(d|\boldsymbol{\theta},M)\,p(\boldsymbol{\theta}|M)}{p(d|M)}, \tag{4.3.1}$$

where $p()$ is the probability, $\boldsymbol{\theta}$ are the physical parameters of the source, M is the model or any other context considered. The first term in the numerator $p(d|\boldsymbol{\theta},M)$ is the likelihood, also denoted as $\mathcal{L}(\boldsymbol{\theta})$. The second term in the numerator $p(\boldsymbol{\theta}|M)$ is the prior of the parameters, usually denoted as $\pi(\boldsymbol{\theta})$, and $p(d|M)$ in the denominator is the evidence $\mathcal{Z}$ or marginal likelihood, which is computed as the integral of the likelihood over the whole parameter's hyper-volume,

$$\mathcal{Z}=\int_{\Theta}\mathcal{L}(\boldsymbol{\theta})\pi(\boldsymbol{\theta})d\boldsymbol{\theta}. \tag{4.3.2}$$

In the following, I drop the indication of the model M unless explicitly needed.

The likelihood for a Gaussian noise with a covariance matrix $\mathbf{C}$ takes the form

$$\mathcal{L}=\frac{1}{\sqrt{\det(2\pi\mathbf{C})}}e^{-\frac{1}{2}(d-h(\boldsymbol{\theta}))^{\dagger}\mathbf{C}^{-1}(d-h(\boldsymbol{\theta}))}, \tag{4.3.3}$$

which can be written as

$$\begin{aligned}\ln\mathcal{L}&=-\frac{1}{2}(d-h(\boldsymbol{\theta})|d-h(\boldsymbol{\theta}))-\frac{1}{2}\ln(\det(2\pi\mathbf{C}))\\&=(d|h(\boldsymbol{\theta}))-\frac{1}{2}(h(\boldsymbol{\theta})|h(\boldsymbol{\theta}))-\frac{1}{2}(d|d).\end{aligned} \tag{4.3.4}$$

Here, I used that the last term in the first equation is a constant and can be neglected, the same applies to the last term in the second equation since it does not depend on the estimated parameters and represents a multiplicative constant in the likelihood. I also used the definition of the noise-weighted inner product, which in the frequency domain is given by

$$(\tilde{a}|\tilde{b})=4\mathrm{Re}\int_0^{\infty}\frac{\tilde{a}(f)\tilde{b}^{*}(f)}{S_n(f)}df, \tag{4.3.5}$$

where S_n is the noise's PSD and the asterisk $(^*)$ denotes the complex conjugate. The noise-weighted inner product in the time domain reads

$$(a|b) = \sum_{i,j=0}^{N-1} a_i \mathbf{C}_{ij}^{-1} b_j, \tag{4.3.6}$$

where i and j run over the covariance matrix elements given by the total time $\sum t_i = N \cdot \Delta t = T$. The full log-likelihood is a sum over the log-likelihoods of the uncorrelated instrumental channels A, E, T,

$$\ln \mathcal{L} = \sum_{I=A,E,T} \ln \mathcal{L}_I \tag{4.3.7}$$

In general, I will ignore channel T, as it is not very sensitive to GWs [104].

At the maximum value of the likelihood, the estimated waveform agrees with the injected signal. That is when $h(\boldsymbol{\theta}) = d$, then Eq. (4.3.4) takes a zero value corresponding to the maximum likelihood. Consequently, the parameters that return the maximum likelihood will be the parameters that coincide with the injected ones. It is worth mentioning that this is true when the waveform model agrees with the true one, keeping in mind that there are several waveforms with more or less parameters that could fit well the data. Nonetheless, only one waveform model would be the correct one. In this Bayesian framework, there exists a way to compute the preference of the data towards one model over another. It is given by the Bayes factor $\mathcal{B}$, defined as the ratio of the evidence of two models

$$\mathcal{B} = \frac{\mathcal{Z}_\alpha}{\mathcal{Z}_\beta} \frac{\pi(M_\alpha)}{\pi(M_\beta)} \quad \rightarrow \quad \log \mathcal{B} = \log \mathcal{Z}_\alpha - \log \mathcal{Z}_\beta. \tag{4.3.8}$$

This means that if the log of the Bayes factor is positive, the evidence of model α is higher than the evidence of the model β, and thus the data is better explained by the model α than by the model β. Note that I assumed the same prior belief for both models $\pi(M_\alpha) = \pi(M_\beta)$ to arrive at the right-hand side equation.

4.4 Detectability of higher harmonics

This section is based on the published article "Detectability of higher harmonics with LISA" [132] written by me and collaborators. However, some modifications were made for a better integration into the manuscript.

This study aims to quantify the ability of LISA to identify the presence of different spherical harmonics in an MBHB event. The detectability of the modes is related to the total SNR, but also to the relative SNR of the modes. In this framework, there are two main parameters to consider in the computation of the SNR: the luminosity distance (D_l) and the mass (M). While the distance is just a scaling factor that affects all modes similarly, the mass moves the signal to lower and higher frequencies affecting the relative weight of the inspiral and merger-ringdown. Since the observed signal is characterized by the redshifted mass, I will distinguish between the source-frame mass and the observed (redshifted) mass.

As an analogy to the luminosity peak in the time domain, I use here an *ad-hoc* frequency-domain definition of a *frequency peak* as the frequency at the maximum value of the observed characteristic rescaled TDI variables[6] for each mode, which I introduce below. This re-scalization serves to avoid an infinity SNR at the zeros of the PSD as a consequence of the arm length's resonances. They are defined as [270]

$$\tilde{a}, \tilde{e} = \frac{e^{-2i\pi f L}}{i\sqrt{2}\sin(2\pi f L)} \times \tilde{A}, \tilde{E}, \tag{4.4.1a}$$

$$\tilde{t} = \frac{e^{-3i\pi f L}}{2\sqrt{2}\sin(\pi f L)\sin(2\pi f L)} \times \tilde{T}, \tag{4.4.1b}$$

where $\tilde{A}, \tilde{E}$ and $\tilde{T}$ are defined in Eq. (4.2.36). With the time-to-frequency correspondence from Eq. (4.2.35), the frequency peak lies at about $2.4 t_M$ (where $t_M = t\, c^3/M\, G$ is an adimensional quantity) after the time of coalescence. In the observational frame of LISA, this parameter corresponds approximately to the beginning of ringdown regime [7].

The redshifted mass of the source will move the frequency peaks through the spectrum, as shown in Fig. 4.4. This feature translates into a dependency on the contribution of each mode given the sensitivity of LISA at the frequency peaks. For this reason, it is interesting to study the contribution of each mode in terms of the mass. Results are shown in the next Section 4.4.1. Once the contribution of different modes in the general case is known, one can focus on a specific event as an example.

4.4.1 Study of the mode contributions to the SNR

The SNR builds up in time and frequency and is defined by ρ as

$$\rho^2 = \sum_{lm} \sum_{l'm'} \sum_{I=A,E} 4\,\mathrm{Re} \int \frac{\mathcal{H}^I_{lm}(f) {\mathcal{H}^I_{l'm'}}^*(f)}{S_n(f)} df, \tag{4.4.2}$$

where the sum over independent channels (index I) extends over channels A, E with the same PSD noise denoted by S_n. The assumed PSD is drawn from the science requirement model SciRD [274] introduced in Sec. 2.4, including the galactic white dwarf confusion noise with subtraction of identified sources over one year. Note that I use $\mathcal{H}_{lm}$ instead of h_{lm}, because LISA's instrumental response and TDI post-processing combining Eqs. (4.2.33) to (4.2.36) are included. They read

$$\mathcal{H}^a_{lm}(f) = h_{lm}(f) \cdot \frac{i\sqrt{2}\sin(2\pi f L)}{e^{-2i\pi f L}} \cdot \Big[(1 + z(f))(\mathcal{T}^{lm}_{13}(f) + \mathcal{T}^{lm}_{31}(f))$$

---

[6] By characteristic I mean the TDI observed channel multiplied by the frequency. A factor 2 is sometimes introduced in the literature.

[7] Keep in mind the discussion on the starting point of the ringdown in Sec. 3.6.1.

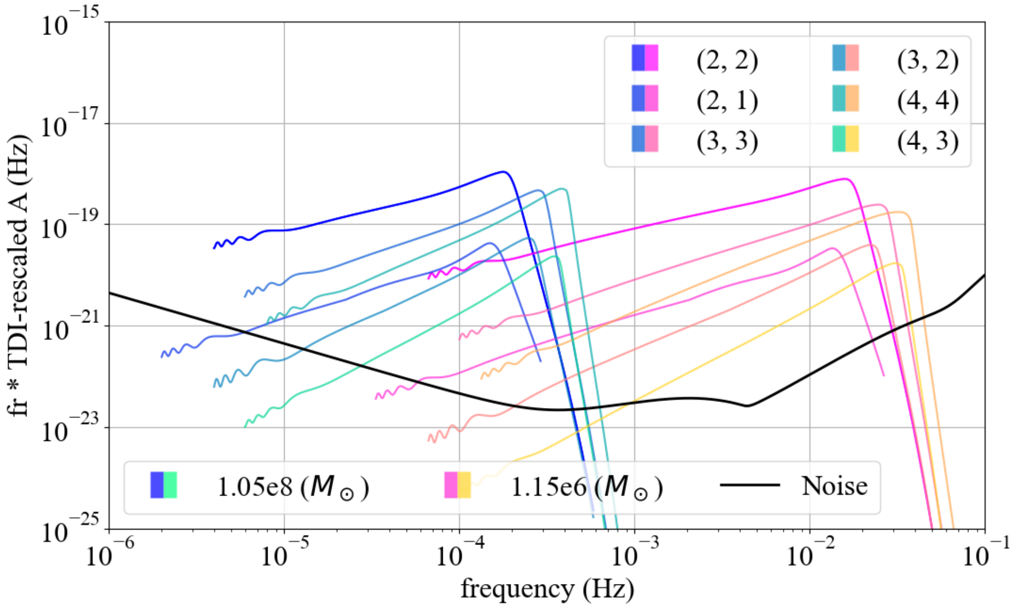

Figure 4.4: Frequency peak dependency of the various harmonic modes for two given sources with different redshifted masses. Cool colors denote a heavy source of $\sim 10^8$ M$_\odot$, while warm colors denote a lighter source of $\sim 10^6$ M$_\odot$.

$$- \mathcal{T}_{32}^{lm}(f) - z(f)\mathcal{T}_{23}^{lm}(f) - \mathcal{T}_{12}^{lm}(f) - z(f)\mathcal{T}_{21}^{lm}(f)\Big] , \tag{4.4.3a}$$

$$\begin{aligned}\mathcal{H}_{lm}^{e}(f) = h_{lm}(f) \cdot \frac{i\sqrt{2}\sin(2\pi f L)}{\sqrt{3}e^{-2i\pi f L}} \cdot \Big[&(1 - z(f))(\mathcal{T}_{31}^{lm}(f) + \mathcal{T}_{13}^{lm}(f)) \\ &+ (2 + z(f))(\mathcal{T}_{21}^{lm}(f) - \mathcal{T}_{23}^{lm}(f)) + (1 + 2z(f))(\mathcal{T}_{12}^{lm}(f) - \mathcal{T}_{32}^{lm}(f))\Big] ,\end{aligned} \tag{4.4.3b}$$

where $z(f) = e^{2i\pi f L}$. For convenience, I use the notation of the inner product of the modes, defined as

$$(lm|l'm') = \sum_{I} 4\,\mathrm{Re} \int \frac{\mathcal{H}_{lm}^{I}(f)\mathcal{H}_{l'm'}^{I}{}^{*}(f)}{S_n(f)} df. \tag{4.4.4}$$

Then the squared SNR can be written as

$$\rho^2 = \sum_{lm} \sum_{l'm'} (lm|l'm'). \tag{4.4.5}$$

In Eq. (4.4.4), the cross-terms $(lm|l'm')$, with $lm \neq l'm'$ have no reason to be positive and can contribute negatively to the total SNR. In other words, the phases can be constructive or destructive, which depend on the values of the ecliptic latitude β and longitude λ, the inclination ι, the phase ϕ, the polarization angle ψ and the mass ratio q. An illustration of this outcome can be seen in Fig. 4.5. For this example, I use the parameters written in Table 4.1 with a redshifted total mass of $\sim 2.44 \times 10^6$ M$_\odot$. In

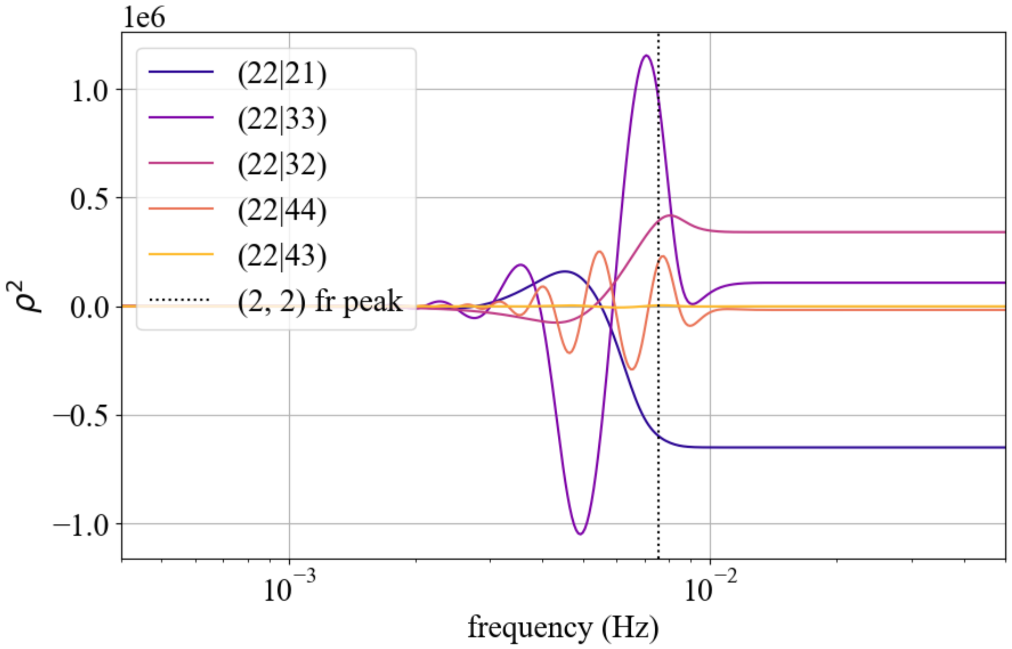

Figure 4.5: Contribution of cross-terms $(22|l'm')$ to ρ^2. We can observe how the cumulative squared SNR changes from positive to negative values and vice-versa until after the ringdown, where it remains constant. The frequency peak of the mode $(2, 2)$ is shown here for guidance. Each mode peaks at a different frequency, so the stabilization period starts at a different point for each pair of modes.

Fig. 4.5, I show the $(22|l'm')$ cross-terms of the accumulated squared SNR ρ^2 varying between positive and negative values depending on the frequency. Note that after a given point towards the end of the coalescence, the SNR remains constant since there is no more contribution either positive or negative. This point is close to the frequency peak for each pair of modes, occurring at a distinct frequency for each mode pair. Therefore, I plot the frequency peak of the $(2, 2)$ mode with a dotted black line as a guide. In Table 4.1, the parameters χ_i represent the aligned dimensionless spin of the two BHs for nonprecessing binaries.

4.4.2 Dependency on mass and frequency

The next natural step to understanding the detectability of modes is to analyze the contribution of each pair of modes to the total SNR for different sources. In general, the SNR depends on all parameters of the source, the distance and the total mass being the dominant ones. To simplify this analysis, I fix most parameters to arbitrary values, listed in Table 4.1 and let the mass vary. Note that the results, particularly the details of the hierarchy between modes and cross-terms, might depend on the choice of the listed parameters. For each source's total mass and frequency bin, I compute the accumulated SNR for each mode and normalize it to the total SNR. Since the ratio of the total mass

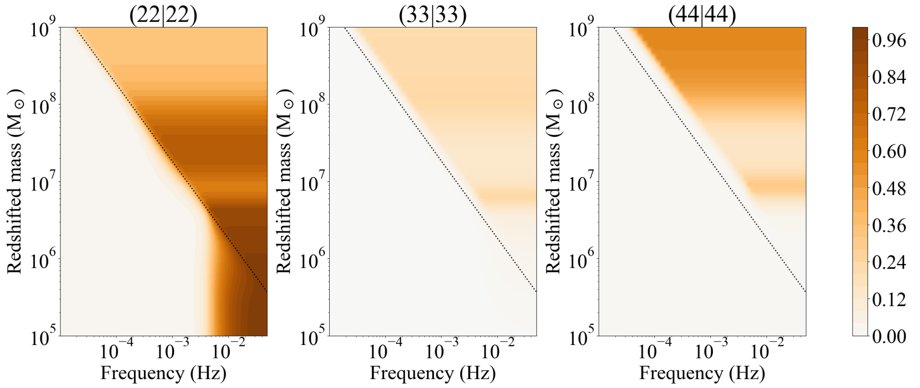

(a) Ratio contribution of the square terms $(lm|lm)$ to the total squared SNR.

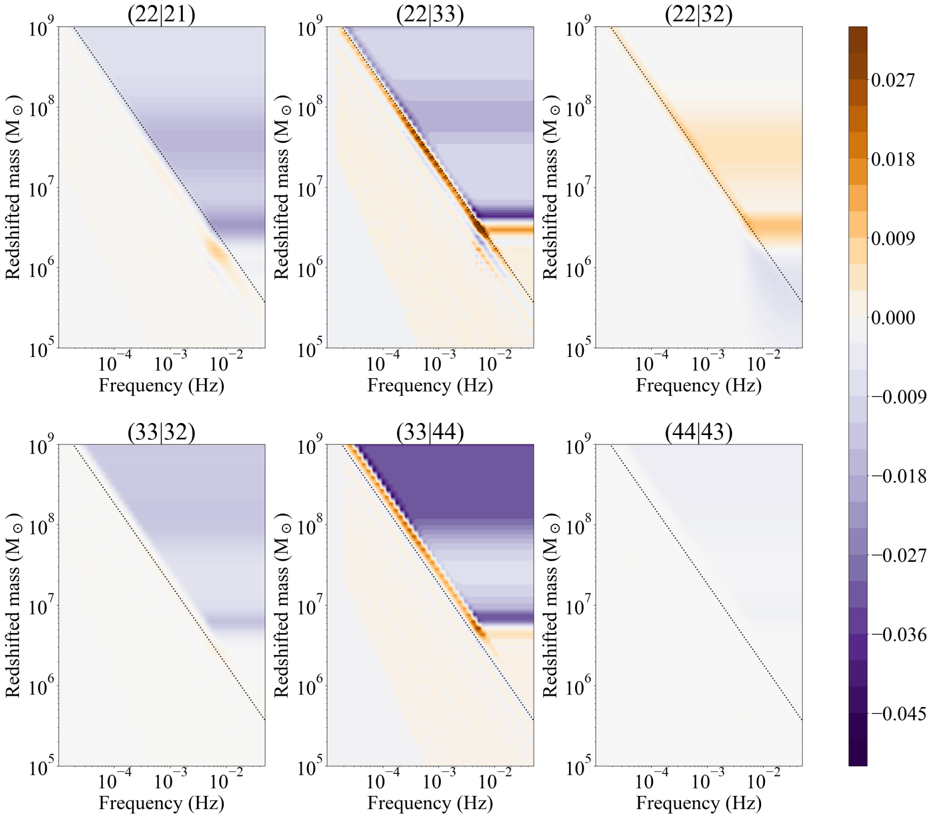

(b) Highest ratio contributions of the cross-terms $(lm|l'm')$ to the total squared SNR.

Figure 4.6: Cumulative contribution to the squared SNR of pairs of modes depending on the total redshifted mass. In the top row, we find the square terms with the largest ratios. The quadrupolar square term represents most of the contribution for low-mass sources, while it slowly decreases for more massive ones. The opposite happens for terms (33|33) and (44|44) albeit to a smaller extent. The cross-terms are shown in the last two rows. They oscillate between $\sim 1\%$ and 5%, especially near the ringdown, illustrated with a dotted line for the mode $(2, 2)$ as guidance. This percentage can represent an SNR of tens for a total SNR of thousands.

Table 4.1: Source parameters in the SSB frame with aligned spins and redshifted masses.

Parameter	Value	Parameter	Value
Mass ($M_\odot$)	$[10^5, 5 \times 10^9]$	β (rad)	$\pi/2$
q (Mass ratio)	2	λ (rad)	π
χ_1	0.5	ϕ (rad)	$\pi/2$
χ_2	0.5	ψ (rad)	$\pi/2$
redshift	3	ι (rad)	$\pi/3$

over the luminosity distance increases for higher masses, the normalization allows me to compare the contribution of each mode regardless of their absolute SNR value.

I gather the results in a set of plots in Figs. 4.6a and 4.6b. Each panel of the figure corresponds to a mode and shows the squared SNR dependence on both the source mass and the observed frequency. Then, for a given mass, we can observe how the squared SNR accumulates in frequency for each pair of modes. Each set of plots has its color bar where warmer colors towards orange-brown correspond to larger accumulated SNR contributions. The numbers at the right of the bars represent the contribution ratio of each pair of modes to the total squared SNR ρ^2. Note that I use squared SNR instead of SNR so that the sum of all contributions is equal to 1. This choice also allows me to highlight the negative contributions that I mentioned before, as well as their direct impact on the likelihood, see Eqs. (4.3.4) and (4.4.5). That said, the most noticeable feature is the positive contribution of the square terms $(lm|lm)$ over all the frequencies, while in contrast, the cross-terms $(lm|l'm')$ can have negative contributions. I decided to plot the frequency peak of the $(2,2)$ mode (diagonal dotted line) as a mapping guide since the contribution to the SNR considerably changes in the merger-ringdown regime. Depending on the mode, the SNR variation will start before or after this frequency line.

In the left plot of Fig. 4.6a, one notes that the contribution of $(22|22)$ to ρ^2 is between 80% to 94% of the total, up to masses $\sim 4 \times 10^6$ $M_\odot$, while it decreases to 30% around masses of $\sim 10^8$ $M_\odot$. The rectangular darker area at the bottom right, between frequencies $[10^{-3} - 5 \times 10^{-2}]$ Hz and masses $[10^5 - 2 \times 10^6]$ $M_\odot$, indicates that most of the SNR comes from the inspiral part. This is expected since the waveform peaks outside or at the limit of the LISA frequency band. The pair $(33|33)$ (in the center) has a small contribution for low masses but exhibits a considerable increase up to 21% for high masses around 10^8 $M_\odot$. Finally, the case of $(44|44)$ (right plot) shows a similar behavior but is augmented by a factor ~ 2.5, representing about 54% of the total SNR for large-mass MBHBs. In other words, if the redshifted total mass of the system is larger than 10^8 $M_\odot$, the contribution of the quadrupolar mode will no longer dominate. It can represent half of the mode $(4,4)$ and only a factor of 1.5 bigger than the mode $(3,3)$. This highlights the importance of including higher harmonics to describe MBHB signals.

The second set of plots in Fig. 4.6b shows the cross-term pairs of modes that make the highest contributions to the squared SNR, representing approximately from 1% to 5%

of the total. This percentage might seem small, but for MBHBs with a total SNR of 1000, the cross-term contribution can be from 10 to 50. Even though the contributions can be negative, I use their absolute value for comparison. The reason is that the sign depends on the extrinsic parameters and the mass ratio, which vary from source to source, but are fixed here to arbitrary values for the sake of an illustration.

The position of the mode's frequency peak relative to the LISA sensitivity curve is driven by the mass of the source. Therefore, the SNR of higher modes can become more relevant than the $(2, 2)$ mode for large mass events.

Dependency on source mass and redshift

To represent the impact of the mass and the distance on the SNR, as mentioned in Sec. 4.4, I show in Figs. 4.7a and 4.7b the contour plots for different modes depending on the total mass in the source frame. I chose a source with the parameters listed in Table 4.1 for the sake of an illustration. However, the contributions would change with different parameters. Note that the lower bound of the total SNR is 10, which is the adopted threshold for MBHB detection in LISA [82; 274].

In these figures, we can see the high contribution of the square terms $|(l, m = l|l, m = l)|^{1/2}$ as well as the highest-contributing cross-terms such as $|(22|21)|^{1/2}$, $|(22|32)|^{1/2}$ and $|(33|32)|^{1/2}$. The pairs $|(22|33)|^{1/2}$ and $|(22|32)|^{1/2}$ exhibit a drop in the SNR for systems with a total source mass around 10^6 $\mathrm{M}_{\odot}$, depending on the redshift. This effect results from the specific choice of parameters of the source. It is also visible in Fig. 4.5, where some cross-terms have a null cumulative contribution to the total squared SNR. For completeness, another contour plot for a source with different parameters, demonstrating the mass and redshift dependence of the modes with a different SNR contribution shape is attached in Appendix B.

To assess how the mass ratio affects the SNR, I show in Fig. 4.8 the contour plots of the mass ratio versus total source mass for the same source with parameters given in Table 4.1 and a fixed redshift of $z = 2$. The absence of contribution at leading PN order of modes with odd m for equal mass ratio, see e.g. [275], is illustrated here. We can also note the importance of higher modes for sources with masses around 10^6 $M_{\odot}$, and mass ratios between 2 and 15.

4.4.3 Data and models

To understand the impact of higher modes in the parameter inference, I inject an MBHB source signal with six modes. The parameters used to generate this source were taken from the LDCWG *Sangria*'s catalog [152], and detailed in Table 4.2, where the subscript L in the extrinsic parameters means that it is expressed in the LISA frame at the time of coalescence t_c. I also use the redshifted chirp mass M_c instead of the mass. The parameters χ_i represent the aligned BH's dimensionless spin for nonprecessing binaries and D_L is the luminosity distance.

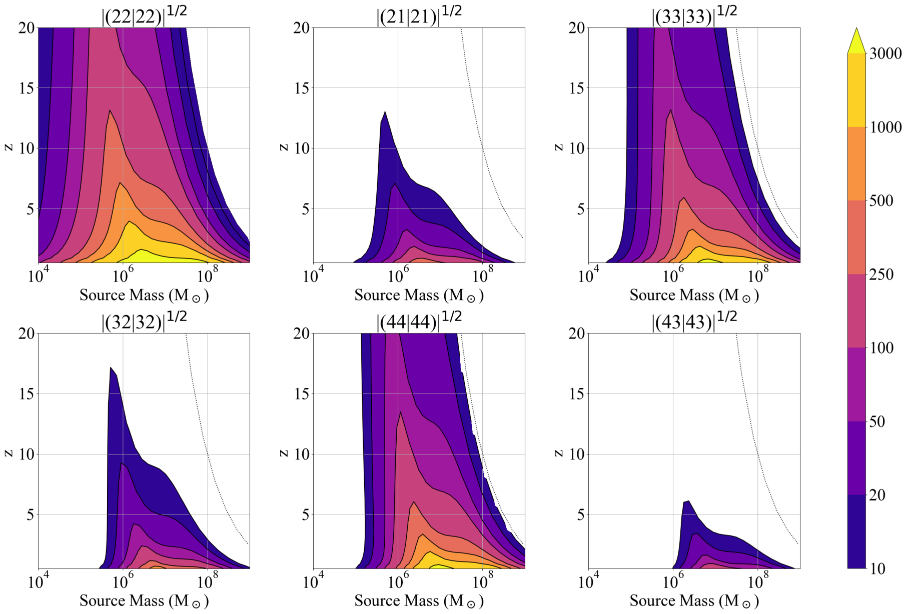

(a) Contour plot with the contributions of square pairs of modes $|(lm|lm)|^{1/2}$.

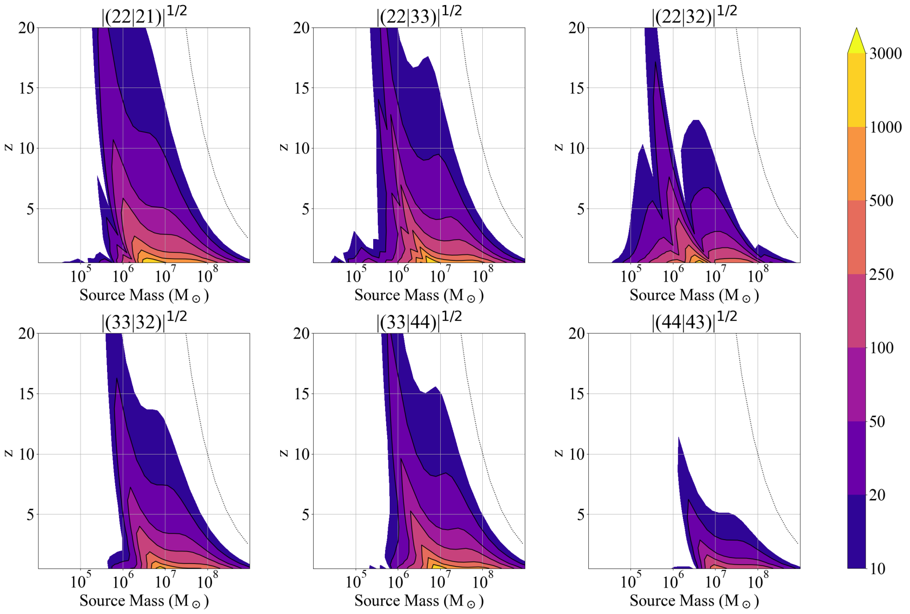

(b) Contour plot with the highest SNR contributions of cross-terms $|(lm|l'm')|^{1/2}$.

Figure 4.7: Contour plot for the root squared absolute cumulative value of contributions $|(lm|l'm')|^{1/2}$. The dotted line corresponds to the total SNR with a threshold ≥ 10, plotted here for comparison. I remark the subdominant contribution of $|(33|33)|^{1/2}$ and $|(44|44)|^{1/2}$ after the quadrupolar square term. Note the 0-contributions in some cross-terms due to the representation of a single system with fixed parameters.

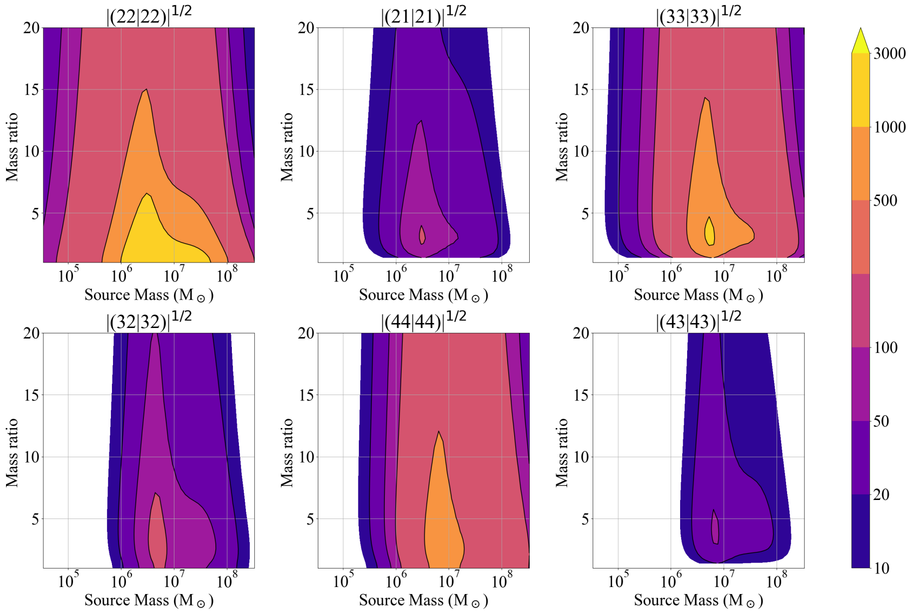

Figure 4.8: Contour plots for mass ratio with respect to the total mass. The plot highlights the contribution of higher modes for sources of $\sim 10^6$ M$_\odot$ and mass ratios up to 15. SNR decreases slowly when increasing the mass ratio by a few units for a fixed mass.

Two datasets were considered, one without noise and another with instrumental noise and the galactic noise with the subtraction of identified sources over one year. The noise was generated with the same PSD assumed in Sec. 4.4.2. Each dataset includes two TDI channels, A and E. In both cases, the frequency band is restricted to the interval $[10^{-5} - 5 \times 10^{-2}]$ Hz. To estimate the source parameter for various models I used a nested sampling algorithm. I chose the sampler `dynesty` [276], as it allows one to obtain approximate evidence estimates (see Sec. 4.3 and particularly Eq. 4.3.2). As a consistency check, one collaborator also ran `ptemcee`, a parallel-tempered Markov Chain Monte Carlo ensemble sampler [277; 278]. We obtained consistent results with the two samplers, with a slightly better convergence for `ptemcee`, which, however, does not allow for direct evidence computation, and integration over the thermodynamis evidence is required. I report `dynesty` results in the following. I use an adaptive heterodyned likelihood to speed up the likelihood computation, which I describe in Sec. 4.4.4, however, one can also see [279; 280] and references therein for more information.

I consider six models for the parameter estimation, where each one describes the waveform with a certain number of modes. The first model generates the gravitational signature with only the quadrupolar mode $(2,2)$. The other models (see Table 4.3 for models' definition) include an increasing number of higher harmonics, ranked by their SNR contribution $(lm|lm)$, as observed in Fig. 4.7a. This amounts to first selecting successive $(l, m = l)$ modes with increasing l and then the $(l, m = l - 1)$ modes.

The used priors are uniform for all parameters in the intervals written in Table 4.2,

Table 4.2: Parameters of the MBHB source with SNR 744 chosen from *Sangria*'s LDC catalog for redshifted mass without precession, along with the flat priors intervals used in the inference.

Parameter	Value	Prior
M_c ($M_\odot$)	857080.8396	$[10^4, 5 \times 10^7]$
q	2.7589	$[1, 10]$
χ_1	-0.5488	$[-1,\ 1]$
χ_2	0.2317	$[-1,\ 1]$
D_L (Mpc)	40084.6792	$[10^4,\ 5 \times 10^6]$
t_c (s)	0.0	$[-600,\ 600]$
β_L (rad)	-0.6186	$[-\pi/2,\ \pi/2]$
λ_L (rad)	2.2782	$[0,\ 2\pi]$
ϕ (rad)	0.2492	$[-\pi, \pi]$
Ψ_L (rad)	1.5158	$[0, \pi]$
ι (rad)	2.5969	$[0, \pi]$

Table 4.3: Each model is indexed according to the number of modes included in the waveform generation.

Model	Modes (l,m)
M_1	(2, 2)
M_2	(2, 2), (3, 3)
M_3	(2, 2), (3, 3), (4, 4)
M_4	(2, 2), (3, 3), (4, 4), (2, 1)
M_5	(2, 2), (3, 3), (4, 4), (2, 1), (3, 2)
M_6	(2, 2), (3, 3), (4, 4), (2, 1), (3, 2), (4, 3)

except for the chirp mass which has a uniform prior in logarithmic scale. I use the whole physically allowed interval for the extrinsic parameters, while a raw estimation of the expected values for the intrinsic ones. I use a narrow prior for the coalescence time as it can easily be spotted in the detection process but with a difference of up to 500 seconds between the LISA and the SSB reference frame. Note that the polarization ψ is allowed to go from 0 to π and not 2π, to prevent parameter degeneracy, given that in the antenna pattern, the polarization is always preceded by a factor 2 as shown in Eq. (4.2.4). The results and the discussion of this analysis are presented in Chapter 5.

The results were obtained using the Cluster of IN2P3, CNRS, where each run took between 20 hs and 25 hs, depending on the number of modes, in a single CPU with 16 Gb of memory. The number of live points was set to 2200, and the convergence was achieved when the error in the evidence (dlogz) reached the 10^{-4} value. This value was selected by analyzing the importance weight and the likelihood Probability Density Function (PDF) for different runs.

4.4.4 Heterodyne likelihood in FD

In a simulation of data without noise, one can use an adaptive frequency grid to describe all the features of a waveform without loss of information. This allows for faster computation of likelihoods since only a hundred points are used to generate the waveform. In a more realistic scenario, where noise enters the detector at a given sampling rate, the use of a frequency grid is no longer possible, as one would be neglecting the covariance matrix between points and information would be lost. Nevertheless, there is a way to compute fast likelihoods accounting for the whole array of frequencies, it is called heterodyne likelihood [279; 280]. The main idea behind this method is to exploit the fact that the data has a two-scale frequency variation. One is given by the slowly changing part of a signal and the second is given by the rapidly changing noise and rapidly changing part of a signal. If the waveform template describing a signal is

$$h(f) = A(f)e^{i\phi(f)}, \tag{4.4.6}$$

then, the ratio of two signals $\zeta(f) = h(f)/\overline{h}(f)$ close to the maximum likelihood, will be a slowly varying function. Here $\overline{h}$ is a reference waveform with a likelihood near the maximum value.

Additionally, knowing that the likelihood of a template waveform $h(f)$ for some data $d(f)$ is

$$\ln \mathcal{L} = -\frac{1}{2}\left(d-h \middle| d-h\right), \tag{4.4.7}$$

one can decompose the likelihood terms into slow varying and fast-varying components, such that

$$\begin{aligned}(d|h) &= 2\int \frac{d(f)h^*(f)+h(f)d^*(f)}{S_n(f)}df \\ &= 2\int \left(\kappa(f)\zeta^*(f)+\kappa^*(f)\zeta(f)\right)df\end{aligned} \tag{4.4.8}$$

where $\kappa(f) = d(f)\overline{h}^*(f)/S_n(f)$ is a rapidly varying function and $\zeta(f)$ the slowly varying function. Similarly one can write

$$\begin{aligned}(h|h) &= 2\int \frac{h(f)h^*(f)+h(f)h^*(f)}{S_n(f)}df \\ &= 4\int \sigma(f)|\zeta(f)|^2 df\end{aligned} \tag{4.4.9}$$

where $\sigma^2(f) = |\overline{h}(f)|^2/S_n(f)$ for the case of LISA is a slowly varying function, except at high frequencies. Moreover, in terms of the reference waveform, the likelihood can be written as

$$\begin{aligned}\ln\mathcal{L} &= -\frac{1}{2}\left(\bar{h}+\bar{r}-h|\bar{h}+\bar{r}-h\right)\\ &= -\frac{1}{2}\left(\bar{r}|\bar{r}\right)-\frac{1}{2}\left(\Delta h|\Delta h\right)+\left(\bar{r}|\Delta h\right),\end{aligned} \tag{4.4.10}$$

where $\bar{r} = d - \bar{h}$ is the reference residual and Δh is the waveform difference between the reference waveform and the estimated waveform. In which case, the slowly varying function becomes $\Delta\zeta(f) = \Delta h(f)/\bar{h}(f) = 1 - \zeta(f)$. Note that, in general, the error introduced by terms of Δh is small when using an adaptive frequency grid. Furthermore, the integrals being sums over frequency can be efficiently computed using an expansion in discrete Legendre polynomials or quadratic polynomials for the real and the imaginary part. In conclusion, the slowly varying functions are fast generated with a frequency grid, while the rapidly varying functions are generated with the full frequency array only once and stored.This allows us to improve the computational time to estimate the parameters of a noisy signal.

4.5 Detectability of GR deviations with QNMs

This section is based on the article "Exploring tests of the no-hair theorem with LISA"[246] written by me and collaborators. However, some modifications were made for a better integration into the manuscript.

To study LISA's sensitivity to probing GR in the ringdown phase of MBHBs, I focus on testing the *no-hair* conjecture. As introduced in Section 3.1, the *no-hair* hypothesis asserts that in GR, Kerr BH are characterized solely by two parameters: mass and spin. Consequently, these two parameters uniquely describe the spacetime manifold, leading to the uniqueness of black holes. This uniqueness also contributes to the so-called information loss paradox, as any two black holes with the same mass and spin parameters are indistinguishable, regardless of their history or origin. However, the information loss issue is beyond the scope of my work and I concentrate on the uniqueness aspect and the description of black holes in terms of mass and spin. This principle holds within GR, but it has been shown that BH spectra might differ in alternative theories of gravity [234–236; 239; 240]. The discrepancies between the expected spectra in GR and those in beyond-GR theories are referred to as "deviations" and are typically measured as fractional deviations from GR. My focus is to quantify LISA's ability to detect these deviations. The advantage of using this framework is that it is model-independent, hence one could constrain different alternative theories with a single analysis.

4.5.1 Data

The analysis procedure consists of generating a toy model describing the ringdown phase of an MBHB as the sum of damped oscillations with the response of LISA. The sum of damped oscillations in the ringdown of MBHB is given by

$$h(t) = \sum_{lmn} h_{lmn}(t)\,{}_{-2}S_{lmn}(a_f\tilde{\omega}_{lmn};\theta,\varphi), \tag{4.5.1}$$

with

$$h_{lmn}(t) = \frac{M_f}{D_l} A_{lmn}(\Xi,t) e^{i(\phi_{lmn}(\Xi,t)-\tilde{\omega}'_{lmn}t)}. \tag{4.5.2}$$

The complex frequency with a tilde includes an allowed fractional deviation from GR in the real and the imaginary part, see Sec. 3.7, as first introduced by [212]

$$\omega'_{lmn} = \omega^{\rm GR}_{lmn}(M_f,a_f)(1+\delta\omega_{lmn}), \tag{4.5.3a}$$
$$\tau'_{lmn} = \tau^{\rm GR}_{lmn}(M_f,a_f)(1+\delta\tau_{lmn}), \tag{4.5.3b}$$

then

$$\tilde{\omega}'_{lmn} = \omega'_{lmn} - i/\tau'_{lmn}. \tag{4.5.4}$$

The GR index indicates the values obtained within the GR framework. There are different ways to compute these complex frequencies, I recommend [182] for a review on this topic. Here I make use of the `qnm` package [194], which is based on a spectral approach [185]. I recall that Ξ stands for the intrinsic redshifted parameters of the progenitors $\Xi = (m_1, m_2, \chi_1, \chi_2)$ and D_l is the luminosity distance.

Spheroidal harmonics can be related to spherical harmonics through

$${}_sS_{lmn} = {}_sY_{lm} + \sum_{l\neq l'} \frac{\langle sl'm|\,\mathfrak{h}_1\,|slm\rangle}{l(l+1)-l'(l'+1)} + \cdots, \tag{4.5.5}$$

where I drop the dependence on $(a_f\tilde{\omega}_{lmn};\theta,\varphi)$ for clarity, and where

$$\mathfrak{h}_1 = a^2\omega^2\cos^2\theta - 2a\omega s\cos\theta. \tag{4.5.6}$$

The functions ${}_sY_{lm}$ are the already discussed spin weighted spherical harmonics and $d\Omega$ is the solid angle. It is easy to see from Eqs. (4.5.5) and (4.5.6), that one recovers the solution for the non-rotating (Schwarzschild) BH in spherical harmonic basis when $a_f \to 0$.

In Sec. 3.6 I introduced mode mixing as a consequence of the representation choice in perturbation theory in terms of spheroidal harmonics, as opposed to the spherical harmonics which is the most natural representation in NR. The relation between both bases can be described by the spherical-spheroidal mixing coefficients, given by

$$\sigma_{l'm'lmn}(a_f) = \delta_{m'm}\int_\Omega {}_{-2}Y^*_{l'm'}(\theta)\,{}_{-2}S_{lmn}(a_f\tilde{\omega}_{lmn};\theta)d\Omega, \tag{4.5.7}$$

Table 4.4: Parameters for MBHB injection

Parameter	Value	Parameter	Value
$m_1(M_\odot)$	9384087	$m_2(M_\odot])$	3259880
χ_1	0.555	χ_2	-0.525
ι (rad)	$\pi/3$	ϕ (rad)	$\pi/4$
β (rad)	$\pi/2$	λ (rad)	$\pi/3$
$D_l(Mpc)$	50000	q	2.878
$M_f(M_\odot)$	$1.2175649\ \times 10^7$	a_f	0.821
$\delta\omega_{220}$	0.0	$\delta\tau_{220}$	0.0
$\delta\omega_{330}$	0.01	$\delta\tau_{330}$	0.05
$\delta\omega_{440}$	0.03	$\delta\tau_{440}$	0.1
SNR	587		

where I use that $S_{lmn}(\theta,\phi) = e^{im\phi}S_{lmn}(\theta)$ and $Y_{lm}(\theta,\phi) = e^{im\phi}Y_{lm}(\theta)$. With this representation, the strain takes the form

$$h_+(t) - ih_\times(t) = \sum_{l'}\sum_{lmn} h_{lmn}(t)\sigma_{l'mlmn}(a_f)_{-2}Y_{l'm}(\theta). \tag{4.5.8}$$

In this work, the amplitudes and phases used in Eq. (4.5.2) belong to fittings made by L. London [204; 281], where the mode mixing is already included. Thus I will consider amplitudes labelled with $(l'mlmn)$ as

$$A_{l'mlmn} = A_{lmn}\sigma_{l'mlmn}. \tag{4.5.9}$$

In order to consider the following three QNMs, namely $[(2,2,0),(3,3,0),(4,4,0)]$, I include $[(2,2,2,2,0),(3,2,2,2,0),(3,3,3,3,0),(3,3,3,3,0),(4,4,4,4,0)]$, see Eq. (4.5.9). Indeed, the resulting signal is a sum of decaying waves with amplitudes and phases for $lmn = [(2,2,0),(3,3,0),(4,4,0)]$.

I also set a fractional deviation to those QNMs equal to $\delta\omega_{lmn} = [0.0, 0.01, 0.03]$ and $\delta\tau_{lmn} = [0.0, 0.05, 0.01]$ in the same QNM order. Of course, more QNMs could and should be added, but to create a proof of concept, I decided to include only these three, leaving more complex searches for future work. I consider input data including a GW signal with and without noise. The sampling rate is set to 1 second as a compromise between the planned sampling rate of 0.25 s, the typical duration of the ringdown for a heavy source (about 7000 s for a 10^7 $M_\odot$) and the number of data points $N = 8192$. The parameters used for the source injection are listed in Table 4.4. Note that I use ι as the inclination angle instead of θ. I also write the ringdown SNR as well as the final parameters for the remnant BH, obtained with Eqs. (3.6) and (3.8) from [129].

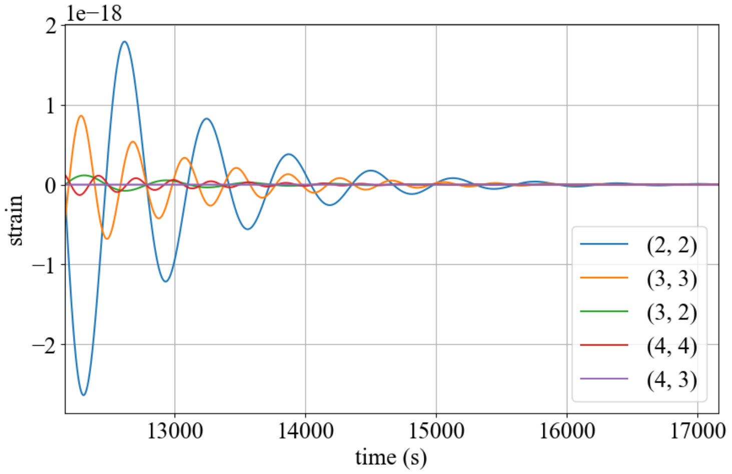

(a) Ringdown strain in spherical harmonics decomposition

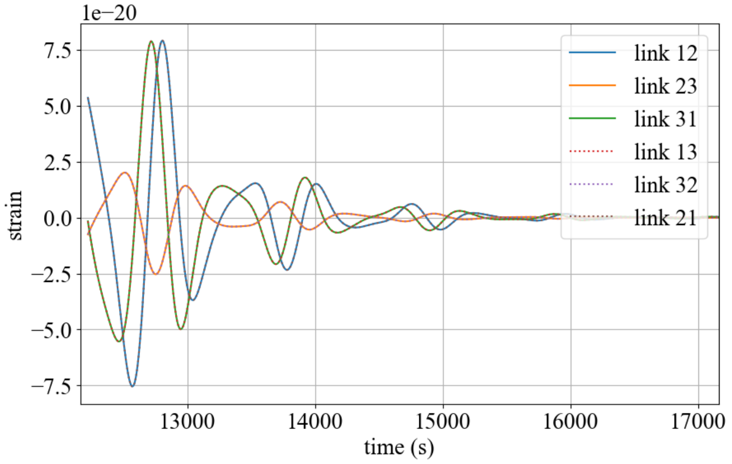

(b) Ringdown strain observed by the links

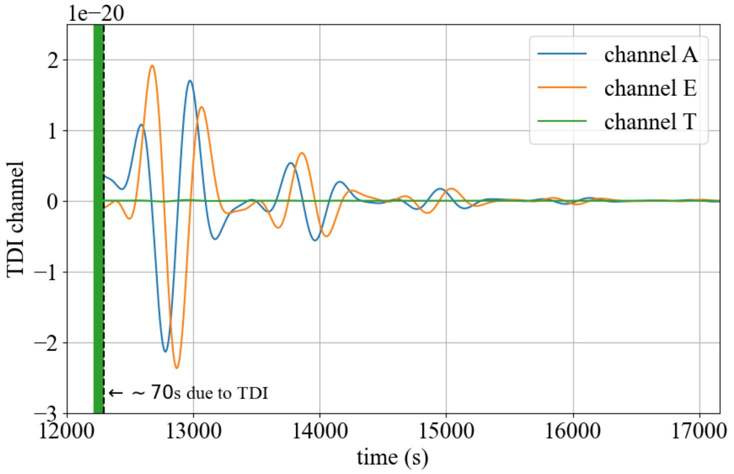

(c) Ringdown strain in TDI channels

Figure 4.9: Ringdown waveform evolution within Lisaring.

4.5.2 Lisaring

As I mentioned before, I had to develop a specific code to deal with ringdown analyses with LISA in the time domain, namely `Lisaring` [265]. The evolution of the parameters listed in Table 4.4 to the final product is shown in Figs. 4.9. Once the ringdown waveform is generated with the previous setup, we can decompose it in terms of spherical harmonics or terms of the plus and cross polarizations $h_+, h_\times$. Then, the six links response are computed with Eq. (4.2.16) with ESA LISA science orbit files [282] generated with the `LISA orbits` package [283]. Afterward, the combination of the links with the appropriated retarded times is in place to produce the TDI channels A, E, and T with Eqs. (4.2.17) to (4.2.19).

One special feature that is worth mentioning is that in the TDI generation, there is a difference of about 70 seconds between the time computed in the first link and the time computed for the last link. Keep in mind that for the TDI 2.0, the combination of eight links with retarded time is needed, this is equivalent to $8.3\,s \times 8 \simeq 67s$, but since the arm lengths vary, this value can be slightly larger. This translates into corrupted data for the first ~ 70 s in the TDI channels, as demonstrated in Fig. 4.9c. Then, one needs to cut those ~ 70 s when performing data analysis. The code performs this cut by default when computing likelihoods.

To finalize this section, as a consistency check, I compared the obtained channel values with the channels generated with the `LISA gwresponse` and `PyTDI` packages for the same waveform. One can see the residuals of both signals in Fig. 4.10. Here I show the residuals for channel X, which are of the order of 10^{-22} (2 orders of magnitude smaller than the signal) resulting from the different conventions in computing TDI. While I compute always the retarded time, `PyTDI` considers a previous point in time and computes the advanced times, then the starting time of the signals differs by about 60 s. Since the signal is expressed with a given cadence, the difference is non-zero, leaving a small residual. Nonetheless, both methods are in good agreement.

4.5.3 Templates

To assess the detectability of deviations from GR in the QNMs I generate a waveform with the features discussed in Sec. 4.5.1 and the response of LISA introduced in Secs. 4.2 and 4.5.2 with the parameters listed in Table 4.4. Then, I try to estimate the injected parameters with a template that can take two forms, as two approaches are being considered: the *agnostic* approach and the *deviation* approach. In the *agnostic* approach one assumes that the ringdown waveform is described by

$$h_+ - ih_\times = \sum_k A_k e^{i(\phi_k - \tilde{\omega}_k t)}. \tag{4.5.10}$$

In this approach, the complex frequency can take any value as well as the amplitudes and phases. Note also that any dependence of the spheroidal harmonic is absorbed in the amplitude and the phase. In this description, no *mode mixing* is specified. For example, in

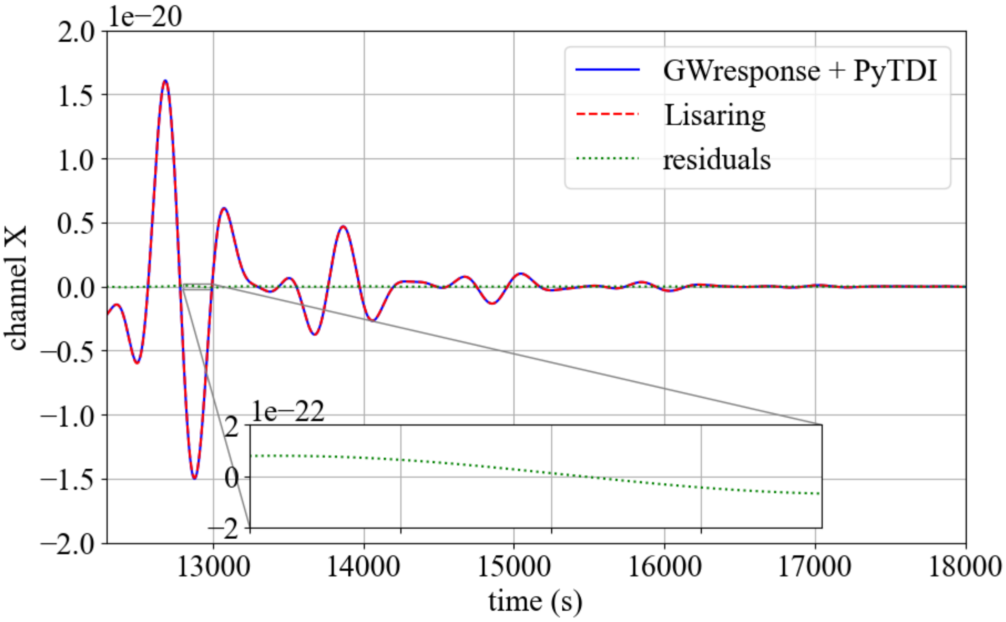

Figure 4.10: Residuals between `GWresponse` + `PyTDI` and `Lisaring`.

this approach, it would not be possible to know how much of the $(2,2,0)$ QNM contribution comes from the spherical harmonic $(2,2)$ or from the $(3,2)$. It differs from Eq. (4.1.1) as no assumption is made on the value of the complex frequency nor the spherical contribution to any QNM. Without loss of generality, we can call this approach "agnostic" despite the fixed number of modes k.

In the *deviation* approach, I assume the framework of GR but allow for a small "deviation" in the complex frequencies, that is

$$h_+ - ih_\times = \sum_{lmn} A_{lmn} e^{-t/\tau'_{lmn} + i(\phi_{lmn} - \omega'_{lmn} t)} \tag{4.5.11}$$

where ω'_{lmn} and τ'_{lmn} are the deviated frequency and damping time from Eqs. (4.5.3). In this case, one recovers GR when the deviations are zero. I impose which QNMs are present and look for each pair of deviations. Then, I compare the results from both approaches and discuss the information one can extract from them.

In this toy model, the injection and the recovery template have the same starting time. By fixing the starting time no error is introduced in the waveform due to the uncertainty of the ringdown starting time. Consequently, I do not try to evaluate any systematic uncertainties coming from the definition of the starting time of the ringdown, which is still under debate [200; 202; 205]. However, when dealing with real data, where one does not know the appropriate starting point, several starting times in the vicinity of the luminosity peak should be considered (see for example [201; 207; 211]). I also fix the sky localization to the true value. Thus, no error from this parameter is introduced in the waveform either. A visual representation of the impact on the ringdown waveform

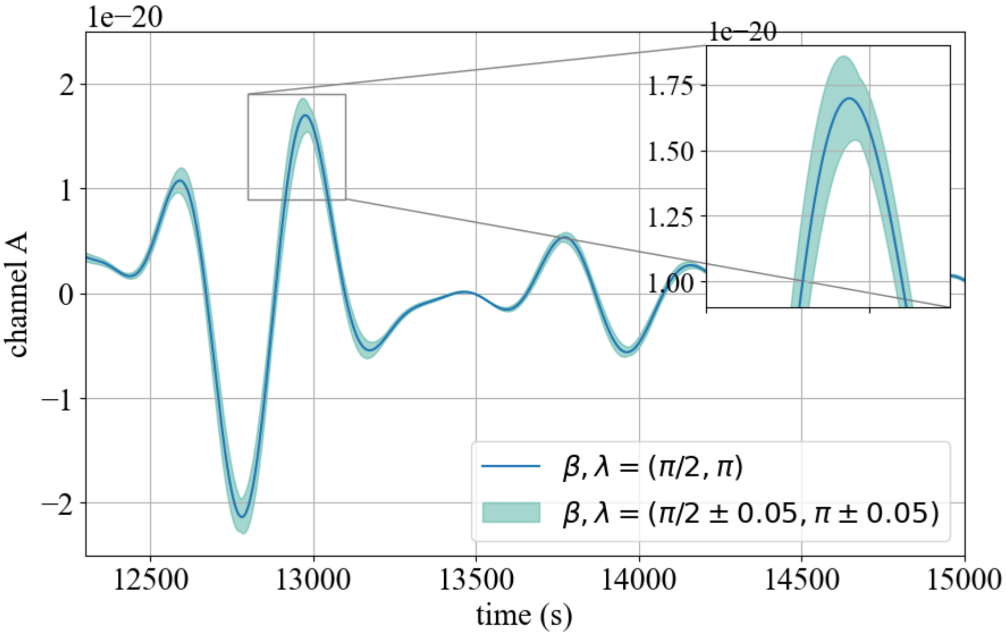

Figure 4.11: Uncertainty for given waveform with a sky localization posterior distribution. The blue line marks a waveform with a fixed sky localization and the shaded light-blue curve represents the waveform's uncertainty if the sky localization has an error of ±0.05 radians $\rightarrow\sim 8$ deg^2.

due to a sky localization error of approximately ±0.05 radians (about ~ 8 deg^2) is shown in Fig. 4.11. Both issues will be left for future exploration.

Before jumping to the results, let us describe one particular feature that I had to analyze to introduce it in `Lisaring` for the computation of the likelihood.

4.5.4 Likelihood computation

One of the major concerns when working in the time domain is the manipulation of the covariance matrix, since its inverse is required to compute the likelihood. To obtain the covariance matrix, I use the same method as in [203] with an analytical PSD. Namely, assuming stationarity, one can generate the covariance matrix as a symmetric Toeplitz matrix, such that

$$\mathbf{C}_{ij} = \rho(|i-j|), \tag{4.5.12}$$

where, $\rho(k)$, $k = |i-j|$, is the Auto-Covariance Function (ACF) that can be estimated from noise-only data in the TD with a length longer than N or as the inverse Fourier transformation from a PSD. In this study, in the absence of real data, I use the latter option generating the ACF from the LISA science requirements document SciRD [274]

PSD [8], which takes the following form

$$\rho(k) = \frac{1}{2T} \sum_{j=0}^{N-1} S(|f_j|) e^{2\pi ijk/N}. \tag{4.5.13}$$

Working with matrices usually demands a lot of computational time and, because of their numerical instability, special care has to be taken. To reduce the computational time, one can take advantage of different methods such as the Cholesky decomposition [284] or the Levinson recursion [285; 286] among others.

The Cholesky method consists of decomposing the covariance matrix into two matrices, a lower triangular matrix and its conjugate transpose such that

$$\mathbf{C}_{ij} = \sum_l L_{il} L^*_{lj}, \tag{4.5.14}$$

then the inner product becomes

$$(a|b) = \sum_{i,j=0}^{N-1} \alpha_i \beta_j, \tag{4.5.15}$$

where

$$\alpha_i = \sum_l L^{-1}_{il} a_l. \tag{4.5.16}$$

For the time domain analysis, I use another method to compute the likelihood which relies on the Preconditioned Conjugation Gradient (PCG) [287] in combination with the Jain method [288], which I explain next. The use of the `bayesdawn` package [289], with the implementation of these two methods allows for fast computation of the vectors

$$\overline{a}_j = a_i \mathbf{C}^{-1}_{ij}. \tag{4.5.17}$$

Then, the inner product of Eq. (4.3.6) becomes a much faster product of vectors

$$(a|b) = \sum_{j=0}^{N-1} \overline{a}_j b_j. \tag{4.5.18}$$

Preconditioned conjugation gradient (PCG)

The conjugation gradient is a numerical technique to solve systems of linear equations $A\,x = b$, where A is a symmetric positive definite matrix. The idea of the method is to solve the equation through a recursion with an initial guess x_0, which gives an initial residual r_0. If one considers a function

$$F(x) = \frac{1}{2} x^T A\,x - x^T b, \tag{4.5.19}$$

---

[8] I introduced the PSD equations of this noise in Sec 2.4.

one can see that its gradient is $F'(x) = A\,x - b$, thus by finding the x that minimizes $F(x)$ is the same as solving $A\,x = b$. For every x, the gradient points in the direction in which $F(x)$ increases the most, whereas the opposite direction points to the critical point and thus to $F'(x) = 0$. Then, the residual at the k iteration $r_k = b - A\,x_k$ decreases until a given tolerance is reached and the algorithm stops. In general, the convergence of a matrix $A_{n\times n}$ is obtained with n iterations, however, the number of iterations will vary with the *condition number* of the matrix. The condition number of a matrix is given by

$$\kappa_A = ||A^{-1}||\,||A||, \tag{4.5.20}$$

then if $\kappa_A \simeq \mathcal{O}(10)$, the matrix is said to be well conditioned and the solution will be found in n iterations, and badly conditioned if the value is much larger than one $\kappa \gg 1$.

The preconditioned conjugation gradient is an extension of the conjugation gradient to solve more challenging problems with an ill-conditioned matrix or even with gaps making it hard to solve[9]. The trick is to solve a related problem $\tilde{A}\,\tilde{x} = \tilde{b}$, with a condition number close to one $\kappa_{\tilde{A}} \simeq 1$. Both systems are related via the following expressions

$$\tilde{A} = B^{1/2}A, \qquad \tilde{x} = B^{1/2}y, \qquad \tilde{b} = B^{1/2}b, \tag{4.5.21}$$

where B could be chosen, for example, as $diag(a_{11}, a_{22}, \ldots, a_{nn})$, but other choices might work as well. Then, instead of solving $A\,x = b$, one should solve the related problem

$$My = \tilde{b}, \tag{4.5.22}$$

where $y = B^{-1/2}x$ and $M = B^{1/2}AB^{1/2}$. Following the technique presented before to solve the system, one obtains the preconditioned solution.

In conclusion, the PCG method is crucial for ill-conditioned matrices, such as the one generated from LISA's ACF, with a condition number of $\kappa \approx 10^7$ [10].

Jain method

The Jain method consists of a fast inversion of a Toeplitz matrix via a Fast Fourier Transform (FFT) [288]. It differs from Levinson's technique to solve these problems, as it is not a recursive algorithm and therefore yields an exact solution in $\mathcal{O}(N\log_2 N)$ computations [288]. Moreover, since the equations are non-recursive, a parallel architecture is possible. It is based on the idea that any banded Toeplitz matrix, also known as non-circulant Toeplitz matrix, can be decomposed in a circular matrix T_c and a perturbation matrix T_b in the following way

$$T = T_c - T_b, \tag{4.5.23}$$

---

[9] In that case the covariance matrix has chunks of lines with zero values.

[10] This value is obtained for an ACF of 22000 points at 0.2 Hz, but it might vary depending on the sampling rate and the length.

where the circulant matrix has the form,

$$T = \begin{bmatrix} t_0 & t_{-1} & \cdots & t_{-p} & 0 & 0 & t_q & \cdots & t_1 \\ t_1 & \ddots & & & \ddots & & & \ddots & \vdots \\ \vdots & & \ddots & & & \ddots & & & t_q \\ t_q & \ddots & & \ddots & & & \ddots & & 0 \\ 0 & & \ddots & & \ddots & & & \ddots & 0 \\ 0 & & & \ddots & & \ddots & & & t_{-p} \\ t_{-p} & \ddots & & & \ddots & & \ddots & & \vdots \\ \vdots & & \ddots & & & \ddots & & \ddots & t_{-1} \\ t_{-1} & \cdots & t_{-p} & 0 & 0 & t_q & \cdots & t_1 & t_0 \end{bmatrix}, \tag{4.5.24}$$

See Fig. 4.12 and Eq. (4.5.24) for a visual representation of the Toeplitz matrices. The advantage of using this decomposition is that the circulant matrix T_c can easily be solved via FFT as the inverse Discret Fourier Transform (DFT) of the sequence $\tilde{y}(\omega) = \tilde{b}(\omega)/\tilde{\lambda}(\omega)$, where the tilde denotes the DFT and [288]

$$\lambda(\omega) = t_0 + \sum_{k=1}^{q} t_k e^{ik\omega} + \sum_{k=1}^{p} t_{-k} e^{-ik\omega}, \tag{4.5.25}$$

with $\omega = 2\pi m/N$, $0 \leq m \leq N-1$, and t_k the values defined in Eq. (4.5.24), and b, y defined in Eq.(4.5.21). Nevertheless, the solution for the circulant matrix T_c can also be obtained via other recursive methods, such as the PCG or Levinson. In that case, one computes afterward the solution for the perturbation matrix T_b, thanks to the relation $\tilde{y}(\omega) = \tilde{b}(\omega)/\tilde{\lambda}(\omega)$. For reference, t_0 is the first element of the ACF, which corresponds to the black color in Fig. 4.12, while t_{-p} is the first element in the first column of T_b and t_q the first element in the first row of T_b, both in light grey.

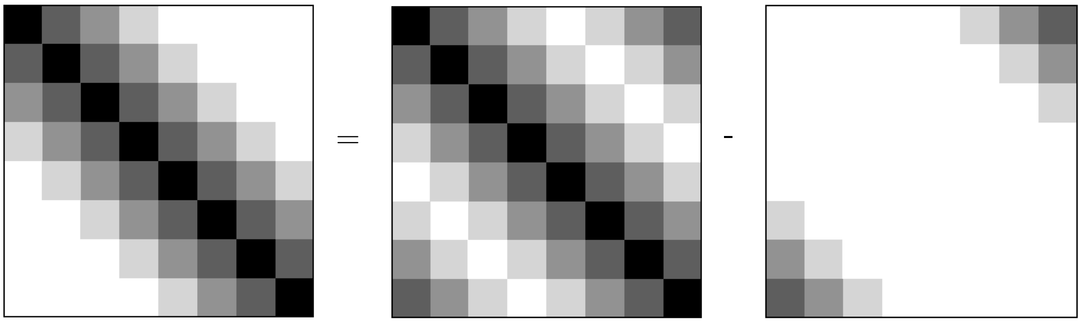

(a) Toeplitz banded matrix T.

(b) Toeplitz circulant matrix T_c.

(c) Toeplitz pertubation matrix T_b.

Figure 4.12: Visual representation of a banded Toeplitz matrix decomposition.

Then, one has to solve the system for the Toeplitz perturbation matrix T_b to find the solution of x that fulfills

$$T\,x = b. \tag{4.5.26}$$

Reformulating, one arrives to

$$T_c\,x = b + T_b\,x \longrightarrow x = y + T_c^{-1} T_b\,x, \tag{4.5.27}$$

where $y = T_c^{-1}\,b$. In that case, and denoting from now on $T_c^{-1} = \mathcal{T}$, one can write,

$$x = y + \mathcal{T}\begin{bmatrix} u \\ 0 \\ v \end{bmatrix}, \tag{4.5.28}$$

with the definitions

$$u = f\,x^f, \qquad v = g\,x^i, \tag{4.5.29}$$

where f and g are respectively the $q \times q$ upper and the $p \times p$ lower triangle matrices of T_b and where I define x^i the $p \times 1$ *initial values* $\{x_1, \cdots x_p\}$ and x^f the $q \times 1$ *final values* $\{x_{N-q+1}, \cdots x_N\}$. Thus, applying the same partition (initial, middle, and final) to the inverse circulant matrix and the circulant result y,

$$\mathcal{T} = \left[\begin{array}{c|c|c} \mathcal{T}^{ii} & \mathcal{T}^{im} & \mathcal{T}^{if} \\ \hline \mathcal{T}^{mi} & \mathcal{T}^{mm} & \mathcal{T}^{mf} \\ \hline \mathcal{T}^{fi} & \mathcal{T}^{fm} & \mathcal{T}^{ff} \end{array}\right], \qquad y = \left[\begin{array}{c} y^i \\ y^m \\ y^f \end{array}\right], \tag{4.5.30}$$

one can obtain with the definitions from Eqs. (4.5.28) and (4.5.29) the identities

$$g^{-1}v = x^i = \mathcal{T}^{ii}u + \mathcal{T}^{if}v + y^i, \tag{4.5.31}$$

$$f^{-1}u = x^f = \mathcal{T}^{fi}u + \mathcal{T}^{ff}v + y^f. \tag{4.5.32}$$

The combination of these identities is the solution of x.

To relate these methods to the computation of the likelihood. The idea is to solve

$$\bar{a}_j(\boldsymbol{\theta}) = a_i(\boldsymbol{\theta})\mathbf{C}_{ij}^{-1}. \tag{4.5.33}$$

For that, I use the algorithm that applies the Jain method to decompose a non-circular Toeplitz matrix into a circulant and a perturbation matrix and then I use the PCG technique to solve the circulant matrix with a large condition number. This is achieved by solving the system $\tilde{A}\tilde{x} = \tilde{b}$ where $\tilde{A}$ is the transformed Toeplitz matrix resulting from

$$\tilde{A} = B^{1/2}A = B^{1/2}\mathbf{C}_{ij}, \qquad \tilde{b} = B^{1/2}a_i = [1\,0\,0\,\cdots 0\,0], \qquad \tilde{x} = \bar{a}_j. \tag{4.5.34}$$

Table 4.5: Comparison of convergence and computational time for computation of vector $\overline{a}_j(\boldsymbol{\theta})$ with different methods.

Method	Computational time (s)	Convergence
Scipy	15.1 ± 1.25	✓
Levinson-Jain	0.099 ± 0.004	✗
PCG-Jain	8.2 ± 0.211	✓
PCG	30 ± 1.37	✗

Once the preconditioned solution is obtained, the solution for the perturbation matrix is computed with Jain's method. Finally, once the vector is obtained, I can compute the product of the vectors

$$(a|b) = \sum_{j=0}^{N-1} \overline{a}_j(\boldsymbol{\theta}) b_j(\boldsymbol{\theta}) = \sum_{j=0}^{N-1} \tilde{x}_j b_j(\boldsymbol{\theta}), \tag{4.5.35}$$

that are the key to the computation of the likelihood in the time domain.

Numerical stability check

To complete this section I show the comparison with the other two methods, just as a consistency check for precision and computational time. Numerical precision in the computation of the vector in Eq. (4.5.33) is required to calculate the likelihood. A vector with numerical instability will translate into a *plateau* likelihood. This means that the likelihood does not have a clear maximum, since it presents a flat behaviour near the true parameters. This feature prevents one from finding the parameters' true values.

To prevent the *plateau* likelihood but also to guarantee the fast but accurate computation of the vector, I compared four methods: *Scipy, Levinson-Jain, PCG-Jain* and *PCG*. The first method uses the `scipy` [290] package to compute the Toeplitz matrix and its inverse. Then, this inverted matrix is used to compute Eq. (4.5.33). The second method uses the Jain method to decompose the matrix in a circulant and a perturbation component while solving the circulant Toeplitz matrix via Levinson's recursion. The third method is similar but solves the matrix via the PCG technique. And lastly, the fourth method is via the PCG technique without a previous Jain decomposition. The numerical stability can be observed in Fig. 4.13. Using the `scipy` method results in a numerically unstable vector because of the high condition number of SciRD's ACF, which is $\kappa_{SciRD} \sim 2 \times 10^6$ for $2^{13} = 8192$ points at 1 Hz. A similar outcome for the Levinson-Jain method, which, after 8192 iterations, the requested tolerance of 10^{-6} was not achieved. The other two methods have equivalent numerical behavior, being the main difference in the convergence and computational time, resumed in Table 4.5. Because of the results of this comparison, I chose the PCG-Jain method to compute the likelihood in the TD.

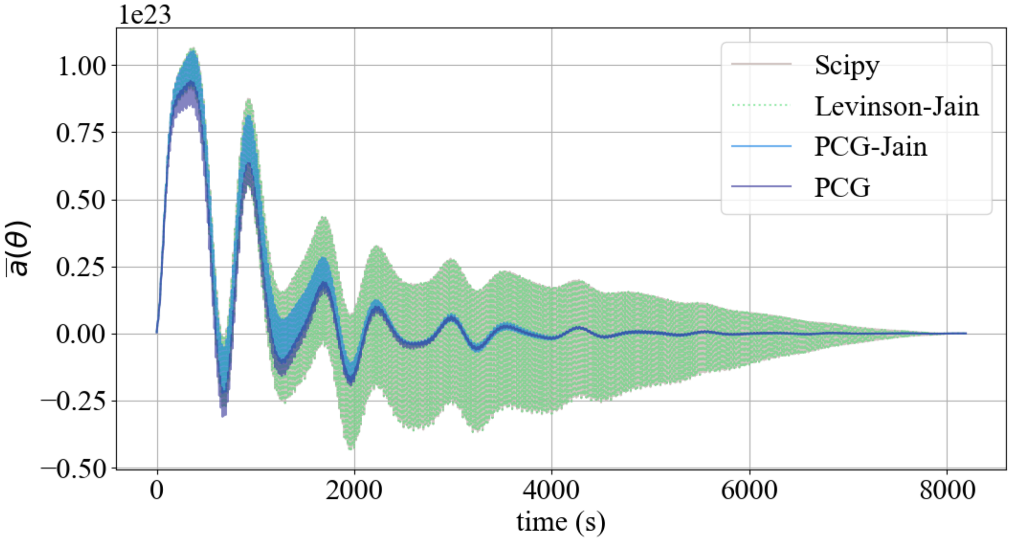

Figure 4.13: Visual representation of the stability of the vector $\overline{a}_j(\boldsymbol{\theta})$, computed with different methods.

Chapter 5

Results

In this chapter, I show and discuss the results obtained in the two different analyses previously introduced.

5.1 Detectability of higher harmonics

This section is based on the published article "Detectability of higher harmonics with LISA"[132] written by me and collaborators. However, some modifications were made for a better integration into the manuscript.

5.1.1 SNR and Bayes factor

Before presenting the Bayes factor and parameter estimation results, I would like to discuss the expectations regarding the contribution of modes. The example considers a source event randomly chosen from the LDCWG Sangria's catalog with an SNR ~ 744, see Table 4.2. Converting the redshifted total mass to the source-frame total mass with a redshift of 4.3, I obtain a value of 2.28×10^5 $\mathrm{M}_\odot$. Using Fig. 4.7, with this source-frame mass, one can expect the term (22|22) to be the dominant contributor, whereas the rest of the SNR will come from (33|33) and (44|44) and the cross-terms (22|21) and (22|32). This is a simple estimation since the source parameters are not precisely the same as the ones listed in Table 4.1, but it will give us a rough estimation.

The actual contribution from each pair of modes is plotted in Fig. 5.1, where I show the squared SNR contribution for each pair of modes for the full IMR signal of the example source. Both axes correspond to the modes, so the intersection represents the pair of modes $(lm|l'm')$. In the diagonal of the matrix-like table, one finds the square terms, while in the upper and lower triangle, one encounters the symmetric cross-terms. The value in each box indicates the squared SNR of each pair of modes, whose absolute value is shown by the color bar. One can see that the pair (22|22) indeed accounts for the largest contribution as expected, followed by the pairs (22|21), (33|33), and (22|33). The color gradient observed when descending in the diagonal line is a consequence of the hierarchical

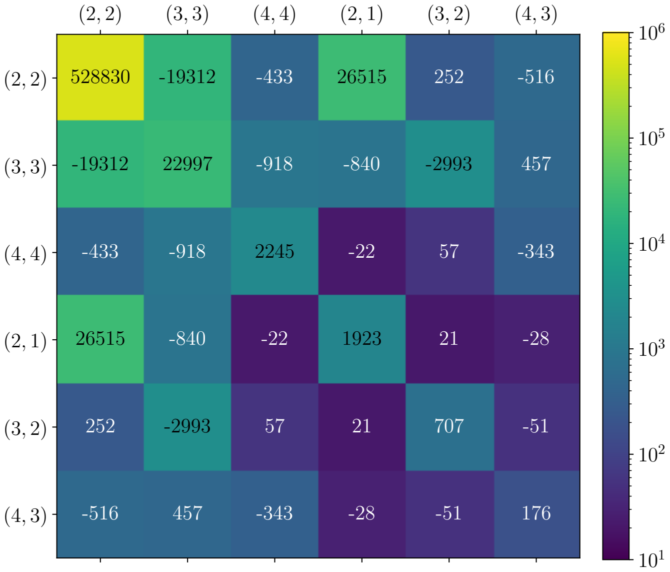

Figure 5.1: Final value of squared SNR of each pair of modes $(lm|l'm')$ for our example. Note the positive values for the square terms and the decreasing values in the diagonal. In contra-position, note the negative values for pairs with different 'm' except for cross-terms (22|21) and (44|32). An interesting result is the relatively high value of (22|21), the second highest value.

ordering of modes. One striking difference with Fig. 4.7 is the high contribution of (22|21) when compared to (33|33), showing that the details of the mode contributions will vary for different sources with different parameters.

Even if the final value of a mode's SNR is small for the complete IMR signal, it does not mean that its impact is negligible in relative terms everywhere in frequency, particularly in the pre-merger phase. This feature can be observed in Fig. 5.2, where I represent the squared SNR absolute value as a function of the frequency. The pairs' contributions are separated into groups to make the figures readable. One can see how some terms dominate in their group below a frequency that approximately corresponds to the merger, after which they later decrease. This happens for the pair (22|32) in the top-right figure or (21|32) in the bottom-left figure. Thus, statements about modes' relative importance, generally depend on the total accumulated SNR.

To quantify LISA's ability to identify the presence of modes, I compute the Bayes factor using the `dynesty` sampler [276]. I compare all the models M_k with $k = 1, \ldots, 5$ with M_6 (the models' definition is presented in Table 4.3). The results gathered in Table 5.1 show clear negative values for all of them. This means the model with six modes is preferred and describes the data better than all other models, as expected. Even the value of -84 (-100 with noise) shows a significant preference for the model M_6 over M_5, where only the mode (4, 3) is absent. Thus, even the weakest modes in this setting should be identified as present in the data, which indicates that LISA observations will be capable

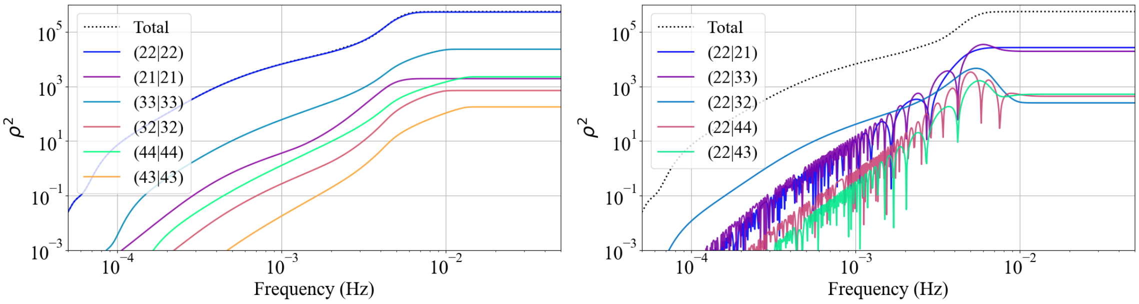

(a) Square terms $(lm|lm)$ (b) Cross-terms $(22|l'm')$

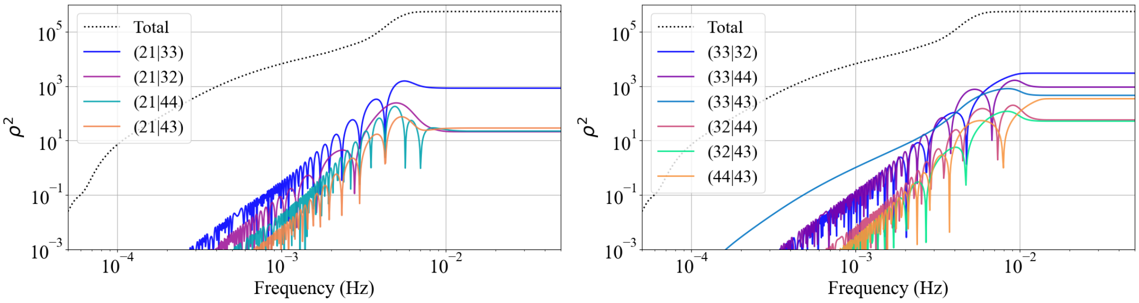

(c) Cross-terms $(21|l'm')$ (d) Cross-terms $(lm|l'm')$

Figure 5.2: Cumulative contribution to the squared SNR (in absolute value) of different pairs of modes depending on the frequency. The upper left figure shows the contribution of the square pairs, where we can see the quadrupolar making the higher contribution. All the other figures show cross-terms, from where we can highlight the contribution of the quadrupolar mode with higher modes $(22|l'm')$, which are predominant over other cross-terms.

of identifying waveform modes beyond the ones available in current waveform models. This result advocates using waveforms with all available higher harmonics to capture all the physics in LISA signals and further developing waveforms with higher mode contents. In the following section, I investigate whether ignoring these weaker higher modes would produce biased parameter estimation results.

5.1.2 Posterior and parameter bias

To assess the impact of the mode's contribution on the estimation of the parameters, I show in Fig. 5.3 the posterior distribution of the logarithm of the chirp mass $\log M_c$, the mass ratio q and individual adimensional spins χ_1, χ_2. Keep in mind, that these intrinsic parameters are relevant to the description of the remnant BH (see Sec. 3.4). The complete array of the parameter's posterior distribution can be found in Fig. B.2 in Appendix B.2.

I show here the six models for comparison. Intersected black lines represent the true values, and each model's posterior distribution is distinguished by the color code indicated in the legend. The parameter estimation for the model with only the quadrupolar mode (green color) leads to biased estimates. As we increase the number of harmonics in the

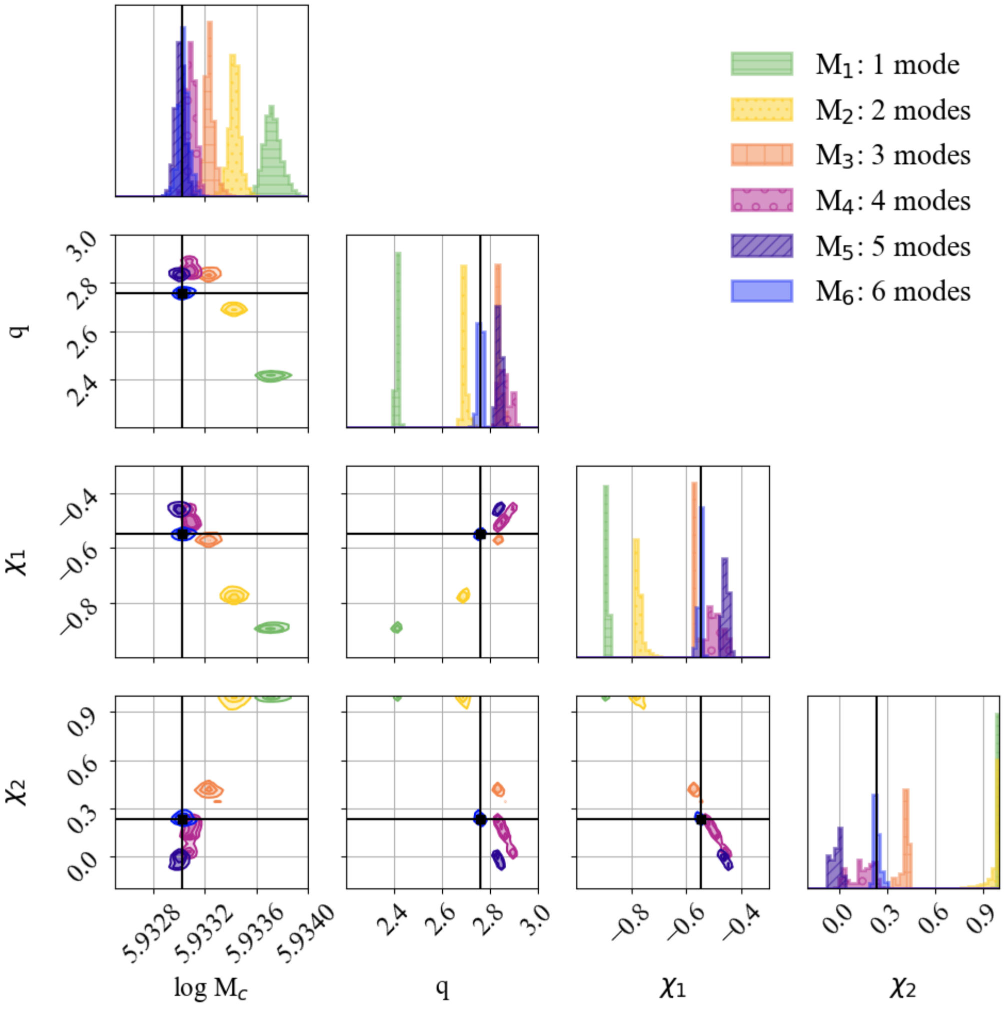

Figure 5.3: Marginalized posterior distribution on mass and spin parameters for noisy data. The six models with different numbers of modes are represented here. The posterior of the model M_6 (blue) finds the true values with high accuracy, while other models tend to induce biases, especially for spin parameters.

Table 5.1: Bayes factor for all models compared to the injected model

Bayes factor	Noiseless dataset	Noisy dataset
$\log(\mathcal{Z}_1/\mathcal{Z}_6)$	-6845	-6873
$\log(\mathcal{Z}_2/\mathcal{Z}_6)$	-976	-1015
$\log(\mathcal{Z}_3/\mathcal{Z}_6)$	-237	-259
$\log(\mathcal{Z}_4/\mathcal{Z}_6)$	-109	-134
$\log(\mathcal{Z}_5/\mathcal{Z}_6)$	-84	-100

Table 5.2: Estimated value for models M_1 and M_6, for the two datasets with noise.

Parameter	True value	Estimated value with M_1 (with noise)	Estimated value with M_6 (with noise)
$\log M_c\ (M_\odot)$	5.93302	$5.93374^{+0.00019}_{-0.00016}$	$5.93304^{+0.00009}_{-0.00010}$
q	2.759	$2.414^{+0.012}_{-0.012}$	$2.759^{+0.013}_{-0.023}$
χ_1	-0.549	$-0.888^{+0.009}_{-0.008}$	$-0.549^{+0.011}_{-0.021}$
χ_2	0.232	$0.996^{+0.004}_{-0.018}$	$0.231^{+0.057}_{-0.030}$

models, the parameter posterior mean values get closer to the injected values. We observe that the posterior of model M_6 (in blue) is centered on the true value for all parameters, which is expected since the signal is injected and recovered with the same model. By comparing models with 3 and 4 modes (M_3 and M_4, orange and pink, respectively), we observe a better estimation of spin parameters when the mode $(2, 1)$ is included in the waveform (model M_4). This observation is consistent with the large relative contribution of $(22|21)$ indicated by Fig. 5.1. The explanation of the importance of the $(2, 1)$ mode and whether this is generic or specific to this example source are left for future investigations. PhenomHM generates the inspiral phase of the waveform with PN approximation, where the $(2, 1)$ mode carries the leading order aligned-spin information [1]. Then, it is not surprising that for highly aligned or anti-aligned spins, this mode becomes important.

In Table 5.2, I list the parameter's injected values and the estimated values, with models M_1 and M_6 in the presence of instrumental and galactic noise. The Table without noise is provided in the Appendix B.2. The super- and subscripts indicate the 68% confidence interval. In both cases, i.e., with and without noise, the model featuring only the dominant quadrupole mode is inaccurate in finding the true values. In contrast, the estimated mean value with all modes is consistent with the injection. Surprisingly, the values obtained with the noisy data and the M_6 template appear closer to the injection than the ones obtained without noise. Note that the posterior distributions are not perfectly Gaussian and the mean value can be shifted due to tails. I performed another run with a different realization of the noisy data, obtaining similar results as the data without noise. The evidence obtained with both noisy realization encompasses the evidence obtained with the data without noise. Therefore, this particular result can be interpreted as

---

[1] See e.g. Eqs. (4.17b) in [275].

a fortuitous outcome of statistical fluctuations. The results of that analysis are shown in the Appendix B. In conclusion, for the medium-SNR and medium-mass case studied (see Fig. 4.7), the absence of higher modes would already result in biased estimated values. These biases would only get worse for higher-SNR and higher-mass systems.

In Fig. 5.4, I illustrate the impact of the parameter biases on the reconstruction of the post-merger waveform. I randomly select 2000 samples from posterior distributions obtained with models M_1, M_3, and M_6 and generate the waveform in the time domain with the same model. Fig. 5.4a serves as a visual representation of the amplitude and phase from the results obtained by each model. We cannot distinguish individual lines due to the small statistical error: the posteriors are centered around biased parameters but with a small dispersion. The waveform reconstruction would therefore be "confidently wrong". Trying to infer a ringdown analysis with IMR information from biased analyses would presumably corrupt GR test. If one compares M_3 and M_6 (in orange and blue, respectively), enlarging the image, one sees visible differences in the post-merger phase. This feature, consistently with the significant Bayes factor for model M_6 over model M_3, highlights the contribution of less dominant modes such as (2,1), (3,2), and (4,3).

One of the tests looking for deviations from GR in ringdown signals consists of comparing the final mass and spin inferred from the ringdown signal with the values derived from the IMR posteriors using formulas fitted on numerical relativity; the consistency between the two estimates is the focus of the test. I do not perform a ringdown analysis here, as it is done in the next section. Still, I illustrate in Fig. 5.4b how the parameter biases found in the IMR parameter estimation would translate into erroneous mass and spin. Using the same fitted formulas as in PhenomHM [131] (see Eqs. (3.6) to (3.8) in [129]), I derived the final mass and spin for 2000 randomly distributed points within the posterior distribution for each model. The IMR parameter biases would translate into significantly biased M_f and a_f. In this figure, the addition of higher modes shows no clear trend for the final mass, but we can appreciate how the introduction of weaker higher modes helps to obtain a more accurate final spin for the remnant BH. Those models are M_4, M_5, and M_6, in pink, purple, and blue, respectively. It is worth mentioning the scattered distribution of M_5, which is the result of the bimodal distribution of individual spins and the mass ratio illustrated in Fig. 5.3.

5.1.3 Modeling error and SNR dependency

The magnitude of the bias on each parameter depends on the SNR and the template waveform used for the inference, hence on the model M_k (with $k = 1, \ldots, 6$). To properly analyze this issue, let's introduce some definitions. Within the Fisher approximation, valid in principle in the high-SNR limit, the statistical error in each parameter σ_θ produced by the noise for a given waveform is determined as

$$\sigma_{\theta_i} = \sqrt{\Gamma^{-1}_{ii}}, \tag{5.1.1}$$

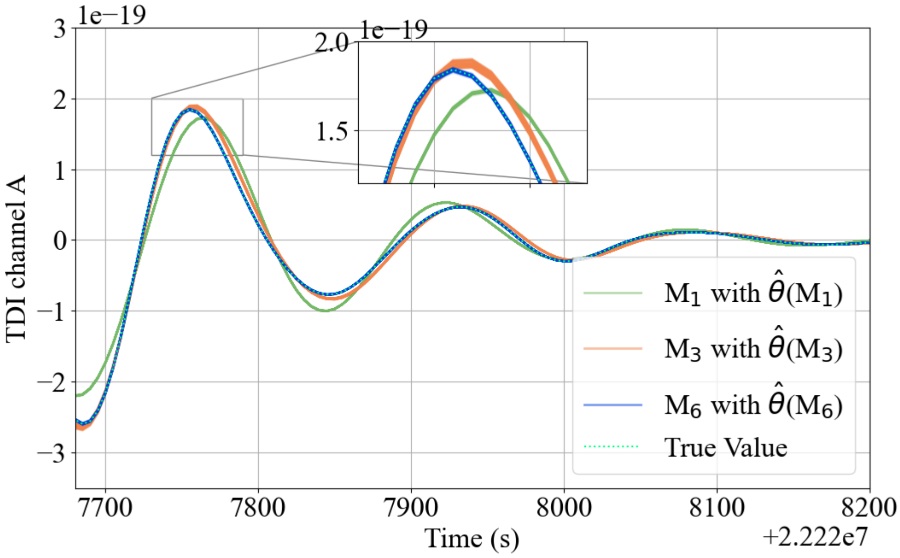

(a) Waveform obtained with models M_1, M_3, and M_6 with parameters sampled from posterior distributions of the corresponding model.

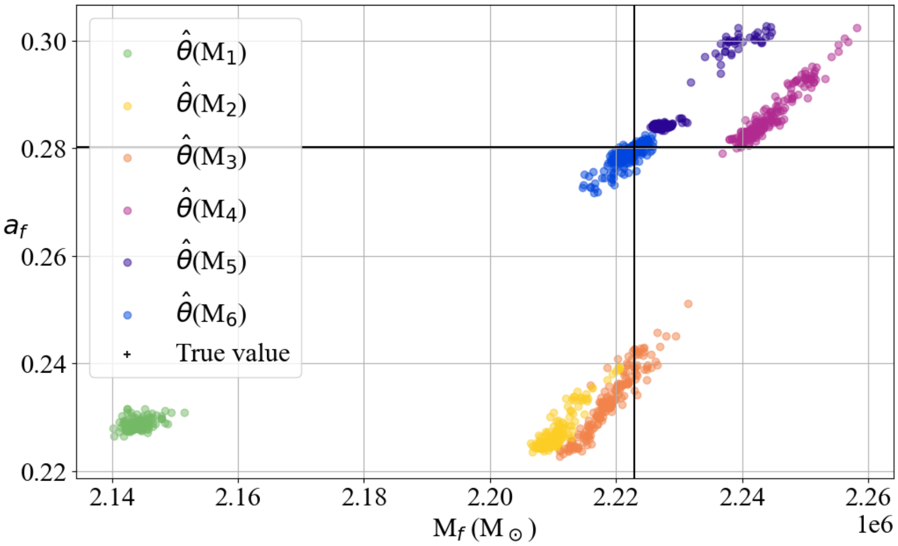

(b) Derivation of mass and spin of the final BH from posteriors distribution using models M_1 to M_6 compared with the true values.

Figure 5.4: Illustrative effect of biased parameters in the ringdown. In the top figure, we see waveforms generated with the same model as the one used in the inference, obtained from 2000 posterior samples for three models $\hat{\theta}(M_{1,3,6})$. We can see the consistency of the models with the injection, albeit its parameter bias. The bottom figure shows the mass and spin of the remnant derived from each set of parameters for all models (colored dots) and the true value (crossing black lines). This is a visual representation of the impact of biased parameters on the remnant BH.

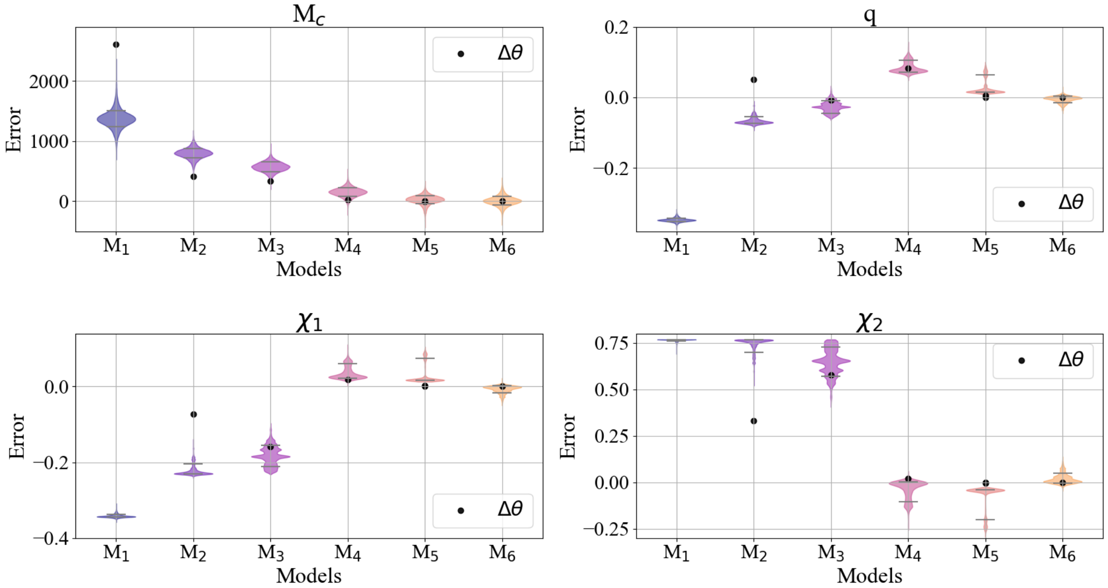

Figure 5.5: Comparison of the error in the intrinsic parameters posterior distribution for all models (M_k, $k = 1, \ldots, 6$ in color) with the error derived from the Fisher approximation (in black). Due to its large value, the Fisher bias for M_1 in the spins and mass ratio lies outside the plot. We observe consistency between the Fisher computation and posteriors for models M_k with $k = 3, 4, 5, 6$ as the bias decreases.

where $\Gamma_{ij} = \left(\frac{\partial h}{\partial \theta_i} | \frac{\partial h}{\partial \theta_j}\right)$ is the Fisher information matrix. In this framework, the statistical error scales directly as SNR^{-1}.

The bias $\Delta\theta(M_k)$ or "modeling error" due to the use of an incorrect template is defined as [291]

$$\Delta\theta_i = \hat{\theta}_i^0 - \hat{\theta}_i^{\text{temp}} = \sum_j \Gamma_{ij}^{-1}(\theta_k) \left(\frac{\partial h_k}{\partial \theta_j} | \delta h_k\right), \tag{5.1.2}$$

where k refers to model M_k, with $k = 1, \ldots, 5$ and $\delta h_k = h_0 - h_k$ is the difference between the true waveform and the template waveform with model M_k. The template model corresponds to waveforms generated with the modes defined in Table 4.3, so δh_k is simply the sum of the ignored modes.

If the statistical error σ_θ is larger than the error produced using an incorrect template $\Delta\theta(M_k)$, one can consider the bias irrelevant. On the contrary, if the statistical error is smaller than the modeling error, the waveform model is not sufficiently accurate to describe the data, and the bias becomes relevant.

I first check in Fig. 5.5 whether the bias observed in the posterior distributions is consistent with the value obtained from the approximate Fisher bias formula in Eq. (5.1.2). I show the bias from each model (black dot) and the error distribution obtained from the sampler (in colors) for intrinsic parameters. In the case of M_1, we observe that the Fisher bias is much larger than the one found by sampling for all parameters, sometimes lying

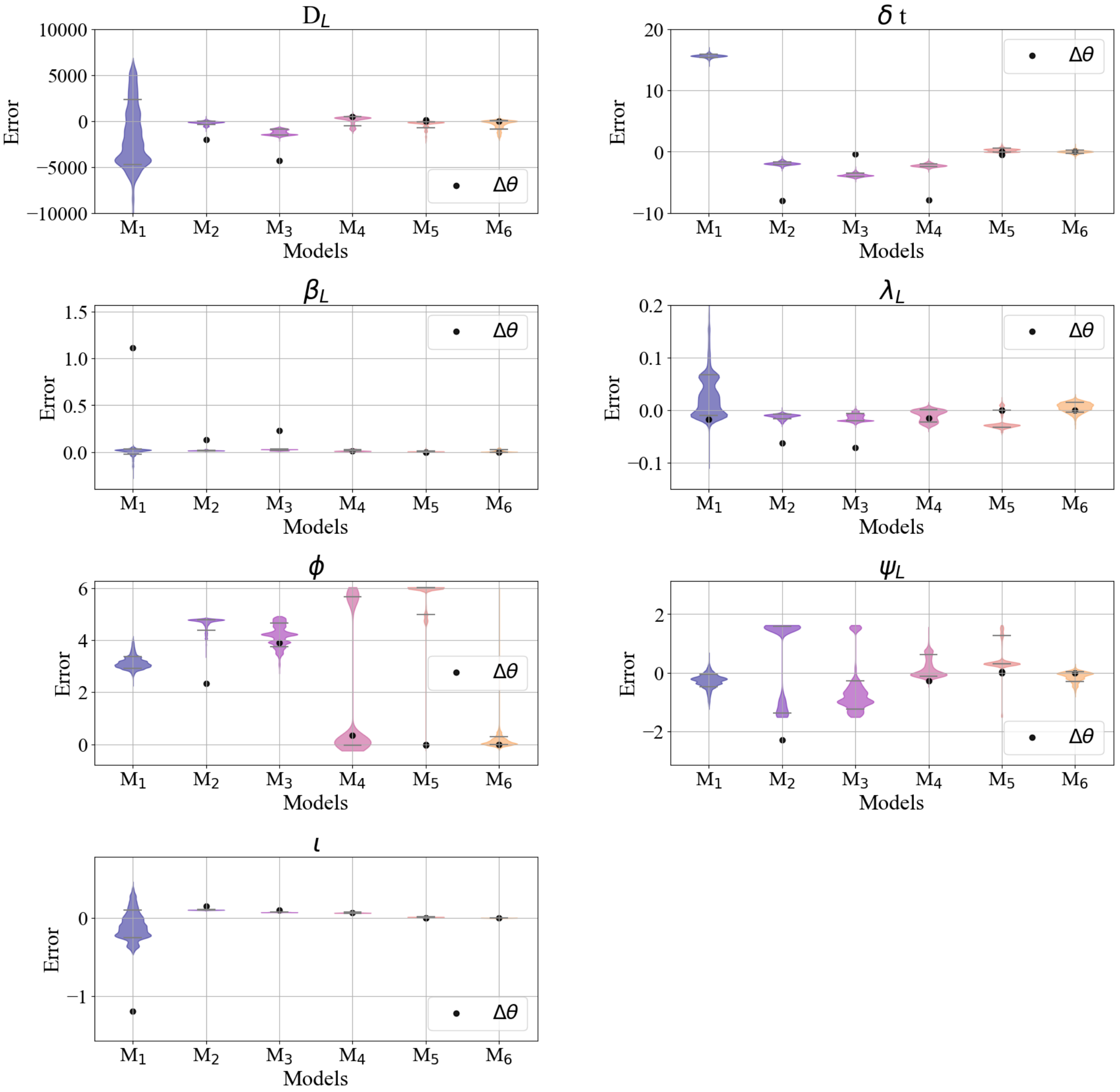

Figure 5.6: Comparison of the error in the posterior distribution of extrinsic parameters for all models (M_k, $k = 1, \ldots, 6$ in color) and modeling error (in black).

outside the plot. For adimensional spins, this may be because their values are limited to the interval [-1, 1] in the sampler, whereas they are unconstrained in the Fisher matrix computation. In the case of M_2, the opposite happens, and the posterior distribution exhibits a slightly larger error than the bias predicted by the Fisher analysis. Overall, from model M_3 to M_6, both errors become more and more consistent as parameter biases shrink. Thus, one can rely on the analytical bias obtained with the Fisher approximation for the intrinsic parameters. The same analysis for extrinsic parameters gave disagreeing results, with typically an overestimation of the bias with the Fisher approximation compared to the sampled posteriors. When comparing the modeling error on the extrinsic parameters obtained from the Fisher information with the ones obtained from posterior distributions, see Fig. 5.6, one can observe some tension. The model M_1 is the least accurate, as some Fisher bias values lie outside the range in the plots. As one introduces more modes, the difference between analytical and experimental results tends toward zero. Thus, one expects the analytical bias to be trustworthy for M_k with $k \geq 4$. As previously mentioned, the discrepancy could come from the constraint set on the parameter space explored by the sampler, which is absent from the Fisher derivation. This can be seen for example in the polarization ψ_L and phase ϕ, where some analytical points are outside the allowed range. Another possible explanation is the multimodality of some extrinsic parameters, such as the ecliptic latitude β_L in LISA's frame and the source inclination ι, especially for M_1. One can also observe that most of the errors obtained with the Fisher information can change if one used for instance adimensional spin parameters such as χ_+ and χ_- instead of individual spins χ_1 and χ_2. Furthermore, the numerics of Fisher matrices are notoriously delicate. The observed discrepancy between extrinsic errors is left for future investigation.

A natural question arises about the minimum SNR at which higher modes become important in the parameter estimation. In other words, given a certain SNR, how many modes do we need to describe the waveform adequately? One way to answer this question is by comparing the approximate statistical error for each parameter σ_θ with the systematic bias induced by an incorrect model $\Delta\theta(M_k)$. This comparison is performed in Fig. 5.7, where I show the errors for the intrinsic parameters as a function of SNR. Varying the SNR amounts to changing the value of the luminosity distance D_L, leaving all other parameters unchanged. The Fisher bias in models M_1 and M_2 are inconsistent with posteriors, as observed in Fig. 5.5. For this reason, I will not discuss them, although they are plotted in the figure. The black diagonal line corresponds to the statistical error in the model parameters (σ_θ), and the color lines represent the modeling error produced by the wrong waveform template (M_k). With the same color code as the modeling error, I mark the value of SNR in dotted lines at which the modeling error becomes higher than the statistical error.

Figure 5.7's top left panel shows that the model M_3 (in pink), which includes modes $(2, 2)$, $(3, 3)$, and $(4, 4)$, does not describe accurately enough the signal for sources with SNR ≥ 129 since the chirp mass bias becomes more significant than the statistical error. Similarly, the model M_4 is sufficient until the SNR reaches 189 and M_5 until 984. Since the SNR of the considered source in this work is around 744, the value of the chirp mass

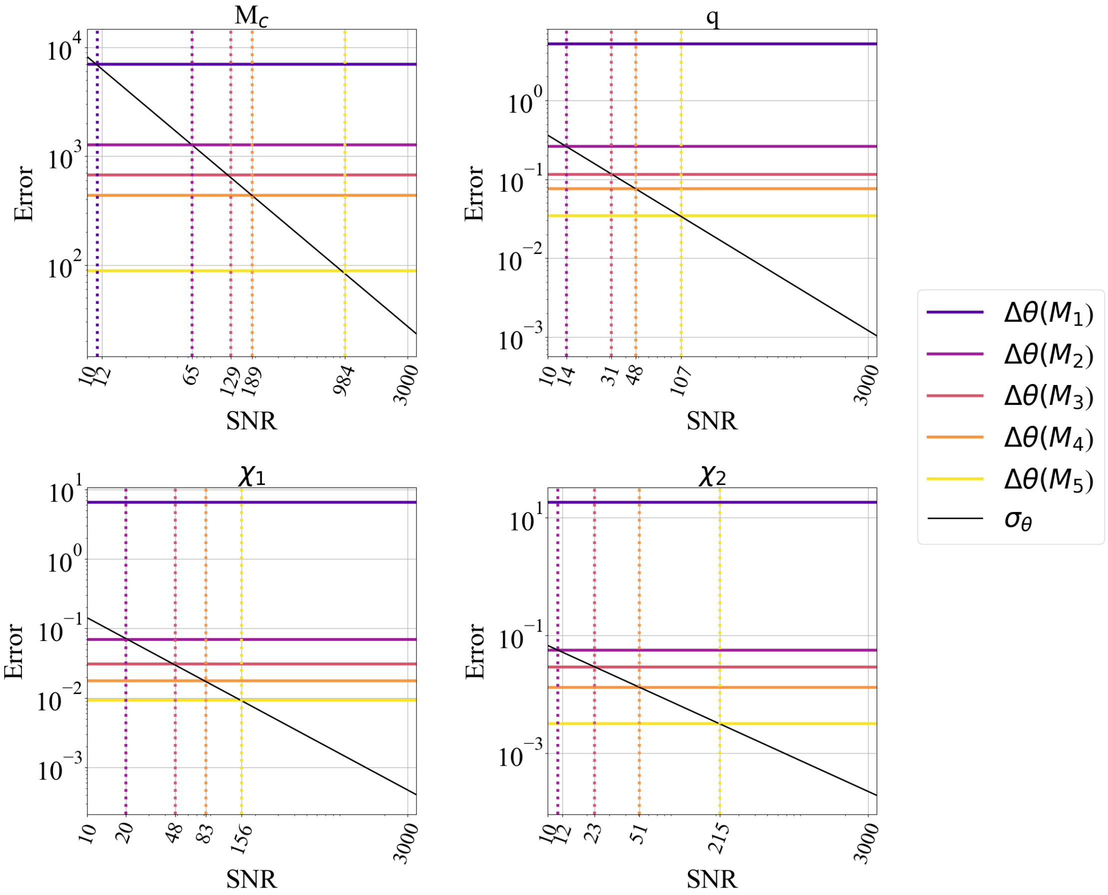

Figure 5.7: Comparison of the statistical error (in black) and modeling errors (in colors) for relevant parameters in function of the SNR. When the statistical error becomes smaller than the modeling error, that model no longer fits the data well and biases the estimated parameters. The SNR for this transition is marked with dotted lines in the correspondent color for each incorrect template (models M_k, $k = 1, \ldots, 5$).

inferred with the model M_5 (in yellow) should be within the estimated error. However, to accurately infer the other parameters, the model M_5 works until an SNR of 107 for the mass ratio, 156 for χ_1, and 215 for χ_2. Then, with an SNR of 744, this model will correctly estimate the chirp mass but induce biases for all other parameters. For consistency, one can look at the inferred values from the Bayesian analysis with M_5 in Fig. 5.3 and confirm this statement within the 68% confidence level.

This analysis does not derive a limit on the number of modes needed to describe an event observed by LISA. Still, it provides maximum SNR values to correctly estimate the parameters with a given model if less than these six modes are present in the waveform. Extrapolating from this example, one finds that generally, sources detected by LISA with SNR of hundreds will require using waveforms with at least six modes to estimate all intrinsic parameters correctly. Note that the Fisher error in Eq. (5.1.1) and its scaling with SNR^{-1} are only approximate and are best valid for high-SNR and nondegenerate posteriors, so this estimate does not replace a complete parameter estimation study, although it gives an idea of the outcome.

5.2 Detectability of GR deviations with QNMs

This section is based on the article "Exploring tests of the no-hair theorem with LISA"[246] written by me and collaborators. However, some modifications were made for a better integration into the manuscript.

In this study, I consider two approaches, an *agnostic* approach, where no assumption on the source parameters is made except on the number of observable QNMs; and the *deviations* approach, where fractional deviations of specific QNMs are estimated. For each approach, I perform two runs: with and without noise. The injected noise corresponds to the instrumental SciRD [2] noise, with the addition of the galactic noise and subtraction of identified sources over one year. In the following, I discuss the results of the noisy dataset obtained with the `dynesty` [276] sampler. In terms of computational resources, for the *agnostic* approach each run took about 24 hrs of CPU in 8 cores, each one with 8 Gb of memory. The number of live points was set to 2048 and the convergence was achieved when the error in the evidence (dlogz) reached the 0.01 value. This value was selected by analyzing the importance weight and the likelihood PDF for different runs. For the second approach, the run took around 10 hrs for the noiseless data and 15 hs for the noisy data. They were also parallelized in 8 cores with 8 Gb memory. The live points and the convergence were set to the same values as in the first approach.

5.2.1 Agnostic approach

As introduced in Sec. 4.5, the parameters used here are $\boldsymbol{\theta} = \{A_k, \phi_k, \omega_k, \tau_k\}$ with $k = 1, 2, 3$ accounting for the three QNMs $[(2,2,0), (3,3,0), (4,4,0)]$. To avoid any degeneracy between the modes, I impose the condition of hyper-triangulation in the frequency.

---

[2] SciRD noise PSD introduced in Sec. 2.4.

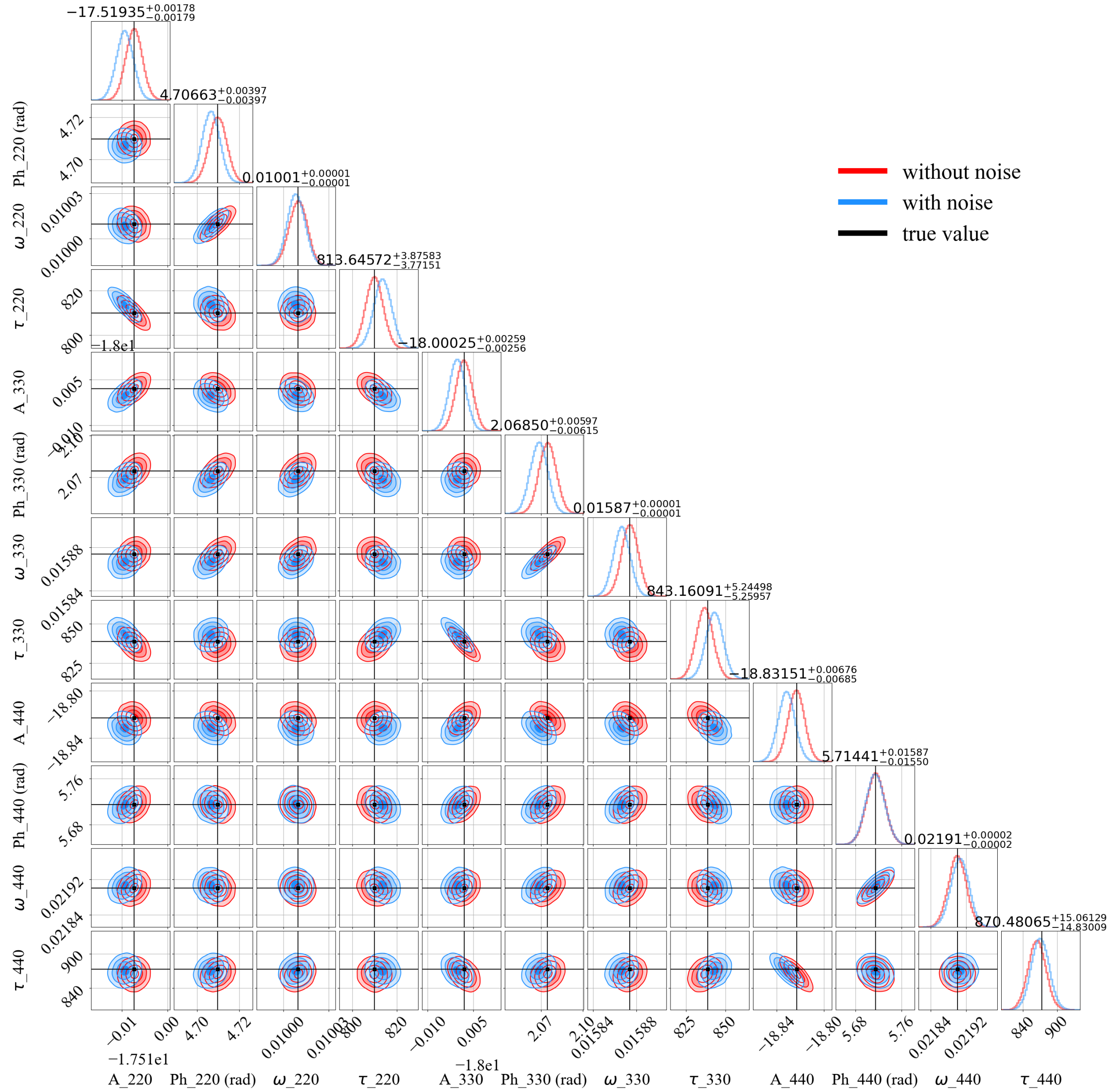

Figure 5.8: Posterior distribution for the *agnostic* case with 4 dimensions per mode $\{A_k, \phi_k, \omega_k, \tau_k\}$. Posterior distribution without noise injection in red, with noise injection in blue, and injected value marked with black lines. Overall, the distributions agree with the true values, with some fluctuations in the noisy case as expected.

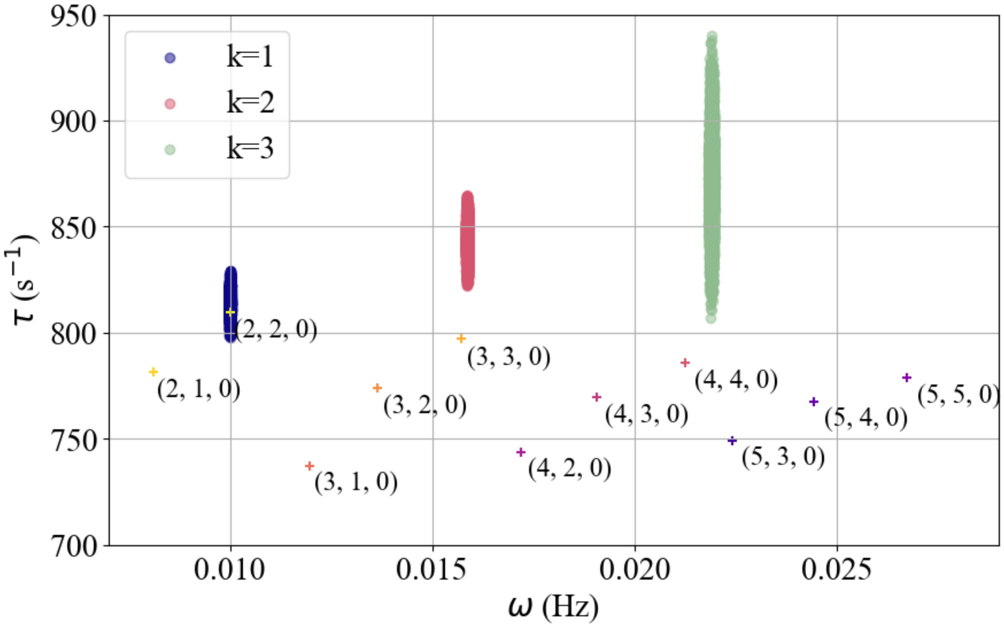

Figure 5.9: Posterior distribution of the pairs of complex frequencies in the spectrum map. Each mode ‘k’ is associated with one color, purple, pink, or green. The spectrum of the true BH is represented with colored crosses with their QNM label nearby.

This condition restricts the second frequency to be larger than the first one, and the third to be larger than the second. Then, the uniform prior of each frequency will decrease with respect to the previous one, like an inverted triangle in the prior volume. The amplitudes have a logarithmic uniform prior in $[-23, -16]$, while the frequency has a uniform prior in $[10^{-5}, 0.1]$ and the damping time in $[1, 10^5]$. The phase is allowed to take any value in the range $[0, 2\pi]$.

In Fig. 5.8, I present the posterior distribution of the injection without noise in red, with noise in blue, and the injected values with black lines. Remember that the values of the deviations injected in the waveform have been introduced in Table 4.4. I show 12 parameters, 4 for each QNM. In general, the Gaussian distributions converge to the true values, with some minor fluctuations in the noisy case, as expected. In the figure I have already labeled the name of the QNMs ’k’ since I know them from the injection. However, in the future LISA data analysis, one will not know which modes are present. Therefore the first thing one should do is to find the QNM corresponding to each label $k = lmn$. The identification of QNMs could be done by comparing the values of the complex frequency (ω_k, τ_k) with pairs of $(\omega_{lmn}, \tau_{lmn})$ corresponding to an assumed mass and spin obtained from an IMR analysis carried out beforehand. I present the idea of this technique in Fig. 5.9. The scatter points correspond to the values of the posterior distribution for $k = 1$ in purple, $k = 2$ in pink, and $k = 3$ in green. The colored crosses correspond to the values of $(\omega_{lmn}, \tau_{lmn})$ easily identified with the QNM labels written nearby. By looking at this figure, one can already notice that there might be a deviation, as there is

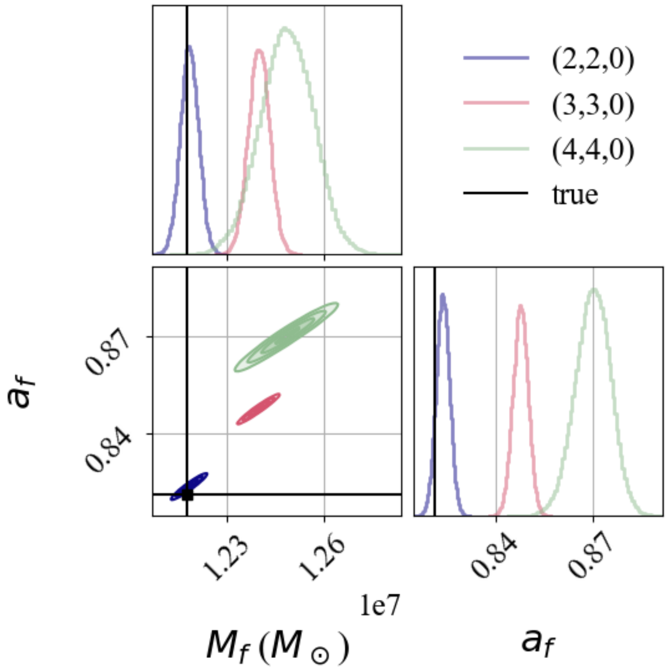

Figure 5.10: Posterior distribution for the mass and spin computed with Eq. (5.2.1) for each pair of $(\omega_{lmn}, \tau_{lmn})$. Note the agreement of (2,2,0) with the true value while the other two modes diverge, making evidence of a deviation from GR in those modes.

only one mode that can be confidently identified with the posterior distributions, that is $k : 1 = (2, 2, 0)$. The other two clusters of points could be assigned to their nearest QNM, namely $k : 2 = (3, 3, 0)$ and $k : 3 = (4, 4, 0)$. At this stage, one could make one of the two following hypotheses:

(i) The IMR estimation is trustworthy and the final mass and spin are taken to be the true values. In this case, the dominant mode could exhibit deviations from GR as well as all the other harmonics.

(ii) The IMR estimation on mass and spin can have systematic errors and therefore the analysis should be done relying only on QNMs. We can identify a QNM that does not present a deviation of GR and assume the inferred mass and spin from that QNM as the true value.

One possible way to check for consistency between QNMs is to trace back the mass and spin of the remnant BH, using, for example, the fittings from [192]:

$$M\omega_{lmn} = f_1 + f_2(1-j)^{f_3}, \tag{5.2.1a}$$

$$\omega_{lmn}\tau_{lmn}/2 = q_1 + q_2(1-j)^{q_3}, \tag{5.2.1b}$$

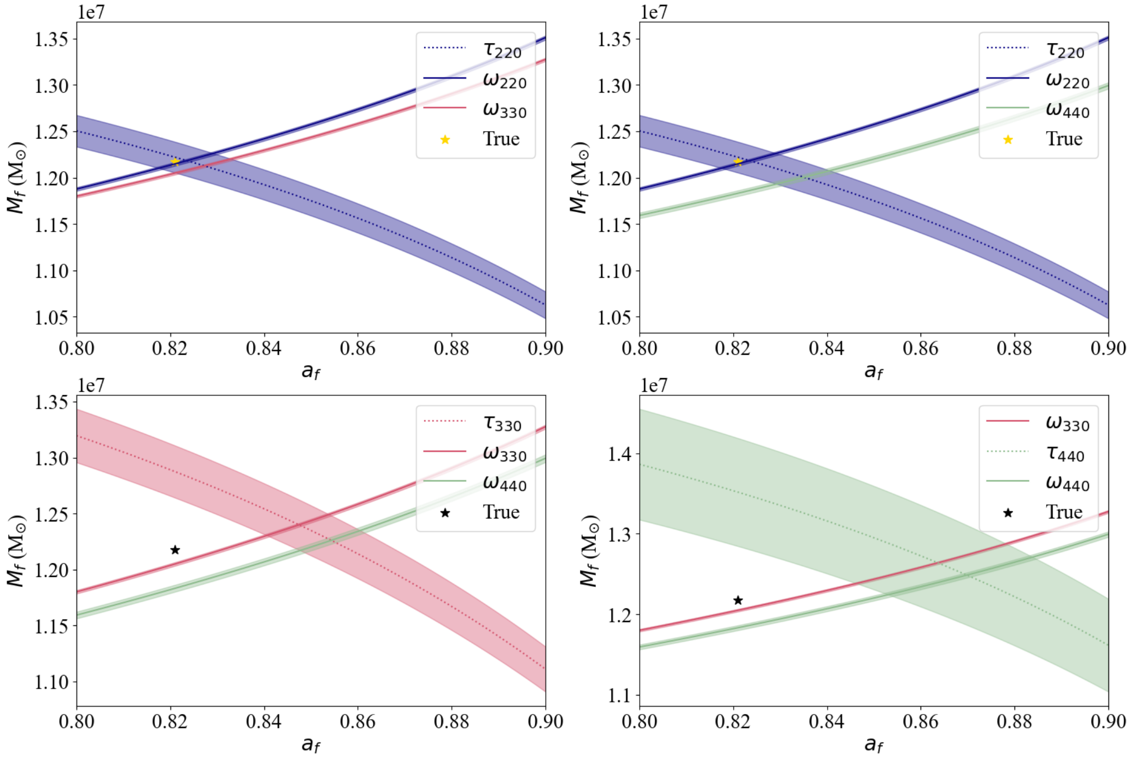

Figure 5.11: Computed mass for spins in the range [0.8-0.9] with Eq. 5.2.1 with a 99% confidence level, from the estimated mean values of $(\omega_{lmn}, \tau_{lmn})$

with f_1, f_2, f_3, q_1, q_2 and q_3 fitting parameters introduced in Table 3.1. The complete tables can be found in [192] as Tables (VIII, IX, X). Thus, with any pair of $(\omega_{lmn}, \tau_{lmn})$ one can compute first the value of the spin and then the value of the mass.

If one takes samples within the posterior distribution of each mode and uses Eqs. (5.2.1), one ends up with a distribution for the mass and the spin as in Fig. 5.10. We could notice already from Fig. 5.9 that the posteriors of the mass and spin obtained from different QNMs would not overlap completely. Here, in Fig. 5.10, we can confirm it by observing three different mean values for the spin without any overlap and three distributions for the mass with overlap between values computed from $(3, 3, 0)$ in pink and $(4, 4, 0)$ in green. Notably, the true value denoted by a black line does not fit perfectly with the mean value of the $(2, 2, 0)$ in purple. This is due to small fluctuations in the (ω, τ) mean value, which can be seen in Fig. 5.8, and the fact that Eqs. (5.2.1) are fitting functions and thus, intrinsic errors of the order of $\sim 1 - 3\%$ [192] are propagated to the mass and the spin.

To better understand the differences in the posteriors, one could alternatively follow the approach adopted in [214]. That is, using Eqs. (5.2.1) to compute the mass for a given spin and compare the values obtained from different QNMs. It is seemingly the same computation as before, but it avoids propagating errors from the spin fitting as it remains fixed. This representation can be seen in Fig 5.11, where the true value is marked with a

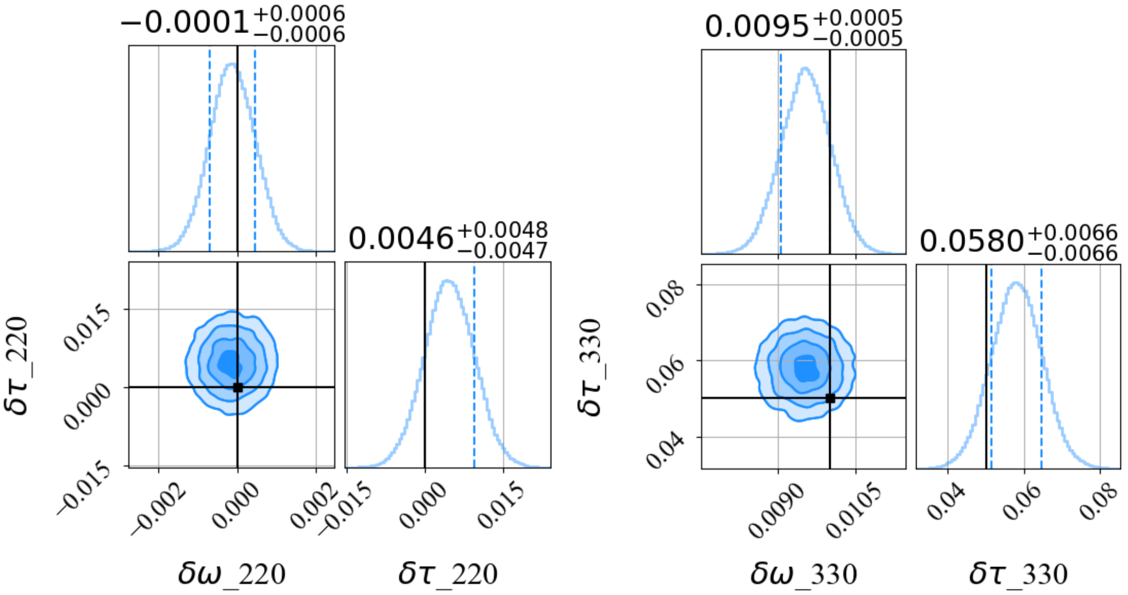

(a) Fractional deviation obtained in ω_{220} and τ_{220}

(b) Fractional deviation obtained in ω_{330} and τ_{330}

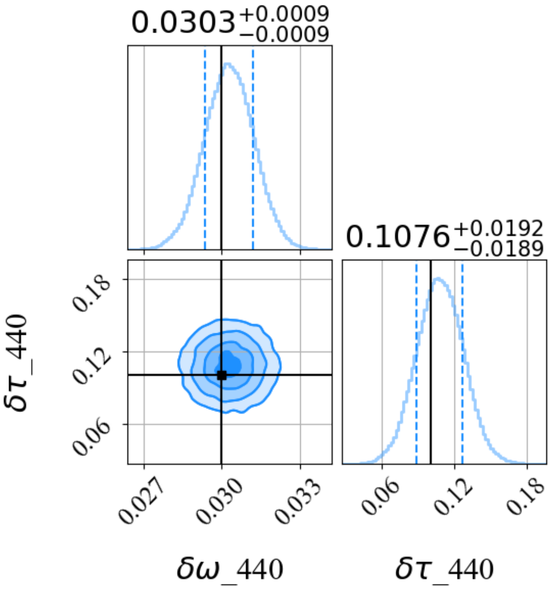

(c) Fractional deviation obtained in ω_{440} and τ_{440}

Figure 5.12: Posterior distribution of the fractional deviations in the complex frequency obtained from the posterior distribution of ω_k, τ_k, with respect to the GR QNMs with true values of M_f, a_f, for $k = lmn$ found in the source.

golden or a black star, and the shadow lines correspond to the 99% confidence level. The standard deviation for the mass is related to the standard deviations of ω and τ. Note the narrow uncertainty bands derived from the frequencies ω_{lmn} for any lmn, as a result of the precision on the frequencies posteriors. The mass and spin obtained from the $(2,2,0)$ mode are consistent with the injected value, while the others exhibit deviations from it and thus from GR.

Using the IMR masses and spins as references

At this stage, we can initiate the discussion on the two hypotheses stated above. I will start with the first assumption (i). Imagine one wants to quantify the deviation at each mode's frequency to put some constraints in an alternative theory. In that case, one has to compare the posterior distributions of frequency and damping time with the QNM values for a BH with the IMR estimated final mass and spin. To simplify, I assume that the parameters estimated from the IMR analysis equal the exact injected values. Results can be seen in Fig. 5.12, where I compute the fractional deviation as the difference between the posterior distribution in each mode and the true complex frequency value normalized by the true value. In this figure, we can see that each posterior agrees with the injected value within 2σ. The dashed blue lines mark the quantiles (0.16, 0.84), i.e. the 1σ distribution.

However, using reference values for the mass and the spin is inconsistent with the agnostic philosophy. Keep in mind that, the mean values estimated from an IMR analysis could present a bias. Moreover, using the whole parameter posterior distribution instead of mean values would better allow for the propagation of uncertainties. Then, the comparison should be made with the complex frequency computed with an IMR posterior distribution of the estimated mass and spin and not only the mean values.

Relying only on QNM characterization

Without a posterior distribution from an IMR waveform inference, I now adopt the second of the two above hypotheses and use the mass and spin obtained from the dominant mode as reference values. While I already showed above that the dominant mode agrees within a 99% credible confidence with the injected parameters, there is a risk in assuming that the $(2,2,0)$ mode does not deviate from GR. Correspondingly, deviations in the dominant mode might also appear. In a beyond-GR theory, the values of QNMs will return different masses and spin highlighting the deviation from GR. Whether it affects the dominant mode or the subdominant modes needs to be studied case by case with different alternative theories.

Now, to quantify the deviations in this framework, one should translate the differences in mass and spin into deviations in ω and τ in terms of $\delta\omega, \delta\tau$, see Eqs. (4.5.3), (4.5.4). To this end, I assumed that the posterior distribution obtained from the $(2,2,0)$ mode is the "true" description of the remnant BH in GR. One can then compute the QNM spectrum with the derived mass and spin from that mode. This computation is shown in Fig 5.13, where we observe the posterior of the three complex frequencies $\tilde{\omega}_{lmn}$ computed

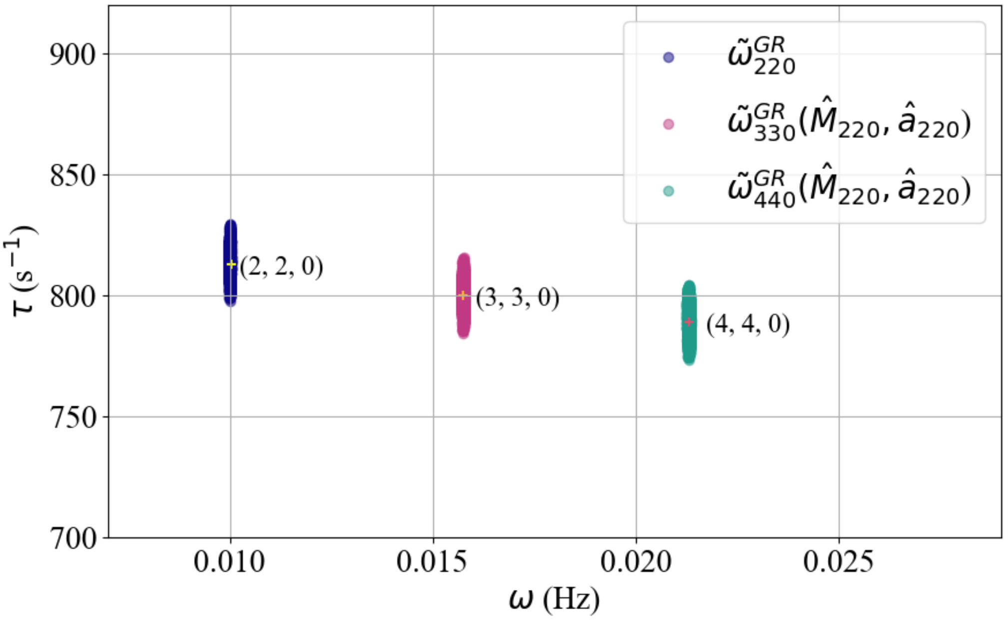

Figure 5.13: Posterior distribution of each mode, generated from the posterior distribution of mass and spin derived from the (2,2,0) mode, compared with true spectrum.

with the mass and spin derived from the dominant mode $\{\hat{M}_{f220}, \hat{a}_{f220}\}$. The GR values are marked with colored crosses on top of the distributions. As stated, deviations might appear in the $(2,2,0)$ mode. Thus, comparing the mass and spin estimated from this BH spectroscopy with those inferred from the full IMR waveform would be informative.

Given the distributions without deviations, one can measure the deviation for each parameter. For that, one needs to compare the obtained complex frequency from the sampler (lmn) with the values of the computed complex frequency obtained with the mass and spin from the $(2,2,0)$ mode $(lmn(\hat{M}_{f220}, \hat{a}_{f220}))$ for each mode. This is analogous as comparing Fig. 5.10 with Fig. 5.13. In Fig. 5.14, the distribution of GR complex frequencies computed with the mass and spin derived from the $(2,2,0)$ mode is shown in pink for the $(3,3,0)$ mode at the top and in the bottom in green for the $(4,4,0)$ mode. We can easily differentiate them from the non-GR values obtained from the sampler in blue. A simple equation to quantify this tension is commonly used [292; 293]

$$N_\sigma = \frac{|\mu_A - \mu_B|}{\sqrt{\sigma_A^2 + \sigma_B^2}}, \tag{5.2.2}$$

where A and B are two different models, μ is the estimated mean value and σ is the standard deviation. This equation gives the number of standard deviations between two posterior distributions in one dimension. This simple definition can be used as a means to estimate uncertainties in the following. For the injected values in Table 4.4, the computed standard deviation from GR values is shown in Table 5.3. Should this be observed, I

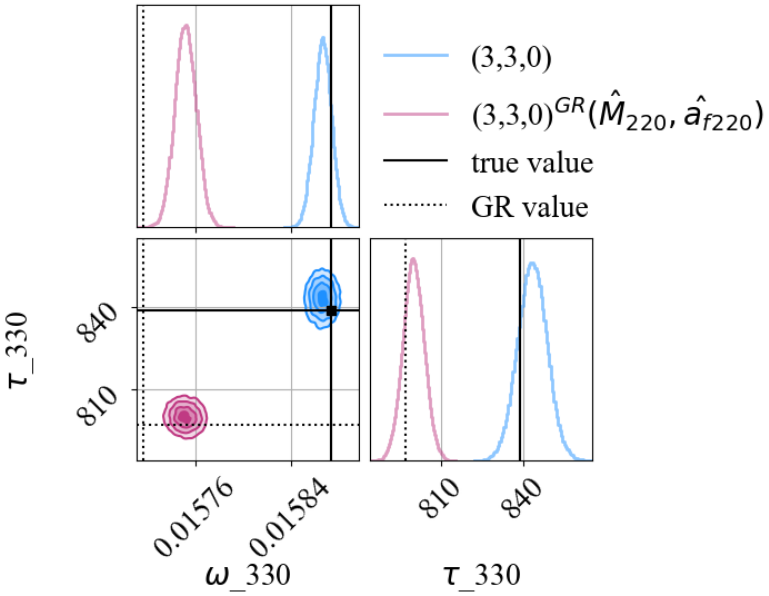

(a) Posterior distribution of ω_{330} and τ_{330} against the distribution within GR.

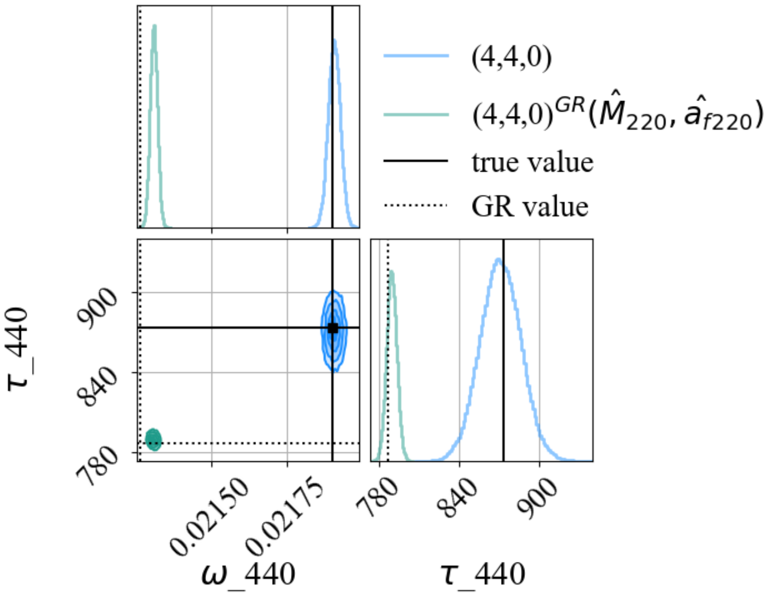

(b) Posterior distribution of ω_{440} and τ_{440} against the distribution within GR.

Figure 5.14: Evidence of deviations in the frequency and damping time computed with the estimated final mass and spin. I show the posterior distribution of the complex frequency for each mode in blue, against the computed posterior distribution in the GR framework for the parameters derived from the $(2, 2, 0)$ modes in pink for the $(3, 3, 0)$ mode at the top and in green for the $(4, 4, 0)$ at the bottom.

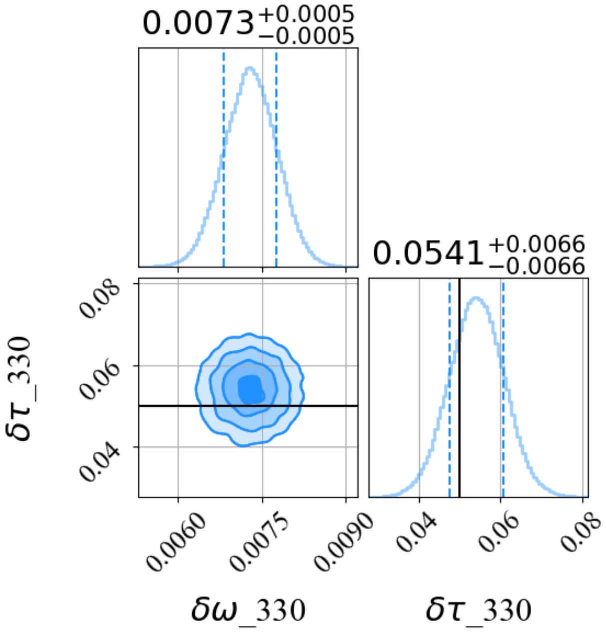

(a) Fractional deviation from GR in $\tilde{\omega}_{330}$.

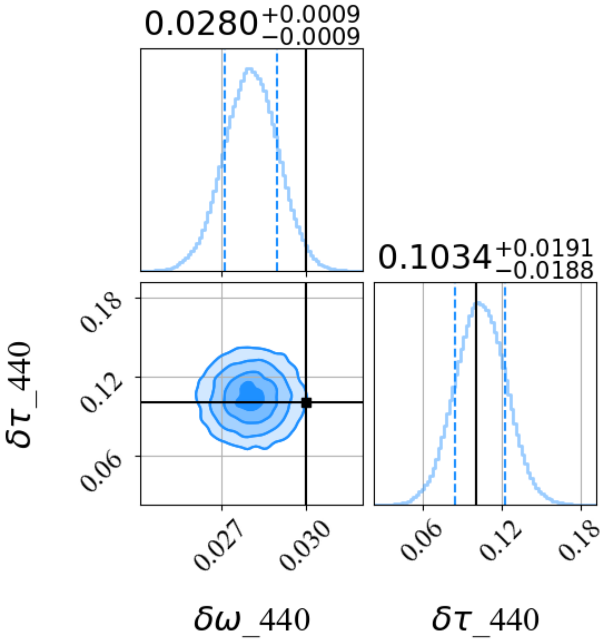

(b) Fractional deviation from GR in $\tilde{\omega}_{440}$.

Figure 5.15: Evidence of deviations in the frequency and damping time computed with the estimated final mass and spin. I show the posterior distributions of the difference of the obtained posterior with respect to the mean value of the estimated GR QNM from $(2, 2, 0)$ mode. By doing so, the fractional deviation becomes evident. One can see the obtained fractional deviation of the $(3, 3, 0)$ mode on the top and of the $(4, 4, 0)$ mode on the bottom. The damping time agrees with the injected value (black lines) for both modes, while the frequency presents a bias due to the high sensitivity to the remnant parameters estimated from the $(2, 2, 0)$ mode.

Table 5.3: Computed uncertainty from GR for the injected parameters in the agnostic case.

	$N_{\sigma^{GR}}$ (3,3,0)	$N_{\sigma^{GR}}$ (4,4,0)
$\delta\omega$	10.31	28.46
$\delta\tau$	7.97	5.62

would have detected a deviation from GR in ω_{330} with more than 10 standard deviations with respect to the $(2,2,0)$ mode. It is also important to note that even though I was able to distinguish a deviation from GR with high precision, the injected value does not correspond to the recovered value, thus indicating a bias.

Therefore, with the hypothesis (*ii*) this kind of analysis would allow us to differentiate GR from another theory. However, if one tries to put constraints on that alternative theory, one might fail as the recovered values of the deviations are not exactly the same as the injected ones. This can be seen in Fig. 5.15, where the injected value (in black) does not appear in the posterior distribution of Fig. 5.14a. Indeed, the estimated value is not consistent with $\delta\omega_{330} = 0.01$. The possible explanation is that I used the GR value inferred from the mass and spin from the distribution obtained with the $(2,2,0)$ mode. Remember that I assumed no deviation from GR in the dominant mode. Even if the mass and spin computed from the $(2,2,0)$ mode agree with the true values, the assumption of non-deviation in this mode might have strong implications, as any fluctuation on the $(2,2,0)$ mode will translate into fluctuations in the estimated mass and spin and therefore in the characterization of the $(3,3,0)$ and $(4,4,0)$ modes. Certainly, the computation of the QNMs highly depends on the mass and spin, thus small variations of those intrinsic parameters translate to larger variations on the complex frequency parameter space.

One can avoid this type of discrepancy by using the posterior distribution of the mass and spin inferred from the full IMR instead of the posterior inferred from the $(2,2,0)$ mode. Again, this implies that the IMR analysis should provide unbiased values. In the present analysis, the mass and spin from the $(2,2,0)$ mode were consistent within 2σ with the injected value.

5.2.2 Deviation approach

In the following, I discuss the results of the *deviation* template. For this search, I defined beforehand which QNMs appeared in the waveform. I also assumed that the dominant mode did not have deviations from GR. Imposing this condition enables us to break the degeneracy between the mode's fractional deviations from GR and the BH mass and spin. Alternatively, one can fix the mass and the spin, but allow the whole QNM spectrum to present deviations.

The parameters used in this approach are $\boldsymbol{\theta} = \{M_f, a_f, A_{220}, \phi_{220}, A_k, \phi_k, \delta\omega_k, \delta\tau_k\}$ with k=$[(3,3,0),(4,4,0)]$. The mass and spin have a uniform prior within a range of 10% around the injected value, this is [0.9, 1.1]$\times M_f$ and [0.9, 1.1]$\times a_f$. The phase has a uniform

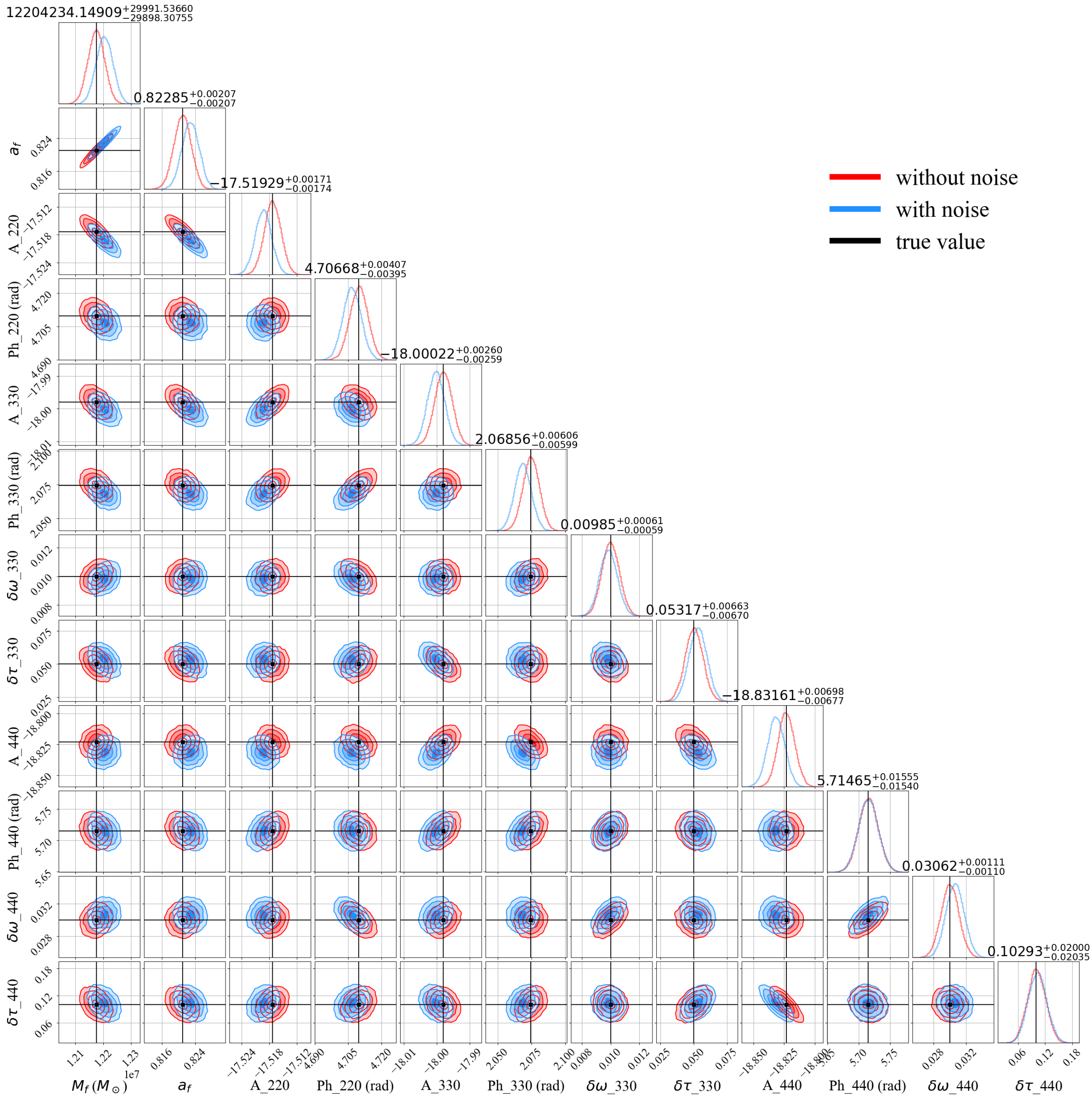

Figure 5.16: Posterior distribution for the *deviation* template. Results are shown without noise injection in red, with noise injection in blue, and the injected values are marked with black lines. Overall the distributions agree with the true values, with some fluctuations in the noisy case as expected.

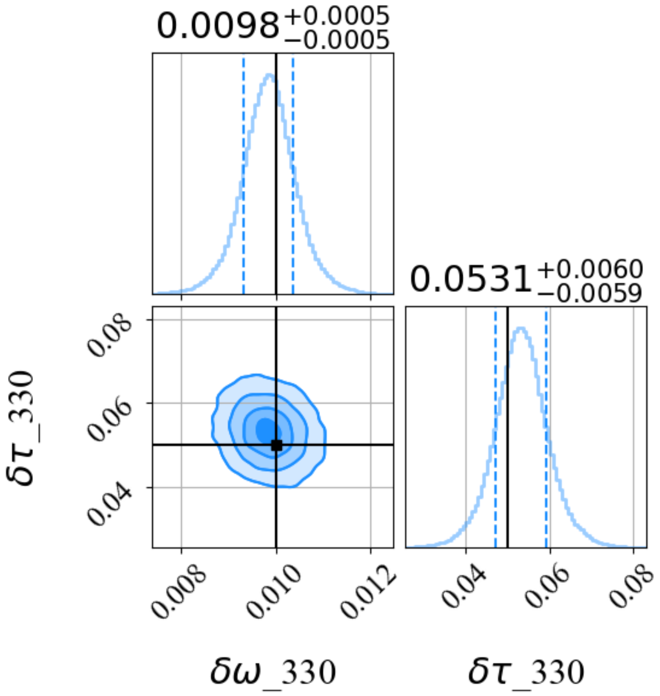

(a) Fractional deviations in $(3, 3, 0)$

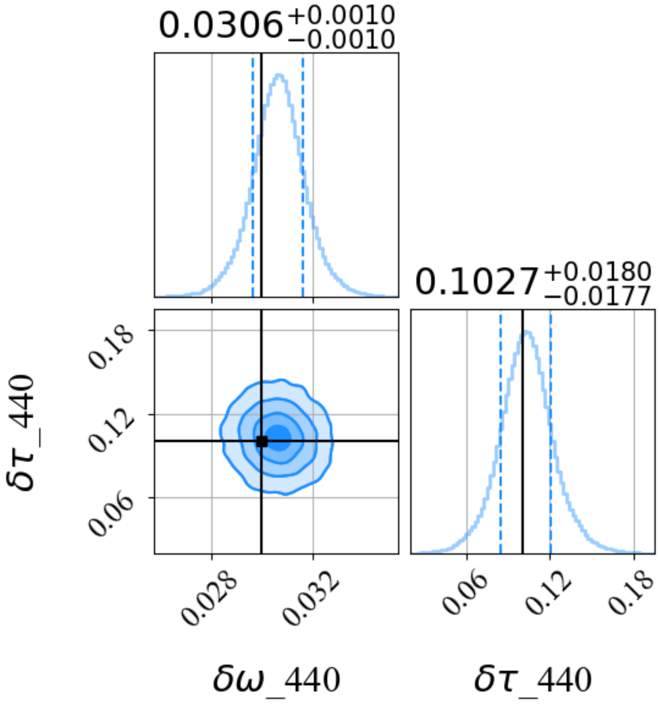

(b) Fractional deviations in $(4, 4, 0)$

Figure 5.17: Posterior distribution of fractional deviations in modes $(3, 3, 0)$ and $(4, 4, 0)$ directly from the sampler. Dashed lines denote the 1σ error and the black lines denote the injected value. Agreeing results with high precision are obtained.

Table 5.4: Computed deviation uncertainty from GR for the injected parameters in the *deviation* approach.

	$N_{\sigma^{GR}}$(3,3,0)	$N_{\sigma^{GR}}$(4,4,0)
$\delta\omega$	16.34	27.81
$\delta\tau$	7.98	5.06

prior in the range [0,2π], while the amplitudes have a logarithmic uniform prior in [-23, -16]. Lastly, the deviations have a uniform prior in the range $\delta\omega, \delta\tau$ = [-0.2, 0.2]. This range arises naturally from the QNMs that I choose, as the relative difference between two QNMs is bigger than 0.2:

$$\frac{|\omega_{220} - \omega_{330}|}{\omega_{220}} > 0.2. \tag{5.2.3}$$

For QNMs with closer spectrum such as $(2, 2, 0)$ and $(2, 2, 1)$, there is a switch on the labels, producing a degeneracy between those two modes and exhibiting a bimodal posterior distribution. For this reason, I did not include the QNM $(2, 2, 1)$ in the analysis, even though its presence might have been detected in GW150914 [207] albeit with small significance, see the discussion [201; 207–211]. I leave the integration of this particular case to be studied in the future.

In Fig. 5.16 I show the posterior distribution with and without noise injection in blue and red respectively. Injected values are marked with black lines. One can observe the consistency between both results with the true values.

Note that in this approach, the analysis is straightforward. The fractional deviations in the spectrum are direct results of the sampler since the deviations found in each QNM already account for the estimated mass and spin. In Fig. 5.17 I zoom in the deviations of the $[(3, 3, 0), (4, 4, 0)]$ modes from Fig. 5.16. The posterior distributions agree with the injected values with high accuracy and precision. The uncertainty on the deviations from GR fractional parameters $\delta\omega$ and $\delta\tau$ with this template are listed in Table 5.4. Under the assumption of no deviation in the $(2, 2, 0)$, the same hypothesis (*ii*) as in the previous analysis, it is possible to derive constraints on an alternative theory, since the injected values are within the posterior distributions. A caution message is imperative here. The template considered, by construction, does not allow deviations in the dominant mode. The effect of a fractional deviation in the $(2, 2, 0)$ mode, when not considered in the search template needs further investigation. Nevertheless, to constrain an alternative theory the model-independent template might not be enough, and specific templates for beyond-GR theories are required.

Given that the value of the standard deviation for each parameter is inversely proportional to the SNR, there is a way to estimate the SNR needed to observe a specific deviation from GR with a given uncertainty in terms of standard deviation. I will expand on this idea in the following section.

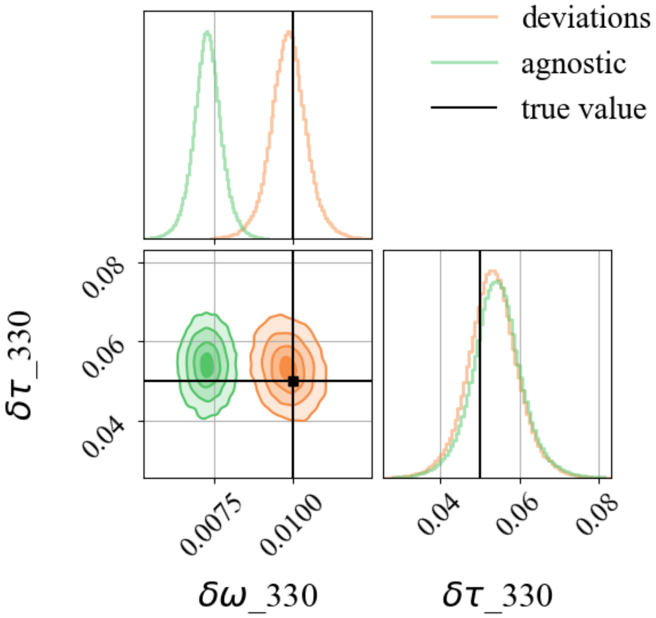

(a) Fractional deviation for $(3,3,0)$ mode with both methods

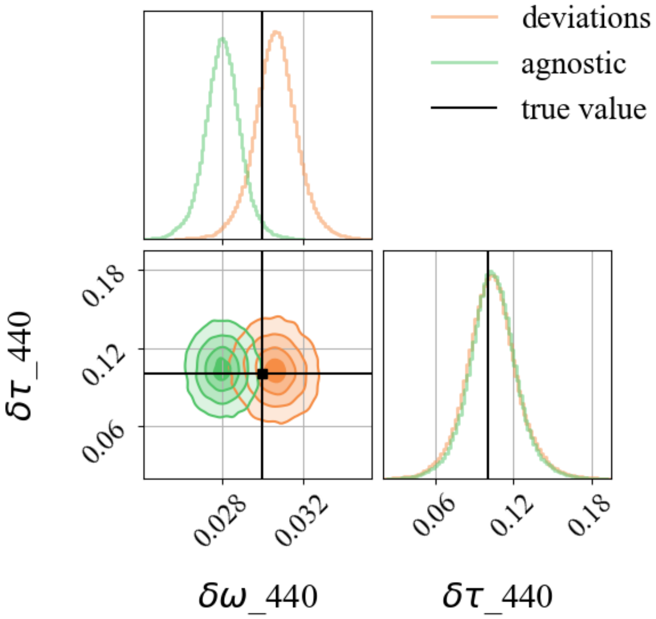

(b) Fractional deviation for $(4,4,0)$ mode with both methods

Figure 5.18: Comparison of the posterior distribution of the fractional deviations for modes $(3,3,0)$ and $(4,4,0)$ for the two different methods. Posterior distribution obtained for the *deviation* approach in orange against the *agnostic* approach in green. Injected values are marked by the black lines intersection.

5.2.3 Discussion

In the perspective of testing the no-hair theorem and possible deviations from GR with the LISA instrument, I explore the extent to which one can extract the largest amount of information through two different analyses in terms of two generic templates. One possible approach is to compare the posterior distribution of fractional deviations in frequency and damping times $\delta\omega_k, \delta\tau_k$ from the different approaches. Thus, the comparison of both methods can be observed in Fig. 5.18, where the posterior distribution of deviations for the *agnostic* approach are shown in orange and the results for *deviations* approach in green. The injected values are denoted by black lines. The second approach gives more accurate results, making it possible to constrain alternative theories to GR. One should keep in mind, however, that the agnostic result is based on the premise that no deviation from GR is allowed in the $(2, 2, 0)$ mode. If one relaxes this constraint and assumes that the IMR estimation is accurate enough to fix the mass and the spin values, then a deviation in the dominant mode can be considered and the deviations of higher harmonics would be consistent with the injected values, as seen in Fig. 5.12. However, this result strongly depends on the estimated mass and spin from the full IMR template, whose values can be biased from the true values if features like higher harmonics, eccentricity, or precession, to name only a few, are not considered.

5.3 Test of GR versus SNR

In this section, I discuss the SNR needed to claim a deviation from GR with different parameters. Towards this goal, I will use the *deviation* template, which provides the best consistency. I compute the standard deviation in the same way as in Eq. 5.1.1,

$$\sigma_{\theta_i} = \sqrt{\Gamma_{ii}^{-1}}, \tag{5.3.1}$$

with Γ_{ii} the Fisher matrix computed as the inner product of the partial derivatives with respect to the parameters, defined in Eq. (4.3.6)

$$\Gamma_{ii} = \left(\frac{\partial a(\boldsymbol{\theta}_i)}{\partial \boldsymbol{\theta}_i} \middle| \frac{\partial b(\boldsymbol{\theta}_i)}{\partial \boldsymbol{\theta}_i} \right). \tag{5.3.2}$$

The results are presented in Table 5.5, showing the consistency between the error obtained from the Bayesian analysis with the Fisher forecast. Even if the Fisher matrix underestimates the uncertainty for $\delta\tau_{440}$, possibly due to the noise injection, one can still extract information from the other parameters.

From Eq. (5.3.1) we see how the value of the uncertainty varies as the inverse of the SNR, so naturally the standard deviation in the different parameters decreases as the SNR increases. Consequently, it is related to a given source's total mass and luminosity distance. One can therefore estimate the deviation uncertainty, needed to claim a deviation from GR with 5σ, for a given mass and redshift. Of course, the number of sigmas N_σ is itself constrained by the value of the fractional deviation, as shown in Eq. (5.2.2).

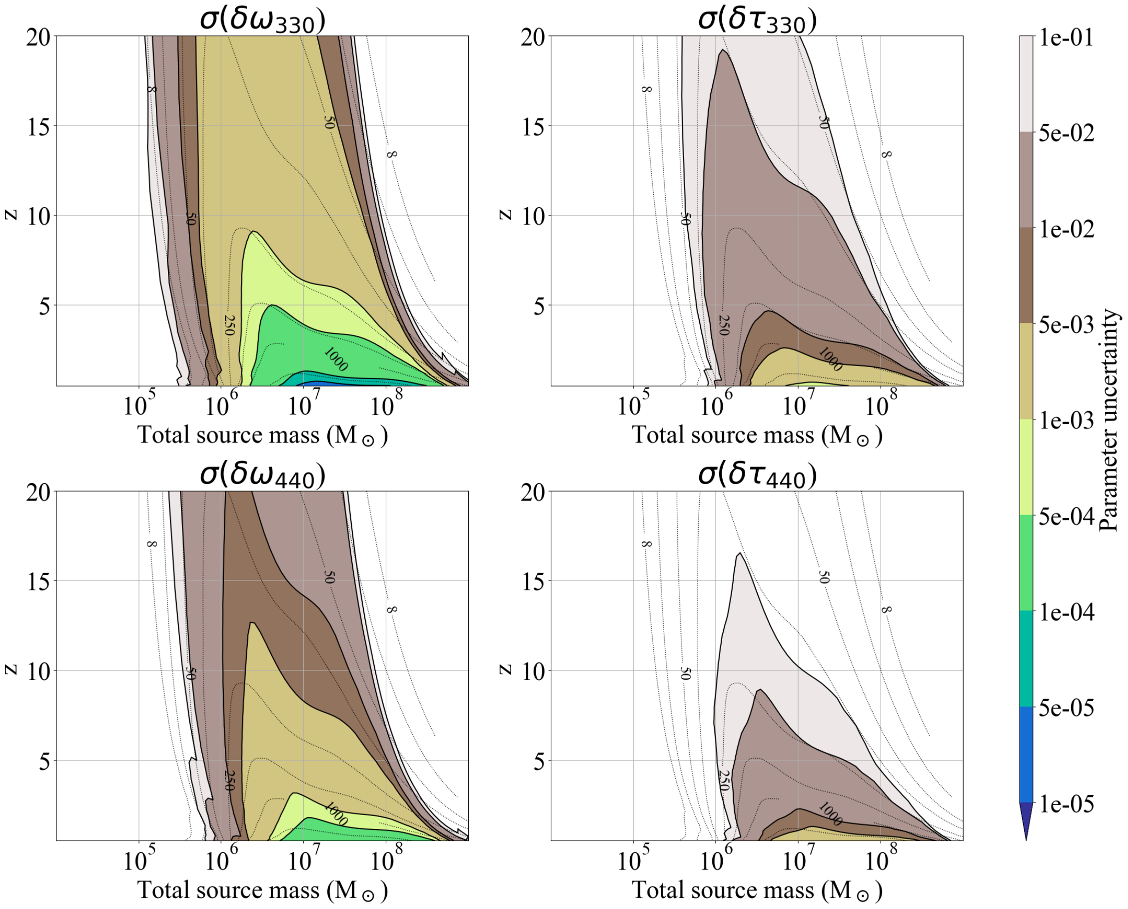

Figure 5.19: Uncertainty for fractional deviations from GR in ω and τ in modes (3,3,0) and (4,4,0) with respect to the source total mass and the redshift. These values are obtained for the fixed parameters listed in Table 4.4.

Table 5.5: Uncertainty computed with the Fisher matrix (second column) and obtained with the sampler (third column).

	σ_{FM}	σ_{sampler}
$\delta\omega_{330}$	0.587×10^{-3}	0.602×10^{-3}
$\delta\tau_{330}$	6.252×10^{-3}	6.648×10^{-3}
$\delta\omega_{440}$	1.047×10^{-3}	1.101×10^{-3}
$\delta\tau_{440}$	11.978×10^{-3}	20.28×10^{-3}

I show in Fig. 5.19 the uncertainty for the parameters with possible deviations from the GR values using the *deviation* template, such as $(\delta\omega_{330}, \delta\tau_{330}, \delta\omega_{440}, \delta\tau_{440})$. Several assumptions have been made from the beginning of the study, therefore the result I present does not provide a general detection forecast. Nevertheless, this analysis provides a qualitative understanding of LISA's ability to observe deviations from GR in the ringdown phase of an MBHB coalescence. The uncertainty on the fractional deviations is represented in terms of the source total mass and the redshift since they are the dominant contributors to the SNR. Note that I let all other source parameters be fixed to the same values listed in Table 4.4. Consequently, the estimates shown in Fig. 5.19 are source-dependent, i.e. valid for the particular BH I chose as a case study. Another choice of BH parameters would change this result. Different inclinations, spins, and mass ratios would inevitably change the relative amplitude between QNMs and thus the uncertainty in each mode's complex frequency.

The color code on the right-hand side of Fig. 5.19 indicates the value of the uncertainty on the fractional QNM frequencies, obtained with the Fisher matrix for the considered example source. For instance, looking at areas where $\sigma \geq 0.001$, LISA should be able to detect deviations from GR in $\delta\omega_{330}$ at the level of 5 standard deviations or more if the deviation from GR is of the order of 0.025 taking $\delta^{GR} = 5\sigma$, for sources between 10^6 to $10^7\ M_\odot$ through the whole universe, i.e. for any redshift. Considering smaller deviations, a deviation from GR of 0.0005 would be distinguishable for sources below redshift 1 and the total mass of the order of $10^7\,M_\odot$. At first glance, one could conclude that the most severe limits will come from the evidence or lack of it in the frequencies $\delta\omega_{lmn}$ because of the high sensitivity of LISA to frequency variations. The expected population of MBHB for heavy seeds encloses sources in the range $[10^4 - 10^7]\,M_\odot$ up to redshift 10. This range is extended to lower mass sources in the case of light seeds [3]. Hence, even if LISA does not observe some of these golden sources, the expectation to test the no-hair theorem in "near" sources in the range of $[10^6 - 10^7]\,M_\odot$ looks very promising.

Chapter 6

Conclusions and prospects

This chapter serves to present the list of conclusions of previous analyses and to comment on future work and prospects.

6.1 Conclusions on detectability of higher harmonics

I studied the contribution of IMR higher modes of an MBHB source to the total SNR. I observed how this contribution depends on the event's redshifted mass through the observed frequency, directly related to LISA's response and sensitivity. I also showed that the cross-terms could contribute constructively or destructively to the total SNR, depending on the signal frequency and observational parameters. I presented a map guide of the relevance of each mode given the mass of an event. I highlighted the role of higher modes for MBHBs with masses above the order of 10^8 $M_\odot$. In LISA, large mass sources enhance the contribution of modes with higher frequencies so that the quadrupolar mode might no longer dominate.

To compare sensitivity performances, I defined different models including different harmonics. One could distinguish higher modes by comparing the Bayesian evidence for different models. In the example of a noisy signal with six modes, the model M_6, which includes the same higher modes as in the injection, was the preferred one, as expected. The model M_6 showed a very significant Bayes factor compared to models with fewer modes. Furthermore, I found that the absence of modes in the waveform template can bias the parameter estimation for high SNR sources due to the non-orthogonality of the modes in the merger-ringdown phase. Biased binary parameters can lead to a biased inference of the remnant BH's mass and spin. This effect can corrupt the *no-hair* theorem test and lead to misinterpretations.

I was able to quantify the SNR needed to distinguish models by comparing statistical errors of the injected waveform parameters with the modeling errors produced using an incomplete template (M_k, $k = 1, \ldots, 5$). In other words, given a certain SNR, I could specify the modes needed to infer the parameters without significant bias. This quantification depends on the actual waveform, which includes six modes in the analysis. In reality, such a situation is unlikely, as we expect more modes in the dynamics. Hence, this study does not derive a limit on the number of observable modes, which is still an open question that can be answered once more harmonics are implemented in the waveforms. However, this work demonstrates the need for higher modes in the waveform templates to perform accurate GW source characterization with LISA. Besides, featuring precession and eccentricity in the inspiral stage will also be necessary, while mode-mixing and non-linearity [196; 204; 215; 221] will become essential features in the ringdown.

The ability of LISA to identify different modes allows me to consider GR tests on more solid grounds, including the test of the *no-hair* theorem, which is the subject of the second study of this manuscript.

6.2 Conclusions on detectability of GR deviations with QNMs

In this study, I used two approaches to explore the *no-hair* theorem with LISA: the *agnostic* approach where no assumption on the source parameters is made except on the number of present QNMs; and the *deviations* approach, where fractional deviations of specific QNMs are targeted.

The advantage of the *agnostic* approach, is that no hypotheses on the event are required, except for the number of QNMs which could also be inferred by performing a Bayesian model comparison not demonstrated here. In this analysis the frequency and damping time for each QNM were estimated. By comparing the mass and spin derived from the complex frequencies I identified different values for each QNM, resulting in inconsistency between QNMs in the GR framework. I also quantified these deviations as fractional deviations from GR, which entails a delicate interpretation of the results depending on the assumptions made. Indeed, the hypothesis of no-GR-deviation in the dominant mode is too restrictive to correctly identify the injected deviation of each QNM, despite being consistent within 2σ with the true values. However, this kind of discrepancy can be circumvented by contrasting the results with the posterior distributions obtained from an IMR analysis, presuming that physical effects like eccentricity or others are included to avoid biased parameters. Hence this procedure requires an unbiased IMR analysis to compare the results to.

The *deviation* approach, showed better results for the fractional deviation values. However, prior assumptions are required to recover the injected values. Particularly, I assumed a fixed number of observable QNMs as well as further constraints in the priors volume. Using the fact that no significant deviation in the dominant mode is observed, one does not need to rely on an IMR analysis since those parameters are estimated. Including the mass and spin in the parameter estimation enables us to absorb small variations that convert into relatively large errors in the complex frequency parameters. Thus, the hypothesis of non-deviation in the dominant mode allows us to find the injected QNM deviations confidently. When allowing deviations in the dominant mode, extra care or further constraints in the priors are necessary due to the degeneracy between M_f, a_f and $\delta\omega_{220}, \delta\tau_{220}$. Such an analysis is left for the future.

In consequence, combining both methods could improve the characterization of possible deviations from GR. Thus, one optimized method would be to perform an *agnostic* search to determine a descriptive set of QNMs and a raw estimation of the mass and spin to be compared to the IMR parameters. Once this is done, specific deviations for each QNM could be targeted, taking special care in the prior probability definition for each mode, as mode degeneracies and label switching may arise.

Finally, I also evaluated the impact of redshift and total mass on the observable deviations from GR in the BH's spectrum with the *deviation* template. From this analysis, I was able to estimate that in the best-case scenario, i.e., with "golden" sources, the strong regime of GR could be tested up to $5\times10^{-3}\%$. However, these sources do not dominate the estimated population of black holes in the heavy or light seeds models. Nevertheless, the prospects of testing GR in the ringdown signal from sources with masses $[10^6 - 10^7]\, M_\odot$ at redshift ≤ 5 are very promising, with a detectable fractional deviation of $\delta\omega_{330} = 5\times10^{-2}\%$ in the $(3,3,0)$ mode's frequency.

6.3 Prospects

Throughout the manuscript, I mentioned that some analyses were left to be explored in the future. A few of them are already in progress and others need extra development.

Regarding the first analysis, that is *Detectability of higher harmonics with LISA*, the fact that ignoring higher harmonics in events with an SNR over a hundred already returned biased parameters is something to be of concern. While waveforms with higher precision including a larger number of higher harmonics are not developed, no major progress can be made in this context.

On the one hand, LVK is gaining sufficient sensitivity that already requires more precise waveforms. Moreover, third-generation detectors are expected to observe events with higher SNR. Thus the need for highly precise waveforms, including precession, eccentricity, and higher harmonics is essential. On the other hand, MBHBs correspond to BHs with a mass of $\sim 10^6 M_\odot$, like the ones in the center of galaxies. Then, these kind of events are expected to take place in very perturbed environments. This means that several effects such as accretion disks, third bodies, or even dark matter need to be included as well. The numerical error in current waveforms exceeds the statistical error expected for third-generation detectors, see for instance [133; 294–296]. In conclusion, more development is required to achieve the waveform precision that third-generation detectors need. Keep in mind that, not only population models might be affected by biased parameters, but also unbiased parameters are crucial to perform GR-tests.

For the case of the second analysis, that is *Detectability of GR deviations with QNMs*, there are still many analyses to conduct. Looking ahead, I aim to exploit the capabilities of my code in various scenarios. Firstly, I intend to expand previous analyses by considering different starting times and addressing a more realistic case. Secondly, I plan to include sky localization in the estimation of the parameters, given that the IMR analyses yield a posterior distribution and not a fixed mean value. By incorporating a larger prior of sky localization and the starting time into the analysis, I aim to investigate how uncertainties in these parameters influence our ability to detect deviations from GR in gravitational wave signals. This examination will provide valuable insights into the robustness of our methods and the reliability of our conclusions when performing GR tests.

In a parallel effort, I am analyzing NR waveforms with the response of LISA, to see if we are sensitive to the same quantity of QNMs that Cheung et al. [197] observed in their study with an infinite SNR. In their work, when a mode's amplitudes did not stabilize after a certain time, that mode was not included. Then, the detectability of the modes was constrained by different starting times. For this reason, in my study, even though the sky localization remains fixed, the starting time is allowed to take different values, since the amplitude of the modes vary with the starting time. This kind of analysis will also allow us to assess the detectability of non-linear modes with LISA. This is a study in progress.

A third study, not yet developed, would be to test LISA's ability to observe isospectrality, which involves examining whether different polarizations exhibit similar QNM spectra. In a broader sense, I aspire to explore various alternative theories of gravity and incorporate them into the code to test their predictions. One other option is to include the theoretical memory effect into the code to perform parameter estimation analysis, see e.g. [266] for a brief but clear summary of memory effects. This can be achieved for instance, through the incorporation of the `GWmemory` package [297].

The idea of having a pipeline dedicated to performing GR tests in MBHB is essential if we want to test GR. This pipeline would constitute another piece in the large structure of global fit that will benefit from the noise level updates. Such incorporation will enable us to probe fundamental physics with massive black hole binaries from the detection of GW with LISA.

Appendix A

Complementary equations and information

A.1 Resolution to the linearized equation

A perturbation on a Minkowski metric is introduced into Einstein's equation, through Eq. (1.1.3), thus

$$\Gamma^{\mu}_{\rho\sigma} = \frac{1}{2}\eta^{\mu\beta}(\partial_\rho h_{\sigma\beta} + \partial_\sigma h_{\rho\beta} - \partial_\beta h_{\rho\sigma}) - \cancel{\frac{1}{2}h^{\mu\beta}(\partial_\rho h_{\sigma\beta} + \partial_\sigma h_{\rho\beta} - \partial_\beta h_{\rho\sigma})}.$$

Since the second term is of the order of h^2 and $|h| \ll 1$, it can be neglected. With these Christoffel symbols, the Riemann tensor takes the form

$$\begin{aligned} R^{\mu}{}_{\nu\rho\sigma} = {} & \partial_\rho\Big[\frac{1}{2}\eta^{\mu\beta}(\partial_\nu h_{\sigma\beta} + \partial_\sigma h_{\nu\beta} - \partial_\beta h_{\nu\sigma})\Big] - \partial_\sigma\Big[\frac{1}{2}\eta^{\mu\beta}(\partial_\nu h_{\rho\beta} + \partial_\rho h_{\nu\beta} - \partial_\beta h_{\nu\rho})\Big] + \\ & \cancel{\frac{1}{4}\Big[\eta^{\mu\beta}(\partial_\lambda h_{\rho\beta} + \partial_\rho h_{\lambda\beta} - \partial_\beta h_{\alpha\rho})\eta^{\lambda\alpha}(\partial_\nu h_{\alpha\sigma} + \partial_\sigma h_{\nu\alpha} - \partial_\alpha h_{\nu\sigma})\Big]} - \\ & \cancel{\frac{1}{4}\Big[\eta^{\mu\beta}(\partial_\lambda h_{\sigma\beta} + \partial_\sigma h_{\lambda\beta} - \partial_\beta h_{\alpha\sigma})\eta^{\lambda\alpha}(\partial_\nu h_{\alpha\rho} + \partial_\rho h_{\nu\alpha} - \partial_\alpha h_{\nu\rho})\Big]}. \end{aligned}$$

Here again, the third and fourth terms are of the order of h^2, then only the first two terms are kept

$$R^{\mu}_{\nu\rho\sigma} = \frac{1}{2}\eta^{\mu\beta}\Big(\partial_\rho\partial_\nu h_{\sigma\beta} + \cancel{\partial_\rho\partial_\sigma h_{\nu\beta}} - \partial_\rho\partial_\beta h_{\nu\sigma} - \partial_\sigma\partial_\nu h_{\rho\beta} - \cancel{\partial_\sigma\partial_\rho h_{\nu\beta}} + \partial_\sigma\partial_\beta h_{\nu\rho}\Big) + \mathcal{O}(h^2).$$

Finally,

$$R^{\mu}_{\nu\rho\sigma} = \frac{1}{2}\Big(\partial_\rho\partial_\nu h^{\mu}_{\sigma} - \partial_\sigma\partial_\nu h^{\mu}_{\rho} - \partial_\rho\partial^{\mu} h_{\nu\sigma} + \partial_\sigma\partial^{\mu} h_{\nu\rho}\Big) + \mathcal{O}(h^2).$$

The Ricci tensors become

$$R_{\nu\sigma} = R^{\mu}{}_{\nu\mu\sigma} = \frac{1}{2}\Big(\partial_\mu\partial_\nu h^{\mu}_{\sigma} - \partial_\sigma\partial_\nu h^{\mu}_{\mu} - \partial_\mu\partial^\mu h_{\nu\sigma} + \underbrace{\partial_\sigma\partial^\mu h_{\nu\mu}}_{\Box h_{\nu\sigma}}\Big) + \mathcal{O}(h^2).$$

The Ricci scalar, or curvature as usually known, results in

$$R = R^{\nu}_{\nu} = g^{\nu\sigma}R_{\nu\sigma} = \frac{1}{2}\Big(\partial_\mu\partial_\nu h^{\mu\nu} + \partial^\nu\partial^\mu h_{\nu\mu} - \partial^\nu\partial_\nu h - \Box h^{\nu}_{\nu}\Big) + \mathcal{O}(h^2) \quad = \partial_\mu\partial_\nu h^{\mu\nu} - \Box h + \mathcal{O}(h^2).$$

Then,

$$\begin{aligned} G_{\mu\nu} &= R_{\mu\nu} - \frac{1}{2}g_{\mu\nu}R \\ &= \frac{1}{2}\Big(\partial_\sigma\partial_\mu h^{\sigma}_{\nu} + \partial_\nu\partial^\sigma h_{\mu\sigma} - \partial_\nu\partial_\mu h - \Box h_{\mu\nu}\Big) - \frac{1}{2}g_{\mu\nu}\Big(\partial_\sigma\partial_\rho h^{\sigma\rho} - \Box h\Big) + \mathcal{O}(h^2) \\ &= \frac{1}{2}\Big(\partial_\sigma\partial_\mu h^{\sigma}_{\nu} + \partial_\nu\partial^\sigma h_{\mu\sigma} - \partial_\nu\partial_\mu h - \Box h_{\mu\nu} - \eta_{\mu\nu}\partial_\sigma\partial_\rho h^{\sigma\rho} + \eta_{\mu\nu}\Box h\Big) + \mathcal{O}(h^2). \end{aligned}$$

Plugging the definition from the Lorenz gauge in Eq. (1.2.2) into Einstein tensor,

$$\bar{h}_{\mu\nu} = h_{\mu\nu} - \frac{1}{2}\eta_{\mu\nu}h \longrightarrow h_{\mu\nu} = \bar{h}_{\mu\nu} + \frac{1}{2}\eta_{\mu\nu}h,$$

one finally obtains,

$$\begin{aligned} G_{\mu\nu} = \frac{1}{2}\Big(&\partial_\sigma\partial_\mu\bar{h}^{\sigma}_{\nu} + \frac{1}{2}\partial_\sigma\partial_\mu\eta^{\sigma}_{\nu}h + \partial_\nu\partial^\sigma\bar{h}_{\mu\sigma} + \frac{1}{2}\partial_\nu\partial^\sigma\eta_{\mu\sigma}h - \partial_\nu\partial_\mu h \\ &- \Box\bar{h}_{\mu\nu} - \frac{1}{2}\Box\eta_{\mu\nu}h - \eta_{\mu\nu}\partial_\sigma\partial_\rho\bar{h}^{\sigma\rho} - \frac{1}{2}\eta_{\mu\nu}\partial_\sigma\partial_\rho\eta^{\sigma\rho}h + \eta_{\mu\nu}\Box h\Big) + \mathcal{O}(h^2). \end{aligned}$$

Working out this expression, one can see that some terms vanish, namely,

$$\begin{aligned} G_{\mu\nu} &= \frac{1}{2}\Big(\partial_\sigma\partial_\mu\bar{h}^{\sigma}_{\nu} + \cancel{\frac{1}{2}\partial_\nu\partial_\mu h} + \partial_\nu\partial^\sigma\bar{h}_{\mu\sigma} + \cancel{\frac{1}{2}\partial_\nu\partial_\mu h} - \cancel{\partial_\nu\partial_\mu h} - \Box\bar{h}_{\mu\nu} \\ &\qquad - \cancel{\frac{1}{2}\Box\eta_{\mu\nu}h} - \eta_{\mu\nu}\partial_\sigma\partial_\rho\bar{h}^{\sigma\rho} - \cancel{\frac{1}{2}\eta_{\mu\nu}\partial_\sigma\partial^\sigma h} + \cancel{\eta_{\mu\nu}\Box h}\Big) + \mathcal{O}(h^2) \\ &= \frac{1}{2}\Big(\partial_\sigma\partial_\mu\bar{h}^{\sigma}_{\nu} + \partial_\nu\partial^\sigma\bar{h}_{\mu\sigma} - \Box\bar{h}_{\mu\nu} - \eta_{\mu\nu}\partial_\sigma\partial_\rho\bar{h}^{\sigma\rho}\Big) + \mathcal{O}(h^2). \end{aligned}$$

Then,

$$-2G_{\mu\nu} = \Box\bar{h}_{\mu\nu} - \partial_\mu\partial^\sigma\bar{h}_{\sigma\nu} - \partial_\nu\partial^\sigma\bar{h}_{\mu\sigma} + \eta_{\mu\nu}\partial^\rho\partial^\sigma\bar{h}_{\sigma\rho} + \mathcal{O}(h^2).$$

Setting the cosmological constant to zero, one obtains the **linearized Einstein field equations**:

$$G_{\mu\nu} = \frac{8\pi G}{c^4}T_{\mu\nu}$$

$$-2G_{\mu\nu} = -\frac{16\pi G}{c^4}T_{\mu\nu} = \Box\bar{h}_{\mu\nu} - \partial_\mu\underbrace{\partial^\sigma\bar{h}_{\sigma\nu}}_{=0} - \partial_\nu\underbrace{\partial^\sigma\bar{h}_{\mu\sigma}}_{=0} + \eta_{\mu\nu}\partial^\rho\underbrace{\partial^\sigma\bar{h}_{\sigma\rho}}_{=0},$$

where the under-braced terms are similar and equal to zero because of the Lorenz gauge, arriving at

$$\Box\bar{h}_{\mu\nu} = -\frac{16\pi G}{c^4}T_{\mu\nu}.$$

A.2 Riemann tensors in NP formalism

I present here, 18 of the 36 Riemann tensors, or a combination of them in the NP formalism as defined in Eq. (3.3.7) in terms of the spin coefficients and the Weyl and Ricci scalars. The remaining 18 are complex conjugates of these equations. They read,

$$R_{1313}: \ D\sigma - \delta\kappa = \sigma\left(3\epsilon - \bar{\epsilon} + \varrho + \bar{\varrho}\right) + \kappa\left(\bar{\pi} - \tau - 3\beta - \bar{\alpha}\right) + \Psi_0, \tag{A.2.1a}$$

$$R_{1314}: \ D\varrho - \bar{\delta}\kappa = \left(\varrho^2 + \sigma\bar{\sigma}\right) + \varrho\left(\epsilon + \bar{\epsilon}\right) - \bar{\kappa}\tau - \kappa\left(3\alpha + \bar{\beta} - \pi\right) + \Phi_{00}, \tag{A.2.1b}$$

$$R_{1312}: \ D\tau - \varDelta\kappa = \varrho\left(\tau + \bar{\pi}\right) + \sigma\left(\bar{\tau} + \pi\right) + \tau\left(\epsilon + \bar{\epsilon}\right) - \kappa\left(3\gamma + \bar{\gamma}\right) + \Psi_1 + \Phi_{00}, \tag{A.2.1c}$$

$$\frac{1}{2}\left(R_{3414} - R_{1214}\right): \ D\alpha - \bar{\delta}\epsilon = \alpha(\rho + \bar{\epsilon} - 2\epsilon) + \beta\bar{\sigma} - \bar{\beta}\epsilon - \kappa\lambda - \bar{\kappa}\gamma + \pi(\epsilon + \rho) + \Phi_{10}, \tag{A.2.1d}$$

$$\frac{1}{2}\left(R_{1213} - R_{3413}\right): \ D\beta - \delta\epsilon = \sigma(\alpha + \pi) + \beta(\bar{\rho} - \bar{\epsilon} - \kappa(\mu + \gamma) - \epsilon(\alpha \bar{-} \bar{\pi}) + \Psi_1, \tag{A.2.1e}$$

$$\begin{aligned}\frac{1}{2}\left(R_{1212} - R_{3412}\right): \ D\gamma - \varDelta\epsilon = {}& \alpha(\tau + \bar{\pi}) + \beta(\bar{\tau} + \pi) - \gamma(\epsilon + \bar{\epsilon}) - \epsilon(\gamma + \bar{\gamma}) \\ & + \tau\pi - \nu\kappa + \Psi_2 + \Phi_{11} - \Lambda,\end{aligned} \tag{A.2.1f}$$

$$R_{2441}: \ D\lambda - \bar{\delta}\pi = (\rho\lambda + \bar{\sigma}\mu) + \pi(\pi + \alpha - \beta) - \nu\bar{\kappa} - \lambda(3\epsilon - \bar{\epsilon}) + \Phi_{20}, \tag{A.2.1g}$$

$$R_{2431}: \ D\mu - \delta\pi = (\bar{\rho}\mu + \sigma\lambda) + \pi(\bar{\pi} - \bar{\alpha} + \beta) - \mu(\epsilon + \bar{\epsilon}) - \nu\kappa + \Psi_2 + 2\Lambda, \tag{A.2.1h}$$

$$R_{2421}: \ D\mu - \varDelta\pi = \mu(\pi + \bar{\tau}) + \lambda(\bar{\pi} + \tau) + \pi(\gamma - \bar{\gamma}) - \nu(3\epsilon + \bar{\epsilon}) + \Psi_3 + \Phi_{21}, \tag{A.2.1i}$$

$$R_{2442}: \ \varDelta\lambda - \bar{\delta}\nu = -\lambda(\mu + \bar{\mu} + 3\gamma - \bar{\gamma}) + \nu(3\alpha + \bar{\beta} + \pi - \bar{\tau}) - \Psi_4, \tag{A.2.1j}$$

$$R_{3143}: \ \delta\rho - \bar{\delta}\sigma = \rho(\bar{\alpha} + \beta) - \sigma(3\alpha - \bar{\beta}) + \tau(\rho - \bar{\rho}) + \kappa(\mu - \bar{\mu}) - \Psi_1 + \Phi_{01}, \tag{A.2.1k}$$

$$\begin{aligned}\frac{1}{2}\left(R_{1234} - R_{3434}\right): \ \delta\alpha - \bar{\delta}\beta = {}& (\mu\rho - \lambda\sigma) + \alpha\bar{\alpha} + \beta\bar{\beta} - 2\alpha\beta + \gamma(\rho - \bar{\rho}) \\ & + \epsilon(\mu - \bar{\mu}) - \Psi_2 + \Phi_{11} + \Lambda,\end{aligned} \tag{A.2.1l}$$

$$R_{2443}: \ \delta\lambda - \bar{\delta}\mu = \nu(\rho - \bar{\rho}) + \pi(\mu - \bar{\mu}) + \mu(\alpha + \bar{\beta}) + \lambda(\bar{\alpha} - 3\beta) - \Psi_3 + \Phi_{21}, \tag{A.2.1m}$$

$$R_{2423}: \ \delta\nu - \varDelta\mu = (\mu^2 + \lambda\bar{\lambda}) + \mu(\gamma + \bar{\gamma}) - \bar{\nu}\pi + \nu(\tau - 3\beta - \bar{\alpha}) + \Phi_{22}, \tag{A.2.1n}$$

$$\frac{1}{2}\left(R_{1232} - R_{3432}\right): \ \delta\gamma - \varDelta\beta = \gamma(\tau - \bar{\alpha} - \beta) + \mu\tau - \sigma\nu - \epsilon\bar{\nu} - \beta(\gamma - \bar{\gamma} - \mu) + \alpha\bar{\lambda} + \Phi_{12}, \tag{A.2.1o}$$

$$R_{1332}: \ \delta\tau - \varDelta\sigma = (\mu\sigma + \bar{\lambda}\rho) + \tau(\tau + \beta - \bar{\alpha}) - \sigma(3\gamma - \bar{\gamma}) - \kappa\bar{\nu} + \Phi_{02}, \tag{A.2.1p}$$

$$R_{1324}:\ \mathit{\Delta}\rho-\bar{\delta}\tau=-(\rho\bar{\mu}+\sigma\lambda)+\tau(\bar{\beta}-\alpha-\bar{\tau})=\rho(\gamma+\bar{\gamma})+\nu\kappa-\Psi_2-2\Lambda, \tag{A.2.1q}$$

$$\frac{1}{2}\left(R_{1242}-R_{3442}\right):\ \mathit{\Delta}\alpha-\bar{\delta}\gamma=\nu(\rho+\epsilon)-\lambda(\tau+\beta)+\alpha(\bar{\gamma}-\bar{\mu})+\gamma(\bar{\beta}-\bar{\tau})-\Psi_3. \tag{A.2.1r}$$

A.3 Bianchi identities in NP formalism

I present the remaining Bianchi identities in the NP formalism introduced in Eq. (3.3.31). Note, that for simplicity I use the covariant derivative notation of dot-comma $R_{13[13;4]}$ instead of $\nabla_{[4}R_{13]13}$.

$$\begin{aligned}R_{13[13;4]}:\ &(\bar{\delta}-4\alpha+\pi)\Psi_0+(4\varrho-D+2\epsilon)\Psi_1-3\kappa\Psi_2=\\&-2\kappa\Phi_{11}-\bar{\kappa}\Phi_{02}+2\sigma\Phi_{10}+(2\epsilon+2\bar{\varrho}-D)\Phi_{01}+\left(\bar{\pi}-2\bar{\alpha}-2\beta+\delta\right)\Phi_{00},\end{aligned} \tag{A.3.1a}$$

$$\begin{aligned}R_{13[13;2]}:\ &(\mathit{\Delta}-4\gamma+\mu)\Psi_0+(4\tau+\beta-\delta)\Psi_1-3\sigma\Psi_2=\\&(2\bar{\pi}-2\beta+\delta)\Phi_{01}-2\kappa\Phi_{12}-\bar{\lambda}\Phi_{00}+2\sigma\Phi_{11}+(\bar{\varrho}+2\epsilon-2\bar{\epsilon}-D)\Phi_{02},\end{aligned} \tag{A.3.1b}$$

$$\begin{aligned}R_{13[21;4]}:\ &\lambda\Psi_0+(2\alpha-\bar{\delta}-2\pi)\Psi_1+(D-3\varrho)\Psi_2+2\kappa\Psi_3=\\&2\varrho\Phi_{11}+\bar{\sigma}\Phi_{02}-2D\Lambda+(\bar{\delta}-2\alpha-2\bar{\tau})\Phi_{01}-2\tau\Phi_{01}-(\bar{\mu}-2\gamma-2\bar{\gamma}+\mathit{\Delta})\Phi_{00},\end{aligned} \tag{A.3.1c}$$

$$\begin{aligned}R_{13[43;2]}:\ &-\nu\Psi_0+(2\mu-2\gamma+\mathit{\Delta})\Psi_1+(3\tau-\delta)\Psi_2-2\sigma\Psi_3=\\&2\tau\Phi_{11}-\bar{\nu}\Phi_{00}-2\varrho\Phi_{12}+2\delta\Lambda+(2\bar{\mu}-2\gamma+\mathit{\Delta})\Phi_{01}+(\bar{\tau}-2\bar{\beta}+2\alpha-\bar{\delta})\Phi_{02},\end{aligned} \tag{A.3.1d}$$

$$\begin{aligned}R_{42[13;4]}:\ &-2\lambda\Psi_1(\bar{\delta}+3\pi)\Psi_2+(2\varrho-D-2\epsilon)\Psi_3-\kappa\Psi_4=\\&-2\mu\Phi_{10}+2\pi\Phi_{11}-2\bar{\delta}\Lambda-\bar{\kappa}\Phi_{22}+(2\bar{\varrho}-2\epsilon-D)\Phi_{21}-(2\bar{\alpha}-2\beta-\bar{\pi}-\delta)\Phi_{20},\end{aligned} \tag{A.3.1e}$$

$$\begin{aligned}R_{42[21;4]}:\ &3\lambda\Psi_2-(\bar{\delta}+4\pi+2\alpha)\Psi_3+(D+4\epsilon-\varrho)\Psi_4=\\&2\sigma\Phi_{11}-\bar{\lambda}\Phi_{00}-2\kappa\Phi_{12}+(2\bar{\pi}-2\beta+\delta)\Phi_{01}-(\bar{\mu}+2\gamma-2\bar{\gamma}-D)\Phi_{02},\end{aligned} \tag{A.3.1f}$$

$$\begin{aligned}R_{42[13;2]}:\ &-2\nu\Psi_1+(3\mu+\mathit{\Delta})\Psi_2+(2\tau-2\beta-\delta)\Psi_3-\sigma\Psi_4=\\&2\pi\Phi_{12}-2\mu\Phi_{11}-\bar{\lambda}\Phi_{20}-2\mathit{\Delta}\Lambda+(2\bar{\pi}+2\beta+\delta)\Phi_{21}+(\bar{\varrho}-2\epsilon-2\bar{\epsilon}-D)\Phi_{22},\end{aligned} \tag{A.3.1g}$$

$$\begin{aligned}R_{42[43;2]}:\ &-3\nu\Psi_2+(2\gamma+4\mu+\mathit{\Delta})\Psi_3+(\tau-4\beta-\delta)\Psi_4=\\&2\lambda\Phi_{12}-2\nu\Phi_{11}-\bar{\nu}\Phi_{20}+(2\bar{\mu}+2\gamma+\mathit{\Delta})\Phi_{21}+(\bar{\tau}-2\alpha-2\bar{\beta}-\bar{\delta})\Phi_{22}.\end{aligned} \tag{A.3.1h}$$

A.4 Power-law tail

As I mentioned in Sec. 3.5.2, when one closes the path of the integral to solve Green's function via the residues theorem, one encounters a power-law tail in addition to the QNMs values. The contribution of this tail in the total mode's waveform can be seen in Fig. A.1, where I show the absolute value of Ψ_4 for a Schwarzschild BH with $(l, m = 2, 2)$. One can subtract the contribution of different overtones to study the residues. Then, when sequentially subtracting waves corresponding to an increasing overtone $(l, m, n = 2, 2, n)$, one can observe the power-law tail emerging as a residual. Note that the tail is about 5 orders of magnitude below the fundamental overtone at $t_M \sim 20$ [1]. As one goes further from the merger, the difference tends to be smaller, reaching a comparable magnitude at $t_M \sim 80$. However, this value is about 10 orders of magnitude smaller than the initial amplitude at $t_M = 0$, hence making it very hard to detect the tail at late times.

---

[1] Keep in mind that $t_M = t\, c^3 / M\, G$ is an adimensional value.

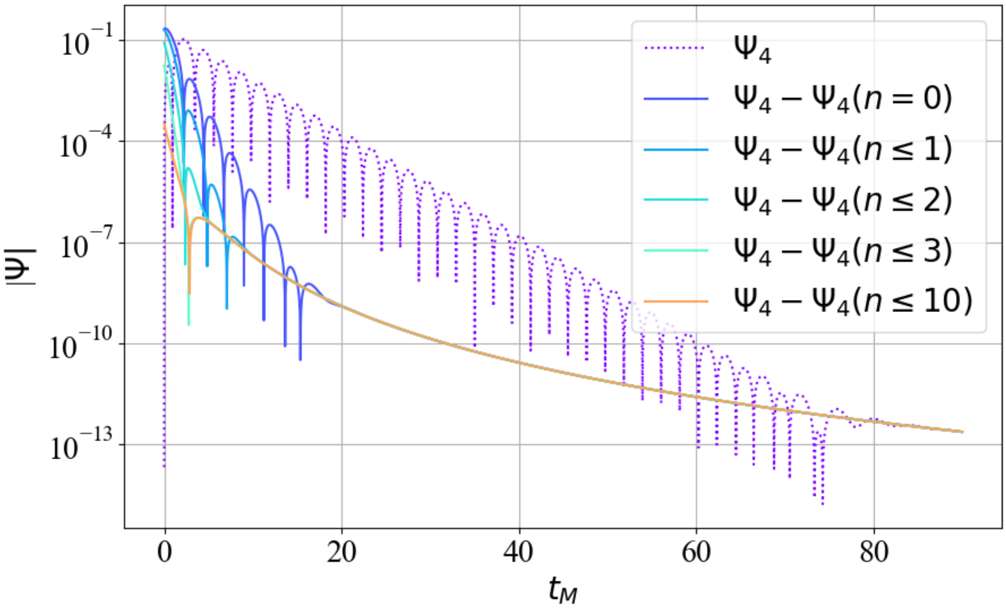

Figure A.1: Presence of the power-law tail in the (l,m = 2,2) mode of a non-rotating BH when the overtones are subtracted. *Data offered by Rodrigo Panosso Macedo.*

Appendix B

Complementary results on the detectability of higher harmonics

B.1 Dependency on source mass and redshift

In order to show how the source parameters impact the null cumulative contribution, I generate a new contour plot of the SNR contribution in terms of the pair of modes in Fig. B.1. For this particular case, I use the parameters listed in Tab. B.1, where I change only the adimentional spins and the mass ratio. Note how the zero SNR contributions are localized at different masses than in Fig. 4.7.

Table B.1: Source parameters in the SSB frame with aligned spins and redshifted masses.

Parameter	Value	Parameter	Value
Mass ($M_\odot$)	$[10^4, 5\times 10^9]$	β (rad)	$\pi/2$
q (Mass ratio)	3	λ (rad)	π
χ_1	0.7	ϕ (rad)	$\pi/2$
χ_2	-0.2	ψ (rad)	$\pi/2$
ι (rad)	$\pi/3$		

B.2 Posterior and parameter bias

I include in Fig. B.2 the posterior distribution for all the eleven parameters for models M_k with $k \geq 2$. The model with only the dominant mode is not included since the posteriors from M_1 are very wide reducing the visibility of the other modes. I also include the estimated values for the noisy and noiseless dataset for the intrinsic parameters in Table B.2.

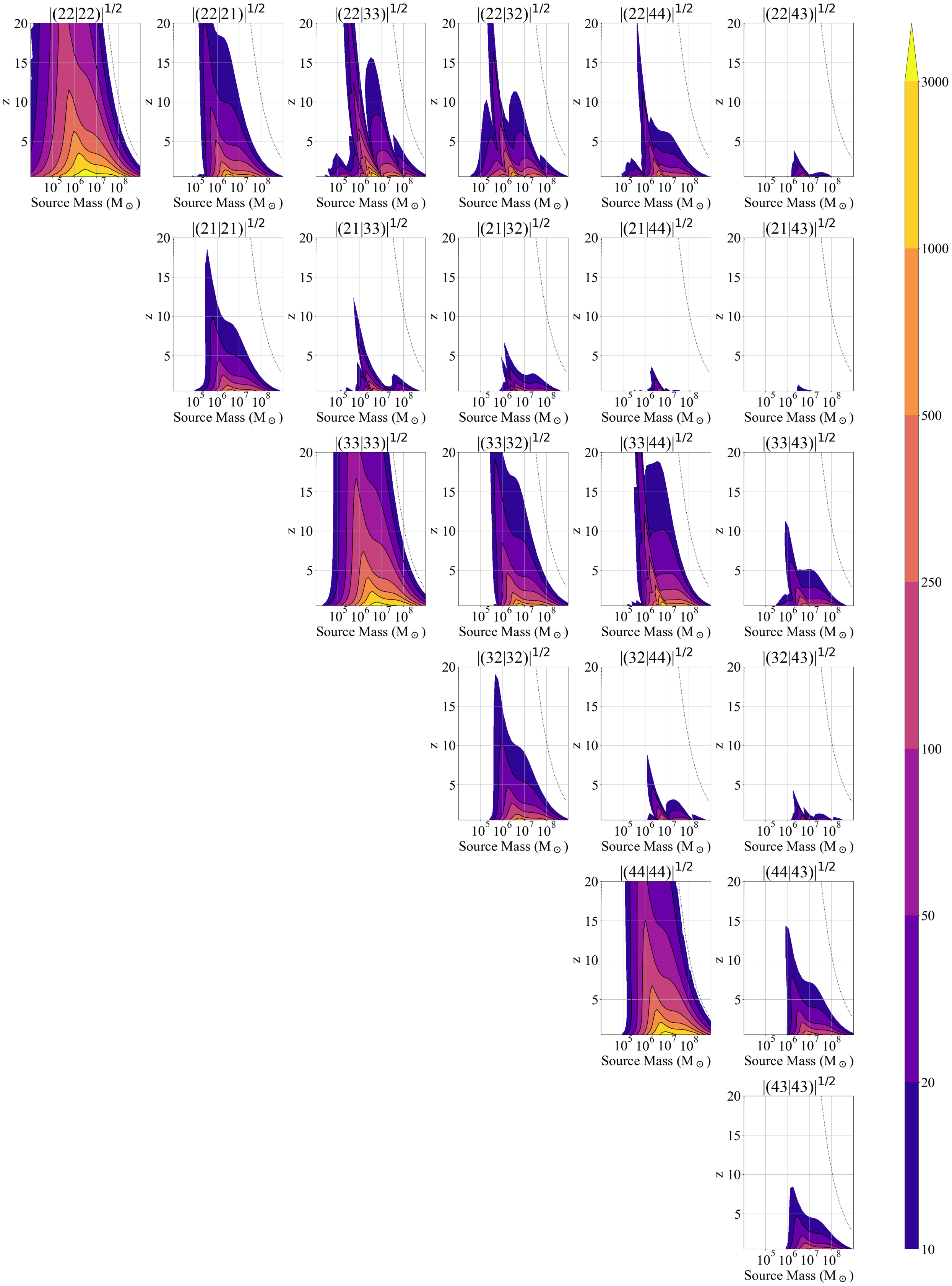

Figure B.1: Contour plot with the contributions of pairs of modes $|(lm|l'm')|^{1/2}$.

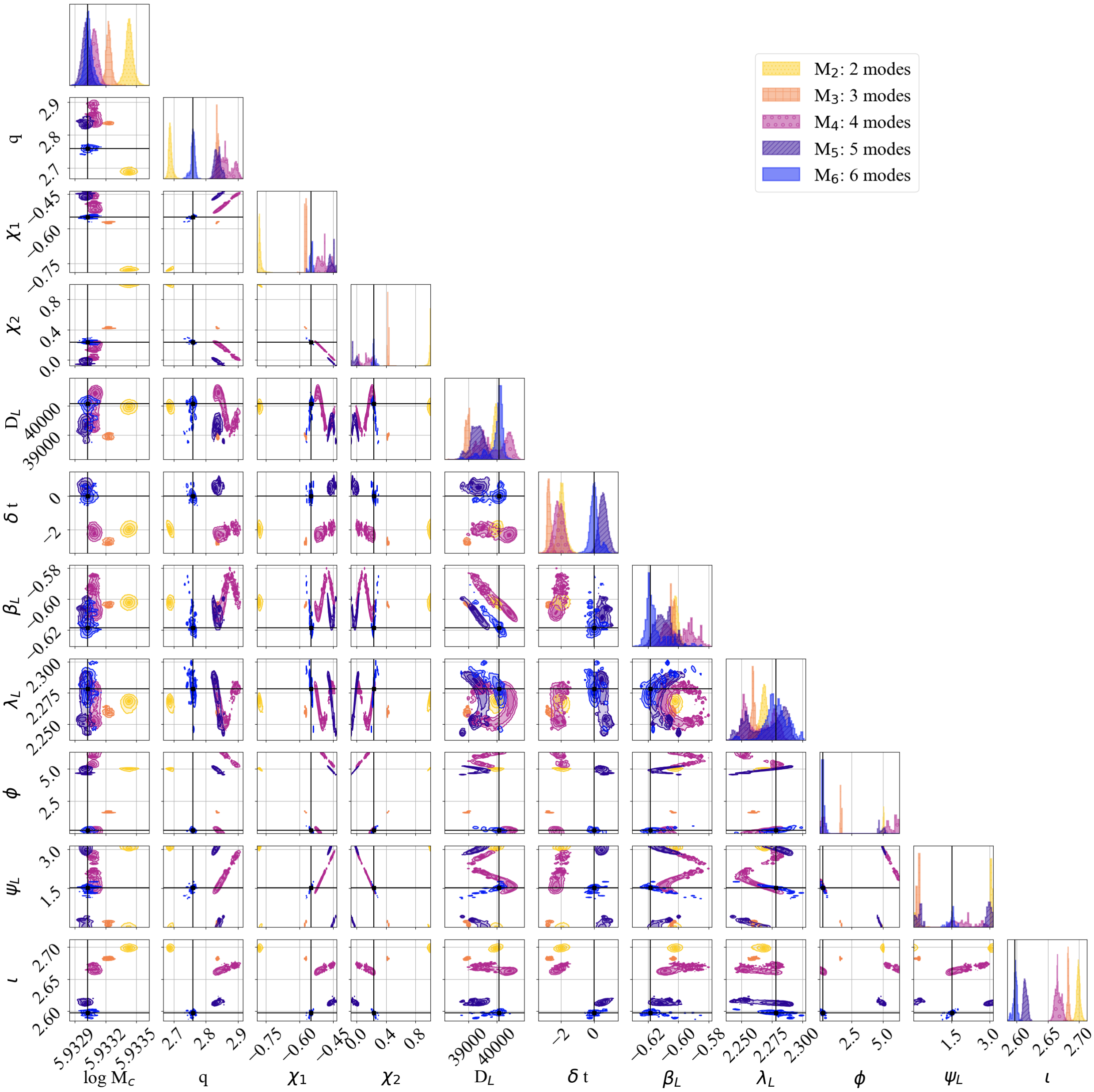

Figure B.2: Marginalized posterior distribution for all parameters for models M_k with $k \geq 2$. Note the high accuracy of the estimated mean value of all parameters found with the model M_6.

Table B.2: Estimated value for models M_1 and M_6, for the two datasets with and without noise.

Parameter	True value	Estimated value with M_1 (noiseless)	Estimated value with M_6 (noiseless)	Estimated value with M_1 (with noise)	Estimated value with M_6 (with noise)
$\log M_c\,(M_\odot)$	5.93302	$5.93371^{+0.00019}_{-0.00016}$	$5.93303^{+0.00010}_{-0.00010}$	$5.93374^{+0.00019}_{-0.00016}$	$5.93304^{+0.00009}_{-0.00010}$
q	2.759	$2.411^{+0.012}_{-0.011}$	$2.751^{+0.019}_{-0.021}$	$2.414^{+0.012}_{-0.012}$	$2.759^{+0.013}_{-0.023}$
χ_1	-0.549	$-0.890^{+0.009}_{-0007.}$	$-0.559^{+0.016}_{-0.024}$	$-0.888^{+0.009}_{-0.008}$	$-0.549^{+0.011}_{-0.021}$
χ_2	0.232	$0.996^{+0.004}_{-0.019}$	$0.261^{+0.064}_{-0.043}$	$0.996^{+0.004}_{-0.018}$	$0.231^{+0.057}_{-0.030}$

The fact that the noiseless dataset returned less accurate parameters than the noisy dataset called the attention of the article's referee [132]. Therefore I show in Fig. B.3 the posterior distribution for all the eleven parameters for models M_6 without noise and with two different noise realizations. This analysis allowed us to confirm that the better estimation for the noisy case than for the noiseless case, is due to a statistical probability. This can also be seen in Table B.3, where I compare the estimated values for the noiseless and both noisy datasets. One can see that the second noise realization estimates less accurate results than the first noise realization. This demonstrates that the first analysis unexpectedly returned very accurate results, but that it is not always the case.

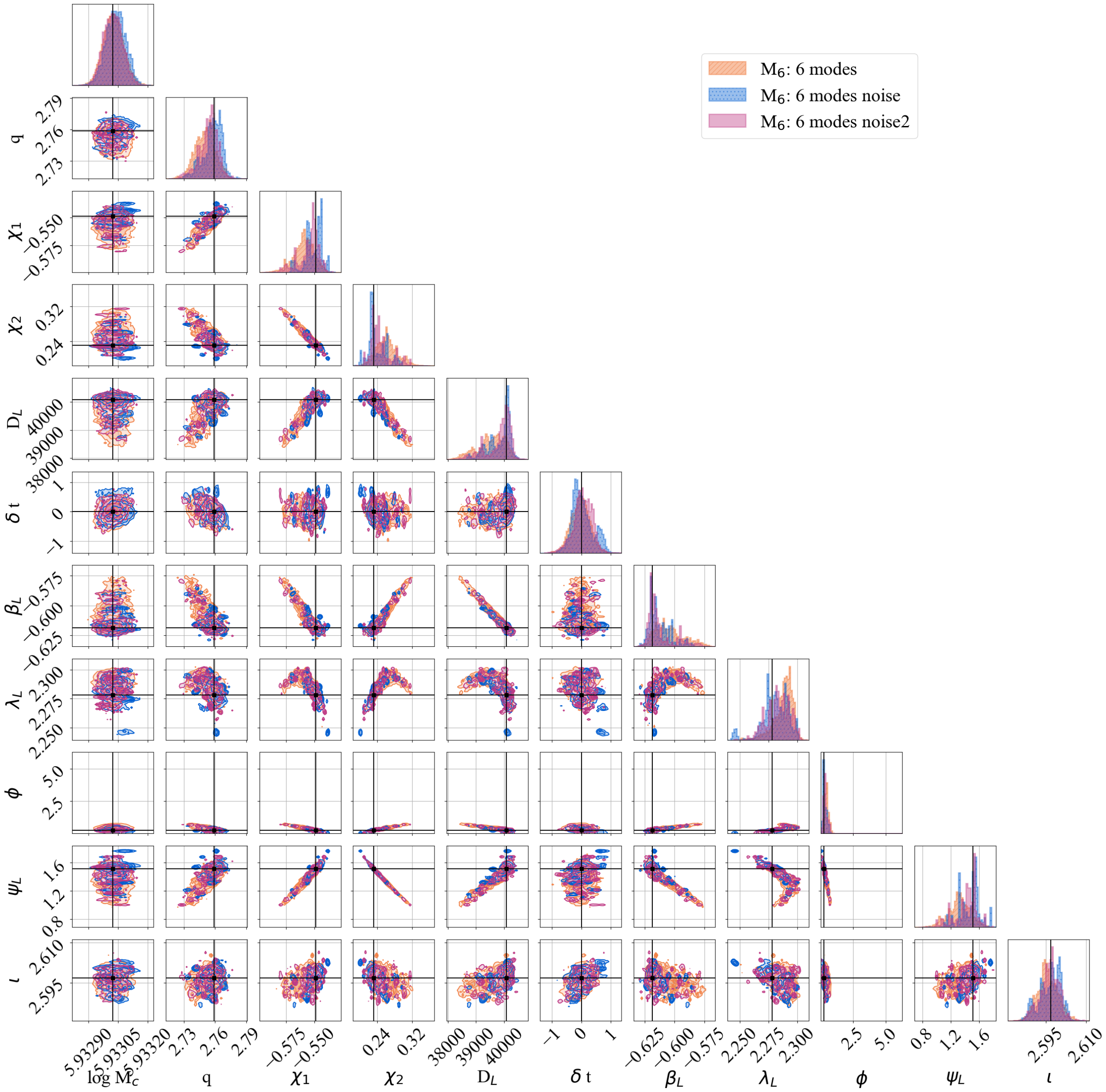

Figure B.3: Marginalized posterior distribution for all parameters for model M_6 without noise and with two different noise realizations.

Table B.3: Estimated value for models M_6 and M_6 with noise, for the two noisy datasets.

Parameter	True value	Estimated value with M_6 (noiseless)	Estimated value with M_6 (with noise)	Estimated value with M_6 (with noise 2)
$\log M_c\,(M_\odot)$	5.93302	$5.93303^{+0.00010}_{-0.00010}$	$5.93304^{+0.00009}_{-0.00010}$	$5.93303^{+0.00010}_{-0.0009}$
q	2.759	$2.751^{+0.019}_{-0.021}$	$2.759^{+0.013}_{-0.023}$	$2.755^{+0.006}_{-0.011}$
χ_1	-0.549	$-0.559^{+0.016}_{-0.024}$	$-0.549^{+0.011}_{-0.021}$	$-0.552^{+0.005}_{-0.013}$
χ_2	0.232	$0.261^{+0.064}_{-0.043}$	$0.231^{+0.057}_{-0.030}$	$0.242^{+0.003}_{-0.014}$
D_l (Mpc)	40085	39588^{+441}_{-640}	40013^{+161}_{-643}	39983^{+214}_{-745}
δ t (s)	0.0	$-0.033^{+0.301}_{-0.324}$	$-0.032^{+0.494}_{-0.256}$	$0.043^{+0.317}_{-0.285}$
β (rad)	-0.619	$-0.606^{+0.016}_{-0.010}$	$-0.616^{+0.012}_{-0.005}$	$-0.617^{+0.019}_{-0.004}$
λ (rad)	2.278	$2.289^{+0.006}_{-0.009}$	$2.281^{+0.010}_{-0.010}$	$2.283^{+0.010}_{-0.011}$
ϕ (rad)	0.245	$0.425^{+0.152}_{-0.142}$	$0.252^{+0.187}_{-0.056}$	$0.312^{+0.199}_{-0.092}$
Ψ (rad)	1.516	$1.325^{+0.154}_{-0.151}$	$1.509^{+0.066}_{-0.194}$	$1.445^{+0.098}_{-0.206}$
ι (rad)	2.597	$2.595^{+0.004}_{-0.004}$	$2.597^{+0.003}_{-0.004}$	$2.596^{+0.003}_{-0.004}$

B.3 List of acronyms

ACF Auto-Covariance Function

ADC Analog to Digital Converter

ASD Amplitude Spectral Density

BH Black Hole

BHB Black Hole Binary

CMB Cosmic Microwave Background

CS Cosmic Strings

DA Data Analysis

DECIGO DECihertz Interferometer Gravitational-wave Observatory

DFT Discret Fourier Transform

DFACS Drag-Free Attitude Control System

d.o.f degrees of freedom

DM Dark Matter

EM Electro-Magnetic

EMRI Extreme Mass-Ratio Inspiral

EOB Effective One-Body

ESA European Space Agency

ET Einstein Telescope

FD Frequency Domain

FFT Fast Fourier Transform

FOPT First-Order Phase Transition

GBs Galactic Binaries

GF Global Fit

GR General Theory of Relativity

GRS Gravitational Reference Sensor

GW Gravitational Wave

IMR Inspiral-Merger-Ringdown

IMRI Intermediate Mass-Ratio Inspiral

ISCO Innermost Stable Circular Orbit

ISI Inter-Satellite Interferometer

JWST James Webb Space Telescope

LDC LISA Data Challenge

LDCWG LISA Data Challenge Working Group

LIGO Laser Interferemeter Gravitational-wave Observatory

LISA Laser Interferometer Space Antenna

LPF LISA Pathfinder

ltt light travel time

LVK LIGO-Virgo-KAGRA

MBH Massive Black Hole

MBHB Massive Black Hole Binaries

MOSA Moving Optical Sub-Assembly

NP Newman-Penrose

NR Numerical Relativity

NS Neutron Star

OB Optical Bench

OMS Optical Metrology System

PBH Primordial Black Holes

PCG Preconditioned Conjugation Gradient

PDF Probability Density Function

PE Parameter Estimation

PN Post-Newtonian

PSD Power Spectral Density

PTA Pulsar Timing Array

QNM Quasi-Normal Mode

RFI Reference Interferometer

RW Regge-Wheeler

S/C Spacecraft

sBH Stellar-Mass Black Hole

sBHB Stellar-Mass Black Hole Binaries

SciRD Science Requirement Document

SF Self-force

SGWB Stochastic Gravitational-Wave Background

SM Standard Model

SMBHB Supermassive Black Hole Binary

SN	Supernova
SNR	Signal-to-Noise Ratio
SPA	Stationary Phase Approximation
SSB	Solar System Barycenter
TD	Time Domain
TDI	Time Delay Interferometry
TM	Test Mass, *often proof mass*
TMI	Test Mass Interferometer
ToA	time of arrival
TT	transverse-traceless
TTL	Tilt-To-Length
USO	Ultra-Stable Oscillator
WD	White Dwarf
Z	Zerilli

Bibliography

[1] M. Maggiore, "Gravitational wave experiments and early universe cosmology," *Physics Reports*, vol. 331, no. 6, p. 283–367, Jul 2000.

[2] M. Maggiore, *Gravitational waves.* Oxford University Press, 2007.

[3] M. Colpi *et al.*, "Lisa definition study report," 2024.

[4] A. Einstein, *The foundation of the General Theory of Relativity.* Princeton University Press, 1915.

[5] A. Einstein, "On the Electrodynamics of Moving Bodies," *Annalen der Physik*, pp. 891–921, 1905.

[6] Planck Collaboration, "Planck 2015 results - XIII. cosmological parameters," *Astronomy and Astrophysics*, vol. 594, p. A13, 2016.

[7] C. W. Misner *et al.*, *Gravitation.* San Francisco: W. H. Freeman, 1973.

[8] B. Allen, "The stochastic gravity-wave background: sources and detection," 1996.

[9] B. Allen and J. D. Romano, "Detecting a stochastic background of gravitational radiation: Signal processing strategies and sensitivities," *Physical Review D*, vol. 59, no. 10, Mar 1999.

[10] J. D. Romano, "Searches for stochastic gravitational-wave backgrounds," 2023.

[11] S. Babak, *Gravitational waves form coalescing binaries.* Morgan & Claypool Publishers, 2020.

[12] LIGO collaboration, "LIGO webpage."

[13] K. D. Kokkotas and B. G. Schmidt, "Quasi-normal modes of stars and black holes," *Living Reviews in Relativity*, vol. 2, no. 1, sep 1999.

[14] C. Caprini *et al.*, "Science with the space-based interferometer elisa. ii: gravitational waves from cosmological phase transitions," *Journal of Cosmology and Astroparticle Physics*, vol. 2016, no. 04, p. 001–001, Apr. 2016.

[15] C. Caprini and R. Durrer, "Gravitational waves from stochastic relativistic sources: Primordial turbulence and magnetic fields," *Physical Review D*, vol. 74, no. 6, Sep 2006.

[16] R. Durrer, "Gravitational waves from cosmological phase transitions," *Journal of Physics: Conference Series*, vol. 222, p. 012021, apr 2010.

[17] M. Hindmarsh *et al.*, "Gravitational waves from the sound of a first order phase transition," *Physical Review Letters*, vol. 112, no. 4, Jan 2014.

[18] C. Grojean and G. Servant, "Gravitational waves from phase transitions at the electroweak scale and beyond," *Physical Review D*, vol. 75, no. 4, Feb 2007.

[19] A. H. Guth, "Inflationary universe: A possible solution to the horizon and flatness problems," *Phys. Rev. D*, vol. 23, pp. 347–356, Jan 1981.

[20] J. R. Espinosa *et al.*, "Energy budget of cosmological first-order phase transitions," *Journal of Cosmology and Astroparticle Physics*, vol. 2010, no. 06, 6 2010.

[21] A. D. Linde, "A New Inflationary Universe Scenario: A Possible Solution of the Horizon, Flatness, Homogeneity, Isotropy and Primordial Monopole Problems," *Phys. Lett. B*, vol. 108, pp. 389–393, 1982.

[22] NASA WMAP collaboration, "WMAP webpage."

[23] Planck collaboration, "Planck webpage."

[24] N. Aghanim *et al.*, "Planck 2018 results: VI. cosmological parameters," *Astronomy and Astrophysics*, vol. 641, p. A6, Sep. 2020.

[25] S. Weinberg, *Cosmology.* John Wiley & Sons Inc., 2008.

[26] W. Hu and M. White, "A CMB polarization primer," *New Astronomy*, vol. 2, no. 4, p. 323–344, Oct 1997.

[27] P. D. Lasky *et al.*, "Gravitational-wave cosmology across 29 decades in frequency," *Physical Review X*, vol. 6, no. 1, Mar 2016.

[28] T. Vachaspati *et al.*, "Cosmic strings," *Scholarpedia*, vol. 10, no. 2, p. 31682, 2015.

[29] M. B. Hindmarsh and T. W. B. Kibble, "Cosmic strings," *Reports on Progress in Physics*, vol. 58, no. 5, p. 477–562, May 1995.

[30] A. Vilenkin, "Cosmic strings," *Phys. Rev. D*, vol. 24, pp. 2082–2089, Oct 1981.

[31] P. Villanueva-Domingo *et al.*, "A brief review on primordial black holes as dark matter," *Frontiers in Astronomy and Space Sciences*, vol. 8, 2021.

[32] E. Bagui *et al.*, "Primordial black holes and their gravitational-wave signatures," 2023.

[33] S. Bird *et al.*, "Did ligo detect dark matter?" *Phys. Rev. Lett.*, vol. 116, p. 201301, May 2016.

[34] S. Clesse and J. García-Bellido, "The clustering of massive primordial black holes as dark matter: Measuring their mass distribution with advanced ligo," *Physics of the Dark Universe*, vol. 15, p. 142–147, Mar. 2017.

[35] JWST collaboration, "James webb space telescope webpage."

[36] H. Atek *et al.*, "Revealing galaxy candidates out to z $\sim$ 16 with jwst observations of the lensing cluster smacs0723," *Monthly Notices of the Royal Astronomical Society*, vol. 519, no. 1, p. 1201–1220, Dec. 2022.

[37] American Physical Society, "APS archives."

[38] S. Gottardo, "New astronomical observations: Joseph weber's contribution to gravitational waves and neutrinos detection," *Substantia*, vol. 1, pp. 61–67, 04 2017.

[39] J. M. Weisberg and J. H. Taylor, "Relativistic binary pulsar b1913+16: Thirty years of observations and analysis," 2004.

[40] R. A. Hulse and J. H. Taylor, "Discovery of a pulsar in a binary system." *The Astrophysical Journal Letters*, vol. 195, pp. L51–L53, Jan. 1975.

[41] J. H. Taylor and J. M. Weisberg, "Further experimental tests of relativistic gravity using the binary pulsar psr 1913+16," *The Astrophysical Journal*, vol. 345, p. 434, Oct. 1989.

[42] B. P. Abbot *et al.*, "Ligo: the laser interferometer gravitational-wave observatory," *Reports on Progress in Physics*, vol. 72, no. 7, p. 076901, jun 2009.

[43] B. P. Abbott *et al.*, "Observation of gravitational waves from a binary black hole merger," *Phys. Rev. Lett.*, vol. 116, p. 061102, Feb 2016.

[44] GEO600 collaboration, *GEO600 interferometer webpage.*

[45] T. Accadia *et al.*, "Virgo: a laser interferometer to detect gravitational waves," *Journal of Instrumentation*, vol. 7, no. 3, p. 3012, mar 2012.

[46] Y. Aso *et al.*, "Interferometer design of the kagra gravitational wave detector," *Phys. Rev. D*, vol. 88, p. 043007, Aug 2013.

[47] LVK collaboration, "Lvk observing plans."

[48] B. P. Abbott *et al.*, "Gw170817: Observation of gravitational waves from a binary neutron star inspiral," *Phys. Rev. Lett.*, vol. 119, p. 161101, Oct 2017.

[49] A. Goldstein *et al.*, "An ordinary short gamma-ray burst with extraordinary implications: Fermi-GBM detection of GRB 170817a," *The Astrophysical Journal Letters*, vol. 848, no. 2, p. L14, Oct. 2017.

[50] Fermi-GBM collaboration, "Fermi GBM webpage."

[51] LIGO-India collaboration, *LIGO-India interferometer webpage.*

[52] Cosmic Explorer collaboration, *Cosmic Explorer interferometer webpage.*

[53] E. steering committee *et al.*, "Einstein telescope: Science case, design study and feasibility

report. et-0028a-20,” 2020.

[54] P. R. Saulson, “If light waves are stretched by gravitational waves, how can we use light as a ruler to detect gravitational waves?” *American Journal of Physics*, vol. 65, no. 6, pp. 501–505, 1997.

[55] J. Aasi *et al.*, “Advanced ligo,” *Classical and Quantum Gravity*, vol. 32, no. 7, p. 074001, Mar 2015.

[56] M. Pitkin *et al.*, “Gravitational wave detection by interferometry (ground and space),” *Living Reviews in Relativity*, vol. 14, no. 1, Jul 2011.

[57] S. Rowan and J. Hough, “The detection of gravitational waves,” no. OPEN-2000-258, 1999.

[58] Y. Gong *et al.*, “Concepts and status of chinese space gravitational wave detection projects,” *Nature Astronomy*, vol. 5, no. 9, p. 881–889, Sep. 2021.

[59] Z. Luo *et al.*, “A brief analysis to taiji: Science and technology,” *Results in Physics*, vol. 16, p. 102918, 2020.

[60] J. Luo *et al.*, “Tianqin: a space-borne gravitational wave detector,” *Classical and Quantum Gravity*, vol. 33, no. 3, p. 035010, jan 2016.

[61] S. Kawamura *et al.*, “Current status of space gravitational wave antenna decigo and b-decigo,” 2020.

[62] R. W. Hellings and G. S. Downs, “Upper limits on the isotropic gravitational radiation background from pulsar timing analysis.” *The Astrophysical Journal Letters*, vol. 265, pp. L39–L42, Feb. 1983.

[63] Janssen, G. H. *et al.*, “Multi-telescope timing of psr j1518+4904,” *Journal of Astrophysics and Astronomy*, vol. 490, no. 2, pp. 753–761, 2008.

[64] R. N. Manchester *et al.*, “The Parkes Pulsar Timing Array Project,” *Publ. Astron. Soc. Austral.*, vol. 30, p. 17, 2013.

[65] F. Jenet *et al.*, “The north american nanohertz observatory for gravitational waves,” 2009.

[66] C. Smarra *et al.*, “Second data release from the european pulsar timing array: Challenging the ultralight dark matter paradigm,” *Physical Review Letters*, vol. 131, no. 17, Oct. 2023.

[67] J. Antoniadis *et al.*, “The second data release from the european pulsar timing array: V. implications for massive black holes, dark matter and the early universe,” 2023.

[68] J. Antoniadis *et al.*, “The second data release from the european pulsar timing array: IV. search for continuous gravitational wave signals,” 2023.

[69] J. Antoniadis *et al.*, “The second data release from the european pulsar timing array: III. search for gravitational wave signals,” *Astronomy and Astrophysics*, vol. 678, p. A50, oct 2023.

[70] J. Antoniadis *et al.*, “The second data release from the european pulsar timing array: II. customised pulsar noise models for spatially correlated gravitational waves,” *Astronomy and Astrophysics*, vol. 678, p. A49, oct 2023.

[71] J. Antoniadis *et al.*, “The second data release from the european pulsar timing array: I. the dataset and timing analysis,” *Astronomy and Astrophysics*, vol. 678, p. A48, oct 2023.

[72] G. Agazie *et al.*, “The nanograv 15 yr data set: Evidence for a gravitational-wave background,” *The Astrophysical Journal Letters*, vol. 951, no. 1, p. L8, jun 2023.

[73] G. Agazie *et al.*, “The nanograv 15 yr data set: Constraints on supermassive black hole binaries from the gravitational-wave background,” *The Astrophysical Journal Letters*, vol. 952, no. 2, p. L37, aug 2023.

[74] D. J. Reardon *et al.*, “Search for an isotropic gravitational-wave background with the parkes pulsar timing array,” *The Astrophysical Journal Letters*, vol. 951, no. 1, p. L6, Jun. 2023.

[75] K. J. Lee, “Prospects of Gravitational Wave Detection Using Pulsar Timing Array for Chinese Future Telescopes,” in *Frontiers in Radio Astronomy and FAST Early Sciences Symposium 2015*, ser. Astronomical Society of the Pacific Conference Series, L. Qain and D. Li, Eds., vol. 502, Feb. 2016, p. 19.

[76] M. T. Miles *et al.*, “The meerkat pulsar timing array: first data release,” *Monthly Notices*

of the Royal Astronomical Society, vol. 519, p. 3976–3991, Mar 2023.

[77] P. Tarafdar *et al.*, "The indian pulsar timing array: First data release," *Publications of the Astronomical Society of Australia*, vol. 39, p. e053, 2022.

[78] H. Xu *et al.*, "Searching for the Nano-Hertz Stochastic Gravitational Wave Background with the Chinese Pulsar Timing Array Data Release I," *Research in Astronomy and Astrophysics*, vol. 23, no. 7, p. 075024, Jul. 2023.

[79] G. Hobbs *et al.*, "The international pulsar timing array project: using pulsars as a gravitational wave detector," *Classical and Quantum Gravity*, vol. 27, no. 8, p. 084013, Apr. 2010.

[80] R. N. Manchester, "The international pulsar timing array," *Classical and Quantum Gravity*, vol. 30, no. 22, p. 224010, Nov. 2013.

[81] J. P. W. Verbiest *et al.*, "The International Pulsar Timing Array: First data release," *Monthly Notices of the Royal Astronomical Society*, vol. 458, p. 1267–1288, May 2016.

[82] P. Amaro-Seoane *et al.*, "Laser Interferometer Space Antenna," *arXiv e-prints*, Feb. 2017.

[83] J.-B. Bayle, "Simulation and data analysis for lisa (instrumental modeling, time-delay interferometry, noise-reduction performance study, and discrimination of transient gravitational signals)," PhD. Thesis, 2019.

[84] M. Armano *et al.*, ""sub-femto-g free fall for space-based gravitational wave observatories: Lisa pathfinder results"," *Phys. Rev. Lett.*, vol. 116, p. 231101, Jun 2016.

[85] M. Armano *et al.*, "Beyond the required lisa free-fall performance: New lisa pathfinder results down to 20 μHz," *Phys. Rev. Lett.*, vol. 120, p. 061101, Feb 2018.

[86] Q. Baghi *et al.*, "Detection and characterization of instrumental transients in lisa pathfinder and their projection to lisa," *Phys. Rev. D*, vol. 105, p. 042002, Feb 2022.

[87] "Esa webpage."

[88] S. Barke *et al.*, "LISA metrology system-final report," 2014.

[89] J.-B. Bayle and O. Hartwig, "Unified model for the lisa measurements and instrument simulations," *Phys. Rev. D*, vol. 107, p. 083019, Apr 2023.

[90] LISA Instrument Group, "Lisa performance model and error budget," Technical report, 2018, lISA-LCST-INST-TN-003.

[91] LISA Instrument Group, "Lisa tilt-to-length and optical alignment analysis," Technical report, 2020, lISA-UOKB-INST-TN-004.

[92] J.-B. Bayle *et al.*, "Adapting time-delay interferometry for lisa data in frequency," *Phys. Rev. D*, vol. 104, p. 023006, Jul 2021.

[93] M. Tinto and S. V. Dhurandhar, "Time-delay interferometry," *Living Reviews in Relativity*, vol. 17, p. 6, Aug 2014.

[94] J. W. Armstrong *et al.*, "Time-delay interferometry for space-based gravitational wave searches," *The Astrophysical Journal*, vol. 527, no. 2, p. 814, dec 1999.

[95] M. Tinto and J. W. Armstrong, "Cancellation of laser noise in an unequal-arm interferometer detector of gravitational radiation," *Phys. Rev. D*, vol. 59, p. 102003, Apr 1999.

[96] M. Tinto *et al.*, "Time-delay interferometry for lisa," *Phys. Rev. D*, vol. 65, p. 082003, Apr 2002.

[97] F. B. Estabrook *et al.*, "Time-delay analysis of lisa gravitational wave data: Elimination of spacecraft motion effects," *Phys. Rev. D*, vol. 62, p. 042002, Jul 2000.

[98] S. V. Dhurandhar *et al.*, "Algebraic approach to time-delay data analysis for lisa," *Physical Review D*, vol. 65, no. 10, May 2002.

[99] K. R. Nayak and J.-Y. Vinet, "Algebraic approach to time-delay data analysis for orbiting lisa," *Phys. Rev. D*, vol. 70, p. 102003, Nov 2004.

[100] M. Tinto *et al.*, "Time delay interferometry with moving spacecraft arrays," *Phys. Rev. D*, vol. 69, p. 082001, Apr 2004.

[101] N. J. Cornish and R. W. Hellings, "The effects of orbital motion on lisa time delay interferometry," *Classical and Quantum Gravity*, vol. 20, no. 22, p. 4851–4860, Oct. 2003.

[102] D. A. Shaddock *et al.*, "Data combinations accounting for lisa spacecraft motion," *Physical Review D*, vol. 68, no. 6, Sep. 2003.

[103] M. Vallisneri, "Geometric time delay interferometry," *Phys. Rev. D*, vol. 72, p. 042003, Aug 2005.

[104] T. A. Prince *et al.*, "Lisa optimal sensitivity," *Phys. Rev. D*, vol. 66, p. 122002, Dec 2002.

[105] M. Muratore *et al.*, "Effectiveness of null time-delay interferometry channels as instrument noise monitors in lisa," *Phys. Rev. D*, vol. 107, p. 082004, Apr 2023.

[106] Q. Baghi *et al.*, "Model-independent time-delay interferometry based on principal component analysis," *Phys. Rev. D*, vol. 104, p. 122001, Dec 2021.

[107] M. Vallisneri *et al.*, "Time-delay interferometry without delays," *Physical Review D*, vol. 103, no. 8, Apr. 2021.

[108] J. N. Reinhardt *et al.*, "Ranging sensor fusion in LISA data processing: Treatment of ambiguities, noise, and onboard delays in lisa ranging observables," *Physical Review D*, vol. 109, no. 2, Jan. 2024.

[109] M. Staab *et al.*, "Laser noise residuals in lisa from onboard processing and time-delay interferometry," 2023.

[110] O. Hartwig *et al.*, "Time-delay interferometry without clock synchronization," *Physical Review D*, vol. 105, no. 12, Jun. 2022.

[111] L. Blanchet *et al.*, "Gravitational-wave phasing of quasicircular compact binary systems to the fourth-and-a-half post-newtonian order," *Phys. Rev. Lett.*, vol. 131, p. 121402, Sep 2023.

[112] F. Pretorius, "Evolution of binary black hole spacetimes," *Phys. Rev. Lett.*, vol. 95, p. 121101, 2005.

[113] S. Collaboration, http://www.black-holes.org/waveforms.

[114] K. Jani *et al.*, "Georgia tech catalog of gravitational waveforms," *Classical and Quantum Gravity*, vol. 33, 10 2016.

[115] B. Aylott *et al.*, "Testing gravitational-wave searches with numerical relativity waveforms: results from the first numerical injection analysis (ninja) project," *Classical and Quantum Gravity*, vol. 26, no. 16, p. 165008, Aug. 2009.

[116] P. Ajith *et al.*, "The ninja-2 catalog of hybrid post-newtonian/numerical-relativity waveforms for non-precessing black-hole binaries," *Classical and Quantum Gravity*, vol. 29, no. 12, p. 124001, Jun. 2012.

[117] B. Wardell *et al.*, "Gravitational waveforms for compact binaries from second-order self-force theory," *Physical Review Letters*, vol. 130, no. 24, Jun. 2023.

[118] A. Pound *et al.*, "Second-order self-force calculation of gravitational binding energy in compact binaries," *Physical Review Letters*, vol. 124, no. 2, Jan. 2020.

[119] K. Mackewicz and R. M. Wald, "Spin self-force," *Phys. Rev. D*, vol. 100, p. 104043, Nov 2019.

[120] J. Mathews *et al.*, "Self-force calculations with a spinning secondary," *Phys. Rev. D*, vol. 105, no. 8, p. 084031, 2022.

[121] T. Islam *et al.*, "Comparing numerical relativity and perturbation theory waveforms for a non-spinning equal-mass binary," *Universe*, vol. 10, no. 1, 2024.

[122] M. van de Meent *et al.*, "Enhancing the seobnrv5 effective-one-body waveform model with second-order gravitational self-force fluxes," 2023.

[123] A. Buonanno and T. Damour, "Effective one-body approach to general relativistic two-body dynamics," *Phys. Rev. D*, vol. 59, p. 084006, Mar 1999.

[124] A. Buonanno and T. Damour, "Transition from inspiral to plunge in binary black hole coalescences," *Phys. Rev. D*, vol. 62, p. 064015, Aug 2000.

[125] T. Damour, "Coalescence of two spinning black holes: an effective one-body approach," *Phys. Rev. D*, vol. 64, p. 124013, 2001.

[126] A. Buonanno *et al.*, "Transition from inspiral to plunge in precessing binaries of spinning black holes," *Phys. Rev. D*, vol. 74, p. 104005, 2006.

[127] T. Damour, “Introductory lectures on the Effective One Body formalism,” *Int. J. Mod. Phys. A*, vol. 23, pp. 1130–1148, 2008.

[128] V. Varma *et al.*, “Surrogate models for precessing binary black hole simulations with unequal masses,” *Phys. Rev. Res.*, vol. 1, p. 033015, Oct 2019.

[129] S. Husa *et al.*, “Frequency-domain gravitational waves from nonprecessing black-hole binaries. i. new numerical waveforms and anatomy of the signal,” *Phys. Rev. D*, vol. 93, p. 044006, Feb 2016.

[130] S. Khan *et al.*, “Frequency-domain gravitational waves from nonprecessing black-hole binaries. ii. a phenomenological model for the advanced detector era,” *Phys. Rev. D*, vol. 93, p. 044007, Feb 2016.

[131] L. London *et al.*, “First higher-multipole model of gravitational waves from spinning and coalescing black-hole binaries,” *Phys. Rev. Lett.*, vol. 120, p. 161102, Apr 2018.

[132] C. Pitte *et al.*, “Detectability of higher harmonics with lisa,” *Phys. Rev. D*, vol. 108, p. 044053, Aug 2023.

[133] V. Kapil *et al.*, “Systematic bias from waveform modeling for binary black hole populations in next-generation gravitational wave detectors,” *Physical Review D*, vol. 109, no. 10, May 2024.

[134] A. J. Chua *et al.*, “Augmented kludge waveforms for detecting extreme-mass-ratio inspirals,” *Physical Review D*, vol. 96, no. 4, Aug. 2017.

[135] M. L. Katz *et al.*, “FastEMRIWaveforms: New tools for millihertz gravitational-wave data analysis,” 4 2021.

[136] M. L. Katz *et al.*, “BlackHolePerturbationToolkit/FastEMRIWaveforms: Frequency Domain Waveform Added!” Jul. 2023.

[137] A. J. Chua and J. R. Gair, “Improved analytic extreme-mass-ratio inspiral model for scoping out eLISA data analysis,” *Class. Quant. Grav.*, vol. 32, p. 232002, 2015.

[138] A. J. Chua *et al.*, “Reduced-order modeling with artificial neurons for gravitational-wave inference,” *Phys. Rev. Lett.*, vol. 122, no. 21, p. 211101, 2019.

[139] A. J. K. Chua *et al.*, “Rapid generation of fully relativistic extreme-mass-ratio-inspiral waveform templates for LISA data analysis,” *Phys. Rev. Lett.*, vol. 126, no. 5, p. 051102, 2021.

[140] R. Fujita and M. Shibata, “Extreme mass ratio inspirals on the equatorial plane in the adiabatic order,” *Phys. Rev. D*, vol. 102, no. 6, p. 064005, 2020.

[141] L. C. Stein and N. Warburton, “Location of the last stable orbit in Kerr spacetime,” *Phys. Rev. D*, vol. 101, no. 6, p. 064007, 2020.

[142] L. Barack and C. Cutler, “LISA capture sources: Approximate waveforms, signal-to-noise ratios, and parameter estimation accuracy,” *Phys. Rev. D*, vol. 69, p. 082005, 2004.

[143] L. Speri *et al.*, “Fast and Fourier: Extreme Mass Ratio Inspiral Waveforms in the Frequency Domain,” 7 2023.

[144] V. Korol *et al.*, “Observationally driven galactic double white dwarf population for lisa,” *Monthly Notices of the Royal Astronomical Society*, vol. 511, no. 4, p. 5936–5947, Feb. 2022.

[145] A. Sesana, “Prospects for multiband gravitational-wave astronomy after gw150914,” *Phys. Rev. Lett.*, vol. 116, p. 231102, Jun 2016.

[146] B. P. Abbott *et al.*, “Search for the isotropic stochastic background using data from advanced ligo’s second observing run,” *Phys. Rev. D*, vol. 100, p. 061101, Sep 2019.

[147] P. Auclair *et al.*, “Cosmology with the laser interferometer space antenna,” *Living Reviews in Relativity*, 2023.

[148] C. Caprini *et al.*, “Reconstructing the spectral shape of a stochastic gravitational wave background with lisa,” *Journal of Cosmology and Astroparticle Physics*, vol. 2019, no. 11, p. 017–017, Nov. 2019.

[149] R. Flauger *et al.*, “Improved reconstruction of a stochastic gravitational wave background with LISA,” *JCAP*, vol. 01, p. 059, 2021.

[150] T. B. Littenberg and N. J. Cornish, “Prototype global analysis of lisa data with multiple

source types," *Physical Review D*, vol. 107, no. 6, Mar. 2023.

[151] LISA Consortium, "Lisa data challenge."

[152] M. Le Jeune and S. Babak, "Lisa data challenge sangria (ldc2a)," Oct. 2022.

[153] P. Amaro-Seoane *et al.*, "Astrophysics with the laser interferometer space antenna," 2022.

[154] K. G. Arun *et al.*, "New horizons for fundamental physics with lisa," *Living Reviews in Relativity*, 2022.

[155] K. S. Thorne, "Multipole expansions of gravitational radiation," *Rev. Mod. Phys.*, vol. 52, pp. 299–339, Apr 1980.

[156] R. Wald, *General Realtivity.* University of Chicago Press, 1984.

[157] S. Chandrasekhar, *The mathematical theory of black holes.* Oxford University Press, 1985.

[158] T. Regge and J. A. Wheeler, "Stability of a schwarzschild singularity," *Phys. Rev.*, vol. 108, pp. 1063–1069, Nov 1957.

[159] F. J. Zerilli, "Gravitational field of a particle falling in a schwarzschild geometry analyzed in tensor harmonics," *Phys. Rev. D*, vol. 2, pp. 2141–2160, Nov 1970.

[160] S. A. Teukolsky, "Perturbations of a Rotating Black Hole. I. Fundamental Equations for Gravitational, Electromagnetic, and Neutrino-Field Perturbations," *The Astrophysical Journal*, vol. 185, pp. 635–648, Oct. 1973.

[161] W. H. Press and S. A. Teukolsky, "Perturbations of a Rotating Black Hole. II. Dynamical Stability of the Kerr Metric," *The Astrophysical Journal*, vol. 185, pp. 649–674, Oct. 1973.

[162] K. Schwarzschild, "On the gravitational field of a mass point according to einstein's theory," 1999.

[163] H. Reissner, "Über die Eigengravitation des elektrischen Feldes nach der Einsteinschen Theorie," *Annalen der Physik*, vol. 355, no. 9, pp. 106–120, Jan. 1916.

[164] G. Nordström, "On the Energy of the Gravitation field in Einstein's Theory," *Koninklijke Nederlandse Akademie van Wetenschappen Proceedings Series B Physical Sciences*, vol. 20, pp. 1238–1245, Jan. 1918.

[165] R. P. Kerr, "Gravitational field of a spinning mass as an example of algebraically special metrics," *Phys. Rev. Lett.*, vol. 11, pp. 237–238, Sep 1963.

[166] E. T. Newman *et al.*, "Metric of a Rotating, Charged Mass," *Journal of Mathematical Physics*, vol. 6, no. 6, pp. 918–919, Jun. 1965.

[167] S. W. Hawking, "Black holes in general relativity," *Communications in Mathematical Physics*, vol. 25, pp. 152–166, 1972.

[168] B. Carter, "Axisymmetric black hole has only two degrees of freedom," *Phys. Rev. Lett.*, vol. 26, pp. 331–333, Feb 1971.

[169] W. Israel, "Event horizons in static vacuum space-times," *Phys. Rev.*, vol. 164, pp. 1776–1779, Dec 1967.

[170] D. C. Robinson, "Uniqueness of the kerr black hole," *Phys. Rev. Lett.*, vol. 34, pp. 905–906, Apr 1975.

[171] S. Chandrasekhar and S. Detweiler, "The quasi-normal modes of the schwarzschild black hole," *Proceedings of the Royal Society of London. A. Mathematical and Physical Sciences*, vol. 344, no. 1639, pp. 441–452, 1975.

[172] R. Penrose, "The question of cosmic censorship," *Journal of Astrophysics and Astronomy*, pp. 233–248, 1999.

[173] S. W. Hawking, "Gravitational radiation from colliding black holes," *Phys. Rev. Lett.*, vol. 26, pp. 1344–1346, May 1971.

[174] S. W. Hawking, "Particle creation by black holes," *Communications in Mathematical Physics*, pp. 199–220, 1975.

[175] D. Christodoulou and S. Klainerman, "The Global nonlinear stability of the Minkowski space," 1993.

[176] S. Klainerman and J. Szeftel, "Global nonlinear stability of schwarzschild spacetime under polarized perturbations," 2018.

[177] S. Klainerman and J. Szeftel, “Kerr stability for small angular momentum,” 2021.

[178] E. Giorgi *et al.*, “Wave equations estimates and the nonlinear stability of slowly rotating kerr black holes,” 2022.

[179] L. Rezzolla, “Gravitational waves from perturbed black holes and relativistic stars,” 2003.

[180] E. Newman and R. Penrose, “An Approach to Gravitational Radiation by a Method of Spin Coefficients,” *Journal of Mathematical Physics*, vol. 3, no. 3, pp. 566–578, May 1962.

[181] J. N. Goldberg and R. K. Sachs, “Republication of: A theorem on petrov types,” *General Relativity and Gravitation*, vol. 41, pp. 433–444, 1962.

[182] E. Berti *et al.*, “Quasinormal modes of black holes and black branes,” *Classical and Quantum Gravity*, vol. 26, no. 16, p. 163001, Jul. 2009.

[183] N. Franchini and S. H. Völkel, “Testing General Relativity with Black Hole Quasi-Normal Modes,” 5 2023.

[184] E. W. Leaver, “An Analytic representation for the quasi normal modes of Kerr black holes,” *Proc. Roy. Soc. Lond. A*, vol. 402, pp. 285–298, 1985.

[185] G. B. Cook and M. Zalutskiy, “Gravitational perturbations of the kerr geometry: High-accuracy study,” *Phys. Rev. D*, vol. 90, p. 124021, Dec 2014.

[186] H.-P. Nollert, “Topical review: Quasinormal modes: the characteristic ‘sound’ of black holes and neutron stars,” *Classical Quantum Gravity*, vol. 16, pp. 159–216, 1999.

[187] S. L. Detweiler, “Resonant oscillations of a rapidly rotating black hole,” *Proc. Roy. Soc. Lond. A*, vol. 352, pp. 381–395, 1977.

[188] S. L. Detweiler, “Black holes and gravitational waves. I. Circular orbits about a rotating hole.” *The Astrophysical Journal*, vol. 225, pp. 687–693, Nov. 1978.

[189] C. V. Vishveshwara, “Stability of the schwarzschild metric,” *Phys. Rev. D*, vol. 1, pp. 2870–2879, May 1970.

[190] G. Pöschl and E. Teller, “Bemerkungen zur quantenmechanik des anharmonischen oszillators,” *Zeitschrift für Physik*, p. 143, 1933.

[191] V. Ferrari and B. Mashhoon, “New approach to the quasinormal modes of a black hole,” *Phys. Rev. D*, vol. 30, pp. 295–304, Jul 1984.

[192] E. Berti *et al.*, “Gravitational-wave spectroscopy of massive black holes with the space interferometer lisa,” *Phys. Rev. D*, vol. 73, p. 064030, Mar 2006.

[193] E. Berti, “Kerr qnm notebook.”

[194] L. C. Stein, “qnm: A Python package for calculating Kerr quasinormal modes, separation constants, and spherical-spheroidal mixing coefficients,” *J. Open Source Softw.*, vol. 4, no. 42, p. 1683, 2019.

[195] L. Magaña Zertuche *et al.*, “High precision ringdown modeling: Multimode fits and bms frames,” *Phys. Rev. D*, vol. 105, p. 104015, May 2022.

[196] M. H.-Y. Cheung *et al.*, “Nonlinear effects in black hole ringdown,” 2022.

[197] M. H.-Y. Cheung *et al.*, “Extracting linear and nonlinear quasinormal modes from black hole merger simulations,” *Phys. Rev. D*, vol. 109, p. 044069, Feb 2024.

[198] F. Echeverria, “Gravitational-wave measurements of the mass and angular momentum of a black hole,” *Phys. Rev. D*, vol. 40, pp. 3194–3203, Nov 1989.

[199] L. London and E. Fauchon-Jones, “On modeling for kerr black holes: basis learning, qnm frequencies, and spherical-spheroidal mixing coefficients,” *Classical and Quantum Gravity*, vol. 36, no. 23, p. 235015, Nov. 2019.

[200] V. Baibhav *et al.*, “Agnostic black hole spectroscopy: Quasinormal mode content of numerical relativity waveforms and limits of validity of linear perturbation theory,” *Phys. Rev. D*, vol. 108, p. 104020, Nov 2023.

[201] M. Giesler *et al.*, “Black hole ringdown: The importance of overtones,” *Phys. Rev. X*, vol. 9, p. 041060, Dec 2019.

[202] S. Bhagwat *et al.*, “Ringdown overtones, black hole spectroscopy, and no-hair theorem tests,” *Phys. Rev. D*, vol. 101, p. 044033, Feb 2020.

[203] M. Isi and W. M. Farr, “Analyzing black-hole ringdowns,” Jul 2021.

[204] L. London *et al.*, “Modeling ringdown: Beyond the fundamental quasinormal modes,” *Phys. Rev. D*, vol. 90, p. 124032, Dec 2014.

[205] S. Bhagwat *et al.*, “On choosing the start time of binary black hole ringdowns,” *Phys. Rev. D*, vol. 97, p. 104065, May 2018.

[206] X. J. Forteza and P. Mourier, “High-overtone fits to numerical relativity ringdowns: Beyond the dismissed $n = 8$ special tone,” *Phys. Rev. D*, vol. 104, p. 124072, Dec 2021.

[207] M. Isi *et al.*, “Testing the no-hair theorem with gw150914,” *Phys. Rev. Lett.*, vol. 123, p. 111102, Sep 2019.

[208] R. Cotesta *et al.*, “Analysis of ringdown overtones in gw150914,” *Phys. Rev. Lett.*, vol. 129, p. 111102, Sep 2022.

[209] M. Isi and W. M. Farr, “Revisiting the ringdown of gw150914,” 2022.

[210] M. Isi and W. M. Farr, “Comment on “analysis of ringdown overtones in gw150914”,” *Phys. Rev. Lett.*, vol. 131, p. 169001, Oct 2023.

[211] G. Carullo *et al.*, “Carullo et al. reply:,” *Phys. Rev. Lett.*, vol. 131, p. 169002, Oct 2023.

[212] I. Kamaretsos *et al.*, “Black-hole hair loss: Learning about binary progenitors from ringdown signals,” *Phys. Rev. D*, vol. 85, p. 024018, Jan 2012.

[213] I. Kamaretsos *et al.*, “Is black-hole ringdown a memory of its progenitor?” *Phys. Rev. Lett.*, vol. 109, p. 141102, Oct 2012.

[214] S. Gossan *et al.*, “Bayesian model selection for testing the no-hair theorem with black hole ringdowns,” *Phys. Rev. D*, vol. 85, p. 124056, Jun 2012.

[215] E. Berti and A. Klein, “Mixing of spherical and spheroidal modes in perturbed kerr black holes,” *Phys. Rev. D*, vol. 90, p. 064012, Sep 2014.

[216] B. J. Kelly and J. G. Baker, “Decoding mode mixing in black-hole merger ringdown,” *Physical Review D*, vol. 87, no. 8, apr 2013.

[217] R. J. Gleiser *et al.*, “Gravitational radiation from schwarzschild black holes: the second-order perturbation formalism,” *Physics Reports*, vol. 325, no. 2, p. 41–81, Feb. 2000.

[218] H. Nakano and K. Ioka, “Second-order quasinormal mode of the schwarzschild black hole,” *Physical Review D*, vol. 76, no. 8, Oct. 2007.

[219] N. Loutrel *et al.*, “Second-order perturbations of kerr black holes: Formalism and reconstruction of the first-order metric,” *Physical Review D*, vol. 103, no. 10, May 2021.

[220] M. Lagos and L. Hui, “Generation and propagation of nonlinear quasi-normal modes of a schwarzschild black hole,” 2022.

[221] K. Mitman *et al.*, “Nonlinearities in black hole ringdowns,” 2022.

[222] A. Joyce *et al.*, “Beyond the cosmological standard model,” *Physics Reports*, vol. 568, pp. 1–98, 2015, beyond the cosmological standard model.

[223] T. Clifton *et al.*, “Modified gravity and cosmology,” *Physics Reports*, vol. 513, no. 1, pp. 1–189, 2012, modified Gravity and Cosmology.

[224] S. Shankaranarayanan and J. P. Johnson, “Modified theories of gravity: Why, how and what?” *General Relativity and Gravitation*, vol. 54, no. 5, May 2022.

[225] N. Frusciante, “Deviations from General Relativity in Cosmology and Astrophysics,” Ph.D. dissertation, SISSA - International School for Advanced Studies, 2014.

[226] D. Lovelock, “The Einstein Tensor and Its Generalizations,” *Journal of Mathematical Physics*, vol. 12, no. 3, pp. 498–501, Mar. 1971.

[227] D. Lovelock, “The Four-Dimensionality of Space and the Einstein Tensor,” *Journal of Mathematical Physics*, vol. 13, no. 6, pp. 874–876, Jun. 1972.

[228] H. RUEGG and M. RUIZ-ALTABA, “The stueckelberg field,” *International Journal of Modern Physics A*, vol. 19, no. 20, p. 3265–3347, Aug. 2004.

[229] E. Barausse *et al.*, “Prospects for Fundamental Physics with LISA,” *Gen. Rel. Grav.*, vol. 52, no. 8, p. 81, 2020.

[230] C. Brans and R. H. Dicke, “Mach’s principle and a relativistic theory of gravitation,” *Phys.*

Rev., vol. 124, pp. 925–935, Nov 1961.

[231] G. W. Horndeski, “Second-order scalar-tensor field equations in a four-dimensional space,” *Int. J. Theor. Phys.*, vol. 10, pp. 363–384, 1974.

[232] T. P. Sotiriou and V. Faraoni, “$f(r)$ theories of gravity,” *Rev. Mod. Phys.*, vol. 82, pp. 451–497, Mar 2010.

[233] C. M. Will, “The confrontation between general relativity and experiment,” *Living Reviews in Relativity*, vol. 17, no. 1, Jun. 2014.

[234] C. Molina *et al.*, “Gravitational signature of schwarzschild black holes in dynamical chern-simons gravity,” *Phys. Rev. D*, vol. 81, p. 124021, Jun 2010.

[235] O. J. Tattersall and P. G. Ferreira, “Quasinormal modes of black holes in horndeski gravity,” *Phys. Rev. D*, vol. 97, p. 104047, May 2018.

[236] J. L. Blázquez-Salcedo *et al.*, “Perturbed black holes in einstein-dilaton-gauss-bonnet gravity: Stability, ringdown, and gravitational-wave emission,” *Phys. Rev. D*, vol. 94, p. 104024, Nov 2016.

[237] M. Srivastava *et al.*, “Analytical computation of quasinormal modes of slowly rotating black holes in dynamical chern-simons gravity,” *Phys. Rev. D*, vol. 104, p. 064034, Sep 2021.

[238] P. A. Cano *et al.*, “Gravitational ringing of rotating black holes in higher-derivative gravity,” *Phys. Rev. D*, vol. 105, p. 024064, Jan 2022.

[239] P. A. Cano *et al.*, “Quasinormal modes of rotating black holes in higher-derivative gravity,” *Phys. Rev. D*, vol. 108, p. 124032, Dec 2023.

[240] L. Pierini and L. Gualtieri, “Quasinormal modes of rotating black holes in einstein-dilaton gauss-bonnet gravity: The first order in rotation,” *Phys. Rev. D*, vol. 103, p. 124017, Jun 2021.

[241] L. Pierini and L. Gualtieri, “Quasinormal modes of rotating black holes in einstein-dilaton gauss-bonnet gravity: The second order in rotation,” *Phys. Rev. D*, vol. 106, p. 104009, Nov 2022.

[242] P. Wagle *et al.*, “Quasinormal modes of slowly-rotating black holes in dynamical chern-simons gravity,” *Phys. Rev. D*, vol. 105, p. 124003, Jun 2022.

[243] A. K.-W. Chung and N. Yunes, “Ringing out general relativity: Quasi-normal mode frequencies for black holes of any spin in modified gravity,” 2024.

[244] A. K.-W. Chung and N. Yunes, “Quasinormal mode frequencies and gravitational perturbations of black holes with any subextremal spin in modified gravity through metrics: The scalar-gauss-bonnet gravity case,” p. 064019, Sep 2024.

[245] J. L. Jaramillo *et al.*, “Pseudospectrum and black hole quasinormal mode instability,” *Phys. Rev. X*, vol. 11, p. 031003, Jul 2021.

[246] C. Pitte *et al.*, “Exploring tests of the no-hair theorem with lisa,” *Phys. Rev. D*, vol. 110, p. 104003, Nov 2024.

[247] J. Aasi *et al.*, “Advanced ligo,” *Classical and Quantum Gravity*, vol. 32, no. 7, p. 074001, mar 2015.

[248] B. P. Abbott *et al.*, “Tests of general relativity with the binary black hole signals from the ligo-virgo catalog gwtc-1,” *Phys. Rev. D*, vol. 100, p. 104036, Nov 2019.

[249] B. P. Abbott *et al.*, “Tests of general relativity with gw150914,” *Phys. Rev. Lett.*, vol. 116, p. 221101, May 2016.

[250] R. Abbott *et al.*, “Tests of general relativity with binary black holes from the second ligo-virgo gravitational-wave transient catalog,” *Phys. Rev. D*, vol. 103, p. 122002, Jun 2021.

[251] R. Abbott *et al.*, “Tests of general relativity with gwtc-3,” 2021.

[252] K. G. Arun *et al.*, “New horizons for fundamental physics with LISA,” *Living Rev. Rel.*, vol. 25, no. 1, p. 4, 2022.

[253] O. Dreyer *et al.*, “Black-hole spectroscopy: testing general relativity through gravitational-wave observations,” *Classical and Quantum Gravity*, vol. 21, no. 4, pp. 787–803, jan 2004.

[254] S. Bhagwat and C. Pacilio, “Merger-ringdown consistency: A new test of strong gravity

using deep learning," *Physical Review D*, vol. 104, no. 2, jul 2021.

[255] V. Gennari *et al.*, "Searching for ringdown higher modes with a numerical relativity-informed post-merger model," *The European Physical Journal C*, vol. 84, p. 233, mar 2024.

[256] A. Ghosh *et al.*, "Constraints on quasinormal-mode frequencies with ligo-virgo binary–black-hole observations," *Phys. Rev. D*, vol. 103, p. 124041, Jun 2021.

[257] E. Maggio *et al.*, "Tests of general relativity in the nonlinear regime: A parametrized plunge-merger-ringdown gravitational waveform model," *Phys. Rev. D*, vol. 108, p. 024043, Jul 2023.

[258] Y. Pan *et al.*, "Inspiral-merger-ringdown multipolar waveforms of nonspinning black-hole binaries using the effective-one-body formalism," *Physical Review D*, vol. 84, no. 12, dec 2011.

[259] "Lisabeta," for the moment only accessible for LISA Consortium members.

[260] A. Toubiana *et al.*, "Measuring source properties and quasinormal mode frequencies of heavy massive black-hole binaries with lisa," *Phys. Rev. D*, vol. 109, p. 104019, May 2024.

[261] R. Brito *et al.*, "Black-hole spectroscopy by making full use of gravitational-wave modeling," *Phys. Rev. D*, vol. 98, p. 084038, Oct 2018.

[262] J.-B. Bayle *et al.*, "LISA GW-response."

[263] M. Staab and J.-B. Bayle, "pyTDI."

[264] J.-B. Bayle *et al.*, "LISA Instrument."

[265] C. Pitte *et al.*, "Lisaring: Ringdown analysis tool for LISA," 2024, in preparation.

[266] M. Favata, "The gravitational-wave memory effect," *Classical and Quantum Gravity*, vol. 27, no. 8, p. 084036, Apr. 2010.

[267] H. Inchauspé *et al.*, "Measuring gravitational wave memory with lisa," 2024.

[268] T. B. Littenberg and N. J. Cornish, "Separating gravitational wave signals from instrument artifacts," *Physical Review D*, vol. 82, no. 10, Nov. 2010.

[269] S. Marsat and J. G. Baker, "Fourier-domain modulations and delays of gravitational-wave signals," 2018.

[270] S. Marsat *et al.*, "Exploring the bayesian parameter estimation of binary black holes with LISA," *Physical Review D*, vol. 103, no. 8, apr 2021.

[271] "Black Hole Perturbation Toolkit," (bhptoolkit.org).

[272] C. Cutler and É. E. Flanagan, "Gravitational waves from merging compact binaries: How accurately can one extract the binary's parameters from the inspiral waveform?" *Physical Review D*, vol. 49, no. 6, pp. 2658–2697, mar 1994.

[273] A. Klein *et al.*, "Gravitational waveforms for precessing, quasicircular binaries via multiple scale analysis and uniform asymptotics: The near spin alignment case," *Physical Review D*, vol. 88, no. 12, dec 2013.

[274] LISA Science Study Team, "LISA Science Requirements Document," ESA, Requirement Document ESA-L3-EST-SCI-RS-001-i1.0, May 2018.

[275] K. G. Arun *et al.*, "Erratum: Higher-order spin effects in the amplitude and phase of gravitational waveforms emitted by inspiraling compact binaries: Ready-to-use gravitational waveforms [phys. rev. d 79, 104023 (2009)]," *Phys. Rev. D*, vol. 84, p. 049901, Aug 2011.

[276] J. S. Speagle, "DYNESTY: a dynamic nested sampling package for estimating Bayesian posteriors and evidences," *Monthly Notices of the Royal Astronomical Society*, vol. 493, no. 3, pp. 3132–3158, Apr. 2020.

[277] W. D. Vousden *et al.*, "Dynamic temperature selection for parallel tempering in markov chain monte carlo simulations," *Monthly Notices of the Royal Astronomical Society*, vol. 455, no. 2, pp. 1919–1937, nov 2015.

[278] D. Foreman-Mackey *et al.*, "emcee: The MCMC hammer," *Publications of the Astronomical Society of the Pacific*, vol. 125, no. 925, pp. 306–312, mar 2013.

[279] N. J. Cornish, "Fast fisher matrices and lazy likelihoods," 2010.

[280] N. J. Cornish, "Heterodyned likelihood for rapid gravitational wave parameter inference," *Physical Review D*, vol. 104, no. 10, nov 2021.

[281] L. London, “Modeling ringdown. ii. aligned-spin binary black holes, implications for data analysis and fundamental theory,” *Phys. Rev. D*, vol. 102, p. 084052, Oct 2020.

[282] W. Martens and E. Joffre, “Trajectory Design for the ESA LISA Mission,” 1 2021.

[283] J.-B. Bayle *et al.*, “LISA orbits,” Apr. 2022.

[284] C. Benoit, “Note sur une méthode de résolution des équations normales provenant de l’application de la méthode des moindres carrés a un système d’équations linéaires en nombre inférieur a celui des inconnues. — application de la méthode a la résolution d’un système defini d’équations linéaires,” *Bulletin géodésique*, vol. 2, pp. 67–77, 1924.

[285] N. Levinson, “The wiener (root mean square) error criterion in filter design and prediction,” *Journal of Mathematics and Physics*, vol. 25, no. 1-4, pp. 261–278, 1946.

[286] J. Durbin, “The fitting of time-series models,” *Revue de l’Institut International de Statistique / Review of the International Statistical Institute*, vol. 28, no. 3, pp. 233–244, 1960.

[287] E. Kaasschieter, “Preconditioned conjugate gradients for solving singular systems,” *Journal of Computational and Applied Mathematics*, vol. 24, no. 1, pp. 265–275, 1988.

[288] A. Jain, “Fast inversion of banded toeplitz matrices by circular decompositions,” *IEEE Transactions on Acoustics, Speech, and Signal Processing*, vol. 26, no. 2, pp. 121–126, 1978.

[289] Q. Baghi, “Bayesdawn: Bayesian augmentation method to handle data gaps in gravitational-wave data analysis.” 2020.

[290] P. Virtanen *et al.*, “SciPy 1.0: Fundamental Algorithms for Scientific Computing in Python,” *Nature Methods*, vol. 17, pp. 261–272, 2020.

[291] C. Cutler and M. Vallisneri, “LISA detections of massive black hole inspirals: Parameter extraction errors due to inaccurate template waveforms,” *Physical Review D*, vol. 76, no. 10, nov 2007.

[292] M. Leizerovich *et al.*, “Tensions in cosmology: A discussion of statistical tools to determine inconsistencies,” *Physics Letters B*, vol. 855, p. 138844, 2024.

[293] P. Lemos *et al.*, “Assessing tension metrics with dark energy survey and planck data,” *Monthly Notices of the Royal Astronomical Society*, vol. 505, no. 4, p. 6179–6194, Jun. 2021.

[294] M. Pürrer and C.-J. Haster, “Ready for what lies ahead? – gravitational waveform accuracy requirements for future ground based detectors,” 2019.

[295] Q. Hu and J. Veitch, “Assessing the model waveform accuracy of gravitational waves,” *Physical Review D*, vol. 106, no. 4, Aug. 2022.

[296] P. Saini *et al.*, “Eccentricity-induced systematic error on parametrized tests of general relativity: Hierarchical bayesian inference applied to a binary black hole population,” *Physical Review D*, vol. 109, no. 8, Apr. 2024.

[297] C. Talbot *et al.*, “Gravitational-wave memory: waveforms and phenomenology,” *Phys. Rev. D*, vol. 98, no. 6, p. 064031, 2018.